



**HAL**  
open science

# Experimental investigation of turbulent premixed flames under modern Spark-Ignition engine-like conditions

Marco Di Lorenzo

► **To cite this version:**

Marco Di Lorenzo. Experimental investigation of turbulent premixed flames under modern Spark-Ignition engine-like conditions. Reactive fluid environment. Université d'Orléans, 2019. English. NNT : 2019ORLE3218 . tel-04643729

**HAL Id: tel-04643729**

**<https://theses.hal.science/tel-04643729>**

Submitted on 10 Jul 2024

**HAL** is a multi-disciplinary open access archive for the deposit and dissemination of scientific research documents, whether they are published or not. The documents may come from teaching and research institutions in France or abroad, or from public or private research centers.

L'archive ouverte pluridisciplinaire **HAL**, est destinée au dépôt et à la diffusion de documents scientifiques de niveau recherche, publiés ou non, émanant des établissements d'enseignement et de recherche français ou étrangers, des laboratoires publics ou privés.

**ÉCOLE DOCTORALE**

**ENERGIE, MATERIAUX, SCIENCES DE LA TERRE ET DE L'UNIVERS**

LABORATOIRE PRISME

**THÈSE** présentée par :  
**Marco DI LORENZO**

soutenue le : 19 Décembre 2019

Pour obtenir le grade de : **Docteur de l'université d'Orléans**

Discipline/ Spécialité : Energétique

**Experimental investigation of turbulent  
premixed flames under modern Spark-  
Ignition engine-like conditions**

**THÈSE dirigée par :**

**Fabrice FOUCHER**  
**Christine MOUNAIM-ROUSSELLE**

Professeur, Université d'Orléans  
Professeur, Université d'Orléans

**RAPPORTEURS :**

**Bénédicte CUENOT**  
**Bruno RENO**

IR-HDR, CERFACS de Toulouse  
Professeur, INSA de Rouen

---

**JURY :**

**Nondas MASTORAKOS (Prés.)**  
**Olivier COLIN**  
**Pierre BREQUIGNY**

Professeur, University of Cambridge  
IR-HDR, IFPEN Rueil-Malmaison  
Maître de Conf., Université d'Orléans



---

# 1. Index

---

<b>1. INDEX.....</b>	<b>5</b>
<b>2. ABBREVIATIONS.....</b>	<b>7</b>
<b>3. RÉSUMÉ EN FRANÇAIS .....</b>	<b>11</b>
<b>1. INTRODUCTION .....</b>	<b>23</b>
1.1. BACKGROUND AND MOTIVATION .....	25
1.1.1. <i>Energy and Environment</i> .....	25
1.1.2. <i>Emissions Standards</i> .....	28
1.2. RESEARCH OBJECTIVE AND TECHNICAL BACKGROUND.....	31
1.3. THESIS OUTLINE .....	33
<b>2. THEORY OF PREMIXED FLAMES .....</b>	<b>37</b>
2.1. LAMINAR PREMIXED COMBUSTION .....	39
2.1.1. <i>Definition of Flame Speed</i> .....	40
2.1.2. <i>Flame Thickness</i> .....	42
2.1.3. <i>Flame Front Stretch</i> .....	43
2.1.4. <i>Combustion Instabilities</i> .....	44
2.1.4.1. Instabilities due to the effect of gravitational forces .....	44
2.1.4.2. Hydrodynamic Instabilities .....	44
2.1.4.3. Thermo-diffusive, or Rayleigh-Taylor, Instabilities .....	45
2.1.5. <i>Expanding Flames Laminar Burning Speed</i> .....	48
2.1.6. <i>Markstein Length and Unstretched Laminar Burning Velocity</i> .....	50
2.2. TURBULENT PREMIXED FLAMES.....	52
2.2.1. <i>Turbulence Statistical Approach</i> .....	52
2.2.2. <i>Kolmogorov Theory and Characteristics Scales</i> .....	53
2.2.3. <i>Interaction between Turbulence and Premixed Flames</i> .....	57
2.2.5. <i>Turbulent Flame Characterization in the case of Spherical Expansion</i> .....	62
2.2.5.1. Stretch of the turbulent flame.....	64
2.2.5.2. Bending Effect .....	64
2.2.6. <i>Turbulent Combustion in Spark-Ignition Engines</i> .....	65
2.2.7. <i>Turbulent Flames at High Karlovitz Number</i> .....	68
2.3. CONCLUSIONS.....	70
<b>3. EXPERIMENTAL SET-UPS .....</b>	<b>73</b>
3.1. SPHERICAL SET-UP – LAMINAR CONFIGURATIONS .....	76
3.1.1. <i>Experimental Limits</i> .....	79
3.1.2. <i>Particular conditions due to the reactive mixture</i> .....	79
3.1.2.1. Uncertainties .....	80
3.2. TURBULENT CONFIGURATION .....	81
3.3. NEW ONE SHOT ENGINE.....	83
3.3.1. <i>NOSE Working Principle and Description</i> .....	83
3.3.2. <i>NOSE Operational Procedure</i> .....	86
3.3.3. <i>Implemented Optical Techniques on NOSE</i> .....	87
3.3.4. <i>NOSE Experimental Tests</i> .....	91
3.3.5. <i>Repeatability Tests</i> .....	91
3.4. NOSE LAMINAR CONFIGURATION .....	93
3.5. AERODYNAMIC CHARACTERIZATION .....	94
3.5.1. <i>Characteristics of the Turbulence</i> .....	94
3.5.2. <i>PIV Investigation and Statistical Approach</i> .....	96

3.5.3.	<i>Turbulence Characterization</i> .....	101
3.5.4.	<i>Summary of NOSE Configurations and Turbulence Properties</i> .....	104
3.6.	CONCLUSIONS.....	106
<b>4.</b>	<b>RESULTS: LAMINAR FLAMES</b> .....	<b>109</b>
4.1.	INTRODUCTION .....	111
4.2.	GASOLINE SURROGATE.....	112
4.6.	TRF-E EXTENDED CONDITIONS .....	124
4.7.	VALIDATION OF NOSE LAMINAR CONFIGURATION .....	126
4.8.	CONCLUSIONS.....	132
<b>5.</b>	<b>RESULTS: TURBULENT FLAMES</b> .....	<b>135</b>
5.1.	INTRODUCTION .....	137
5.2.	SPHERICAL VESSEL TURBULENT FLAME SPEED .....	141
5.2.1.	<i>Insight on Flame Characteristics</i> .....	141
5.2.2.	<i>Reference Cases, Wrinkling Factor and Barycenter Displacement</i> .....	143
5.2.3.	<i>Karlovitz-based Comparison</i> .....	146
5.3.	NOSE TURBULENT FLAME SPEED .....	150
5.3.1.	<i>Evaluation of Classical Correlation for Turbulent Flames</i> .....	153
5.4.	CONCLUSIONS.....	158
<b>6.</b>	<b>CONCLUSIONS AND PERSPECTIVES</b> .....	<b>161</b>
6.1.	PERSPECTIVES .....	167
<b>7.</b>	<b>REFERENCES</b> .....	<b>169</b>
<b>1.</b>	<b>ANNEX A: FLAME STRETCH</b> .....	<b>179</b>
<b>2.</b>	<b>ANNEX B: MINIMUM AND MAXIMUM RADIUS</b> .....	<b>183</b>
	<i>Minimum radius: ignition effects</i> .....	183
<b>3.</b>	<b>ANNEX C: DETAILS OF NOSE SET-UP</b> .....	<b>187</b>
	<i>Error in the evaluation of the internal temperature</i> .....	188
<b>4.</b>	<b>ANNEX D: COMPLEMENTARY DATA FOR TURBULENT FLAMES INVESTIGATION</b> .....	<b>189</b>

---

## 2. Abbreviations

---

$A$	Surface element
$A_L$	Area of the laminar expanding flame
$A_T$	Area of the turbulent expanding flame
$c_p$	Specific heat capacity at constant pressure
$C$	Correction factor for Schlieren radius
$C_\varepsilon$	Dissipation rate normalized with respect to the turbulent kinetic energy
$D_m$	Molecular diffusivity
$D_{th}$	Thermal diffusivity
$Da$	Damkohler number
$E$	Reaction activation energy
$E(\kappa)$	Turbulent energy spectrum, function of the wavenumber
$f_0$	Fan rotation frequency
$I_0$	Mean stretch factor
$k$	Turbulent Kinetic Energy
$K$	Stretch rate
$K_C$	Stretch rate relative to the flame front curvature
$K_S$	Stretch rate relative to the tangential and normal strain due to the flow
$Ka$	Karlovitz number
$Ka_B$	Karlovitz number considering Blint's flame thickness definition
$L_b$	Markstein Length
$L_T$	Integral length
$L_{U_x}$	Longitudinal integral length of the U component
$L_{U_y}$	Transversal integral length of the U component
$L_{V_x}$	Transversal integral length of the V component
$L_{V_y}$	Longitudinal integral length of the V component
$Le$	Lewis number
$Le_c$	Critical Lewis number
$Le_{eff}$	Effective Lewis number
$Le_E$	Lewis number of the exceeding species
$Le_D$	Lewis number of the limiting species
$m_{u,i}$	Unburned gases mass inside the sphere with radius $R_j$
$m_{u,o}$	Unburned gases mass outside the sphere with radius $R_j$
$m_{b,i}$	Burned gases mass inside the sphere with radius $R_j$
$m_{b,o}$	Burned gases mass outside the sphere with radius $R_j$
$\vec{n}$	Normal vector
$P$	Pressure
$P_i$	Initial pressure
$P_{ref}$	Reference pressure
$q'$	Turbulent intensity
$r$	Radius
$R_f$	Flame radius
$R_j$	Mean radius between $R_r$ and $R_r$
$R_{min}$	Minimum radius to avoid spark ignition effect
$R_{min}$	Maximum radius to avoid wall effect
$R_{mean}$	Mean radius
$R_p$	Mean minimum radius of the turbulent flame that contains all the burned gases
$R_r$	Mean maximum radius of the turbulent flame that contains only burned gases

## ABBREVIATIONS

---

$R_S$	Radius gathered from Schlieren images
$R_f$	Mean minimum radius of the turbulent flame that contains all the burned gases
$R_u$	Generic autocorrelation coefficient function of $(x, y, z, t)$
$R_v$	Volume-based equivalent radius
$Re_L$	Reynolds number based on the laminar flame
$Re_T$	Reynolds number considering viscosity of the unburned gases
$Pr$	Prandtl number
$Sc$	Schmidt number
$S_C$	Consumption velocity
$S_L$	Laminar burning velocity
$S_L^0$	Unstretched laminar burning velocity
$S_{Lref}^0$	Reference unstretched laminar burning velocity
$S_T$	Turbulent burning velocity
$t_L$	Laminar flame characteristic time
$t_K$	Kolmogorov scale characteristic time
$t_T$	Integral scale eddies characteristic time
$T$	Temperature
$T_{ad}$	Adiabatic flame temperature
$T_f$	Final temperature
$T_i$	Initial temperature
$T_{ref}$	Reference temperature
$T_T$	Integral time scale
$\vec{u}$	Velocity vector
$\vec{u}_g$	Velocity of the fresh gases
$u'_{rms}$	Root mean square of the horizontal component of the velocity fluctuation
$u'_{tot}$	Horizontal component of the total velocity fluctuation
$U(x, y, z, t)$	Velocity of the turbulent flow
$\overline{U(x, y, z, t)}$	Mean velocity of the turbulent flow
$u(x, y, z, t)$	Fluctuation component of the turbulent flow
$v_{O_2,ref}$	Reference oxygen volume percentage in the mixture
$v_{O_2}$	Oxygen volume percentage in the mixture
$v'_{rms}$	Root mean square of the vertical component of the velocity fluctuation
$v'_{tot}$	Vertical component of the total velocity fluctuation
$V$	Volume
$V_{u,i}$	Unburned gases volume inside the sphere with radius $R_j$
$V_{u,o}$	Unburned gases volume outside the sphere with radius $R_j$
$V_{b,i}$	Burned gases volume inside the sphere with radius $R_j$
$V_{b,o}$	Burned gases volume outside the sphere with radius $R_j$
$V_L$	Laminar flame propagation speed
$V_L^0$	Unstretched laminar flame propagation speed
$\vec{w}$	Front flame displacement vector
$Y_F$	Fuel mass fraction
$Y_O$	Oxidant mass fraction
$Y_k^b$	k-species of the burned gases mass fraction
$Y_k^u$	k-species of the unburned gases mass fraction
$Y_P^b$	Products mass fraction in the burned gases
$Y_R^u$	Reactants mass fraction in the unburned gases
$\beta$	Reduced activation energy
$\delta_L$	Generic laminar flame thickness
$\delta_L^0$	Thermo-diffusive laminar flame thickness
$\delta_L^B$	Blint's laminar flame thickness
$\delta_T$	Turbulent flame thickness

## ABBREVIATIONS

---

$\varepsilon$	Energy dissipation rate
$\eta_K$	Kolmogorov scale length
$\vartheta$	Angle
$\kappa$	Wavenumber
$\lambda$	Taylor length scale
$\lambda_u$	Thermal conductivity of the unburned gases
$\mu$	Dynamic viscosity
$\nu$	Kinetic viscosity
$\xi$	Infinitesimal spatial displacement
$\rho$	Density
$\rho_u$	Unburned gases density
$\rho_b$	Burned gases density
$\tau$	Infinitesimal time increase
$\phi$	Equivalence ratio
$\dot{\omega}_r$	Reaction rate reactants
$\dot{\omega}_p$	Reaction rate products
<i>ANR</i>	Agence Nationale de la Recherche
<i>BDC</i>	Bottom Dead Center
<i>CAD</i>	Crank Angle Degree
<i>CFD</i>	Computational Fluid Dynamics
<i>CO</i>	Carbon Monoxide
<i>CO<sub>2</sub></i>	Carbon Dioxide
<i>CR</i>	Compression Ratio
<i>EGR</i>	Exhaust Gas Recirculation
<i>DNS</i>	Direct Numerical Simulation
<i>DVS</i>	Double-View Schlieren
<i>HIT</i>	Homogeneous Isotropic Turbulence
<i>ICE</i>	Internal Combustion Engine
<i>LES</i>	Large Eddy Simulation
<i>LV</i>	Large Volume
<i>MACDIL</i>	Moteur Allumage Comande à fort DILution
<i>NOSE</i>	New One Shot Engine
<i>NO</i>	Nitrogen monoxide
<i>NO<sub>2</sub></i>	Nitrogen dioxide
<i>O<sub>2</sub></i>	Diatomic oxygen molecule
<i>PIV</i>	Particle Image Velocimetry
<i>PRF</i>	Primary Reference Fuel
<i>RON</i>	Research Octane Number
<i>SI</i>	Spark Ignition
<i>SV-HTI</i>	Small Volume – Hight Turbulent Intensity
<i>SV-Std</i>	Small Volume – Standard piston trajectory
<i>TDC</i>	Top Dead Center
<i>TRF</i>	Toluene Reference Fuel
<i>TRF-E</i>	Toluene Reference Fuel – with Ethanol addition



## 3. Résumé en Français

---

De nos jours, la protection de l'environnement, la consommation de l'énergie et le contrôle de la pollution sont, dans le monde entier, des problématiques sociétales des plus urgentes. Des données récentes sur le changement climatique et la qualité de l'air montrent que, au cours des trente dernières années, l'augmentation de la consommation d'énergie a été attestée d'environ 30% et que cela continue. En général, les projections montrent que les combustibles fossiles seront encore la plus importante source d'énergie en 2040, représentant 70% de la demande globale.

L'utilisation des combustibles fossiles implique l'émission de polluants de gaz à effet de serre, qui font l'objet de plusieurs lois de plus en plus sévères. Un des effets les plus importants de cette pollution est représenté par les gaz à effet de serre (Greenhouse Gases, GHG). On estime que ces gaz sont responsables d'une augmentation de la température moyenne globale d'environ 0.61°C, qui atteindra probablement dans les prochaines décades, 2 à 6°C. Actuellement, le transport est responsable d'environ 30% de la demande énergétique et donc de la production de pollution. Parmi ce pourcentage on compte une contribution du 40% de part de véhicules légers. C'est, sans aucun doute, dû à l'utilisation massive des carburants d'origine fossiles dans le secteur du transport. Les prévisions montrent que même si les solutions totalement électriques ou hybrides augmentent, les technologies basées sur les carburants fossiles représenteront encore une grosse partie de l'ensemble. Les constructeurs doivent donc se focaliser sur l'amélioration des technologies actuelles, afin de satisfaire les normes et diminuer l'impact des moteurs à combustion interne (Internal Combustion Engines, ICEs) sur l'environnement.

Dans le but d'augmenter l'efficacité des ICEs et, en particulier, des moteurs à allumage commandé (Spark-Ignition, SI), l'une des technologies les plus prometteuses est le '*downsizing*'. L'idée des moteurs downsizés est de réduire la taille du moteur, soit la chambre de combustion proprement dite et par là-même toutes les masses qui sont en jeu ainsi que le frottement. Pour préserver le rendement, il est alors nécessaire de booster les conditions d'admission du mélange réactive, grâce à l'utilisation d'un turbocompresseur qui puisse augmenter la pression et la température des gaz libérés dans le cylindre. Malheureusement, cette stratégie est responsable d'apparition d'anomalies de combustion pendant le fonctionnement du moteur, comme par exemple le cliquetis (*knock*). Pour éviter ou contrôler l'apparition de ces

phénomènes la stratégie la plus efficace semble être la dilution soit par les gaz d'échappement (EGR, Exhaust Gas Recirculation) soit en augmentant la quantité de gaz brûlés résiduels (IGR, Internal Gas Recirculation). D'autre part, la combustion des mélanges fortement dilués en conditions thermodynamiques particulièrement sévères est difficilement prévisible.

C'est précisément dans ce cadre qu'a été initié le projet ANR MACDIL (Moteurs à Allumage Commandé à fort DILution, ANR-15-CE22-0014), coordonné par l'IFPen, afin de fournir des modèles prédictifs pour le développement des moteurs à allumage commandé du futur. Pour atteindre cet objectif, ce projet repose sur une approche globale, avec d'une part la modélisation de la chimie des processus réactifs, d'autre part la modélisation numérique pour les phénomènes de combustion et enfin d'une partie expérimentale qui doit aider, supporter et valider les travaux des autres groupes. Ce travail de thèse s'insère dans la partie expérimentale de ce projet. L'objectif final est de combler le manque dans la littérature actuelle en ce qui concerne les flammes turbulentes en expansion. En fait, il existe une zone quasi-inexplorée du diagramme de Peters-Borghgi, dans laquelle les flammes qui se développent dans la chambre de combustion des moteurs SI downsized, avec une forte dilution, se placent. Cette zone-là est caractérisée par des nombres de Karlovitz supérieurs à 1. Or,  $Ka$  est l'un des paramètres qui permet de définir le seuil limite entre le régime dit de 'flamelets' et le régime de flammes épaissies. L'exploration de la transition en ces deux régimes est toujours nécessaire et permettrait d'améliorer la prédictibilité des modèles numériques actuels, principalement basés sur l'hypothèse de flamelets.

Pour arriver à cet objectif, plusieurs étapes sont nécessaires. La première est de choisir un mélange simple d'espèces chimiques, comme carburant modèle pour une essence commerciale. Ce '*surrogate*', ici le TRF-E (Toluene Reference Fuels, avec ajout de d'éthanol au 5%vol) a été validé en caractérisant la vitesse de flamme laminaire et sa réponse à l'étirement, via la longueur de Markstein, en comparant avec l'essence qu'il doit représenter. La vitesse de combustion laminaire est un paramètre fondamental, caractéristique intrinsèque d'un mélange air/combustible donné. A partir de l'observation directe d'une flamme qui se propage sphériquement, l'évolution du rayon de flamme permet de remonter facilement à la vitesse de propagation laminaire à étirement nul,  $V_L^0$ . Dans cette étude, un montage Double-View Schlieren (DVS) a été réalisé pour obtenir le rayon mais aussi permettre la vision de la flamme selon deux perspectives perpendiculaires. Le rayon de la flamme extrapolé à partir des images Schlieren donne la vitesse de propagation de flamme laminaire étirée,  $V_L$ . A partir de cette

vitesse,  $V_L^0$  est obtenue en utilisant une corrélation non-linéaire dans laquelle existe un terme d'étirement,  $K$  et la longueur de Markstein,  $L_b$ . Le passage entre le terme  $V_L^0$  et la vitesse de combustion laminaire non étirée,  $S_L^0$  est possible en introduisant le facteur d'expansion  $\frac{\rho_b}{\rho_u}$ .

L'enceinte sphérique utilisée a été détaillée dans la thèse de Galmiche (2014). Elle peut être chauffée jusqu'à une valeur maximale de 473 K et une pression maximale initiale du mélange de 10 bar. Un ensemble des débitmètres gazeux et liquide permet d'injecter la quantité désirée de chaque composant du mélange, y compris les composants liquides vaporisés. Un ventilateur à l'intérieure de la chambre est utilisé pour homogénéiser le mélange injecté. Ce ventilateur est ensuite stoppé 10 seconds avant l'allumage afin que le mélange gazeux soit au repos avant l'étincelle que c'est réalisé par deux électrodes en tungstène. Enfin, quatre fenêtres en quartz permettent l'observation directe de la flamme.

Les flammes de prémélange essence/air et TRF-E/air ont été évaluées à  $T = 473$  K et 1 bar, sans dilution et en fonction de la richesse  $\phi$ . Puis pour une même température initiale, la dilution a été variée de 0% à 10% et à 20%, et la pression de 1 à 2, 3 et 5 bar. La comparaison entre les deux mélanges montre que le comportement dynamique est tout à fait similaire et valide le choix du TRFE comme surrogate comme le montre la Figure 66. La matrice de données expérimentales obtenue est suffisamment conséquente pour extraire les coefficients d'une corrélation empirique universelle permettant d'estimer la vitesse de combustion laminaire non étirée. Cette base de données a été étendue en étudiant les mêmes combinaisons de dilution et de pression mais à la température initiale de 373 et 423 K, cela dans le but de permettre aux partenaires cinétiens du projet MACDIL de développer un mécanisme de chimie cinétique du TRF-E, qui est en cours de finalisation (Catoire et al., à paraître).

Malgré cela, l'enceinte sphérique ne permet pas d'obtenir des conditions initiales proches de celles obtenues au moment de l'allumage dans un moteur downsized, en termes de pression et de température. C'est pour cette raison qu'un autre dispositif a été utilisé et amélioré, basé sur NOSE (New One Shot Engine). Au contraire de l'enceinte de combustion sphérique, la chambre de combustion de NOSE et sa configuration de fonctionnement ont été entièrement réalisées durant ce travail de thèse et une partie importante a été de caractériser les conditions initiales générées.

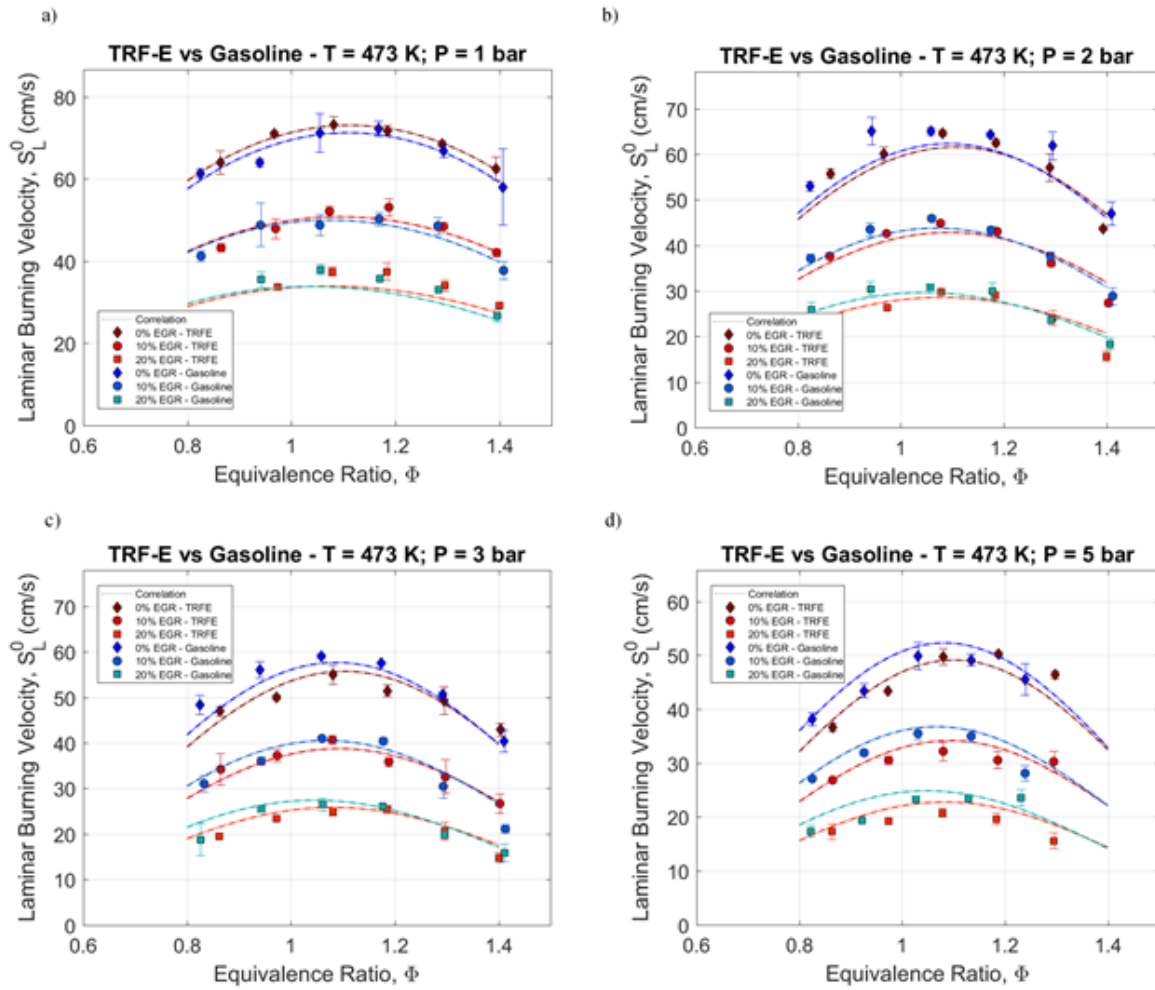


Figure 1. TRF-E and gasoline unstretched laminar burning velocities comparison at different pressure values (Figures a, b, c, d) and fixed temperature ( $T = 473$  K) for three dilution rates.

NOSE repose sur le principe d'une compression adiabatique pour générer des conditions initiales dans la chambre de combustion. Cette compression est obtenue grâce à un monocylindre Diesel, spécifiquement modifié pour fonctionner de manière contrôlée et non cycliquement. De cette manière, les conditions thermodynamiques et du mélange sont proprement contrôlés, mesurables et répétables. La tête du cylindre et du piston ont été modifiées pour offrir une flexibilité appréciable à la manip. Il est ainsi possible de changer la chambre de combustion, pour accentuer par exemple la turbulence. L'utilisateur peut grâce au contrôle du piston par un moteur électrique designer des trajectoires afin d'obtenir les conditions désirées, et surtout réduire la vitesse du piston proche du point mort haut pour atteindre et maintenir des hautes conditions de pression et de température durant plusieurs millisecondes, appelé 'plateau'. L'analyse de différentes trajectoires et configurations a permis

de choisir trois configurations (LV, SV-Std et SV-HTI) pour l'étude des cas turbulents et une configuration pour l'étude des cas laminaires.

Dans notre étude on a utilisé, pour la configuration laminaire, un premier point à la pression de 5 bar et une température de 473 K, puis une autre à une pression de 21 bar avec trois températures, 473, 500 et 525 K, qui est une configuration très difficile à obtenir via d'autres dispositifs. Cette étude en laminaire a permis de valider et de mettre en évidence les limites de ce dispositif. Comme le dispositif est dynamique, la flamme n'est pas parfaitement sphérique comme dans l'enceinte laminaire et est inévitablement déformée par l'écoulement. Cependant, les résultats très similaires entre l'enceinte sphérique et le NOSE pour les mêmes conditions initiales ont confirmé la validité des mesures, de la méthodologie mise en place et des hypothèses faites. Les points réalisés à 21 bar et 473, 500 et 525 K ont alors été réalisés en étudiant différents pourcentages de dilution (10%, 20% et 30%) pour différents valeurs de  $\phi$ . Comme pour l'étape précédente, les valeurs de la vitesse de combustion laminaire et de la longueur de Markstein ont été extrapolées. Un premier résultat très important a été obtenu est le fait que les vitesses fondamentales de flamme laminaire obtenues expérimentalement sont très proches de celles prédites par le modèle cinétique (erreur relative inférieure à 10%) ainsi que celles par la corrélation mathématique empirique optimisée à partir des données sur l'enceinte sphérique (erreur dans l'ordre du 5%).

L'étude de la propagation de flamme turbulente a été ensuite réalisée en utilisant les deux dispositifs expérimentaux et pour NOSE, les 3 configurations décrites ici (Figure 39):

- NOSE LV (Large Volume) : les volumes initial et final ont été beaucoup augmentés grâce à l'utilisation d'un rehausse entre le corps du cylindre et sa tête, où il se trouve la chambre de combustion, permettant de générer des conditions finales de 8 bar et 373 K.
- NOSE SV-Std (Small Volume - Standard) : la chambre dessinée ici permet d'atteindre 21 bar et 605 K pendant le plateau.
- NOSE SV-HTI (Small Volume – High Turbulence Intensity) : c'est une configuration géométriquement égale à la précédente mais dans laquelle la trajectoire n'est plus standard pour atteindre un niveau de turbulence plus important. Dans la trajectoire classique le piston parte du Point Mort Bas (PMB) et vient fortement accéléré par le moteur. Quand il arrive près du Point Mort Haut (PMH), le moteur commence à le ralentir et maintient une vitesse réduite et presque constante pendant le plateau.

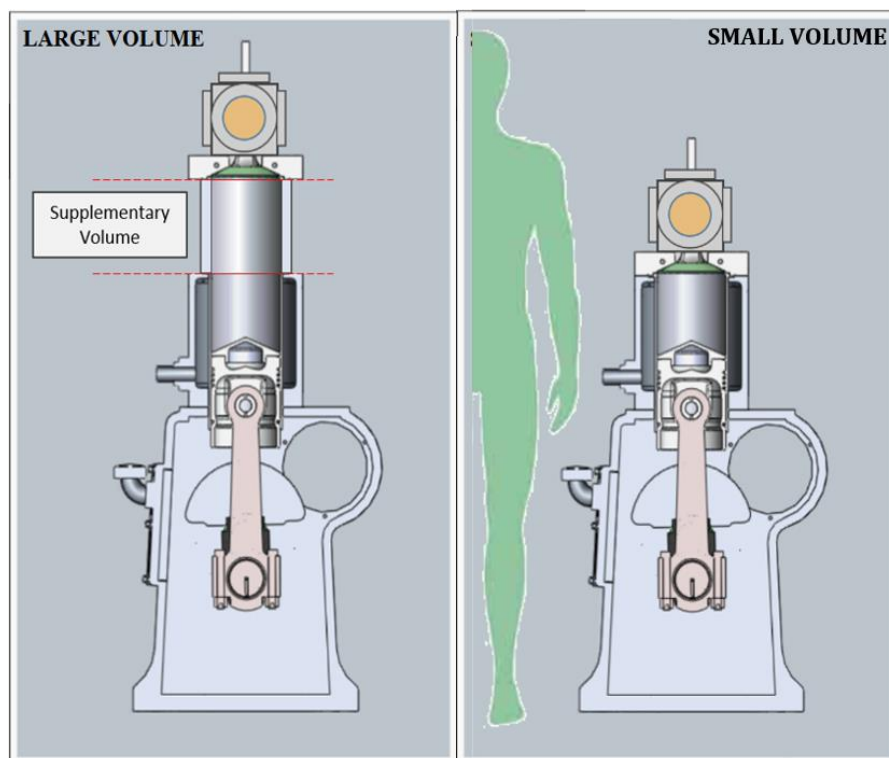


Figure 2. Scheme of the two NOSE configurations: Large Volume (LV) on the left and Small Volume (SV) on the right.

Dans les configurations turbulentes, la turbulence est générée grâce à une grille placée entre la tête du cylindre et la chambre de combustion. Cette grille a été modélisée par l'IFPEN dans le cadre du projet MACDIL. Pour valider les prédictions, la technique PIV (Particle Image Velocimetry) a été utilisée pour caractériser l'aérodynamique interne dans la chambre de combustion du NOSE. Les résultats de cette analyse ont produit l'ensemble de caractéristiques fondamentales de la turbulence pour chaque configuration. En plus, la possibilité d'une configuration laminaire, sans grille, et avec un rapport de compression très bas a été validée. En introduisant des hypothèses plausibles, les conditions de turbulence homogène et isotrope (Homogeneous Isotropic Turbulence, HIT) ont été vérifiées pour les trois configurations turbulentes de manière acceptable. On présente ci-dessous un résumé des propriétés principales de l'intensité turbulente ( $q'$ ) et de l'échelle de longueur intégrale ( $L_T$ ) pour chaque configuration :

- NOSE LV :  $q' = 2.31$  m/s -  $L_T = 2.35$  mm ;
- NOSE SV-Std :  $q' = 2.70$  m/s -  $L_T = 2.07$  mm ;
- NOSE SV-HTI :  $q' = 3.29$  m/s -  $L_T = 2.07$  mm ;

Avec comme définition,  $q' = \sqrt{\frac{u'^2 + v'^2 + w'^2}{2}}$ , et  $u'$ ,  $v'$  et  $w'$  les 3 composantes de la fluctuation de vitesse. Quant à  $L_T$ , elle représente les tourbillons générés en écoulement turbulent qui contiennent la plus grande partie de l'énergie cinétique turbulente,  $q'^2$ . Selon la théorie de la cascade de Kolmogorov, un écoulement turbulent est caractérisé par l'existence, l'interaction et l'évolution des vortex (eddies) des différentes tailles. De  $L_T$ , on passe à des tourbillons de taille intermédiaire, dite échelle de Taylor, dans laquelle les instabilités des tourbillons de taille  $L_T$  provoquent la dégradation des tourbillons de plus en plus petits transportant l'énergie. Ces petits tourbillons sont appelés échelle de Kolmogorov,  $\eta_K$ , et dissipent l'énergie turbulente par viscosité.

A partir des champs de vitesse et en supposant l'écoulement principalement en 2D, l'évaluation des coefficients d'autocorrélation permet de trouver les quatre composantes de l'échelle de longueur intégrale : les deux composants longitudinales dans la direction horizontal et vertical ( $L_{U_x}$  et  $L_{V_y}$ ) et les deux composants transversales ( $L_{U_y}$  et  $L_{V_x}$ ). Les conditions de turbulence homogène et isotrope sont vérifiées si :  $L_{U_x} = 2 L_{U_y}$  ;  $L_{V_y} = 2 L_{V_x}$  ; et  $\frac{u'^2}{v'^2} = 1$ .

La connaissance des propriétés de la turbulence est fondamentale pour l'estimation des nombres adimensionnels associés à l'écoulement. On trouve le nombre Reynolds associé à la longueur intégrale :  $Re_L = \frac{q' L_T}{S_L^0 \delta_L^0}$  (avec  $\delta_L^0$  l'épaisseur de flamme laminaire), qui décrit l'interaction de la flamme avec la plus large échelle de la turbulence. Puis, le nombre de Damkohler :  $Da = \frac{L_T S_L^0}{q' \delta_L^0}$ , que représente le rapport entre le temps caractéristique turbulent et le temps caractéristique chimique. Et, finalement, le nombre de Karlovitz :  $Ka = \left(\frac{\delta_L^0}{L_T}\right)^{\frac{1}{2}} \left(\frac{q'}{S_L^0}\right)^{\frac{3}{2}}$ , qui tient en compte l'interaction de la flamme avec les structures les plus petites de l'écoulement (échelle de Kolmogorov).

La connaissance de ces nombres adimensionnels donne des indications sur le régime de combustion dans lequel la flamme se déroulera. Cette distinction se fait souvent en utilisant le diagramme de Peters-Borghgi, représenté en Figure 61 et Figure 78, dont la définition des différents régimes de combustion est encore sujet à discussion. Les limites par exemple du régime de flamelets sont encore le sujet de nombreux travaux :  $Ka < 1$  ou jusque 100. Le problème principal reste que selon la manière dont la variation du  $Ka$  est obtenue, la dynamique

de la flamme résultante peut varier énormément. Il est certain que les travaux récents restent encore très peu nombreux sur des conditions proches de celles d'un moteur *downsized* actuel.

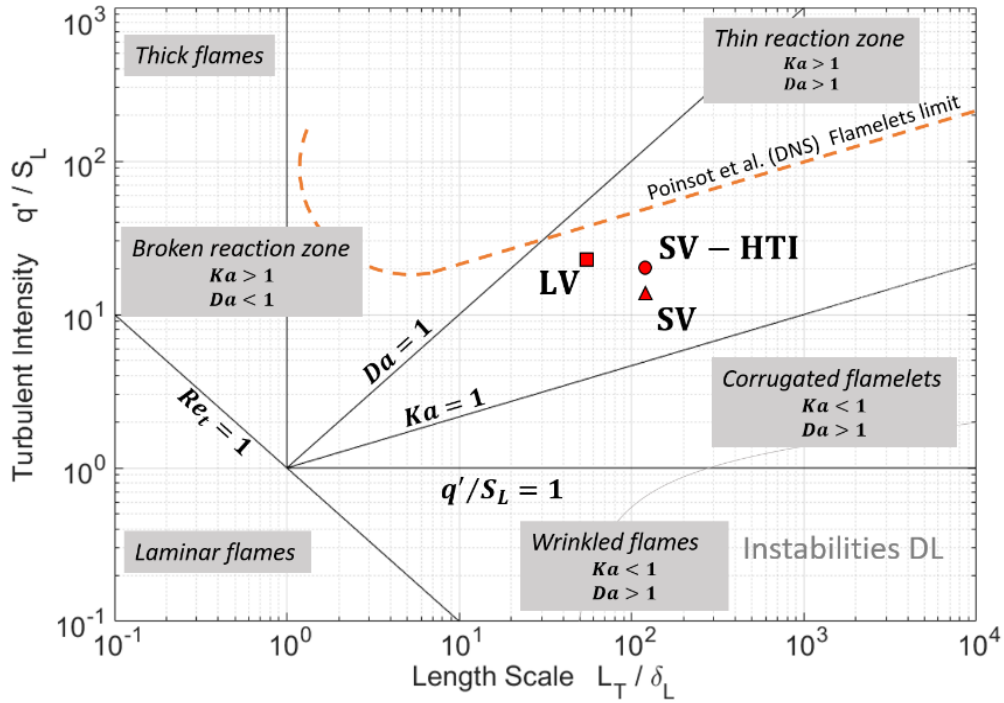


Figure 3. Peters-Borghi diagram with evaluated Karlovitz number for NOSE set-ups.

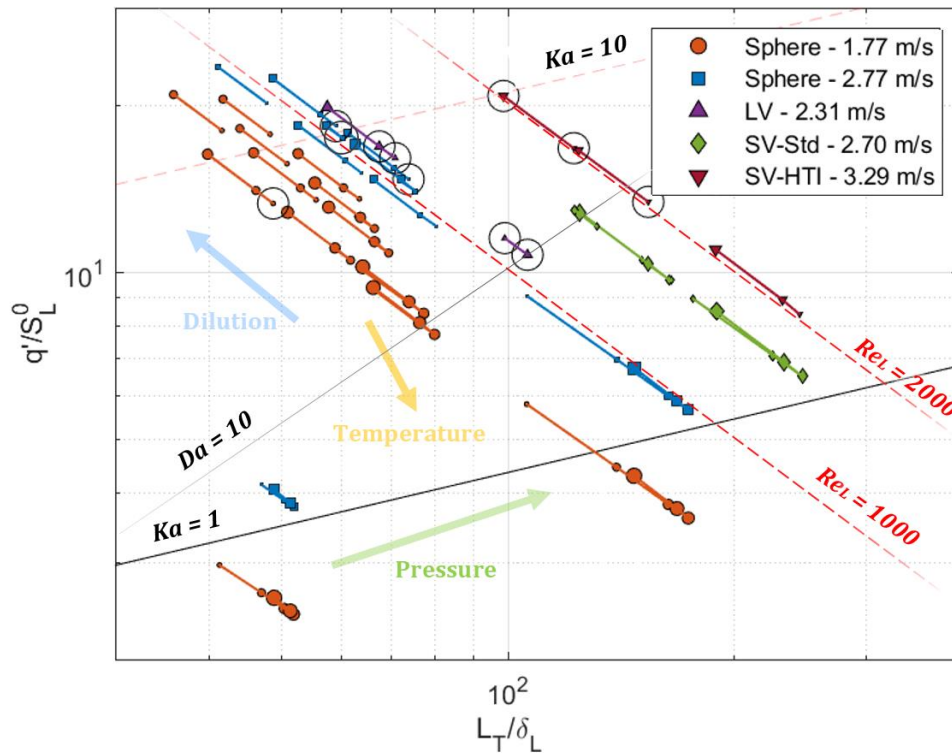


Figure 4. All investigated experimental data in Peters-Borghi diagram. Size of symbol proportional to the equivalence ratio. Circle markers indicate the flames slowed down during their evolution.

La complémentarité des deux dispositifs expérimentaux a été une fois de plus utilisée pour étendre les plages de configurations, jusqu'à arriver à plus de 30 combinaisons de pression, températures et dilution. Grâce à 6 ventilateurs une turbulence homogène et isotrope est obtenue au centre de l'enceinte, deux intensités ont été choisies (1.77 et 2.77 m/s). La grande partie des tests effectués sur l'enceinte sphérique ont été effectués à 5 bars et couvrent un large éventail de nombres de Karlovitz, en variant les températures, l'intensité turbulente et la dilution. Des tests de référence à 1 bar, 473 K et dilution à 0% ont également été utilisés à titre de comparaison directe pour observer l'effet de la dilution croissante et la variation de pression entre 1 et 5 bars. Une forte augmentation des taux de dilution, de 20% à 30%, entraîne une réduction de la vitesse de propagation de la flamme turbulente,  $V_T$ , tandis que l'augmentation de la pression de 1 à 5 bars entraîne une augmentation de  $V_T$ . D'autre part, la pression et la dilution contribuent toutes deux à réduire les oscillations du facteur de plissement. Les mesures du déplacement des barycentres confirment le déplacement important de la flamme lors de la propagation lorsque les conditions sont particulièrement sévères. En augmentant la richesse, on aide généralement à réduire le déplacement de la flamme. Pour des valeurs  $\frac{q'}{s_L} > 10$  et  $\frac{L_T}{\delta_L^0} > 50$ , des forts taux d'étirement locaux entraînent la formation de poches à la surface de la flamme. Dans des conditions thermodynamiques défavorables ( $EGR > 25\%$  et  $T < 400$  K) et une turbulence modérée (par exemple,  $q' = 1.77$  m/s dans l'enceinte sphérique), les poches créées à la surface de la flamme restent sur le front de la flamme. Ce comportement peut provoquer une surestimation de la vitesse de propagation de la flamme. Lorsque  $Re > 1000$ , les poches sont détachées du front de flamme et presque immédiatement éteintes. Ainsi, lors de la propagation, la flamme est effectivement érodée par ce type de phénomènes, ce qui conduit à une évolution de la  $V_T$  en fonction de  $Rs$  (rayons détecté par Schlieren), constante ou décroissante.

De manière générale, l'impact de  $Re$ ,  $Ka$  et la vitesse de propagation de la flamme sur le nombre a été clairement identifié : par exemple, l'augmentation de  $Ka$  entraîne une légère réduction de  $V_T$ , alors que l'augmentation du  $Re$  l'augmente. D'autres études ont mis en corrélation des évidences similaires avec l'augmentation de  $Ka$  et de  $Re$  qui réduisent ou augmentent respectivement le plissement de la surface de la flamme. De plus, l'augmentation de la vitesse de propagation de la flamme observée avec la richesse a été confirmée.

Grâce à une augmentation de la pression initiale jusque 21 bars, il a pu être mis en évidence que le déplacement des points sur le diagramme de Peters-Borghini suit la loi du second degré de la diminution de la vitesse de combustion laminaire. En comparant les mêmes gammes de  $Ka$ , les flammes obtenues dans le NOSE sont à des  $Re$ . Or, selon ce qui a été observé dans d'autres travaux et dans la présente étude, au sein du régime du flamellet, l'augmentation de  $Re$  conduit à une augmentation du plissement de la surface de la flamme et donc à une vitesse de turbulence accrue. Une explication possible de la vitesse de propagation relativement faible observée sur NOSE concerne la diminution de la longueur intégrale. Dans la littérature, on supposait que plus la longueur intégrale était basse, plus il existait un effet affaiblissant le plissement du front de la flamme. Lorsque  $\frac{q'}{S_L}$  était fixé et que la longueur intégrale doublait, la vitesse de la flamme turbulente augmentait de plus de 50%, certainement à cause de deux phénomènes contrebalancés. En fait, lorsque  $q'$  augmente, il se produit un élargissement du spectre turbulent, une augmentation de la surface de la flamme mais, d'autre part, des tourbillons plus petits affectent la surface de la flamme, ce qui entraîne une perte de surface due aux effets de déformation et de courbure. Au contraire, lorsque la longueur intégrale est doublée, les deux phénomènes agissent dans le même sens, avec à la fois l'élargissement du spectre des tourbillons et la diminution de l'effet d'affaiblissement à petite échelle. Néanmoins, la comparaison entre les tests effectués sur les deux configurations NOSE SV montre que l'effet des variations de  $Re$  et de  $Ka$  est similaire à celui observé sur l'enceinte sphérique à une pression inférieure et à une longueur intégrale supérieure. Une autre possibilité concerne un effet de pression qui devient dominant après un certain seuil. Dans la littérature, il a été constaté que le changement de pression à  $Re$  constant entraîne une réduction de la vitesse de la flamme turbulente, tandis que si  $Re$  augmente en conséquence de l'augmentation de la pression, la propagation de la flamme est améliorée.

Pour conclure, des corrélations récentes proposées en littérature ont été testées. Aucune de ces corrélations ne peut suivre les forts changements en termes de pression, dilution et richesse. Une nouvelle corrélation a été proposée sur la base de nos données :  $\frac{S_T}{S_L} \frac{1}{Da} \propto Ka$ . Une intéressante amélioration de cette corrélation peut être obtenue par une étude future plus détaillée de l'effet de la longueur intégrale ou par l'introduction du nombre de Lewis dans l'analyse.





---

# **1. Introduction**

---



## 1.1. BACKGROUND AND MOTIVATION

### 1.1.1. Energy and Environment

At the present day, environment protection, energy consumption and control of pollutant emissions are worldwide the most urgent and important themes to face. Recent evidences about climate change and air quality drop should act as the most noticeable warning bells. One need only to think that, in the last thirty years, the increase of energy consumption has been attested to about 30% [1] and, year by year, it still increases. Moreover, just a small part of this global primary energy demand is represented by renewables energies, as shown in Figure 5 [2]. Despite renewables is currently the energy sector with the highest growing rate, projections from [2], [3] highlight that, in 2040, fossil fuels will still supply more than 70% of world energy demand.

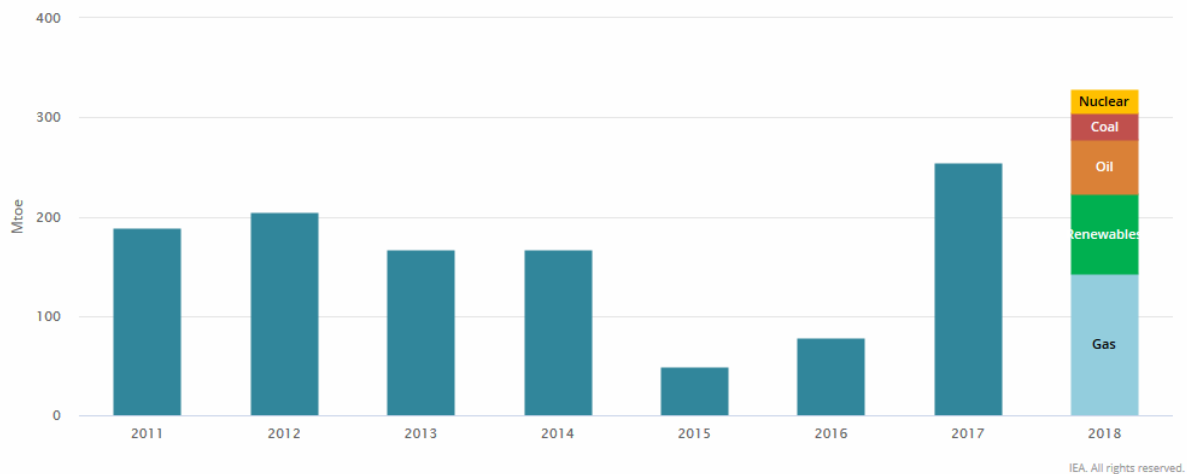


Figure 5. Annual change in global primary energy demand [2].

The consequence of this large fossil fuels exploitation directly affects the environment in several ways. One of the most important impact is, now, the greenhouse effect. Figure 6 shows the global quantity of carbon emission introduced in the atmosphere since the beginning of the last century. This impressive amount of greenhouse gases (GHG), according to estimations [1], is responsible of a global average surface temperature increase around 0.61 °C. The effects of this apparently slight temperature increase start to be noticeable. If this trend will continue the foreseen further increase will be between 2 and 6 °C within the end of this century and, that is why, this problem must be seriously tackled worldwide.

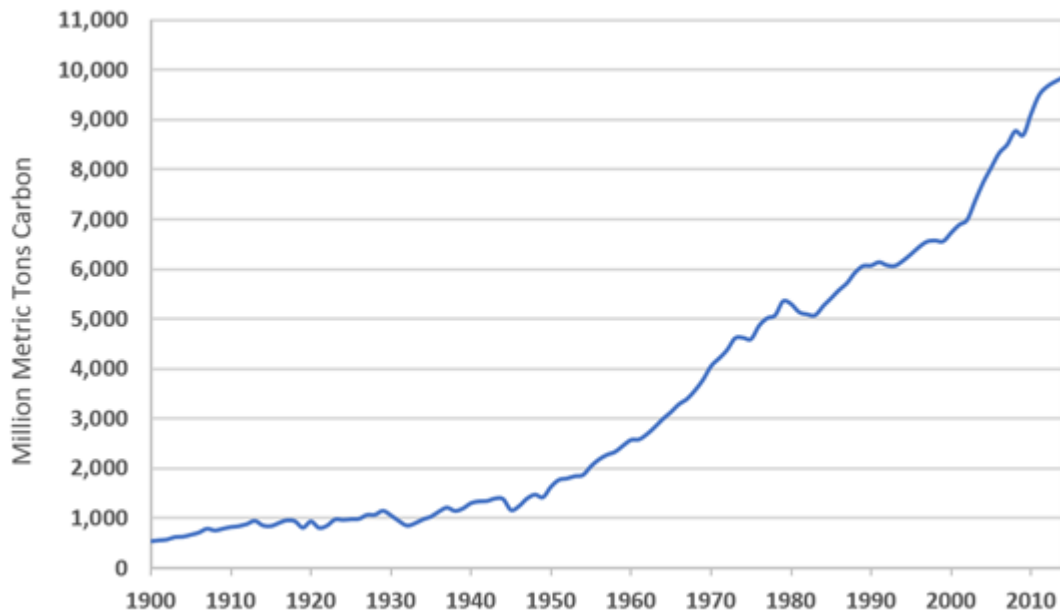


Figure 6. Global carbon emissions from fossil fuels, 1900-2014 [4]

Currently, three main sectors that are shared the great part of global energy consumption, i.e. industry, households and transport, are responsible of the great part of the air pollutants production. Moreover, the impact of these three sectors continues to be in equilibrium even if the global energy demand increases, as shown for the EU28 scenario in Figure 7.

Despite the remarkable technology development, transportation sector still largely exploits fossil fuels and contributes to a consistent percentage of the global air pollutant emissions [5]. Figure 8 quantifies this contribution relatively to the EU28 in 2016. Main air pollutants are taken into account, highlighting the non-negligible impact of road transport with respect to the overall percentage in the production of almost each species. Particulate matter (PM), Nitrous Oxides (NO<sub>x</sub>), and Non-methane volatile organic compounds (NMVOCs) are harmful and directly affect the air quality. Carbon monoxide (CO) is the world first cause of gas poisoning. Alongside these species, transport sector strongly contributes 20% to the global Carbon Dioxide (CO<sub>2</sub>) emissions with 40 % due to light duty vehicles, as indicated in Figure 8 and Figure 9. As CO<sub>2</sub> results from the oxidation of carbon in fuels during combustion it is the major greenhouse gas since the beginning of the industrial era.

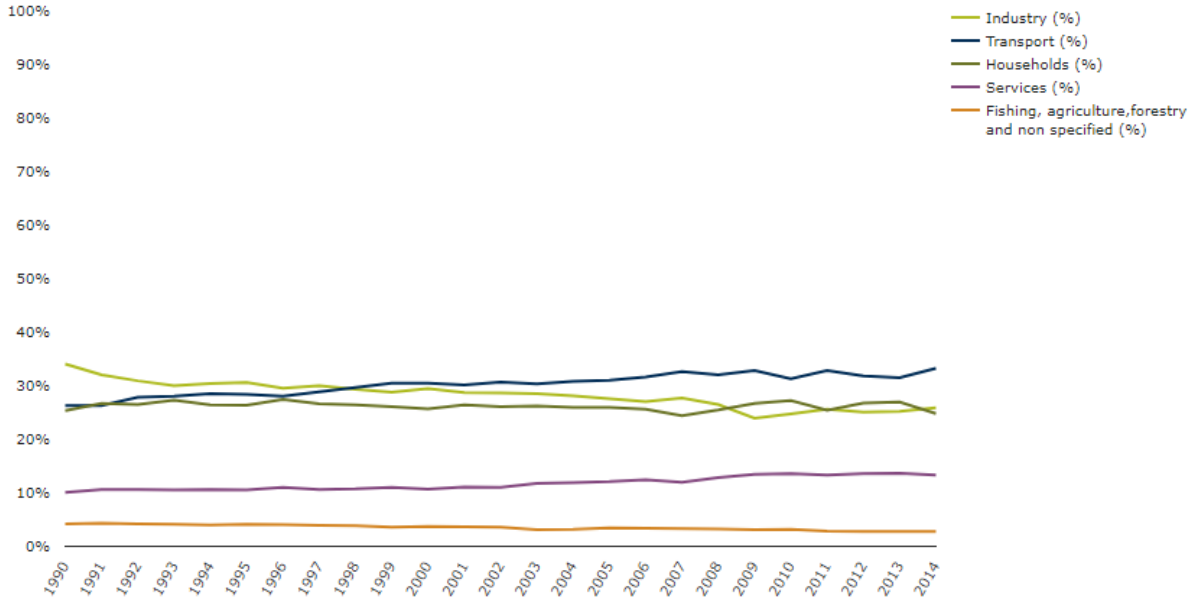


Figure 7. EU28 final energy consumption by sector [6].

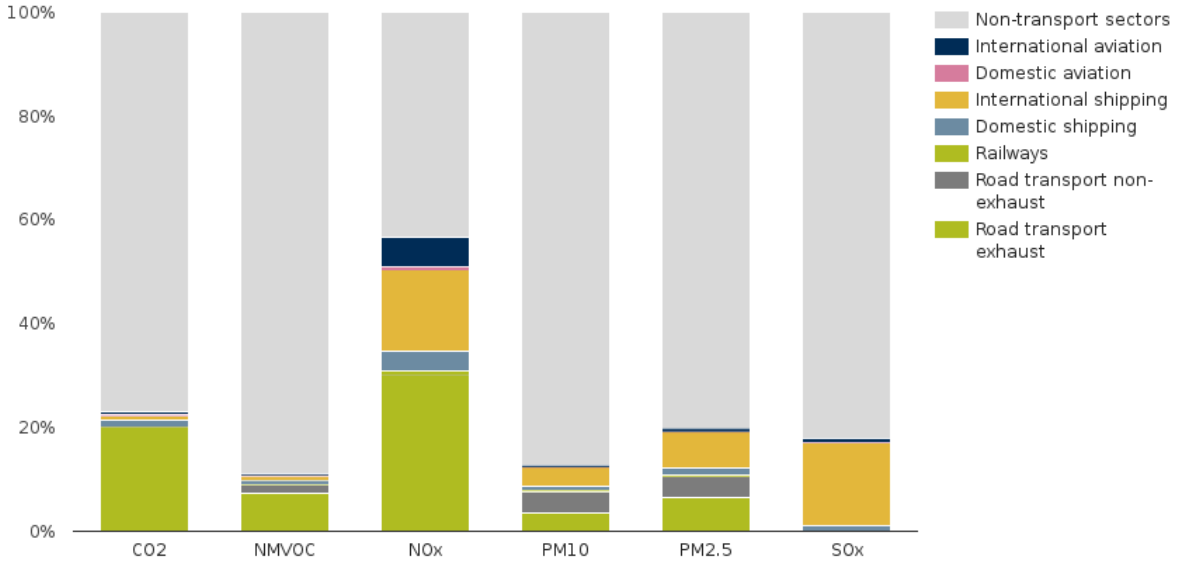


Figure 8. Contribution of the transport sector to total emissions of the main air pollutants - 2016 [6].

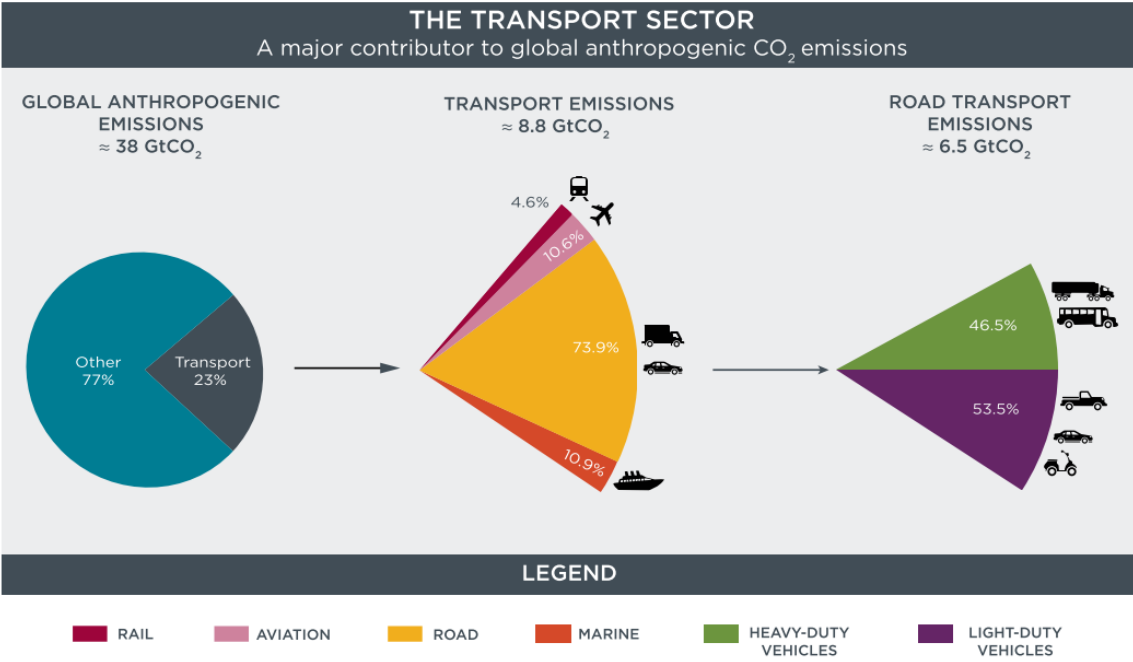


Figure 9. Distribution of CO<sub>2</sub> emissions in the transportation sector - 2014 [7].

### 1.1.2. Emissions Standards

As a matter of fact, despite the increasing development and implementation of alternative energy sources and systems, internal combustion engines (ICEs) still represent the reference technological solution in the automotive sector. This is why one main existing challenge concerns the increase of efficiency to improve the fuel economy and the decrease of pollutant emissions. Engine constructors have to comply with more and more stringent regulation maintaining vehicles performance [5]. Figure 10 compares the recent years trend in CO<sub>2</sub> emissions regulations and the near future targets between the main automotive markets. The European Union represents the most virtuous example, followed by South Korea that has one of the higher relative decreasing rate. With its high percentage of hybrid vehicle, Japan already met its 2020 target in 2013. If Japan continues to reduce CO<sub>2</sub> emissions at the same rate, it will reach 82 g/km in 2020, quite below the near future target of all the other countries. Starting from an historical laggard role, Canada and U.S. have now become leaders, with strict long-term standards. Indeed, the percentages reported in Figure 11 demonstrate that countries with relative high baseline could aspire to achieve large reduction in few years by adopting aggressive policies.

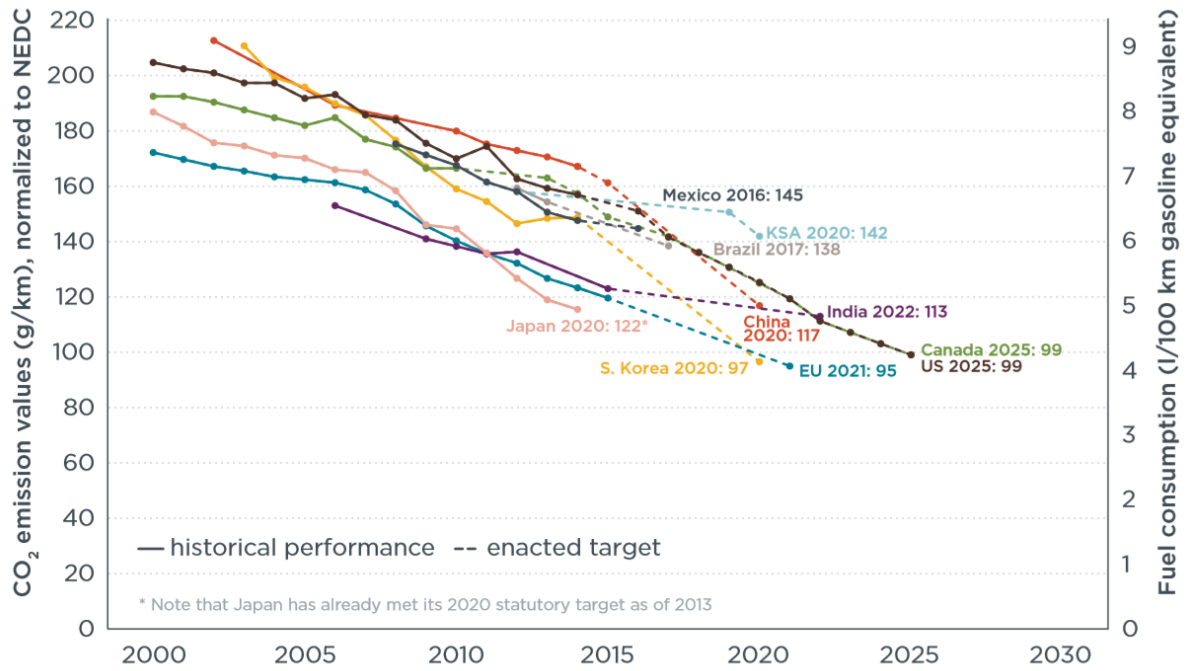


Figure 10. Global comparison of CO<sub>2</sub> emissions trend and near future target. [7]

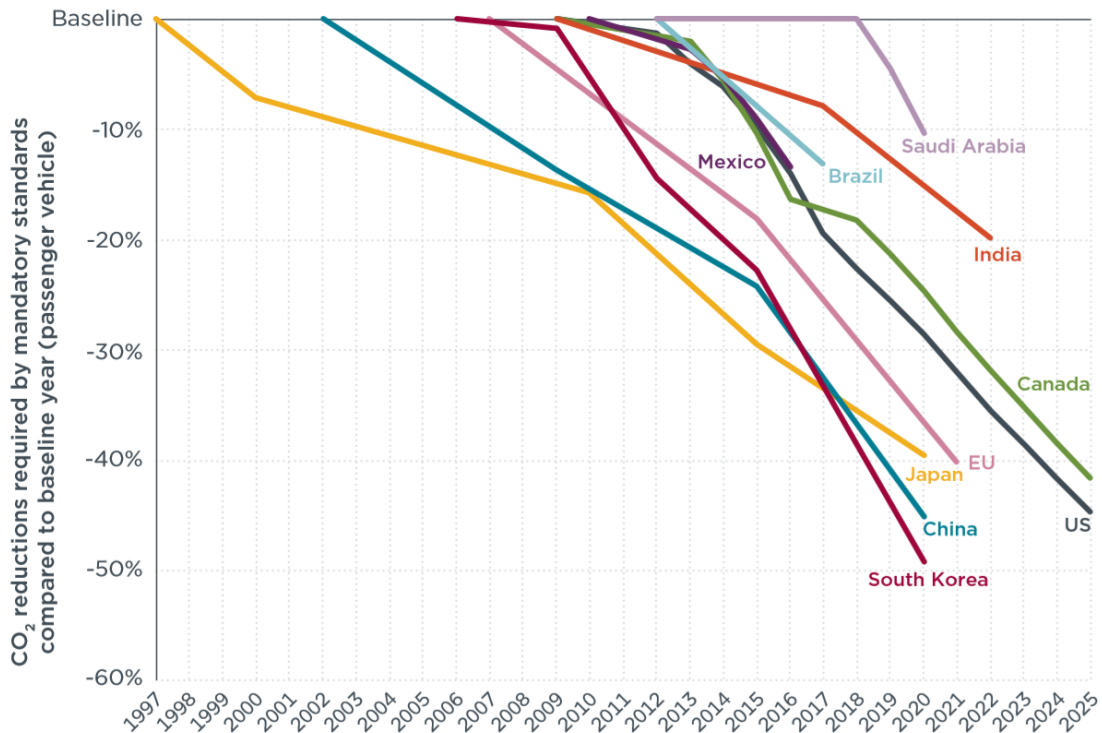


Figure 11. Global comparison of CO<sub>2</sub> emissions percentage trend and near future target. [7]

Anyway, these drastic near future targets, in order to almost cut the current CO<sub>2</sub> emissions, give an idea of the challenge that automotive research is currently facing around the world. In order to mitigate CO<sub>2</sub> emissions from the transportation sector, the European community introduced a series of standards, ‘the European Emission Standards’, to define the acceptable limits for exhaust emissions of new vehicles sold in the European Union (EU) and European Economic Area (EEA) member states. Moreover, with regard to CO<sub>2</sub>, a target of 95 grams per kilometer will be applied from 2021, with drastic reductions in the near future. Figure 12 shows how far the projections are from the more and more stringent objectives for near and remote future. The 2050 goal foresees a reduction near to 90% that is quite distant from current projections.



Figure 12. EU28 near and remote future target of CO<sub>2</sub> emissions [6].

## 1.2. RESEARCH OBJECTIVE AND TECHNICAL BACKGROUND

While the introduction of electrical and hybrid powertrains is undoubtedly a promising way to reduce the environmental impact of transportation, a full conversion of all transportation systems to an electric powertrain presents several issues and is going to take time. It is clear that thermal powertrain will still largely exist in the more or less long term, even incorporated in hybrid electric vehicles.

Table 1. Fleet specification of passenger car fleet [8].

Passenger car fleet	Brazil (2013)	China (2014)	EU-28 (2015)	India (2015)	Japan (2011)	Mexico (2014)	Saudi Arabia (2012)	South Korea (2014*)	U.S. (2015)
Sales (million)	3.0	20.7	13.7	2.8	3.5	0.7	0.4	1.4	7.5
Engine displacement (L)	1.4	1.7	1.6	1.3	1.4	1.8	2.3	2.0	2.4
Engine power (kW)	76	98	93	59	78	95	120	120	149
Curb weight (metric tons)	1.1	1.4	1.4	1.1	1.2	1.2	1.4	1.5	1.6
Footprint (m <sup>2</sup> )	3.7	4.1	4.0	3.5	3.7	3.8	4.2	4.2	4.3
Fuel consumption - NEDC (l/100km)	6.8	7.3	5.1	5.3	5.8	6.3	6.8	6.4	6.8
CO <sub>2</sub> emission - NEDC (g/km)	154	171	120	123	136	147	158	148	158
Petrol	6%	98%	44%	47%	86%	99%	-	51%	94%
Diesel	0%	2%	52%	50%	0%	1%	-	39%	1%
Hybrid-electric	0%	0%	2%	0%	13%	0%	-	0%	5%
Others	94%	0%	2%	3%	1%	0%	-	10%	0%
Manual transmission	83%	49%	75%	92%	1%	56%	-	2%	6%
Automatic transmission	17%	51%	25%	8%	99%	44%	-	98%	95%

\* South Korea footprint reflects 2011 fleet, engine power reflects 2013 fleet  
Data sources: (Marklines, 2016; Mock, 2016), additional ICCT internal databases

Chart reported in Table 1 summarizes the current passenger car fleet specification relative to the key automotive markets worldwide. These data point out that ICEs currently represent the dominant technology for transportation and, among liquid fuels, gasoline is the most widely used fuel for light-duty vehicles. It appears plausible that, even though its share is intended to decline in the next decades, spark ignition (SI) engines fueled with gasoline will remain the main thermal powertrain for the next decades. Therefore, the need to reduce the CO<sub>2</sub> and pollutant emissions, by improving efficiency as example, remains a major objective for the ICEs development.

Nevertheless, due to the highly advanced technology already reached in the current state of art of ICEs, it appears clear that any further improvement requires implementation of new technologies, refinement of existing concepts and investigation of previously unexplored combustion conditions. Today, one of the major routes towards a high efficiency SI engine is the ‘*downsizing*’, which consists in increasing the engine load through displacement reduction and turbocharging. Reducing the engine dimensions means fewer and smaller cylinders, that is, minimized internal friction, thermal losses and masses moved. This leads to a boost in fuel economy (potentially around 20%) by also cutting CO<sub>2</sub> emissions. Moreover, by looking at the Torque/Speed diagram, one can observe the gain in terms of operational

regime of a downsized engine with respect to a standard one (Figure 13). In fact, the normal driving zone is better exploited with a downsized engine, even though a turbocharger is necessary to compensate the power loss. Turbocharging implies the strong increase of temperature and pressure during combustion that may lead to abnormal combustions phenomena. In order to contain these occurrences, high level of dilution rate has to be used, mainly by using the Exhaust Gases Recirculation (EGR). However, as the stability of the engine, related to the stability of the combustion processes is strongly affected by the dilution level, increasing the tolerance of SI engines to high dilution remains a major technical challenge. To avoid empirical design matrix, the help of modelling tools remains one of the keys to optimization of ‘high diluted’ turbocharged engine. In fact, the prediction from the tools of the behavior of downsized engine at high dilution rate remains not sufficiently accurate. Current state of the art misses the adequate tools to correctly predict the combustion of premixed flame in operating conditions induced by the downsizing strategy.

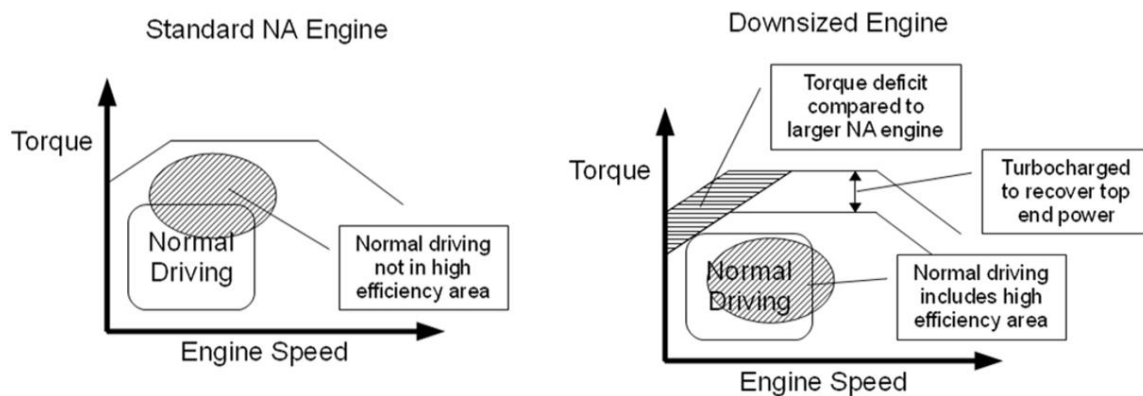


Figure 13. Torque/Speed curves comparison for standard and downsized engine.

### 1.3. THESIS OUTLINE

This PhD study takes place in the major context of an ANR project ‘MACDIL’ (Moteur Allumage Commandé à fort taux de DILution, ANR-15-CE22-0014) that aims to provide accurate and reliable predictive models for future SI engines design.. For that, it is fundamental to fill the lack of experimental data that are currently gathered quite far from real operating conditions. The strategy of the MACDIL project consists in a thorough approach including model development and improvement, (turbulent premixed combustion and chemical kinetic models) and validation thanks to dedicated experimental database. The present PhD work is dedicated to the experimental investigation of turbulent expanding premixed flames under downsized SI engine-like conditions, i.e. high pressure and temperature, high turbulent intensity and high dilution rate. Different intermediate steps are required to reach such final objective as: first, it is fundamental to validate a purposely-designed surrogate to represent the combustion properties and behavior of real gasoline. Second, the experimental investigation of premixed expanding flames are done both in laminar and turbulent conditions, thanks to two different and complementary experimental set-ups: a classic, and well-known, spherical vessel already characterized in previous work ([9], [10]) and the New One Shot Engine (NOSE), with a dedicated combustion chamber, designed, characterized and validated as part of the present work.

Chapter 2 of this manuscript is dedicated to the fundamental theory of laminar and turbulent premixed flames. For the laminar part the concepts of combustion and expanding spherical flames will be introduced, important definition of fundamental parameters as well as flame characteristics and instabilities will be introduced. For the turbulent part, a first definition of Homogeneous Isotropic Turbulence (HIT) will be given. Moreover, turbulence and flame interaction will be treated and important dimensionless numbers introduced. This will allow a detailed explanation of the Peters-Borghgi diagram that will be used as a guideline in the settlement of the investigated experimental points. A review of current models for turbulent premixed combustion will be also presented.

Chapter 3 presents an overview on the experimental strategy of the work, including the milestones fixed and solved following the development of the whole experimental campaign. The two experimental set-ups used for laminar and turbulent flames characterization are fully described. Firstly, the spherical vessel, already characterized and validated in previous works in its laminar and turbulent configuration. Successively, the NOSE apparatus, with a large part dedicated to its validation. The optical techniques implemented and used on both the experimental set-ups are detailed and the measurement procedure is discussed. The experimental procedure and the working concept of NOSE, together with the properties of flexibility and repeatability are investigated and discussed. Then, the aerodynamic characterization of the flow field inside the NOSE combustion chamber is presented. Finally, all NOSE configurations (three for turbulent cases and one for laminar conditions) are summarized.

Chapter 4 presents the results obtained in laminar environment, firstly on the spherical vessel and, successively, on NOSE. As first result, the validation of TRF-E as gasoline surrogate through the comparison between gasoline and TRF-E properties is presented with the suggestion of a mathematical empirical correlation to estimate the laminar burning velocity. Then, NOSE set-up is validated by directly comparing measurements obtained at identical experimental conditions on spherical vessel and NOSE. Using experimental points at high pressure the TRF-E laminar burning velocity database was significantly enlarged and the mathematical correlation was further refined.

Chapter 5 presents the results of the turbulent flame investigation. The study was firstly performed exploiting the experimental limits of the spherical vessel and building a large reference database. Successively, using NOSE, the experimental database was enlarged up to cover interesting, and almost unexplored, zones of the Peters-Borghi diagram, reproducing engine-like conditions. Different characteristics and properties of the obtained flames are evidenced and discussed. Moreover, limits in the measurements and a possible shifting of combustion regime are pointed out. Finally, the extrapolated turbulent flame propagation speed is presented and analyzed.

This manuscript is ended by the summary of the results obtained during this PhD study, some considerations and possible perspectives.





---

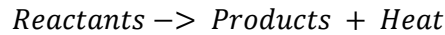
## **2. Theory of Premixed Flames**

---



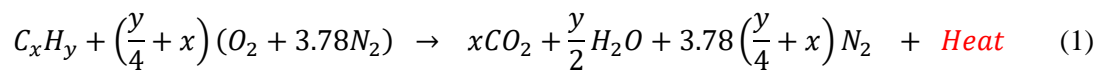
## 2.1. LAMINAR PREMIXED COMBUSTION

A combustion process is defined as the ensemble of the elementary chemical chain reactions that lead to the global, high- temperature, exothermic chemical reaction



Where, as reactant one identifies the reductant (fuel) and the oxidant (usually oxygen in the atmospheric air), and the products are often in gaseous form. The heat produced self-sustains the combustion. Reactants can be in different states of matter and can be separated (diffusive flame) or mixed (premixed flame). Depending on the characteristics of the reactants, heat released and products nature change. The combustion process requires an initial activation energy that must be sufficient to trigger the chemical radical reactions.

The focus of the present work will be on the premixed flames, using a hydrocarbon as fuel and the air (synthetic air composed by 79.1 % N<sub>2</sub> and 20.9 % O<sub>2</sub>, which is the real oxidant specie) as oxidant. For this couple of reactants the following balanced global chemical reaction is obtained:



Depending on the fuel/oxidant couple, flammability limits of the mixture change. These are function of the thermodynamic conditions and, moreover, of the fuel/oxidant ratio. The stoichiometric ratio between these two species is defined as the exact quantity of oxidant required to completely oxidize the fuel. Starting from this definition, the equivalence ratio,  $\phi$ , is the ratio between the actual fuel to oxidizer ratio divided by the stoichiometric ratio:

$$\phi = \frac{\frac{Y_f}{Y_o}}{\left(\frac{Y_f}{Y_o}\right)_{st.}} \quad (2)$$

The theory of Mallard and Le Châtelier (1883) describes the combustion process of premixed flames identifying different zones. As illustrated in Figure 14, the fresh gaseous mixture is separated from the burned gases by the preheating zone and the reaction zone. The heat flux from the zone of reaction and the zone of burned gases increases the temperature of the fresh gases in the preheating zone of thickness  $\delta_p$ . The first elementary chemical reactions that are triggered in this zone are usually considered negligible with respect to the effect of the thermal diffusion. On the contrary, in the reaction zone,

identified by the thickness  $\delta_r$  and also called flame front, the heated reductant and oxidant species completely react. The overall process is governed by molecular and thermal diffusion.

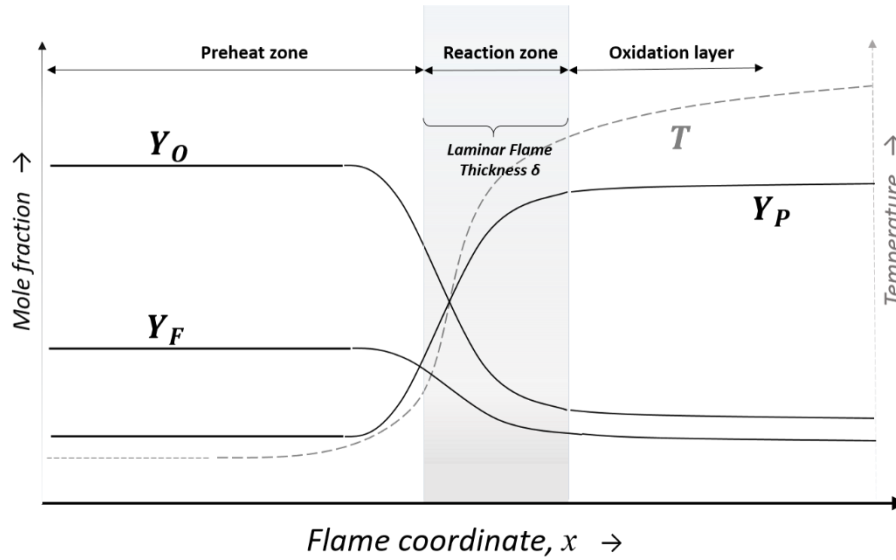


Figure 14. Model of a laminar premixed flame.

### 2.1.1. Definition of Flame Speed

As seen, according to this model, if the fresh gaseous mixture is in stationary conditions or laminar flow, or in, the flame can be defined as a thin surface that divides products and reactants, i.e., burned gases from fresh ones. In order to consume the fuel, the flame front advances toward the fresh gases. The definition of flame propagation velocity becomes self-evident and underlies the combustion theory. Despite this, several definitions exist in the current literature, as well as several methods to determine it. In the following the two definitions given by Poinot and Veynante [11] are reported:

- the laminar burning velocity,  $S_L$ , which is a global parameter directly linked to the reactants consumption rate,  $S_C$ .
- the flame propagation speed  $V_L$ , which is an absolute velocity that corresponds to the normal velocity at which the flame front moves with respect to reference system.

In Figure 15, two temperature iso-surfaces of a flame front at time  $t$  and  $t+dt$  are represented. Starting from a generic point, located on the first iso-surface, let us define a normal to the surface,  $\vec{n}$ , and identify the velocity  $\vec{w}$  as the displacement of the flame front, with respect to the reference system.. In such described system, the velocity  $\vec{u}_g$  is the displacement velocity of the fresh gases in front of the flame front and, by definition, the laminar burning velocity  $S_L$  is normal to the flame front, hence

$$\vec{w} = S_L \vec{n} + \vec{u}_g \quad (3)$$

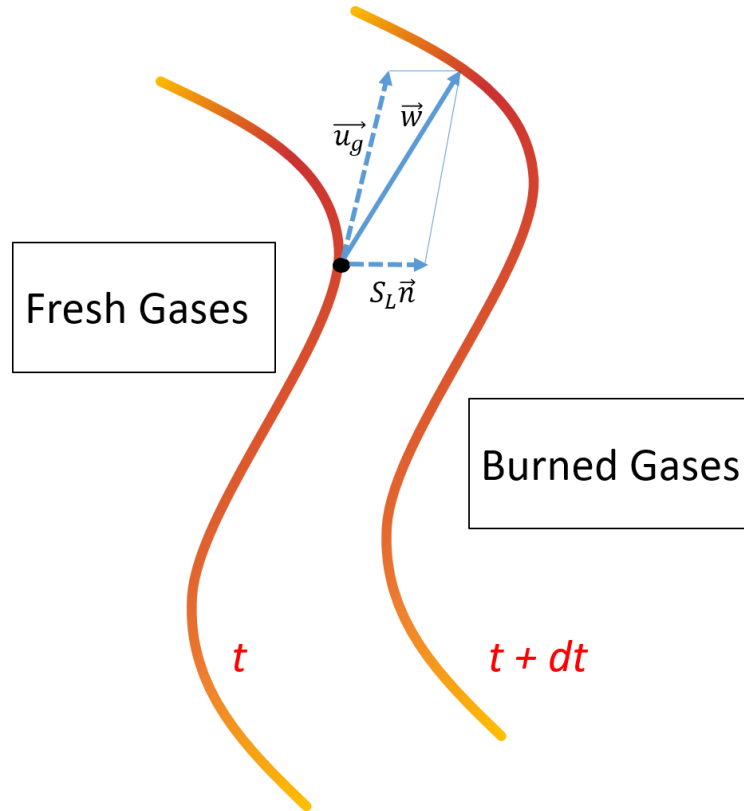


Figure 15. Flame speed definition.

By considering a spherical flame, both velocities,  $\vec{w}$  and  $\vec{u}_g$  are coincident with the normal  $\vec{n}$ . This allows the definition of the flame propagation speed  $V_L$  normal to the flame surface and defined as  $V_L = \vec{w} \cdot \vec{n}$ , that is equal to the sum of the laminar burning velocity  $S_L$  and the fresh gases velocity:

$$V_L = S_L + u_g \quad (4)$$

The flame front displacement is strictly dependent on the flame geometry. It is then necessary to introduce the concept of flame stretch (detailed in Sub-section 2.1.3), as well as the unstretched flame propagation speed and the unstretched laminar burning velocity, respectively  $V_L^0$  and  $S_L^0$  (further discussed in Sub-section 2.1.6). The latter corresponds to the particular case of plane, adiabatic and unstretched flame.

The unstretched laminar burning velocity is a fundamental parameter, directly related to the combustion chemistry, since it is dependent on the reactants consumption velocity  $S_C$ . This velocity can be computed using the reaction rate,  $\dot{\omega}_r$  of one of the reactants or the formation rate,  $\dot{\omega}_p$  of one of the combustion products, coupled respectively with the mass fraction  $Y_R^u$ , for the reactant ( $u = \text{unburned zone}$ ), or  $Y_P^b$ , for the product ( $b = \text{burned zone}$ ):

$$S_C = -\frac{1}{\rho_u Y_R^u} \int_{-\infty}^{+\infty} \dot{\omega}_r dn = \frac{1}{\rho_u Y_P^b} \int_{-\infty}^{+\infty} \dot{\omega}_p dn \quad (5)$$

where  $\rho_u$  is the specific volume of the fresh gases. Calling  $\dot{\omega}_k$  the rate of reaction or production of the generic species of the chemical reaction, one can rewrite:

$$S_C = \frac{1}{\rho_u (Y_k^b - Y_k^u)} \int_{-\infty}^{+\infty} \dot{\omega}_k dn \quad (6)$$

As the  $S_C$  is strictly dependent on the chemical mixture characteristics, it is self-evident that the unstretched laminar burning velocity  $S_L^0$  is a fundamental property of the specific air/fuel couple.

### 2.1.2. Flame Thickness

In Section 2.1, the combustion model was introduced assuming the flame front as a thin surface that separates reactants and products. However, the definition of flame thickness,  $\delta_L$ , represents a crucial topic in the literature and, nowadays, several models exist in order to quantify this parameter [12], [13]. One generally used definition is the one of Poinso et al. [14]. By assuming the Schmidt number ( $Sc$ ) is equal to 1,

$$Sc = \frac{\mu}{\rho D_m} = \frac{\nu}{D_m} = 1 \quad (7)$$

where  $D$  is the molecular diffusivity,  $\mu$  is the dynamic viscosity and  $\nu$  is the kinematic viscosity. So  $Sc = 1$  implies that propagation is driven by heat conduction only, leading to the following expression for  $\delta_L^0$ :

$$\delta_L^0 = \frac{\lambda_u}{\rho_u c_{p_u} S_L^0} \quad (8)$$

where  $\lambda_u$  is the thermal conductivity of the fresh gases (expressed in  $W m^{-1}K^{-1}$ ),  $\rho_u$  the specific volume (expressed in  $kg m^{-3}$ ),  $c_{p_u}$  the specific heat capacity at constant temperature (expressed in  $J K^{-1}kg^{-1}$ ) of the reactants mixture and  $S_L^0$  the unstretched laminar burning velocity. This definition of  $\delta_L^0$  is deduced starting from the equilibrium between the thermal diffusion and the species diffusion across the flame front. This is why this definition of the flame thickness is also called *thermo-diffusive* flame thickness. This classical expression of the flame thickness actually underestimates the real flame thickness by a factor around 5 [11]. Alternative formulations have been developed to get a better approximation as the Blint's one [15]:

$$\delta_L^B = 2\delta_L^0 \left(\frac{T_f}{T_i}\right)^{0.7} \quad (9)$$

where  $T_i$  and  $T_f$  are, respectively, the initial temperature and ‘the’ flame temperature, usually replaced by the adiabatic flame temperature  $T_{ad}$ . The Blint’s flame thickness definition is more representative of the reality and commonly used in numerical simulations [11].

### 2.1.3. Flame Front Stretch

The idea of the flame stretch rate was figured out by the works of Clavin [16], Karlovitz [17] and Markstein [18]. With the term stretch rate one refers to two different phenomena acting on the flame evolution: the flame front curvature and the velocity gradients acting in front of the flame front. Stretch may cause variations of the flame propagation speed [17], [18] and, thus, of the laminar burning velocity. Local flame extinctions may arise if the stretch rate is too intense. However, these phenomena also depend on the thermodynamic conditions and on the mixture composition.

The stretch rate represents the rate at which the surface of an element on the flame surface increases during the flame front propagation. Therefore, according to Williams [19] the stretch rate can be computed as:

$$K = \frac{1}{A} \frac{dA}{dt} \quad (10)$$

where  $A$  is the surface of an element of the flame front. In the literature several mathematical definitions of the stretch rate  $K$  exist [20]–[22]. As shown in ANNEX A from Candel and Poinso [14] the total stretch rate is the sum of two different contributes:

$$K = K_S + K_C \quad (11)$$

Bradley and co-workers [23] found that these two components of the stretch rate proposed by Candel and Poinso [14] can be re-written in the simple form if the case of spherically propagation flame::

$$K_S = \frac{2}{R_f} u_g \quad (12)$$

and

$$K_C = \frac{2}{R_f} S_L \quad (13)$$

The mutual relations between  $S_L$ ,  $u_g$  and  $V_L$ , lead to the following equation for the stretch rate:

$$K = \frac{2}{R_f} V_L \quad (14)$$

### 2.1.4. Combustion Instabilities

Combustion instabilities may arise during the flame front propagation due to several physical mechanisms, leading to its local deformation or abnormal displacement. The interaction between the thermal and the molecular diffusivity is one of the main factor that causes local inhomogeneity and instabilities.

#### 2.1.4.1. *Instabilities due to the effect of gravitational forces*

The gravity field can play an important role in the flame propagation instabilities insurgence because the burned and the unburned gases have different densities, the latter are heavier than the first ones. That is why, the premixed flames are stables if the flame front is propagating downward, in the same direction of the gravity field, since the heavier unburned gas lie at the bottom with respect to the lighter burned ones. On the contrary, if the flame is propagating upward, the unburned gases will move in the opposite sense, causing an equilibrium instable. Anyway, this phenomenon may arise, for spherical flames, only when the laminar burning velocity is sufficiently low to allow the insurgence of the disequilibrium between buoyancy and gravitational forces.

#### 2.1.4.2. *Hydrodynamic Instabilities*

Earlier works by Darrieus [24] and Landau [25] identified the hydrodynamic instability in premixed flames, isolating the phenomenon with respect to the effect of thermal and molecular diffusivity. The basic assumption of the model is that the flame thickness is infinitesimal and the flame structure unaltered. The so-called Darrieus-Landau instabilities are caused by the unburned gases undergo a high acceleration through the flame front due to the different specific volume of burned and unburned gases. This expansion factor,  $\rho_u/\rho_b$ , is around 7 for common hydrocarbons, leading to a high specific volume gradient across the flame front in order to assure the mass flow conservation.

Let suppose that a flame front, initially plane, undergoes a perturbation such that it causes a curvature of certain amplitude in the flame front. As shown in Figure 16, the unburned gases represents the reference for the definition of convex and concave curvatures of the flame front. Figure 16 indicates how the current flow lines diverge and converge, respectively, when approaching convex and concave wrinkles. Therefore, the local unburned gas speed,  $u$ , locally decreases in the first case (upper part of Figure 16) and increases in the second one (lower part of Figure 16), in order to grant the mass flow conservation. On the contrary, the unstretched laminar burning velocity,  $S_L^0$ , remains unchanged. This

behavior amplifies the wrinkles amplitude and highlights the intrinsically unstable nature of the flame front.

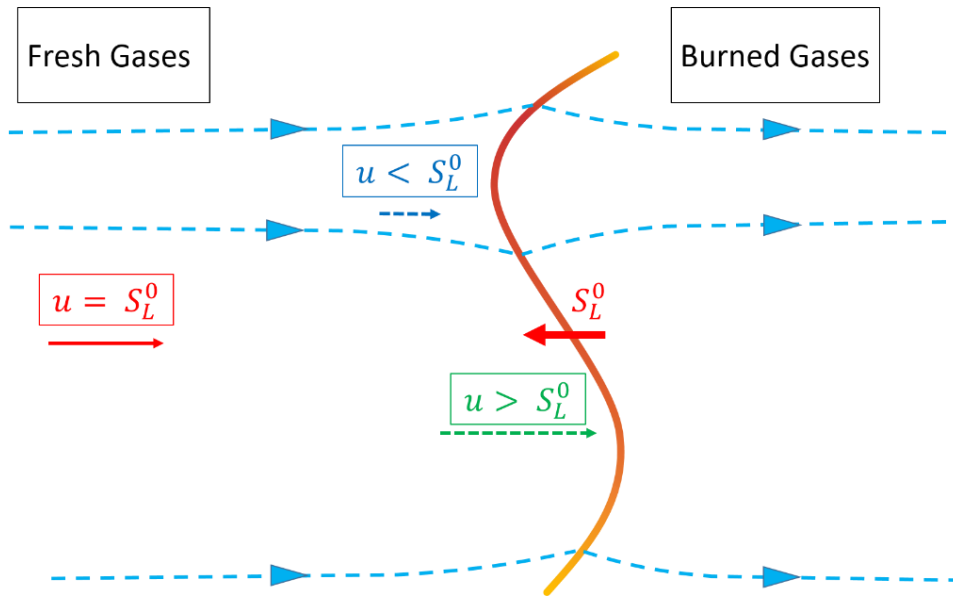


Figure 16. Scheme of the Darrieus-Landau (or hydrodynamic) instabilities.

As the hydrodynamic instabilities depend on the high specific volume gradient across the flame front, the thinner the flame front, the higher the gradient will be, increasing the hydrodynamic instabilities insurgence. As the flame thickness decreases with pressure increase, the higher the pressure, the earlier the flame front will become wrinkled, during its expansion, due to the Darrieus-Landau instabilities [26]. This phenomenon leads to the occurrence of the so-called *cellularity* on the flame surface of an expanding spherical flame. Cellularity alters the laminar behavior of the premixed flames and, for this reason, limits the experimental investigation and the time of meaningful observations.

#### 2.1.4.3. Thermo-diffusive, or Rayleigh-Taylor, Instabilities

Thermal and molecular diffusivities have a key role in the flame front propagation and its evolution. The heat flux and the mass flux, in fact, are directly proportional to the thermal diffusivity,  $D_{th}$  and the molecular diffusivity,  $D_m$  of the reactive mixture, respectively. These fluxes are normal to the reaction zone and opposite in direction. The heat flux is directed to the pre-heating zone, starting from the flame surface, while the mass flux carries the reactive, and pre-heated species from the pre-heating zone to the flame front. The concurrent effects of these fluxes can lead to the flame instability or, its stabilization. That is why the ratio between thermal and molecular diffusivities, called Lewis number,  $Le$ , is a crucial parameter in the thermo-diffusive instabilities evaluation. Lewis number, in fact, takes into account the concurrent effects of heat and mass flux:

$$Le = \frac{D_{th}}{D_m} \quad (15)$$

Figure 17 (a) shows the destabilizing case for  $Le < 1$ , while Figure 17 (b) the stabilizing one, for  $Le > 1$ , taking into account an initially slightly perturbed laminar flame front. In the first case, the molecular diffusivity is greater than the thermal one. For concave wrinkles, the species diffusion leads to a local excess of reactants while the heat flux is weak, thus the pre-heating zone increases locally reducing the stretched laminar burning velocity,  $S_L$ , with respect to the unstretched one,  $S_L^0$ . For the convex wrinkle, though the molecular diffusion is important, there is not an excessive input of reactant species, allowing the fast consumption of the latter and the local  $S_L$  increases. The overall effect tends to accentuate the perturbation, leading to an unstable flame front.

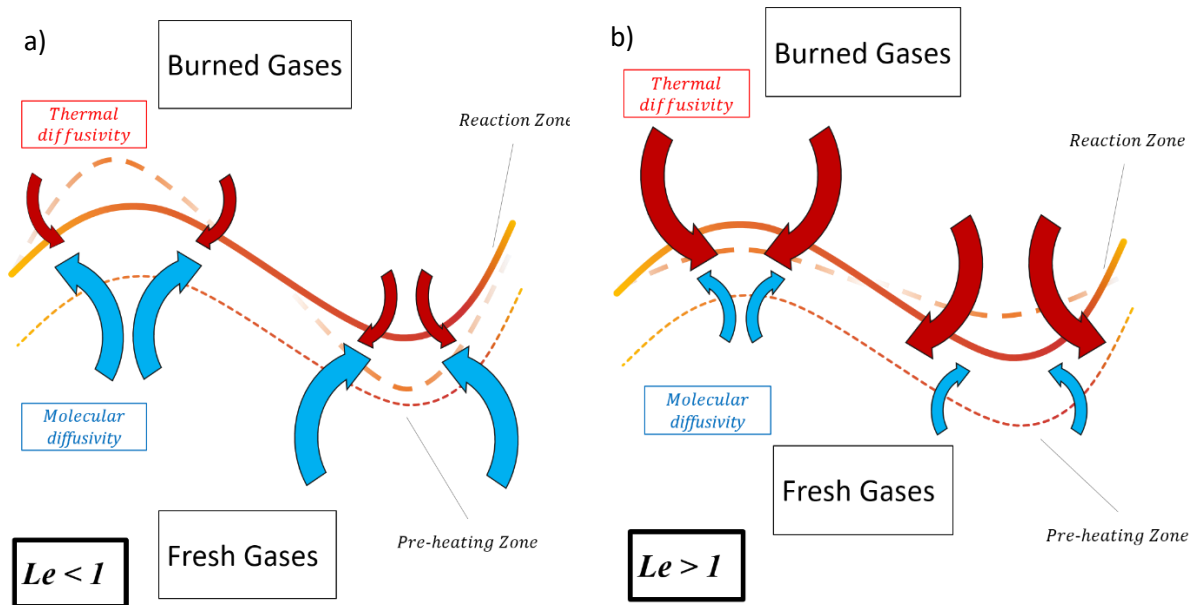


Figure 17. Thermo-diffusive instabilities: a)  $Le < 1$  instable flame; b)  $Le > 1$  stable flame.

On the contrary, when  $Le > 1$ , the  $S_L$  undergoes a local increase with respect to the  $S_L^0$ , in the concave wrinkle. This is due to the fact that the heat flux is sufficient to pre-heat the reactant species in the pre-heating zone, despite the flame front concave shape, since these species are diffused less intensively. On the other hand, the molecular diffusion is not sufficient to supply the flame front in view of the high thermal diffusion and, consequently, the  $S_L$  locally decreases. The outcome of these phenomena is the stabilization of the flame front. In case of Lewis number equal to 1, the equilibrium between thermal and molecular diffusion subsists and the source of instability are not of thermo-diffusive nature. Anyway, the actual Lewis number, at which this instability occurs, may differ from the theoretical one and, in literature, it is named critical Lewis number,  $Le_c$  [16]. As figured out by Williams [27], this critical Lewis number can be obtained by the following equation:

$$Le_c = 1 - \frac{1}{\beta} \frac{2\sigma \ln(\sigma)}{\int_0^{\sigma-1} \frac{1}{x} \ln(1+x) dx} \quad (16)$$

where  $\sigma$  is the ratio between the specific volumes, that is, the expansion ratio,  $x$  is the distance and  $\beta$  is the reduced activation energy, computed as:

$$\beta = \frac{E(T_{ad} - T_i)}{R T_{ad}} \quad (17)$$

where  $R$  is the ideal gas constant,  $E$  the reaction activation energy [28],  $T_i$  the initial unburned gases temperature and  $T_{ad}$  the flame adiabatic temperature.

In the evaluation of the Lewis number the equivalence ratio of the mixture has a key role, as the Lewis number changes according to the concentration of the limiting species ( $O_2$  for poor mixtures and fuel components for rich mixtures) and of the exceeding species ( $N_2$  for air/fuel mixtures). That is why is necessary to consider an effective Lewis number,  $Le_{eff}$ , using the approach of Bechtold and Matalon [28] to obtain a weighted average between the Lewis numbers of the limiting ( $Le_D$ ) and the exceeding ( $Le_E$ ) species. The effective Lewis number is:

$$Le_{eff} = 1 + \frac{(Le_E - 1) + (Le_D - 1)A}{1 + A} \quad (18)$$

Where  $A$  is defined as  $A = 1 + \beta(\theta - 1)$ , with  $\theta = \phi$  if the mixture is rich, or  $\theta = 1/\phi$  if lean. Thermo-diffusive instabilities produce smaller cellules with respect to the cellularity caused by Darrieus-Landau instabilities. While the latter are mainly caused by a high pressure, for the great part of long-chain hydrocarbons, the thermo-diffusive instabilities occurrence increases with the richness of the reactive mixture. Moreover, these two kinds of instabilities may act simultaneously and reduce the range over which the rays can be analyzed drastically.

As previously introduced, the Lewis number is the ratio between thermal and molecular diffusivity. The thermal diffusivity can be computed as:

$$D_{th} = \frac{\lambda}{C_p \rho_u} \quad (19)$$

where the thermal conductivity of the reactive mixture is computed as follows:

$$\lambda = \frac{1}{2} \left[ \left( \sum_{j=1}^n X_j \lambda_j \right) + \frac{1}{\sum_{j=1}^n X_j / \lambda_j} \right] \quad (20)$$

with  $X_j$  and  $\lambda_j$  that are, respectively, the molar fraction and the thermal conductivity of the species  $j$ , computed through empiric relations function of the temperature [29].

On the other hand, the molecular diffusivity,  $D_m$ , directly depends on the molecular diffusivity of the limiting species  $k$  in the reactive mixture, and can be computed as:

$$D_m = \frac{1 - Y_k}{\sum_{j \neq k}^n X_j / D_{jk}} \quad (21)$$

where  $Y_k$  is the mass fraction of the  $k$  species and  $D_{jk}$  are the molecular diffusivities of the  $j$  species into  $k$ , calculated through empiric relations function of the temperature [29].

Finally, one observes that the Lewis number is directly proportional to the thermal conductivity,  $\lambda$ , of the mixture and to the molecular diffusivity,  $D_j$ , of the species  $j$ , and inversely proportional to the density,  $\rho_u$ , of the unburned mixture. The thermal conductivity does not depend on pressure. On the contrary, the molecular diffusivity of the species  $j$ ,  $D_j$ , and the specific volume,  $\rho_u$ , are, respectively, inversely and directly proportional to the pressure. Therefore, the Lewis number is independent on pressure. Due to the aforementioned empiric correlations, functions of the temperature, for the determination of  $\lambda_j$  and  $D_{jk}$ , it exists a slight Lewis number dependence on temperature. Anyway, this dependence is negligible with respect to the equivalence ratio increase and becomes less and less important for richer mixtures, as pointed out by Galmiche [30].

### 2.1.5. Expanding Flames Laminar Burning Speed

In case of spherical premixed flames, the stretched flame propagation speed,  $V_L$ , corresponds to the flame radius variation rate:

$$V_L = \frac{dR_f}{dt} \quad (22)$$

This flame radius,  $R_f$  can be directly determined from the experiments. Then, by considering the expansion factor, that is the ratio between burned and unburned gases specific volume, one can obtain:

$$S_L = \frac{\rho_b}{\rho_u} V_L \quad (23)$$

However, Eq. (22) neglects several physical phenomena:

- The effect of the initial spark causes an augmentation of the initial laminar burning velocity and, in addition, an increase of the burned gases temperature.

- The curvature and the diffusive processes affect the flame propagation speed (but the effect decreases with the increase of the radius), as well as the burned gases temperature.
- The fact that the combustion process is confined influences the flame evolution and, for relatively long radii, the increase of pressure has to be taken into account.

The demonstration of Bonhomme [31] correlates the flame propagation speed to the gas consumption velocity,  $S_C$ , representing a more suitable approach. As already presented in previous sub-section, the Eq. (6) of the gas consumption velocity,  $S_C$ , is function of the reaction rate  $\dot{\omega}_k$  of the species  $k$ . Considering the spherical flame:

$$S_C = \frac{1}{\rho_u(Y_k^b - Y_k^u)r^2} \int_0^{R_0} \dot{\omega}_k r^2 dr \quad (24)$$

where  $R_0$  is the internal radius of the spherical flame. On the other hand, the conservation equation of the species  $k$  is:

$$\frac{\partial \rho Y_k}{\partial t} + \vec{\nabla}(\rho(u_i + V_{k,i})Y_k) = \dot{\omega}_k \quad (25)$$

with  $u_i$  and  $V_{k,i}$  that are the fluid velocity and the diffusion velocity of the species  $k$ , respectively. The integration of the conservation equation, in the integration domain  $0 \leq r \leq R_0$ , yields:

$$\frac{dM_k}{dt} + 4\pi R_0^2 \rho_u Y_{k(r=R_0)} [u_{r(r=R_0)} + V_{k,r(r=R_0)}] = \int_0^{R_0} \dot{\omega}_k 4\pi r^2 dr \quad (26)$$

The term  $M_k$  is the total mass of the species  $k$ ,  $M_k = \int_V \rho Y_k dV$ ; the second term the total flux of the species  $k$  at the radius  $r = R_0$ ; at the second member of the equation one can substitute the term with the initial  $S_C$  definition given in Eq. (5):

$$\frac{dM_k}{dt} + 4\pi R_0^2 \rho_u Y_{k(r=R_0)} [u_{r(r=R_0)} + V_{k,r(r=R_0)}] = S_C 4\pi r^2 \rho_u [Y_k^b - Y_k^u] \quad (27)$$

If the geometry is closed, at  $r = R_0$ , the velocities  $u_r$  and  $V_{k,r}$  are equal to 0. The species  $k$  can be a reactant or a product. Considering a product species and defining a constant sphere with mean radius  $r_p$  and products mass  $M_p$ , the following equivalence is verified:

$$r_p^3 = \frac{M_p}{\frac{4}{3}\pi \bar{\rho}_b Y_p^b} \quad (28)$$

where  $Y_p^b$  is the mass fraction of one product species and  $\bar{\rho}_b$  is the spatial averaged density of the product gases between  $r = 0$  and  $r = r_p$ .

Then, from Eq. (27) and (28), the gas consumption velocity can be written in the following form:

$$S_c = \frac{\bar{\rho}_b}{\rho_u} \frac{dr_p}{dt} + \frac{r_p}{3\rho_u} \frac{d\bar{\rho}_b}{dt} \quad (29)$$

Eq. (29) does not require that the flame thickness is infinitesimal. On the other hand, the assumptions of homogenous density of gases, and their invariance in time, hold. In addition, one assumes that the initial value of the unburned gases density  $\rho_u$  does not change, neglecting the walls confinement effect. The latter hypothesis is reasonable if considering the initial volume enough large. On the contrary, the averaged burned gases density is supposed equal to the equilibrium one  $\rho_b^{eq}$ . The validity of this assumption decays with the increase of the laminar thickness, even though the  $\bar{\rho}_b$  may be considered constant in time if the combustion is isobaric. In these conditions the gas consumption velocity become:

$$S_c = \frac{\rho_b^{eq}}{\rho_u(t=0)} \frac{dr_p}{dt} \quad (30)$$

The flame radius experimentally detected that was named  $R_f$  is different from  $r_p$  because it depends on the adopted optical technique. Anyway, these two radii tend to coincide when the flame thickness decreases during the flame propagation. This allows the assumption  $R_f \approx r_p$ .

### 2.1.6. Markstein Length and Unstretched Laminar Burning Velocity

Markstein firstly pointed out the existence of a relationship between the local propagation speed of the front flame and its local stretch [32]. Further works of Clavin [16], [33] and Matalon [34] confirmed this relationship and furnished a linear equation to correlate stretched and unstretched flame propagation speed:

$$V_L = V_L^0 - L_b K \quad (31)$$

where  $V_L^0$  is the unstretched flame propagation speed and  $L_b$  is the Markstein length for the burned gases and directly depends on the mixture properties. This relation assumes that the stretch is enough weak to involve a ratio  $V_L/V_L^0$  close to 1. It was then demonstrated by Halter et al. [35] and Kelley and Law [36] that the relation between the flame propagation speed and the stretch is better described by a non-linear equation:

$$\left(\frac{V_L}{V_L^0}\right)^2 \ln\left(\frac{V_L}{V_L^0}\right) = -\frac{2L_b K}{V_L^0} \quad (32)$$

However, as pointed out by Chen and Ju [37] several stringent hypotheses yield at the base of this relation:

- The flame propagation is considered as quasi-stationary.
- Radiation transfer is negligible. This is a strong hypothesis in case of highly CO<sub>2</sub> diluted flames [38]–[40].
- The flame thickness is negligible with respect to the radius  $R_f$ .
- The activation energy of the mixture is enough elevated to allow the assumption of a reaction chemistry infinitely fast.
- The phenomenon is adiabatic. That is consistent with the reality since the high thermal inertia of combustion chamber.
- The spark ignition initial energy does not influence the flame.
- The wall effect, that is the confinement of the flame, is negligible. This hypothesis can be assumed if the radius of the flame is relatively low with respect to the vessel size.
- The burned gases are considered at rest.

These two last points will be discussed in Chapter 3. Anyway, previous work of Kelley et Law [36] had extensively treated these two effect in the extrapolation of the flame propagation speed (Figure 18).

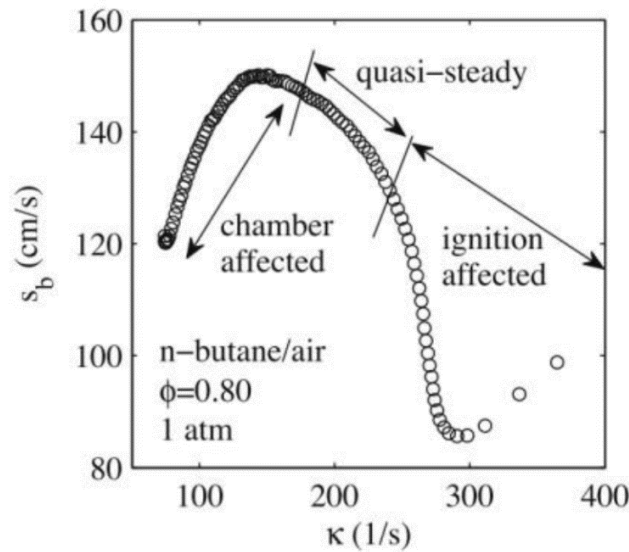


Figure 18. Effects of chamber confinement and spark ignition system on the evolution of the flame propagation speed,  $V_L$  (that here is noted  $s_b$ ), as function of the stretch rate  $K$  [36].

Finally, assuming the validity of the Eq. (32), the unstretched laminar burning speed  $S_L^0$  is determined from the unstretched laminar flame propagation velocity by introducing the expansion factor  $\rho_b/\rho_u$

$$S_L^0 = \frac{\rho_b^{eq}}{\rho_u} V_L^0 \quad (33)$$

## 2.2. TURBULENT PREMIXED FLAMES

### 2.2.1. Turbulence Statistical Approach

The chaotic nature of turbulent flows involves an incredibly high number of phenomena, of different nature, that hinder the exact mathematical description of such turbulent systems. For applicative or practical purposes the use of simpler models, usually with strong hypotheses, and statistical approaches are still necessary.

It is possible to decompose the velocity of the turbulent flow  $U(x, y, z, t)$  in an averaged value and aleatoric fluctuations, according to Reynolds definition:

$$U(x, y, z, t) = \overline{U(x, y, z, t)} + u(x, y, z, t) \quad (34)$$

The root mean square of these fluctuations is named *turbulent intensity*:

$$u'_{rms}(x, y, z, t) = \sqrt{\overline{u^2(x, y, z, t)}} \quad (35)$$

If the fluctuations are not dependent on space then the turbulence is *homogeneous*. If they are also independent on the rotation of the reference system the turbulence is *isotropic*. This idealized condition was described by Taylor [41] and named HIT, *Homogeneous Isotropic Turbulence*. It is characterized by an ideally unlimited spatial domain and the invariance with respect to translation, rotation and symmetry plans.

The importance of the HIT model is due to the possibility of greatly simplify the Navier-Stokes equations. Moreover, this kind of turbulence can be described through a low number of parameters. Anyway, even though the major vortex that generate the turbulence are non-homogeneous and non-isotropic, the derived small vortex tend to locally evolve toward quasi-homogeneous and isotropic conditions.

The turbulent kinetic energy can be determined as:

$$k = \frac{3}{2} q'^2 \quad (36)$$

where  $q'$  is the turbulent intensity associated to a HIT, that is computed using the fluctuations the three velocity components  $u'$ ,  $v'$  and  $w'$ :

$$q' = \sqrt{\frac{u'_{rms}{}^2 + v'_{rms}{}^2 + w'_{rms}{}^2}{2}} \quad (37)$$

### 2.2.2. Kolmogorov Theory and Characteristics Scales

The generic turbulent flow is characterized by an infinite number of vortices of different sizes, responsible of the turbulence and the energy and mass transport. According to the theory of Kolmogorov (1941), the ensemble of vortices of a turbulent flow can be modeled as a cascade of eddies of different size. The kinetic energy is mainly carried on by the large vortices and converted into internal energy by viscous shear stress. Then, the large eddies are progressively dissipated in smaller structure. This process continues, originating smaller and smaller vortices and causing the dissipation of the major part of the energy associated to the turbulent motion. It is therefore evident that it is necessary to continuously furnish energy to sustain the turbulent flow.

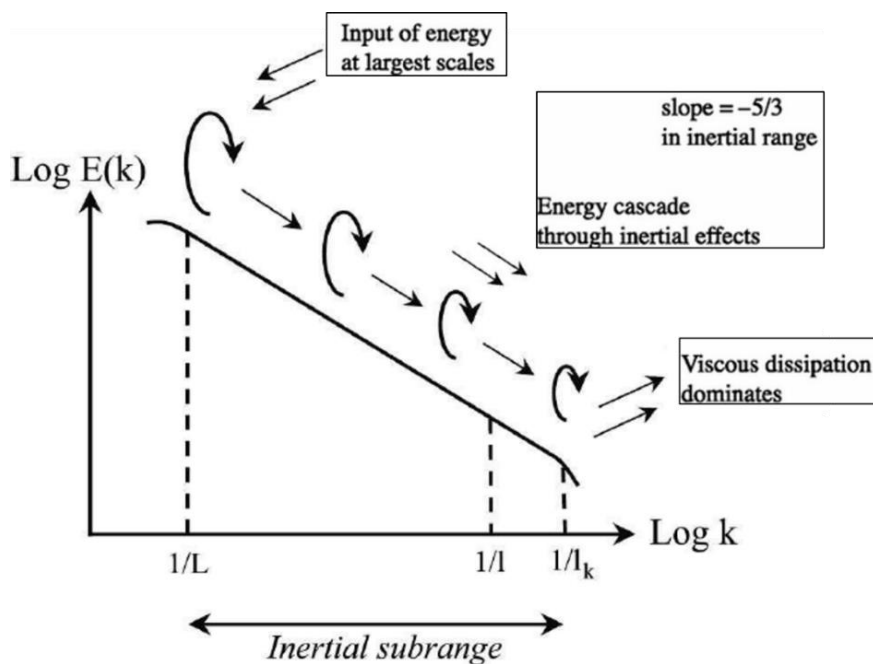


Figure 19. Scheme of the Kolmogorov turbulence cascade model.

Figure 19 shows the Kolmogorov cascades scheme and the three domains just described. The curve represent the energy spectrum  $E(\kappa)$  associated to the turbulent flow with the kinetic energy  $k$ . The term  $\kappa = 2\pi/l$  is the *wavenumber* associated to the vortex of characteristic length  $l$ . The wavenumber is the spatial frequency of a wave that measures the number of cycles per unit of distance. The energy spectrum is:

$$k = \int_0^{\infty} E(\kappa) d\kappa \quad (38)$$

The Taylor scales regime is the inertial zone, in which the energy is transferred. The curve inclination in this range is proportional to  $\kappa^{-5/3}$ . The eddies hierarchy so-described can be divided in three main categories according to the following length scale of the vortexes.

- a) The integral length scale,  $L_T$ , includes the largest structures, in which the great part of the turbulent kinetics energy of the system is present. This domain is characterized by low frequency and high wavelength, almost independent on the viscosity of the fluid but strictly depends on the geometry of the system. The associated integral time scale,  $T_T$ , can be computed by analyzing the autocorrelation time coefficient,  $R_u(\tau)$ , of the fluctuation component  $u(x, y, z, t)$ :

$$R_u(0,0,0,\tau) = \frac{\overline{u(x, y, z, t) \cdot u(x, y, z, t + \tau)}}{\sqrt{\overline{u^2(x, y, z, t)}} \sqrt{\overline{u^2(x, y, z, t + \tau)}}} \quad (39)$$

The integral time scale represents the time interval in which it exists a correlation between  $u(t)$  and  $u(t + \tau)$ , so the time during which the velocity fluctuation is still correlated to itself. Clearly, when  $\tau = 0$  this coefficient is 1. Then, as the time increases it decades and, when it reaches 0 it means that there is no more dependence between  $u(t)$  and  $u(t + \tau)$ . The integral time scale is then evaluated as the area under the autocorrelation time coefficient curve

$$T_T = \int_0^{\infty} R_u(0,0,0,t) dt = \int_0^{t_0} R_u(0,0,0,t) dt \quad (40)$$

where  $t_0$  correspond to the first zero of the function.

In the same way, the autocorrelation spatial coefficient,  $R_u(\xi_x, \xi_y, \xi_z, 0)$ , represents the spatial correlation of two points in the velocity field of the generic fluctuations component, evaluated at  $\tau = 0$ . In other words, the distance within which it exists a dependence between the fluctuation components  $u(x, y, z, 0)$  and  $u(x + \xi_x, y + \xi_y, z + \xi_z, 0)$ :

$$R_u(\xi_x, \xi_y, \xi_z, 0) = \frac{\langle u(x, y, z, t) \mid u(x + \xi_x, y + \xi_y, z + \xi_z, \tau) \rangle}{\sqrt{\overline{u^2(x, y, z, t)}} \sqrt{\overline{u^2(x + \xi_x, y + \xi_y, z + \xi_z, \tau)}}} \quad (41)$$

Considering a 2D velocity field, the autocorrelation of the components  $u$  and  $v$  can be evaluated with respect to an infinitesimal displacement along  $x$  or  $y$  direction. So, one can identify the longitudinal and transversal integral length scale:

$$\left\{ \begin{array}{l} L_{U_x} = \int_0^{\infty} R_u(\xi_x, 0, 0, 0) d\xi_x \\ L_{U_y} = \int_0^{\infty} R_u(0, \xi_y, 0, 0) d\xi_y \\ L_{V_x} = \int_0^{\infty} R_v(\xi_x, 0, 0, 0) d\xi_x \\ L_{V_y} = \int_0^{\infty} R_v(0, \xi_y, 0, 0) d\xi_y \end{array} \right. \quad (42)$$

The longitudinal and transversal integral lengths of the component  $u'$  are, respectively,  $L_{U_x}$  and  $L_{U_y}$ . While,  $L_{V_y}$  and  $L_{V_x}$  are the longitudinal and transversal integral lengths of the component  $v'$ .

According to the definitions of Taylor [41] and van Karman and Howarth [42], conditions of HIT can be assumed if the following two conditions are verified:

$$L_{U_x} = 2 L_{U_y} \quad \text{and} \quad L_{V_y} = 2 L_{V_x} \quad (43)$$

$$\frac{u'_{rms}{}^2}{v'_{rms}{}^2} = 1 \quad (44)$$

If these conditions are verified the integral length scale characteristic of the system can be determined as the mean of the two longitudinal integral length of the components  $u$  and  $v$ . In the present work the just described procedure for the evaluation of the integral length scales was used. Then, according to the literature, other options exist. If the mean flow  $\overline{U(x, y, z, t)}$  is non-zero the following relationship holds [43]:

$$L_T = \overline{U} * T_T \quad (45)$$

so it is possible to associate the integral length scale to the integral time scale  $T_T$ . On the contrary, if the mean flow  $\overline{U(x, y, z, t)}$  is null it is necessary to introduce the term  $\bar{s}$ , named *pseudo-convective velocity*, that represent the mean velocity relative to a Gaussian probability law of the tridimensional velocity field for a HIT. Then, the integral length scale is [44]:

$$L_T = \bar{s} * T_T \quad (46)$$

where

$$\bar{s} = \sqrt{\frac{8}{\pi}} q' \quad (47)$$

The determination of the integral length scale is fundamental for the evaluation of the Reynolds number that describes the ratio between the turbulent motion and the viscous forces:

$$Re_T = \frac{q' L_T}{\nu} \quad (48)$$

where  $\nu$  is the fluid kinetic viscosity (expressed in  $m^2/s$ ).

- b) The Taylor scales are characterized by vortices of intermediate size, related to the instabilities of the integral scale eddies and responsible of the energy transfer from largest to smallest structures. The Taylor length scale, usually named  $\lambda$ , represents the characteristic length at which the viscous dissipation plays a dominant role. The exact equation for the kinetic energy dissipation rate  $\varepsilon$  is:

$$\varepsilon = \nu \overline{\left( \frac{\partial q'_i}{\partial x_j} + \frac{\partial q'_j}{\partial x_i} \right) \frac{\partial q'_i}{\partial x_i}} \quad (49)$$

If the hypotheses of HIT hold the kinetic energy dissipation rate  $\varepsilon$  can be expressed as [45]:

$$\varepsilon = 15\nu \frac{q'^2}{\lambda^2} = C_\varepsilon \frac{q'^3}{L_T} \quad (50)$$

where  $C_\varepsilon$  is the normalized dissipation rate. Burattini et al. [46] showed that this value may vary between 0.5 and 2.5 depending on the experimental set-up and on the initial conditions. Anyway, the exact evaluation of this coefficient is still constantly challenged. In the present study it will be approximated as  $C_\varepsilon \sim 1$ . The Taylor length scale  $\lambda$ , then, becomes:

$$\lambda \approx \sqrt{15 \frac{L_T \nu}{q'}} \quad (51)$$

that can be re-arranged as

$$\frac{\lambda}{L_T} \approx \sqrt{\frac{15}{Re_T}} \quad (52)$$

- c) The Kolmogorov length scales,  $\eta_K$ , are representative of the smallest eddies, where the energy transported by the larger vortexes is finally dissipated as internal energy. These structures have

high frequency and tend to be locally homogeneous and isotropic. Using a dimensional approach, with the kinetic viscosity expressed in  $m^2/s$  and the dissipation rate  $m^2/s^3$ , the Kolmogorov length scale can be estimated as

$$\eta_K = \left( \frac{\nu^3}{\varepsilon} \right)^{\frac{1}{4}} \quad (53)$$

Assuming the aforementioned hypothesis for the Taylor length scale (that is,  $C_\varepsilon \sim 1$ ), it is possible to simplify Eq. (53) using the previously introduced equation of the dissipation rate (Eq. (50)). In this way, one obtains:

$$\eta_K = \left( \frac{\nu^3 L_T}{q'^3} \right)^{\frac{1}{4}} \quad (54)$$

Eq. (54) can be re-arranged to obtain a direct relationship with the Reynolds number associated at the largest eddies scale:

$$\frac{\eta_K}{L_T} \approx Re_T^{-3/4} \quad (55)$$

### 2.2.3. Interaction between Turbulence and Premixed Flames

The interaction between the flame front of a mixture and the rotational turbulent flow (vortices or eddies) defines the type of combustion regimes in which the combustion is set. The Karlovitz number,  $Ka$  was addressed as one fundamental parameter to distinguish different combustion regimes on the Peters-Borghgi diagram [27], [47]–[49]. It is defined as the ratio between the characteristic time of the chemical reactions and the one of the smallest turbulent structures, that is, the Kolmogorov length scale. Figure 20 reports the Peters-Borghgi diagram, in which the Karlovitz number and other important dimensionless parameters appear: the Damkohler number,  $Da$  and the Reynolds number,  $Re_T$ . By using the thermo-diffusive laminar flame thickness and the unstretched laminar burning velocity, the characteristic time of the laminar flame is:

$$t_L = \frac{\delta_L^0}{S_L^0} \quad (56)$$

The characteristic time of the turbulence is derived from the turbulent intensity and the integral length:

$$t_T = \frac{L_T}{q'} \quad (57)$$

Finally, the characteristic time associated to the Kolmogorov scale structures is:

$$t_K = \left(\frac{\nu}{\varepsilon}\right)^{\frac{1}{2}} \quad (58)$$

Then, the aforementioned three dimensionless numbers can be expressed in the following form:

$$Ka = \frac{t_L}{t_K} = \frac{\delta_L^0}{S_L^0} \left(\frac{\nu}{\varepsilon}\right)^{-\frac{1}{2}} \quad (59)$$

$$Da = \frac{t_T}{t_L} = \frac{L_T S_L^0}{q' \delta_L^0} \quad (60)$$

$$Re_L = \frac{q' L_T}{S_L^0 \delta_L^0} \quad (61)$$

These three dimensionless number represent the interaction of the flame with the smallest turbulent structures ( $Ka$ ), with the chemistry ( $Da$ ), and with the large turbulent eddies ( $Re_L$ ). While the Damkohler and the Reynolds number can be easily evaluated with Eq. (60) and (61), respectively, being all the quantities experimentally measurable, Karlovitz number expression must be further simplified. Once again it is possible to use the approximated equation of the dissipation rate (Eq. (50)) and the hypothesis of Schmidt number (presented in Sub-section 2.1.2) equal to 1 (yielding  $\nu \approx D_{ch}$ ). Since  $D_{ch} = \delta_L^0 S_L^0$ , the explicit form of the Karlovitz number expression can be written as:

$$Ka = \frac{\delta_L^0}{S_L^0} \left(\frac{\nu L_T}{q'^3}\right)^{-\frac{1}{2}} = \left(\frac{\delta_L^0}{L_T}\right)^{\frac{1}{2}} \left(\frac{q'}{S_L^0}\right)^{\frac{3}{2}} \quad (62)$$

This expression of the Karlovitz number is usually solved using the thermo-diffusive flame thickness. On the other hand, using other more restrictive definitions of the flame thickness (as the one of Blint [15]), yields higher Karlovitz numbers due to the increase of the flame thickness estimation. For the sake of consistency, in the following, the diffusive flame thickness will be used to plot points on Peters-Borghgi diagram as in Figure 20. Each point on this logarithmic diagram depends on the interaction between the turbulence and the flame front. In particular, the ratios  $u'/S_L^0$  and  $L_T/\delta_L^0$  are taken into account, and the hypothesis of HIT is assumed.

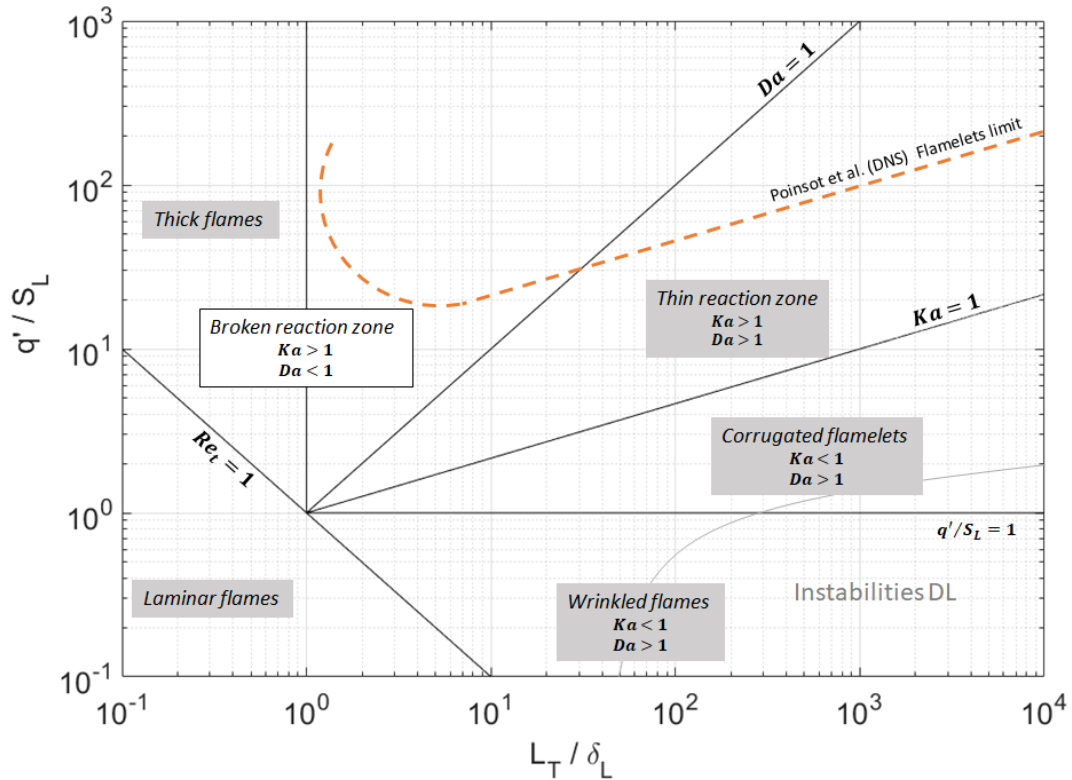


Figure 20. Peters-Borghi diagram.

Referring to Figure 20, the first zone is the pseudo-laminar flame region for  $Re_T < 1$  where the turbulent intensity is very low or because the viscosity is high. Alongside this simple case, other three main zones exist for  $Re_T > 1$ . The first is the region in which flamelet model is a good approximation of the real physical phenomenon. According to this model, the flame is considered as asymptotically thin and locally laminar even if the turbulence can wrinkle the flame surface [50], [51]. So the main effect of turbulence is to increase the flame surface. For  $Ka < 1$  the turbulent eddies cannot enter into the flame structure but just wrinkle or corrugate its surface (if the ratio  $u'/S_L$  increases). Williams identified the threshold between the wrinkled and the corrugated zones in the flamelet region [27] as below:

- If  $u'/S_L^0 < 1$  the turbulent fluctuations are slower than the unstretched laminar burning velocity, so the flame surface is just wrinkled by the flow but there is no interaction between the flamelet and the turbulent structures (Figure 21).
- If  $u'/S_L^0 > 1$  the eddies can strongly affect the structure of the flame front, eventually causing pockets of fresh gases in the burned gases and vice versa (Figure 22).

The validity of the flamelet model may start to fade in the second region, the so-called distributed (or thin) reaction zone. Since  $Da < 1$ , the laminar flame propagation is still faster than the turnover of the largest eddies. With respect to the previous case, however, the Karlovitz number is now greater than 1. This means that the smallest vortices, at the Kolmogorov scale, can enter the flame structure, causing

high strain rates that lead to a wider distribution of the flame structure and, possibly, local quenching. Figure 23 shows the scheme of this kind of flame characterized by a thicker flame thickness  $\delta_L^0$ . Finally, if both the Karlovitz and the Damkohler numbers are greater than 1, also until the largest eddies can penetrate the flame structure, until local extinction. This regime is called well-stirred reactor (or broken reaction zone).

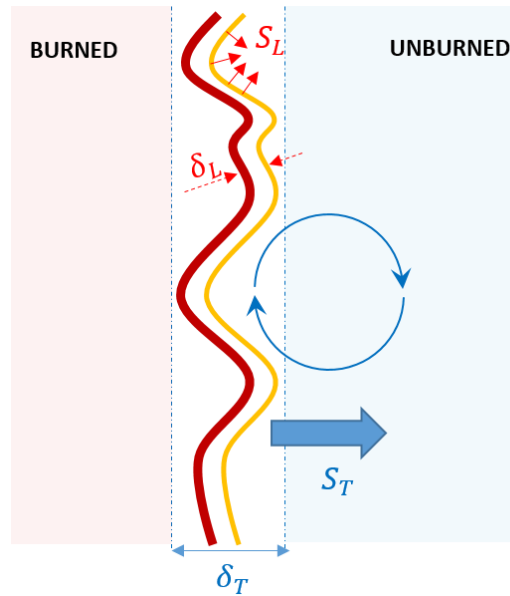


Figure 21. Scheme of the *wrinkled flames* regime.

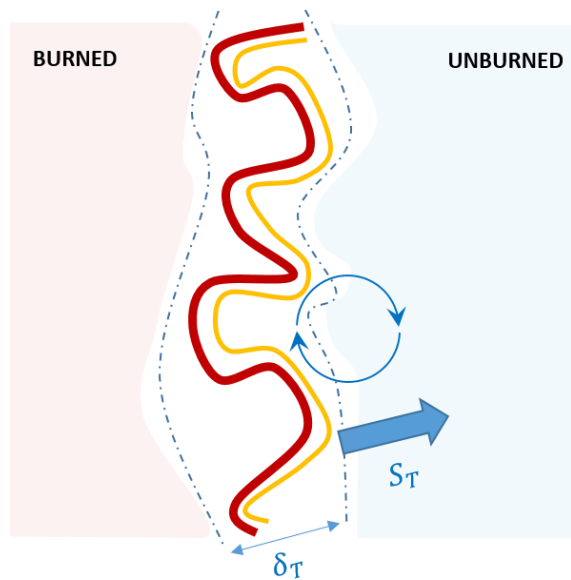


Figure 22. Scheme of the *corrugated flamelet* regime.

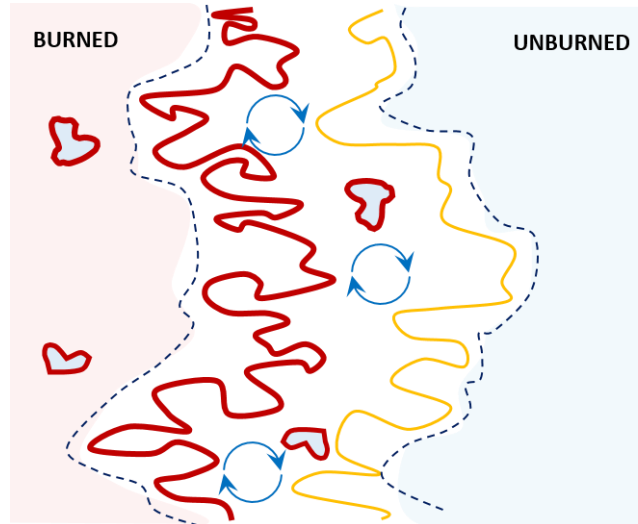


Figure 23. Scheme of the *thin reaction zone* regime.

#### 2.2.4. Flamelet Regime Model and Validity Limits

As previously discussed, the flamelet model assumes that the flame is composed of several infinitely small laminar flame elements, which are wrinkled by the turbulent flow. So, the turbulence increases the flame surface, which induces the turbulent flame brush (also called ‘thickness’  $\delta_T$ ) and the turbulent burning velocity  $S_T$ , as schematizes in Figure 21 and Figure 22.

From the early work of Damköhler [52], in 1940, and further study of Driscoll [53], a relation between  $S_T$  and the turbulent flame surface  $A_T$  is widely used as:

$$\frac{S_T}{S_L^0} = \frac{A_T}{A_L} I_0 \quad (63)$$

where the term  $I_0$  is called mean strain factor [54].

The real threshold at which the flamelet model fades is still an open topic. The Klimov-Williams criterion limits its validity at  $Ka < 1$ . It is evaluated through a dimensional analysis on the Peters-Borghini diagram but it does not take into account the viscous effect of the fluid at Kolmogorov scale. In this respect the work of Driscoll [53] enlarges this limit up to  $Ka = 10$ .

In 1991, Poinso et al. faced the problem of interaction between flame surface and turbulence using DNS [55]. In this way, they found out that flame front is more resistant to the quenching due to vortices than expected from theory. In fact, as described by Peters [56], the whole flame thickness is divided in different zones. The chemically inert preheat zone is followed by a thin inner layer in which the fuel is attacked by radicals. This layer controls the flame structure and its thickness is:

$$\delta_{inn} = \delta * \delta_L^0 \quad (64)$$

where  $\delta$  is a factor of the order of 0.1. Using this thickness the actual inner layer-based Karlovitz number is  $Ka_\delta = 1$ , that corresponds to a classical Karlovitz number of 100. Poinot et al. considered  $Ka = 180$  and  $Ka = 25$ , which induce  $\delta_{inn} = 0.2 \delta_L^0$  and  $\delta_{inn} = 0.07 \delta_L^0$ , respectively and showed from DNS that the eddies at Kolmogorov scale can significantly alter the pre-heating zone but they cannot enter the thinner reaction zone. According to these results, it could be considered that the flamelet regime can actually be extended at higher Karlovitz numbers. Further work of Dinkelacker [57] experimentally pointed out that the stretch of the flame front plays a dominant role in the internal structure of the flame and that the validity of the flamelet model fades for  $Re_T > 600$ .

### 2.2.5. Turbulent Flame Characterization in the case of Spherical Expansion

As introduced in the previous section, as well as for the laminar case, it is convenient to introduce a turbulent burning velocity  $S_T$  and a turbulent flame thickness  $\delta_T$ . Considering a section of an expanding turbulent flame, one can identify a minimum, a maximum and a mean radius according to the wrinkling of the flame surface.

The difference between  $R_{min}$  and  $R_{max}$  is the turbulent flame thickness, while the value  $R_{mean}$  is used to compute the turbulent burning velocity from the generic definition:

$$S_T = \frac{\rho_b}{\rho_u} \frac{dR_{mean}}{dt} \quad (65)$$

Bradley et al. [58] and Haq [59] defined a radius,  $R_v$ , more consistent with the real mean radius of the turbulent flame as corresponding to the radius of the sphere such that the volume of the burned gases outside this sphere is equal to the volume of the unburned gases inside. As shown in Figure 24, it exists a radius  $R_r$  that is the maximal radius containing only burned gases. On the contrary, it exists a radius  $R_t$  that contains all the burned gases, but clearly a part of unburned gases as well. Considering a radius  $R_j$  between  $R_r$  and  $R_t$  one can write the mass flux equilibrium through the surface of the sphere with radius  $R_j$ :

$$\frac{d(m_{b,i} + m_{b,o})}{dt} = 4\pi R_j^2 \rho_u S_{T,j} \quad (66)$$

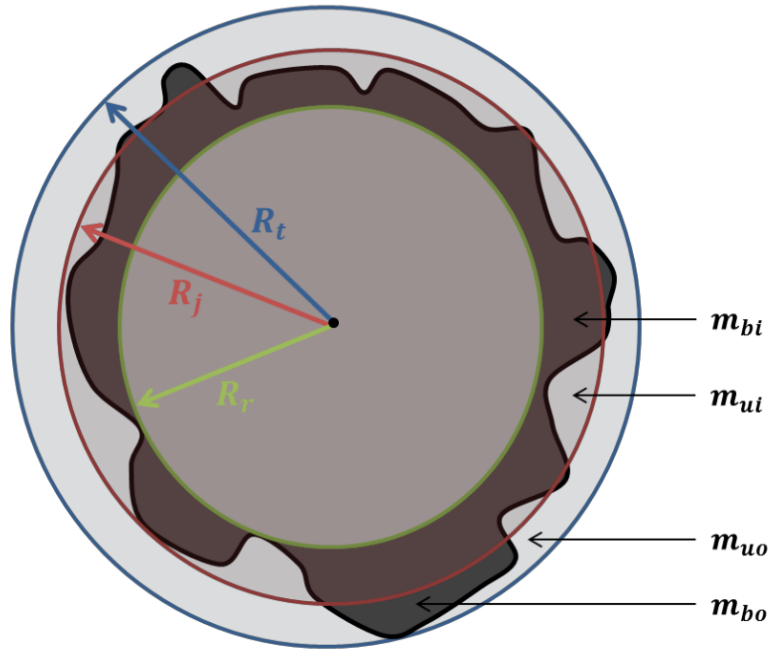


Figure 24. Scheme of a turbulent expanding flame and radii definitions, adapted from [10].

with  $m_{b,i}$  and  $m_{b,o}$  that are, respectively, the mass of burned gases between  $R_r$  and  $R_j$  and the mass of burned gases between  $R_j$  and  $R_t$ . It is also possible to explicit the term  $m_{b,i}$  as function of  $m_{u,i}$ , the mass of unburned gases inside the volume between  $R_r$  and  $R_j$ :

$$m_{b,i} = \left( \frac{4}{3}\pi R_j^3 - \frac{1}{\rho_u} m_{u,i} \right) \rho_b \quad (67)$$

Considering the density of burned and unburned gases constant in time (isobaric combustion) the previous mass flux balance becomes:

$$4\pi R_j^2 \rho_u S_{T,j} = \left( 4\pi R_j^2 \frac{dR_j}{dt} - \frac{1}{\rho_u} \frac{dm_{u,i}}{dt} \right) \rho_b + \frac{dm_{b,o}}{dt} \quad (68)$$

Using the definition of  $R_v$  means that:

$$V_{b,o} = V_{u,i} \quad \xrightarrow{\text{yields}} \quad \frac{m_{b,o}}{\rho_b} = \frac{m_{u,i}}{\rho_u} \quad (69)$$

and, thus,

$$S_T = \frac{\rho_b}{\rho_u} \frac{dR_v}{dt} \quad (70)$$

### 2.2.5.1. Stretch of the turbulent flame

It was presented, in previous section about laminar flame, that the flame stretch  $K$  is expressed as:

$$K = -\vec{n}\vec{n} : \vec{\nabla}\vec{u}_g + \vec{\nabla} \cdot \vec{u}_g + S_L^0 \vec{\nabla} \cdot \vec{n} \quad (71)$$

This equation was defined by Candel and Poinso [14] for laminar expanding spherical flames, in which the tangential component  $K_t$  is negligible, and for planar flames, in which the curvature effect is null.

Renou et al. [60], by measuring the velocity of unburned gases of a turbulent expanding flame, pointed out that the tangential contribution can be neglected, only if the turbulent intensity is low (in the study  $q' = 0.18 - 0.34$  m/s, was used), due to the dominant effect of the expansion. Also recent work of Chaudhuri et al. [61] demonstrated the major importance of the pure curvature term,  $S_L^0 \vec{\nabla} \cdot \vec{n}$  with respect to the shear stresses acting on the surface. It seems then plausible to use, as in laminar case, the stretch rate definition of Williams [19]. As reported in Eq. (10), this definition is based on the evolution of the flame surface:

$$K = \frac{1}{A_T} \frac{dA_T}{dt} \quad (72)$$

Even though the flame stretch is given by the local fluid velocity and shape of the flame front, simplifications can be introduced in specific cases [62]. As already shown in previous work of Brequigny et al. [63], the same definition used for laminar case can eventually be applied to turbulent case using the turbulent flame surface  $A_T$  as an estimate of a global averaged flame stretch.

### 2.2.5.2. Bending Effect

Several works in literature pointed out that the laminar burning velocity does not increase indefinitely with the turbulent intensity [53], [56], [64]–[68]. On the contrary, it exists a  $u'$  limit at which the  $S_T$  value stagnates or even decreases. This phenomenon is called '*bending*', and the value of turbulent intensity at which it arises is a function of the fuel, the equivalence ratio of the mixture and the boundary conditions [64], [69]. Figure 25 shows the results obtained by Abdel-Gayed [70] for a mixture propane/air.

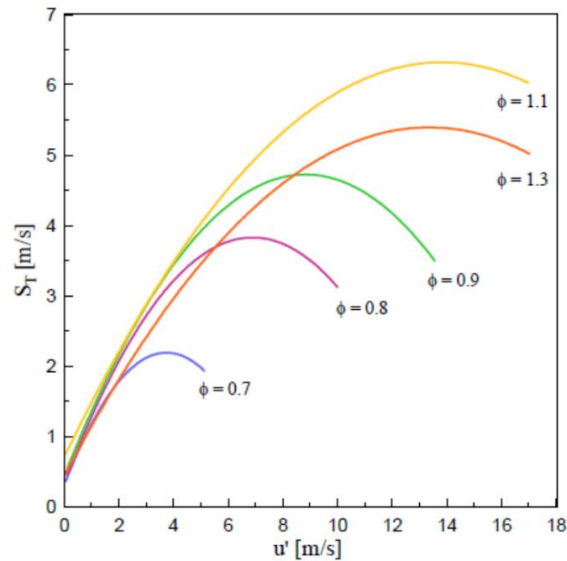


Figure 25. Evolution of  $S_T$  as a function of the turbulent intensity for a mixture air/propane [70].

### 2.2.6. Turbulent Combustion in Spark-Ignition Engines

In SI engine, the turbulent combustion regime was addressed in the corrugated flamelet zone or in the thin reaction zone [71]–[73]. The values of both ratios  $u'/S_L^0$  and  $L_T/\delta_L^0$  are a function of the operating conditions of the engine. As example, as the turbulent intensity increases with the engine regime, the position of the initial point is shifted upward on the Peters-Borghi diagram; or also as the laminar burning velocity and the laminar flame thickness decrease with the pressure increase, the position is shifted rightward. Figure 26 (a), from work of Linse et al. [72] illustrates this behaviour. Mounaïm-Rousselle et al. [73] investigated also the effect of EGR dilution on the flame propagation. As the diluted flame has lower laminar burning velocity and thicker laminar flame thickness, the ratio  $u'/S_L^0$  increases and the ratio  $L_T/\delta_L^0$  decreases, causing a shifting on the Peters-Borghi diagram to the left and to the top as in Figure 27 (b). Since most of models for the SI engine simulation are based on the flamelet model [74]–[76], they are not accurate in the case of boosted operating conditions, i.e. at high pressure with strong diluted mixtures, needed to counteract abnormal combustion phenomena and reduce NOx formation [77], [78].

However, as discussed, it is still necessary to find a solution at the drop in performances. The effect of high dilution rate on the flame causes a strong reduction in the combustion velocity. This means that it is necessary to anticipate the ignition time to compensate the slow flame propagation (Figure 28). The problem of this strategy is that the more the spark is anticipated the less favourable are the thermodynamic conditions inside the cylinder. The result is a strong instability of the engine operating conditions [79], [80], as reported in the example in Figure 29.

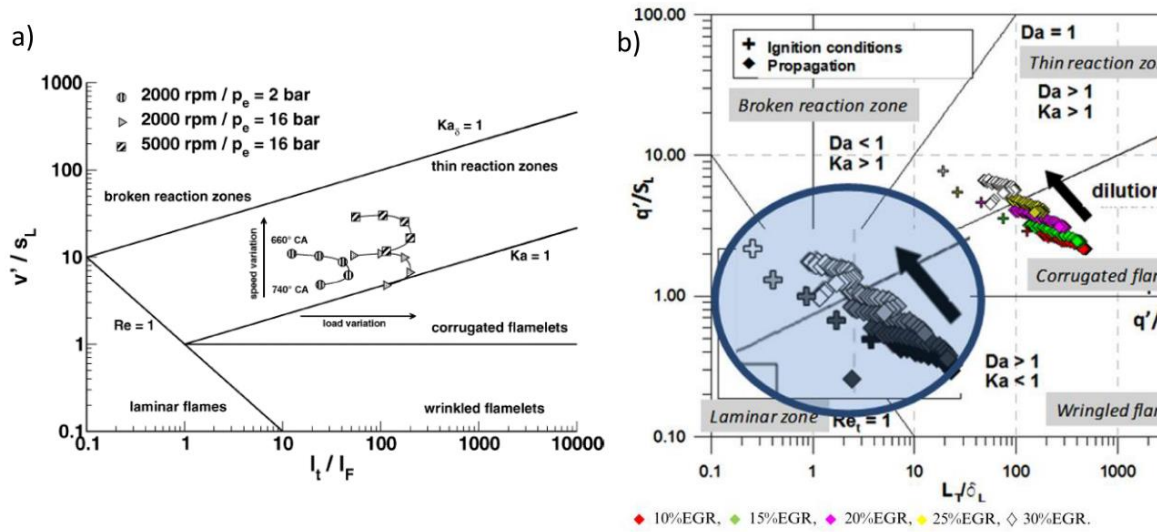


Figure 26. a) Effects of initial pressure and turbulence variation on Peters-Borghi diagram from Linse et al. [72]; b) Effect of dilution increase on Peters-Borghi diagram from Mounaïm-Rousselle et al. [73].

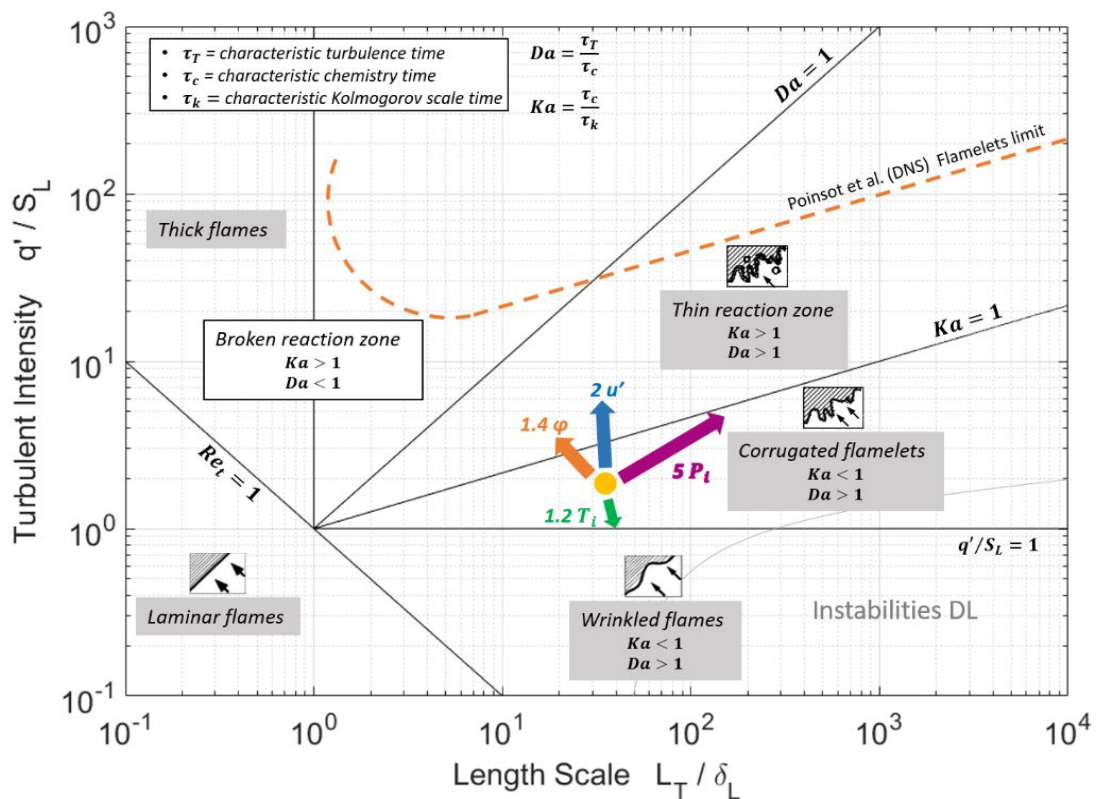


Figure 27. Resume of the combustion regimes on the Peters-Borghi diagram and the effect of increasing different parameters, adapted from [30].

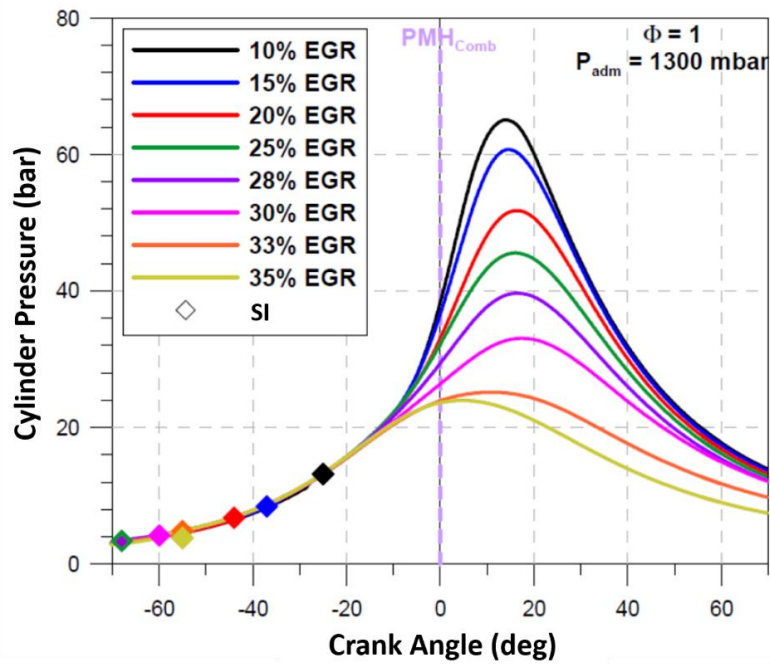


Figure 28. Cylinder pressure evolution for different dilution rates, adapted from [80].

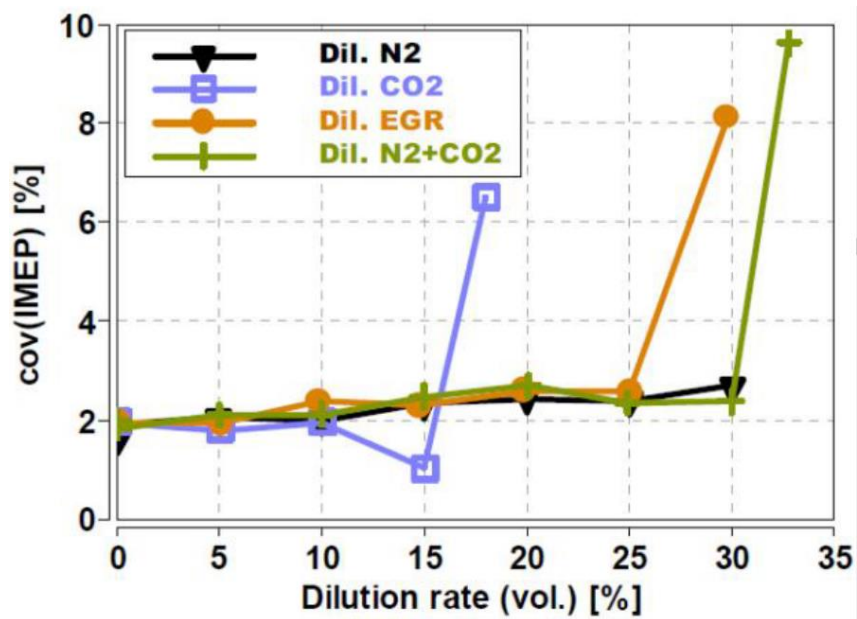


Figure 29. IMEP (Integrated Mean Effective Pressure) covariance as function of dilution rate and diluting species (with  $T_i = 313\text{ K}$  and  $P_i = 1.7 - 2.5\text{ bar}$ , increasing with the dilution rate), adapted from [79].

### 2.2.7. Turbulent Flames at High Karlovitz Number

The investigation of turbulent burning velocity,  $S_T$ , considered as the main parameter of turbulent premixed flames, motivated several studies in the recent decades. Nevertheless, the great part of these works were conducted at atmospheric pressure and room temperature conditions ([44], [53], [65]) and only recently researchers are focusing on experiments at higher thermodynamic conditions. More and more studies considered the effect of pressure, but mainly at room temperature ([58], [68], [81]–[83] among the others), as only a few high temperature ([84]–[86]). Among these, Jiang et al. [86] investigated expanding premixed methane/air flames for a temperature between 300 and 423 K and a pressure from 1 to 5 bar, with a turbulent intensity,  $q'$  from 1.43 to 5.6 m/s. Despite this appreciable range of conditions, the integral length considered was very important, i.e. between 34.4 and 45 mm, without the investigation of dilution effect. Kobayashi et al. [85], on the contrary, focused on the effect of dilution up to 10% CO<sub>2</sub> dilution rate, using a methane/air Bunsen-type burner in a high-pressure chamber (5 and 10 bar) at 573 K. They associated the decrease of the turbulent burning velocity to the decrease in local burning velocity due to the flame stretch, through the Markstein length. But, they observed that CO<sub>2</sub> dilution reduces the wrinkling scale of the mixture CH<sub>4</sub>/air, increasing the mean volume of the turbulent flame region demonstrating the possibility of restrict the combustion oscillation of premixed gas turbines.

Only few studies are for liquid fuel [87]–[90], as the one of Lawes et al. [89] focused on iso-octane/air flame propagation in a turbulent vessel from 1 to 10 bar with  $q'$  from 0.5 to 6 m/s. In this study, quenching phenomena were observed at  $\phi = 0.8$  and  $q' > 2$  m/s. Moreover, the increase of  $q'$  led to a shift of the maximum equivalence ratio at which the  $S_T$  peak is observed. At low  $q' = 1$  m/s,  $S_T$  was observed to remain constant while for  $q' > 4$  m/s it increased slightly.

Scattering in results and observations, within the topic of the turbulent premixed flames, derives from the use of very different experimental set-ups in which the fundamental properties of the turbulence may strongly vary from one study to another. In addition to the case of spherically expanding flames, and other recent set-ups that investigated a standing flame in a shock tube [91], the Bunsen-type burner is one of the most used technology to investigate turbulent flames at high Karlovitz numbers. Only one work by Liu et al. [92] directly focused on the Karlovitz number effect on turbulent expanding flames. In this study, Karlovitz number ranges from 0.4 to 4.3, with a pressure increase up to 10 bar but a large integral length value between 23.2 and 45 mm. It was found that, to increase  $S_T$ , the intensification effect caused by an enhancement of the turbulent intensity is much more effective than the instabilities generated by pressure increase. But, more important, the work shows that the turbulent burning velocity decreases with increasing pressure in a minus exponential manner similar to  $S_L$ , when Reynolds number is constant. But, if  $Re$  increases the turbulent burning velocity increases.

Studies carried out on Bunsen-type burner usually focus at higher ranges of Reynolds and Karlovitz numbers exploiting very high values of  $q'$  [53], [93]–[95] with also the investigation of the limits of the different combustion regimes zones on the Peters-Borghi diagram. In this respect, recent works of Driscoll et al. [96] and Skiba et al. [93], redefined limits and definitions of the most important combustion regimes on the Peters-Borghi diagram, considering intense turbulence cases ( $Re_T > 2800$  or  $Ka > 100$ ) and concluded that some of the usual limits fail in prediction and unification of experiments and DNS available in literature. This implies that more investigation is necessary to conclude about the existence of a net boundary between the different combustion regimes.

But one difficulty is due to the difficulty to compare results from experimental set-up, and a great number of variables that play a role in the  $S_T$  determination. For this reason, most of the time the way is to find an universal correlation to predict the turbulent flames behavior from the knowledge of the most important fundamental parameters [97]. The investigation of classic correlations [97], [98] and the formulation of new ones, are still an open topic. Remarkable works, in this sense, are those of Chaudhuri et al. [82], Wu et al. [83] and Nguyen et al. [99], performed on spherically expanding flames. Wu et al. [83] observed the local quenching for lean mixture ( $\phi = 0.8$ ) and high turbulent intensity ( $q' = 5.24$  m/s), and proposed a new version of the correlation initially proposed by Chaudhuri et al. [82]. In more recent study, Nguyen et al. [99] tried to improve three recent correlations by adding the effect of the Lewis number.

## 2.3. CONCLUSIONS

As pointed out in the last sub-section, the evident lack in the current literature must be filled. The present work aims to cover unexplored conditions on the Peters-Borghi diagram, for what concerns central-ignited expanding flames. The combination of temperatures, pressures, dilution rates and fundamental turbulence properties was never investigated in other studies. This induces the novelty of this work but also inherent difficulties due to the lack of literature references for results comparison.

In addition, the present work will use a four-components fuel as gasoline surrogate for the turbulent premixed flames investigation, while very few studies with liquid fuels exist in the current literature, as aforementioned. The characterization of the laminar flame behavior of this surrogate fuel as a function of the initial conditions (pressure, temperature, equivalence ratio and dilution rate) is essential, as well as its validation as a surrogate of a commercial gasoline.





---

## **3. Experimental Set-ups**

---



The choice of a surrogate is argued and laminar burning velocity of both gasoline and surrogate was measured, using a spherical vessel. Finally, the laminar burning velocity database of the TRF-E was enlarged to cover all the possible experimental limits of the spherical vessel.

Successively, the TRF-E was characterized in turbulent conditions, switching the configuration of the spherical vessel set-up from laminar to fan-stirred generated turbulence. The experimental limits of the spherical vessel were reached in terms of pressure, temperature and, also, turbulent intensity. Therefore, as they are quite far from real engine operational conditions, a new dedicated experimental set-up, the so-called NOSE, was characterized and exploited. NOSE set-up allows to simulate SI engine-like conditions in both laminar (under strong hypotheses) and turbulent conditions. At the same time, it offers some of the typical advantages of a spherical vessel:

- Accurate control of the mixture composition, including EGR.
- Minimization of temperature stratification occurrence.
- Knowledge of internal main parameters and of turbulence properties.

The further and final step consisted in testing the TRF-E under both laminar and turbulent conditions exploiting the operational flexibility of NOSE. This allowed to characterize turbulent and laminar expanding premixed flames under dilution and thermodynamic conditions similar to the ones of a downsized SI engine.

Successively, the TRF-E was characterized in turbulent conditions, switching the configuration of the spherical vessel set-up from laminar to fan-stirred generated turbulence.

The further and final step consisted in testing the TRF-E under both laminar and turbulent conditions exploiting the operational flexibility of NOSE. This allowed to characterize turbulent and laminar expanding premixed flames under dilution and thermodynamic conditions similar to the ones of a downsized SI engine.

### 3.1. SPHERICAL SET-UP – LAMINAR CONFIGURATIONS

The spherical vessel used in the present work was validated, described and largely characterized by previous works of Galmiche [30], [69]. This experimental set-up allows both laminar and turbulent flame propagation investigations. The main characteristics are summarized below. The 200 mm inner diameter stainless steel vessel (i.e. inner volume of 4.2 l) is equipped with four quartz windows of 70 mm diameter. A heater wire resistance is placed on the outer surface to heat the chamber up to 473 K (limit of the internal seal). Figure 30 presents an overview of the whole apparatus.

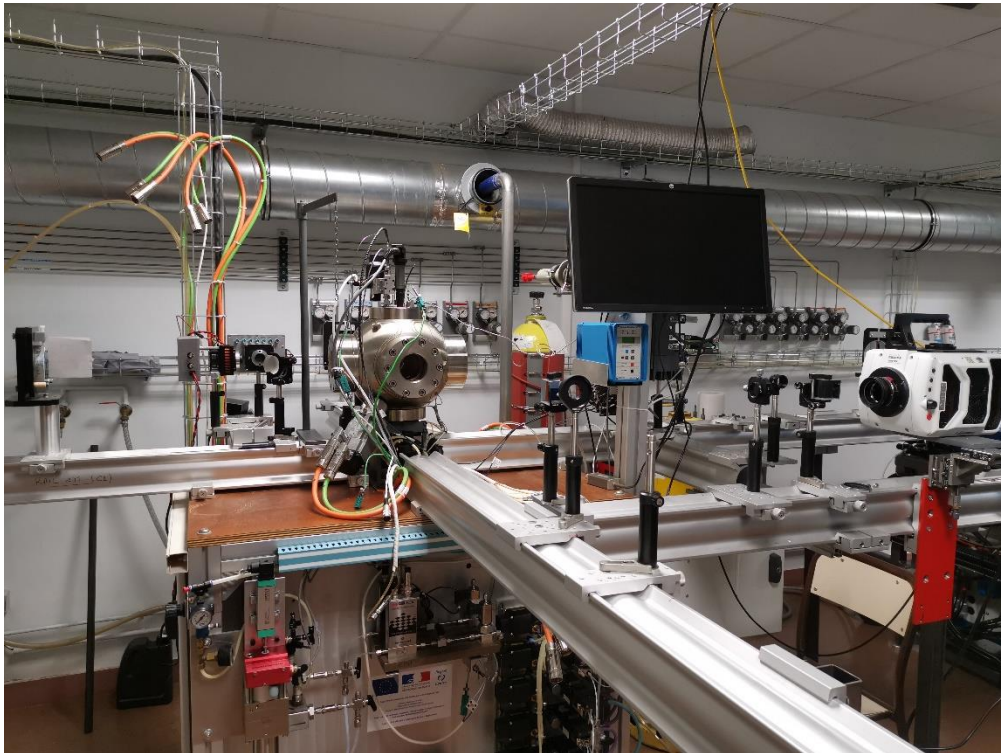


Figure 30. Overview of the whole spherical vessel apparatus.

A vacuum pump is used to extract all the gases before starting each test, until a minimal pressure of 0.005 bar. After that, a set of gaseous flowmeters (Brooks 5850S, 2 NL/min for air, 0.5 NL/min for CO<sub>2</sub> and 0.5 NL/min for N<sub>2</sub>) allows to inject the different gases according to the desired composition. In this respect, the composition of the synthetic air is 20.9% O<sub>2</sub> and 79.1% N<sub>2</sub>. In parallel, two liquid flowmeters (Bronkhorst mini CORI-FLOW 30 g/h) allow the fuel injection and eventually, the water if requested in the diluent composition. The liquid intakes are heated in order to grant a minimal vaporization temperature of 373 K. Inside the combustion chamber a fan assures the homogeneity of the gaseous mixture, during the filling process, consequently to the injection. Anyway, for laminar cases, this single fan is stopped 10 s before the ignition in order to grant that the flow is at rest, avoiding the development of turbulent perturbations. For each test, a maximum tolerance of 3% was accepted for the

initial pressure, while for the initial temperature a discrepancy of 2 K is accepted with respect to the fixed value. After each test, the injected quantities of liquids and gases are verified to determine the real equivalence ratio at which the experiment was performed. The maximum error is limited to 5% with respect to the nominal value. For all the data provided in the following, real values of equivalence ratio are considered and not the nominal ones.

The ignition is realized through two tungsten electrodes, with a diameter of 0.5 mm and 1.5 mm apart from each other, powered by a conventional capacitive discharge ignition system. The charging time of the ignition coil is set to 3 ms in the present experiments, resulting in a discharge energy of about 100 mJ. Further details on the ignition system can be found in [69], [100], [101]. Previous works (Galmiche [30], Bradley et al. [102]) showed that the first energy supply from the ignition system only affects the first instant of the flame propagation. Therefore, the more energy the supply of energy in the first moments will be energetic the faster the first phase of propagation will be but, after that, the flame propagation is independent of the ignition system.

A Double-Views Schlieren configuration was implemented in the combustion vessel to provide simultaneously two views of the flame propagation recorded in just one High Speed Phantom v1610 camera, as reported schematically in Figure 31. The aim is to evaluate the electrodes effect on the flame or the detection of possible irregularities and/or anisotropies in the flame spherical shape, by giving a tridimensional idea of the flame evolution. During post-processing phase, the maximum flame diameter observed is near 50 mm, as the diameter of the plano-convex lens. The burned gas volume is then 1.6% with respect to the total volume. Therefore, under these conditions, the pressure during the observed flame evolution can be considered constant and equal to the initial value  $P_i$ .

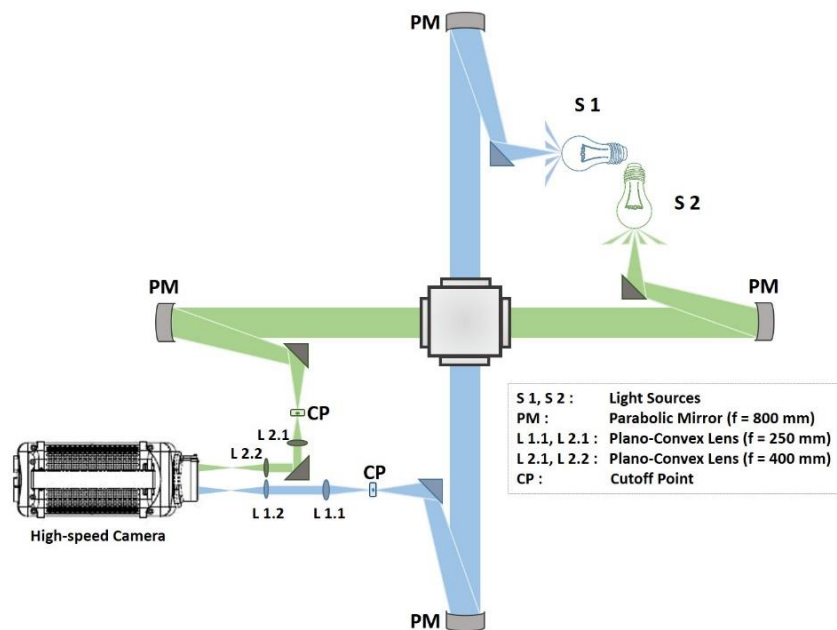


Figure 31. Scheme of the Double-View Schlieren set-up.

Two lamps are used as light sources and a set of mirrors, both planar and convex, ensures that the light beam is, respectively, well-oriented and parallel. As reported in the scheme in Figure 31, the light is firstly directed to a parabolic mirror, with a focal length of 800 mm, that is the same distance from the light source, obtaining a parallel beam. After the combustion chamber, another parabolic mirror, equal to the first, is used to converge the light to the cutoff point. Through other two plano-convex lens (with focal length of 250 and 400 mm) the light beam path is optimized to correctly impact the camera objective with the optimal size. The frame rate was fixed at 7000 fps, with a resolution of 1280x800 pixel<sup>2</sup> and a ratio mm/pixel equal to 0.1097.

The Schlieren technique detects the first derivative of the temperature, while shadowgraphy captures the second one. This means that the advantage of Schlieren consists in obtaining better contrasted images with respect to shadowgraphy, that is really important for high diluted flames (lower adiabatic flame temperatures).

An example of Double-Views of flame is presented in Figure 32. The assumption of a spherical evolution of the flame is consistent. The images post-processing was performed using a MATLAB routine that subtracts the background and performs the binarization of the image. Moreover, a low pass filter is applied in order to smooth the contour and decrease the noise. From the contour, the burnt gas area is computed and, then by considering the flame spherical, an equivalent radius as

$$R_s = \sqrt{\frac{A}{\pi}} \quad (73)$$

The flame propagation velocity can be estimated as the time derivative of the radius

$$V_s = \frac{dr_f}{dt} \quad (74)$$

and the stretch rate by Eq. (14) (from [103]).

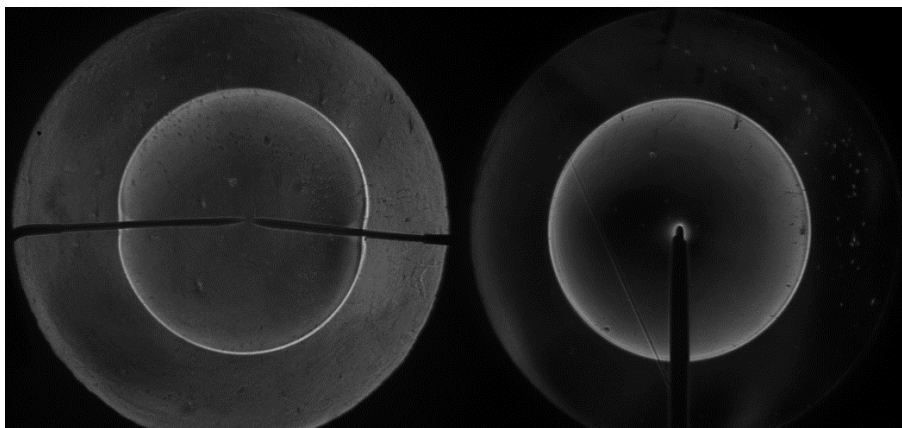


Figure 32. Example of flame visualized through the DVS technique.

### 3.1.1. Experimental Limits

In the present section, the current experimental limits of the spherical vessel set-up will be discussed. In fact, the gathering of meaningful data can be hindered by precise technical and physical limits of the apparatus. Firstly, the ignition system effect described in the previous section imposes the definition of a minimum radius,  $R_{min}$  that is not affected by the initial energy release of the spark. On the other hand, in order to respect the hypotheses already discussed in the previous chapter (Sub-section 2.1.6), a maximum radius,  $R_{max}$  above the which the wall effects are no more negligible has to be defined also. In addition, the presence of the electrodes affects the flame evolution both physically and from the thermodynamic point of view through thermal losses. Finally, some particular conditions of the flame (e.g. the cellularity discussed in Section 2.1.4), or flammability limits, can introduce significant experimental difficulties.

Further details on the determination of the  $R_{min}$  and the  $R_{max}$  are reported in the ANNEX B. The present study will take into account only flame radii,  $R_f$ , comprised in the range  $R_{min} = 5$  mm and  $R_{max} = 25$  mm to determine the unstretched laminar burning velocity  $S_L^0$ .

### 3.1.2. Particular conditions due to the reactive mixture

In addition to the physical limits of the experimental set-up, other critical aspects may limit the experimental investigation. These occurrences are mostly related to the mixture nature and thermodynamic conditions.

As seen in Sub-section 2.1.4, several combustion instabilities may affect the flame evolution. In Paragraph 2.1.4.2, it was discussed the effect of increasing pressure on the flame: reducing the flame thickness leads to higher gradient across the flame surface and, thus, early insurgence of Darrieus-Landau (or hydrodynamic) instabilities. On the other hand, increasing the equivalence ratio leads to lower effective Lewis number ( $Le_{eff}$ , Paragraph 2.1.4.3) and this promotes the arising of Rayleigh-Taylor (or thermo-diffusive) instabilities. Therefore, rich mixture, under high initial pressure, are subject to the concurrent effects of hydrodynamic and thermos-diffusive instabilities. As pointed out by Bradley et al. [26] the cellularity may increase the estimated flame propagation speed. The result is an onset on the  $V_L$  extrapolation curve, as displayed in the example in Figure 33. Therefore, the arising of cellularity reduces the range of meaningful radii that can be considered in the flame propagation speed extrapolation.

Finally, the last critical aspect concerns the flammability limits. The increase of the dilution rate, in fact, reduces the equivalence ratio range in which is possible to successfully ignite the mixture. On the other hand, as recently pointed out by Manna et al. [104], the increase of the dilution rate contrasts the cellularity insurgence.

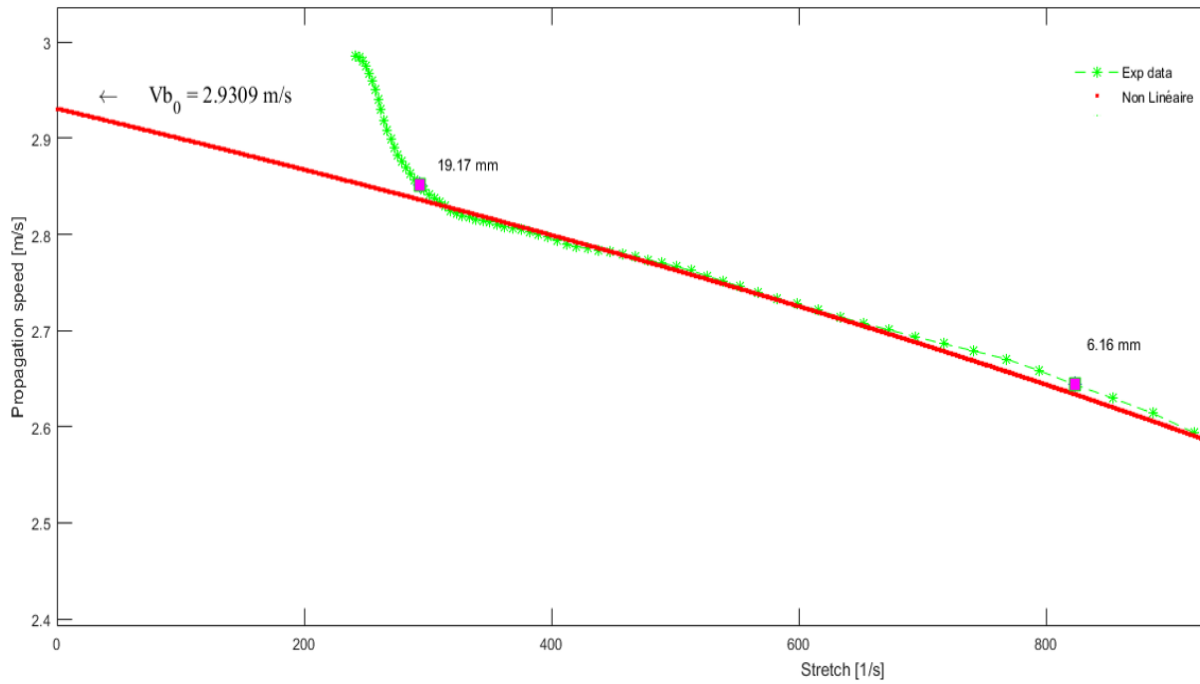


Figure 33. Example of the onset in the flame propagation speed extrapolation, due to cellularity insurgence.

### 3.1.2.1. Uncertainties

For what concerns the laminar burning velocities extrapolation, the data reliability must be evaluated in terms of both experimental limits (*e.g.* misfire due to high dilution percentage at low temperature and pressure that reduce the flammability limits, or cellularity due to high pressure and/or equivalence ratio) and post-process uncertainties. Among these latter, the use of the non-linear equation previously introduced yields more precise results with respect to the linear one, especially when the burned gases' Markstein length reaches or exceeds the unity [105]. As discussed in the Sub-section 3.1.1, ignition effect and walls influence reduce the range of the radii ( $\sim 5\text{--}25$  mm). The arising of early cellularity for relatively high pressure, or equivalence ratio, may further reduce this range [106]. Moreover, the contour detection scripts may introduce subsequent errors that must be taken into account [107]. For all these reasons, it is important to remark that the error bars displayed in the following subsections will be representative not only of the corrected standard deviation but also of the post-process uncertainties introduced and are computed by adding the different uncertainties *in quadrature*.

$$err_{tot} = \sqrt{(err_{post-process})^2 + (err_{statistic})^2} \quad (75)$$

### 3.2. TURBULENT CONFIGURATION

The spherical vessel described in the previous Section 3.1 not only allows a high flexibility in terms of mixture and thermodynamic conditions, but also the investigation of both laminar and turbulent flames. In fact, by increasing the number of fans from one (used in laminar configuration to homogenize the mixture) to six, it is possible to generate a forced turbulence inside the combustion chamber.

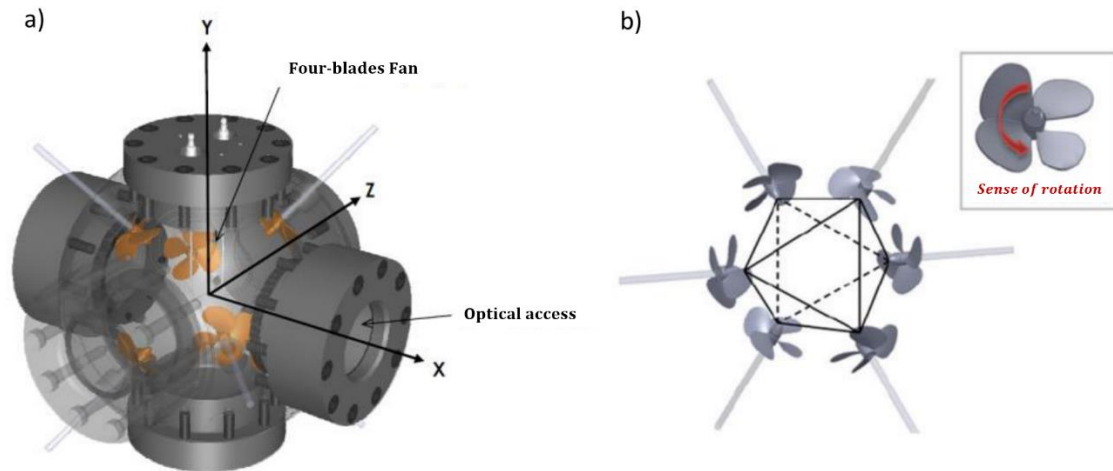


Figure 34. Fans configuration and fan details, adapted from [30].

Each fan is composed by four blades, with a diameter of 40 mm and a pitch of 35.6 mm, located from the wall. These six fans are located as shown in Figure 34. The rotation speed of each fan can be varied from 0 to 17000 rpm. This apparatus was investigated, described and validated by Galmiche et al. [9], [30]. It was shown that the generated turbulence can be considered homogeneous and isotropic (HIT), at least in a 20 mm radius sphere around the center of the vessel as highlighted in Figure 35 (a) and (b). Moreover, the integral length scale, estimated in this region of interest is 3.4 mm and constant as a function of fan velocity.

From Galmiche, a correlation between the fans speed and the turbulent fluctuations generated. was suggested as [9]:

$$q' = (0.0104/60) * \omega$$

where  $\omega$  is the fans rotation speed.

Table 2 resumes the turbulent intensities that it is possible to generate in the vessel according to the work of Galmiche [30].

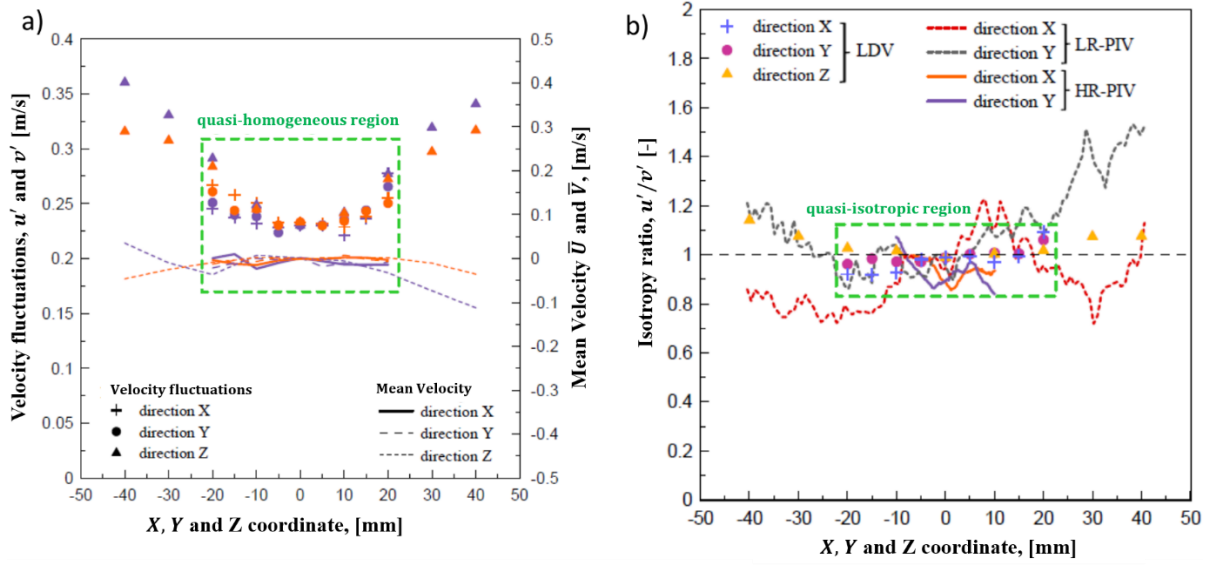


Figure 35. Evaluation of homogeneity and isotropy hypotheses, adapted from [30].

Table 2. Turbulent intensity values depending on the fans rotation speed.

Fans rotation speed, $\omega$ [rpm]	2000	4000	6000	8000	10000	12000	14000	16000
Turbulent Intensity, $q'$ [m/s]	0.35	0.69	1.04	1.39	1.73	2.08	2.43	2.77

### 3.3. NEW ONE SHOT ENGINE

#### 3.3.1. NOSE Working Principle and Description

The working principle of NOSE consists in using an ideally adiabatic compression process to accurately reproduce high temperature and pressure conditions. The core of the experimental set-up apparatus was firstly characterized and fully described in recent work of Nilaphai [108], first developed to reach high pressure and temperature conditions representative of Conventional Diesel Combustion engines. A scheme of NOSE set-up is given in Figure 36.

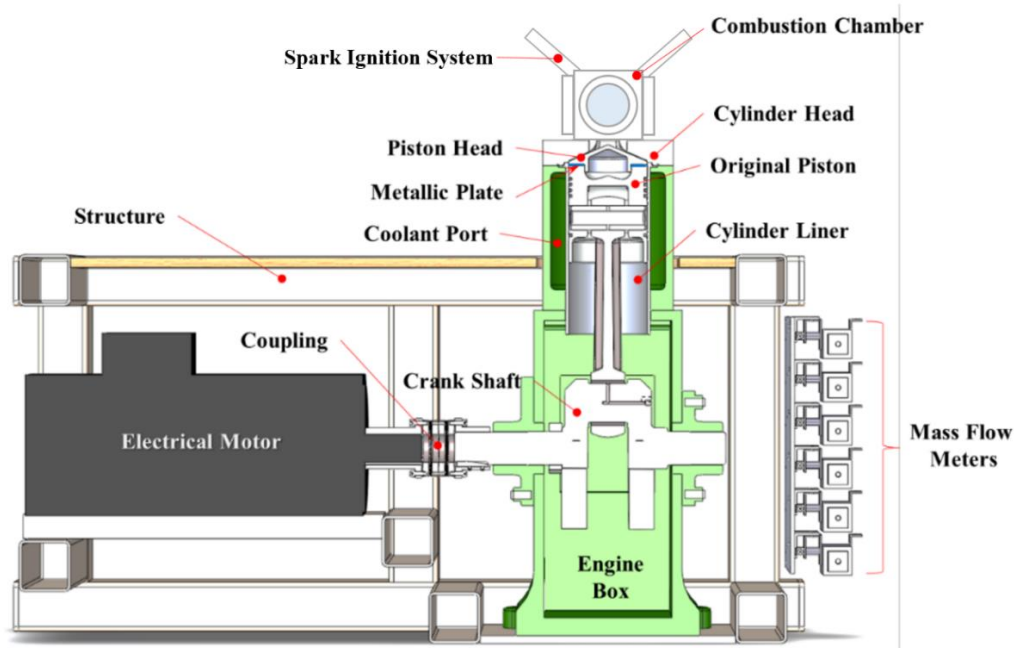


Figure 36. Scheme of the whole NOSE apparatus, adapted from [108].

The core of the bench is a single-cylinder 18 horsepower diesel engine with an initial volume of 3600 cm<sup>3</sup>, a bore diameter of 155 mm and a stroke of 177.8 mm. The initial and final volumes can be varied by adding a plate of a specific thickness between the head and the body of the piston (see ANNEX C for further details). This allows to provide different initial Compression Ratio (CR) from 12.3:1 eventually to 15:1, considering the original design volumes at the Bottom Dead Center (BDC) and at the Top Dead Center (TDC). The cylinder head hosts the intake, the exhaust, the purge, the vacuum pump lines and the dedicated combustion chamber, as shown in Figure 38. As the name suggests, the apparatus does not operate cyclically. From specific initial conditions, it is possible to maintain during a sufficient time interval, thermodynamic conditions at the end of the compression phase. For that, a brushless DC motor (PHASE Automation U31340) coupled with a high-performance electric motor driver (PHASE Automation AxM300-400) is used. This system can reach a maximum speed of 1500 rpm and a maximum torque of 1100 Nm. The piston is driven by the electric motor following the

trajectory designed by the operator. The driven force must counteract the pressure increase and the internal friction of the oil-lubricated cylinder-piston system. For this reason, a highly accurate closed-loop velocity feedback function was developed for NOSE, allowing a real-time control on piston velocity during the compression process. In this way, it is possible, for the operator, to design a suitable ‘trajectory’ as a function of the objective of the experiments, it means that the rotational speed evolves during the single shot. The main target is usually to slow down the piston near the TDC in order to reach that point sufficiently slowly to maintain the thermodynamic conditions target during few ms and reducing noise and vibrations of the system. The minimum velocity is comprised between 50 and 100 rpm, the duration of the so-called *plateau* (that is the range in which inside conditions are almost constant) strictly between 5-10 to 25-30 ms depends on the initial parameters and the trajectory. Figure 37 shows an example of trajectory.

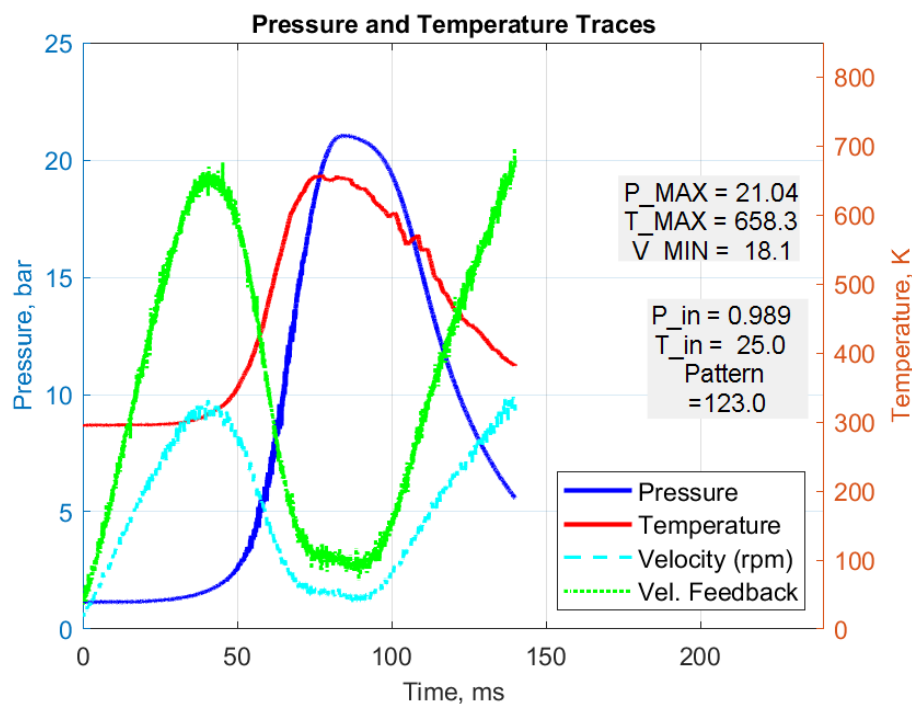


Figure 37. Example of trajectory (SV configuration with standard trajectory).

The designed chamber is internally spherical shaped with a 40 mm radius, equipped with four cylindrical quartz windows of 18 mm radius. Four resistive heaters can be used to warm up the chamber. Two tungsten electrodes compose the spark ignition system. Between the combustion chamber and the cylinder head a smooth connection or a grid can be added to modify the internal flow field of the compressed gaseous mixture inside the chamber. Further details on the grid geometry will be discussed in the next Section 3.4.

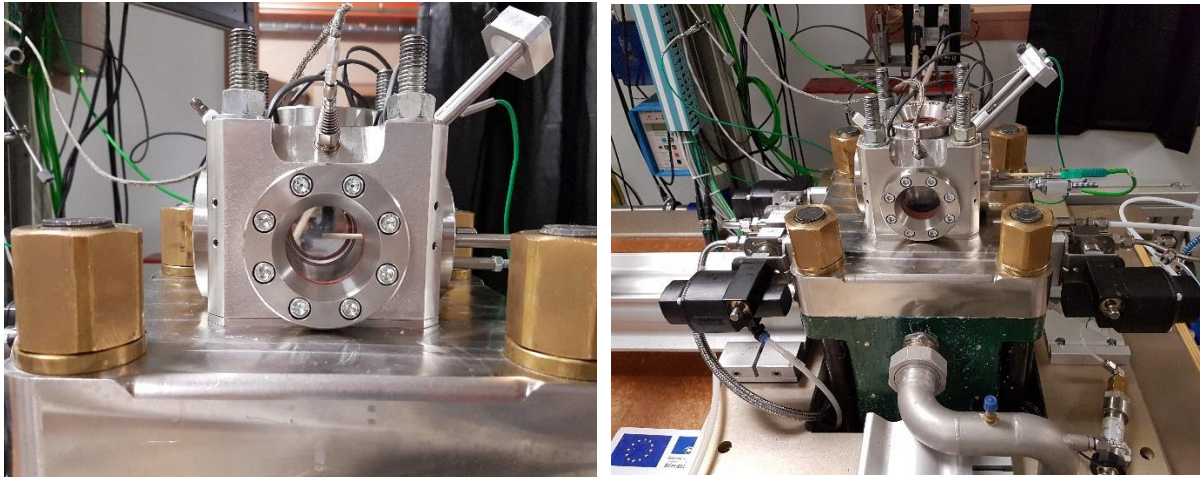


Figure 38. Combustion chamber views.

Considering the combustion chamber with the thinner plate (i.e. minimum CR), the standard configuration has an initial volume of  $V_i = 3729.72 \text{ cm}^3$  with a final volume  $V_f = 381.52 \text{ cm}^3$ . This set-up is called Small Volume (SV) configuration with a CR equal to 9.78. By using another extension, the initial volume becomes  $6747.72 \text{ cm}^3$ , and the final volume  $3399.52 \text{ cm}^3$ , which generates Large Volume case (LV), with a small CR of 1.99. Figure 39 shows a scheme of the two configurations.

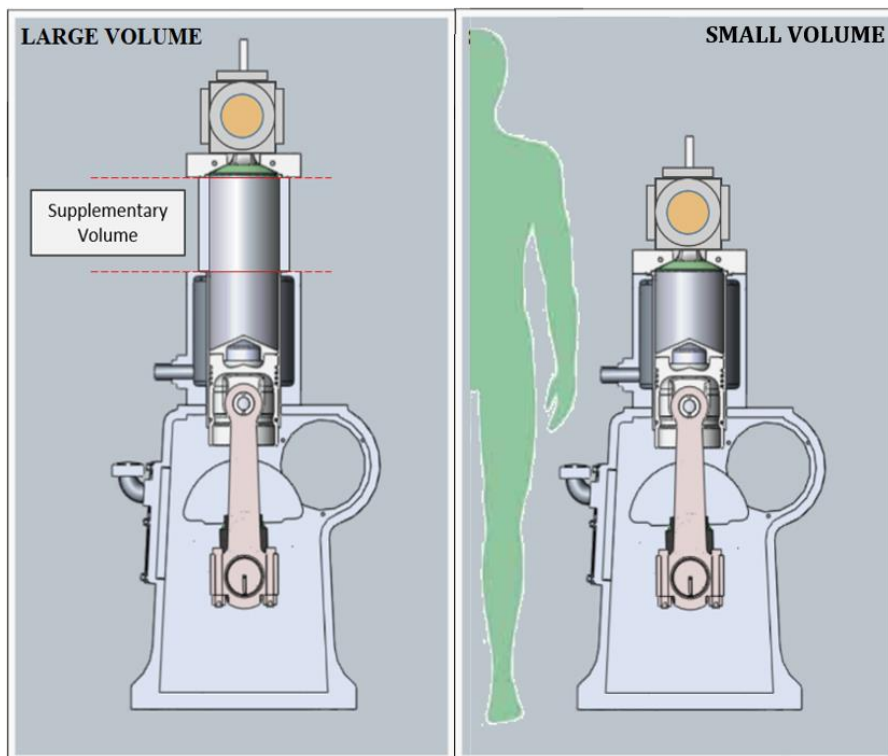


Figure 39. Scheme of the two NOSE configurations: Large Volume (LV) on the left and Small Volume (SV) on the right.

### 3.3.2. NOSE Operational Procedure

Operational procedure consists, at first instance, in warming up the system at the desired initial temperature. With a maximum initial temperature of 473 K for the combustion chamber and 373 K for the cylinder/piston system. If the extension is mounted, a dedicated heating system is used to provide the energy to warm up the whole piece up to a maximal temperature of 400 K. Once the desired temperature is reached (according to the targeted one at the TDC), the piston is normally positioned at the BDC and the vacuum realized. Then the operator must set the initial pressure value and the mixture composition in order to get the final target near the TDC. The initial gaseous mixture composition is obtained using four BROOKS® model 5860S gas flow meters, to supply N<sub>2</sub>, O<sub>2</sub>, CO<sub>2</sub>, CH<sub>4</sub>, as example and two Bronkhorst mini CORI-FLOW (30 g/h) liquid flow meters, to inject water and liquid fuels. By setting the desired mixture molar fractions, this set of flow meters provides to inject the correct volume of each component with a precision of  $\pm 0.7\%$ . Liquid components are carried on by the gas flow inside a heated capillary tube, allowing the vaporization. A manual valve allows to feed a supplementary seeder line, if Particle Imaging Velocimetry or tomography have to be implemented. In this case, an additional capillary tube passes through a Venturi's tube seeder filled with silicon oil. Both lines converge to the intake closed before each run. Other three valves control the purge, the exhaust and the vacuum pump lines.

A piezo-electric low-pressure sensor KISTLER Type 7001 tracks pressure during the filling process. This sensor is mounted before the intake valve in order to prevent overpressure during the compression and, eventually. The maximum initial pressure is 10 bar, which is the limit of the transducer. A high-pressure sensor KISTLER Type PAA-33X/80794, instead, is used to follow the pressure evolution inside the chamber during the shot. The temperature of the cylinder and of the chamber is following thanks to two temperature sensors. The gas temperature evolution inside the chamber can be tracked by using a 13  $\mu\text{m}$  K-type thermocouple, as shown in Figure 40, in non-reactive conditions to validate the temperature homogeneity and repeatability during experiments. This thermocouple can be displaced along the chamber axes to monitor the temperature in different points. It is composed by a protective movable ceramic casing, with two ducts in which the two metal wires are accommodated. The thermocouple bead is exposed to the flow, as in Figure 4 (c) in the ANNEX C. This figure also highlights the recirculation effects due to the protective case that can alter the temperature measurement precision during the expansion phase (as discussed in Sub-section 3.3.5).

Pressure, temperature, crank angle degree, velocity feedback and electric motor response are recorded as a function of time through a National Instrument Compact RIO at 250 kHz. The ad-hoc configured Lab-View software allows the control of the system, by adjusting the piston velocity trajectories, monitoring the main parameters and phasing the trigger signals (spark timing, high-speed camera, laser pulse, etc.). After each test, gases are expelled through the exhaust line and a purging line with dry air at 7 bar is opened to clean residuals.

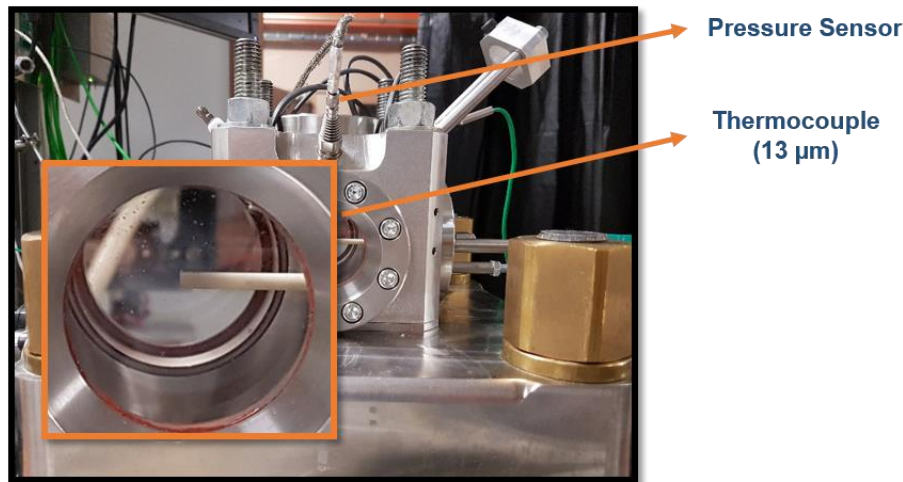


Figure 40. Details of the combustion chamber main sensors, pressure transducer and thermocouple.

### 3.3.3. Implemented Optical Techniques on NOSE

Three optical techniques were complementary implemented on NOSE bench. PIV is fundamental for the aerodynamic characterization of the experimental set-up, while tomography and Double-View Schlieren (DVS) were used to obtain images of the performed combustion tests.

The PIV set-up requires a High Speed Phantom v1610 camera, a high frequency and high power laser Dual Hawk HP (9.4 mJ/pulse, 532 nm wavelength and 120 ns pulse duration), a seeder (silicon oil particles) and a set of lens. Figure 41 schematically shows the PIV configuration. A cylindrical lens with focal length of 50 mm is firstly used to expand the laser beam in vertical direction. The subsequent spherical lens, with focal length of 500 mm, slightly changes the beam divergence in vertical direction causing, instead, the convergence to the focal point (at the combustion chamber center) in the horizontal sense. The result is a laser sheet with 1 mm homogeneous thickness among the combustion chamber cross-section. High-speed camera is positioned perpendicularly to this laser plan. The maximum power of the laser is 230 W, while maximum frequency of single pulse is 25 kHz. Therefore, in order to perform high-speed double-frame PIV analysis with very short  $dt$  between the two frames (down to 3  $\mu$ s) the laser uses two different source to generate the light beam. By phasing these two single laser with a certain delay, it is then possible to perform PIV analysis at very high frequency (that is, very short  $dt$ ). Anyway, the frequency at which each couple of image is acquired it is obviously limited by the maximum frequency of the single laser. In the present analysis an overall frequency of 8 kHz was used, with a  $dt = 10 \mu$ s and an image resolution of 768x768 px<sup>2</sup>, that is, a ratio  $\mu$ m/pixel equal to 18.6  $\mu$ m/px. Since the complexity of the system, the camera and the laser must be externally controlled by the

dedicated software DAVIS (LaVision). Once the control unity receive the trigger from the NOSE control system, the software takes control of the devices to phase images recording, adjust digital optical set-up of the camera and synchronize it with the laser. An example of particles visualization and relative velocity field is shown in Figure 42.

Post-processing is firstly performed on DAVIS, correcting images if necessary, and computing the vector fields. The following part of the post-process is practiced on MATLAB and it will be describe in the next section.

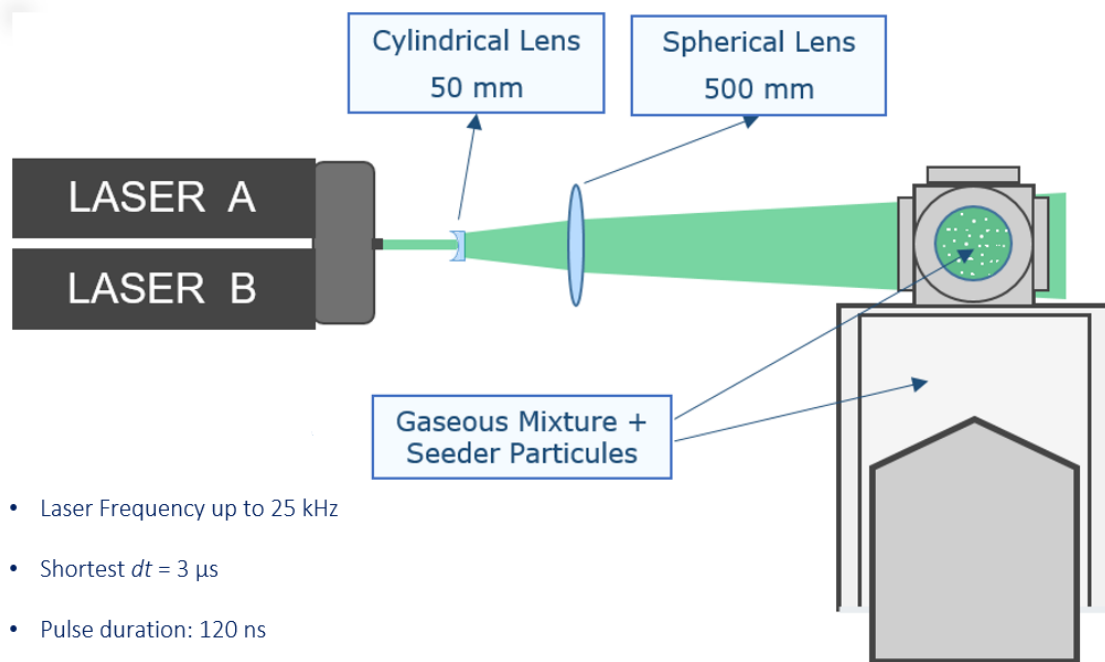


Figure 41. Scheme of the PIV set-up.

The tomography technique basically exploits the same devices configuration of the PIV. The main differences are the reactive conditions and the use of a filter on the camera objective. The filter is for the correspondent wavelength of the laser, that is 532 nm. The reactive conditions imply the presence of the tungsten electrodes (that for PIV tests are removed to avoid metal reflection and obstacles in the camera view) and the flame propagation that is supposed to be observed. The expanding flame is captured along just one section, which corresponds to the laser sheet. In this way it is possible to avoid common superimposition problem of Schlieren technique with turbulent flames [58]. On the other hand, very high Karlovitz numbers recreated on NOSE generate turbulent flames that may extremely shift with respect to the chamber center and, thus, out from the laser sheet plan.

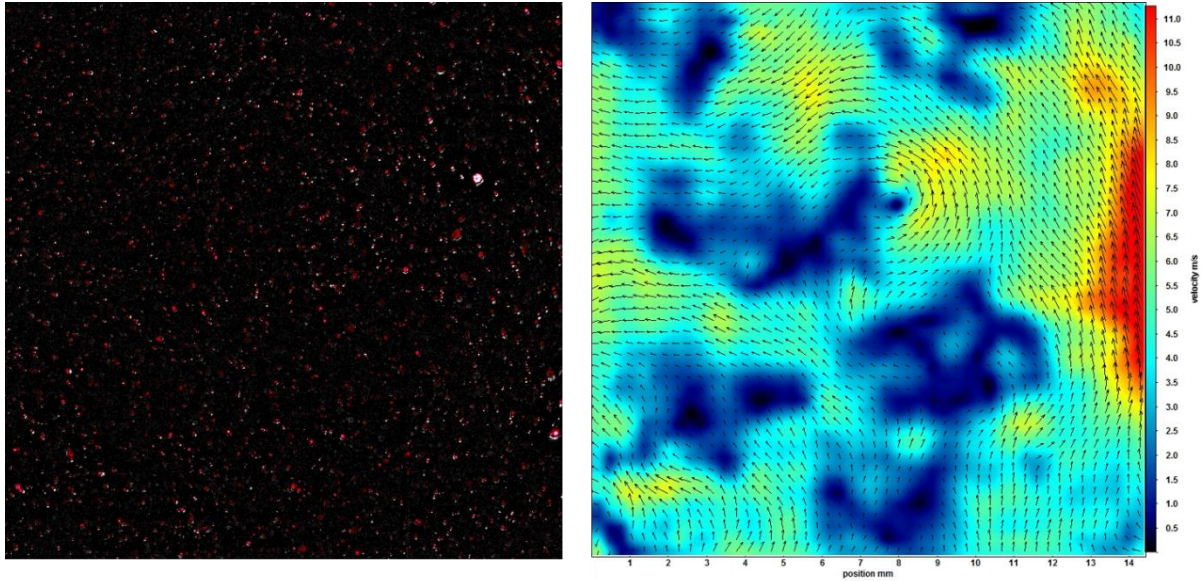


Figure 42. Example of particles visualization (on the left) and relative velocity field (on the right).

On the contrary, Schlieren technique, and especially Double-View Schlieren, drastically increase the possibility of capturing flame evolution in time. A Double-View Schlieren enables to simultaneously have two different views of the flame propagation recorded in just one High Speed Phantom v1610 camera. The aim is the detection of possible irregularities and/or anisotropies in the flame spherical shape, by giving a tridimensional idea of the flame evolution. This aspect is useful in laminar conditions, and the principle of the Schlieren technique was already introduced and discussed in the relative Section 3.1. In case of turbulent flames, the double-view approach becomes particularly important. The set-up configuration is similar to the one already presented in Section 3.1. Two LED lamps, with a pinhole of 1 mm, are used as light sources and a set of mirrors, both planar and convex, ensures that the light beam is, respectively, well-oriented and parallel. As reported in the scheme in Figure 43, the light is firstly directed to a parabolic mirror, with a focal length of 520 mm, that is the same distance from the light source, obtaining a parallel beam. After the combustion chamber, another parabolic mirror, identical to the first, is used to converge the light to the cutoff point. Through two plano-convex lenses (with focal length of 250 and 200 mm) the light beam path is optimized to correctly impact the camera sensor with the optimal size. Images were captured with a resolution of  $1280 \times 800$  pixel<sup>2</sup>, offering a ratio mm/pixel equal to 0.0653. The frame rate was varied between 5000 or 8000 fps depending on the case.

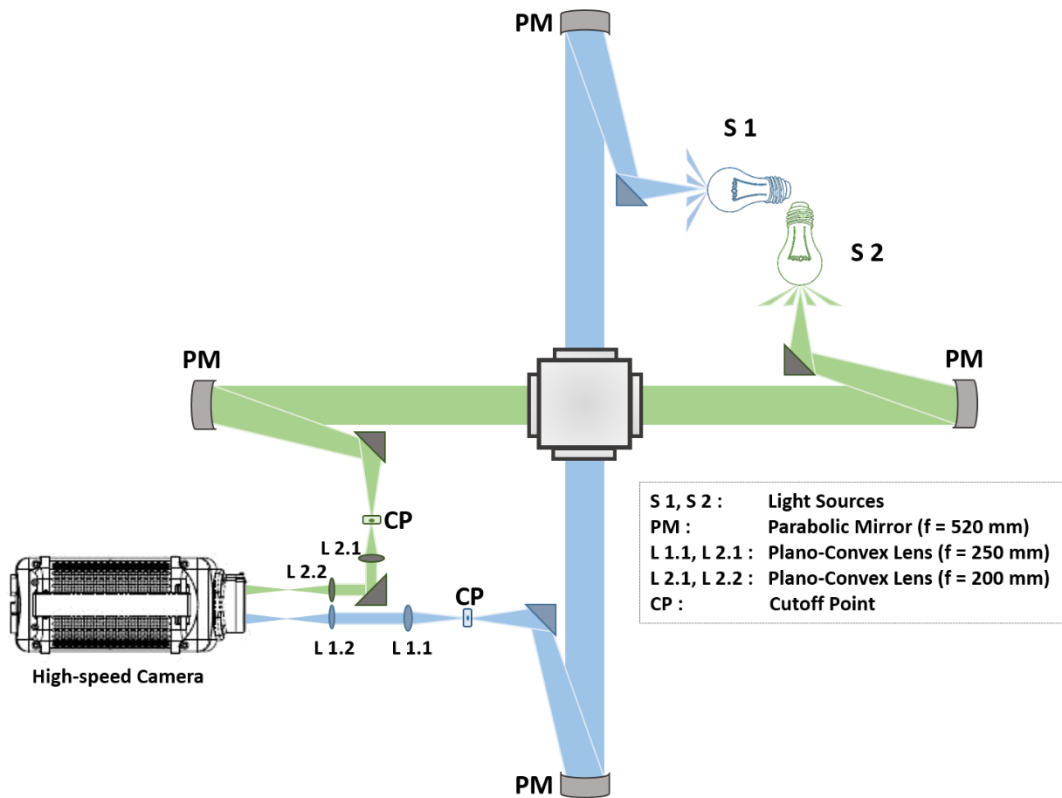


Figure 43. Scheme of the DVS implemented in NOSE set-up.

As said, using a DVS allows the evaluation of the tridimensional shape of the flame. Furthermore, it is possible to compute the volume of the expanding flame and trace its evolution. This is useful in particular for turbulent flame in which the equivalent radius based on the area may lack in consistency with the actual tridimensional shape of the flame.

Currently, the volume evaluation is obtained through an *ellipse method*. The two images (i.e. left and right) are analyzed section by section, taking each 1-pixel row and detecting a left and a right radius at each step. These two radii are the minor and major axis of the ellipse that better fits the contour of that section. The sum of all the ellipses represents the total volume of the flame. Clearly, this volume overestimates the real one in case of turbulent flame because the wrinkling of the flame is not taken into account. Moreover, using two Schlieren images means that the two contours already overestimate the real ones. Despite this, the volume overestimation normally does not significantly vary during the flame propagation, justifying the use of an equivalent radius based on the flame volume. Figure 44 shows an example of this measurement procedure.

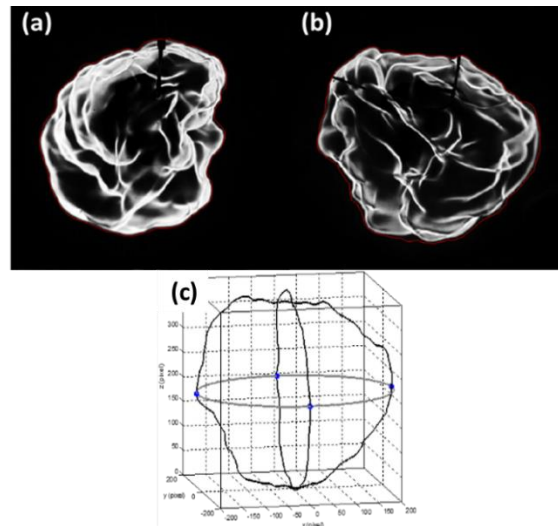


Figure 44. Exploitation of the DVS for the evaluation of the flame volume using the ellipse method, adapted from [90].

### 3.3.4. NOSE Experimental Tests

The experimental investigation on NOSE should be conducted in different, sequential, dependent phases. Once the potentially interesting experimental points are identified, a repeatability test must be conducted in order to evaluate the test-to-test reproducibility of the targeted ambient conditions and the stability of the designed trajectory. Successively, for each configuration, Particle Image Velocimetry (PIV) technique was used to evaluate the internal flow fields, to characterize the eventual turbulence and its evolution, especially during the plateau. An sufficient number of shots has to be ran in order to correctly characterize the aerodynamics. In the end, the same experimental point should be tested in reactive conditions several times. First tests are useful for the correct phasing of the spark ignition timing thanks to visualization technique as laser Mie scattering tomography or double-view Schlieren. To be ensured about the initial pressure and temperature, the combustion has to be realized during the ‘plateau’ and also without flame shift upward or downward. In case of highly turbulent flames, the number of tests has to be increased in order to get enough meaningful data, counteracting the turbulent nature of the flame propagation.

### 3.3.5. Repeatability Tests

During the development and the optimization phase of NOSE, one laminar configuration and three main turbulent configurations were identified and characterized:

- A low temperature and low pressure (LTLP) conditions (using LV configuration);
- A high temperature and high pressure (HTHP) conditions (using SV configuration);
- A high temperature and high pressure conditions with high turbulent intensity (HTI), using SV configuration and a particular piston movement trajectory to increase the turbulence generation.

The two HTHP differ only in the resulting turbulence intensity. In fact, in one case the piston starts at the BDC ( $180^\circ$  CAD) and normally performs one ‘tour’ before returning at the initial position. In the other case, a new trajectory was designed to increase the turbulent kinetic energy (TKE) without changing CR (and thus the *plateau* thermodynamic parameters). Before starting, the piston is slowly moved backward at  $80^\circ$  CAD in order to take advantage of the initial non-zero velocity of the piston. In this manner, it is possible to better counteract the system internal resistance by accelerating more before sharply slowing down at the TDC. Thereafter, this high turbulent intensity configuration will be called SV-HTI, while the standard one simply SV. Figure 45 shows the repeatability of 10 tests performed for these three configurations. Error bars generally appear quite small except for the temperature curve starting from the beginning of the expansion phase. This is supposed to be the effect of the thermocouple design. The pressure increase during the compression phase compresses the gas inside the ceramic tube. Then, the air is blown out by the pressure decrease at the beginning of the expansion phase, directly impacting the thermocouple. Anyway this partial leak of accuracy can be considered unimportant since it always occurs after the *plateau*.

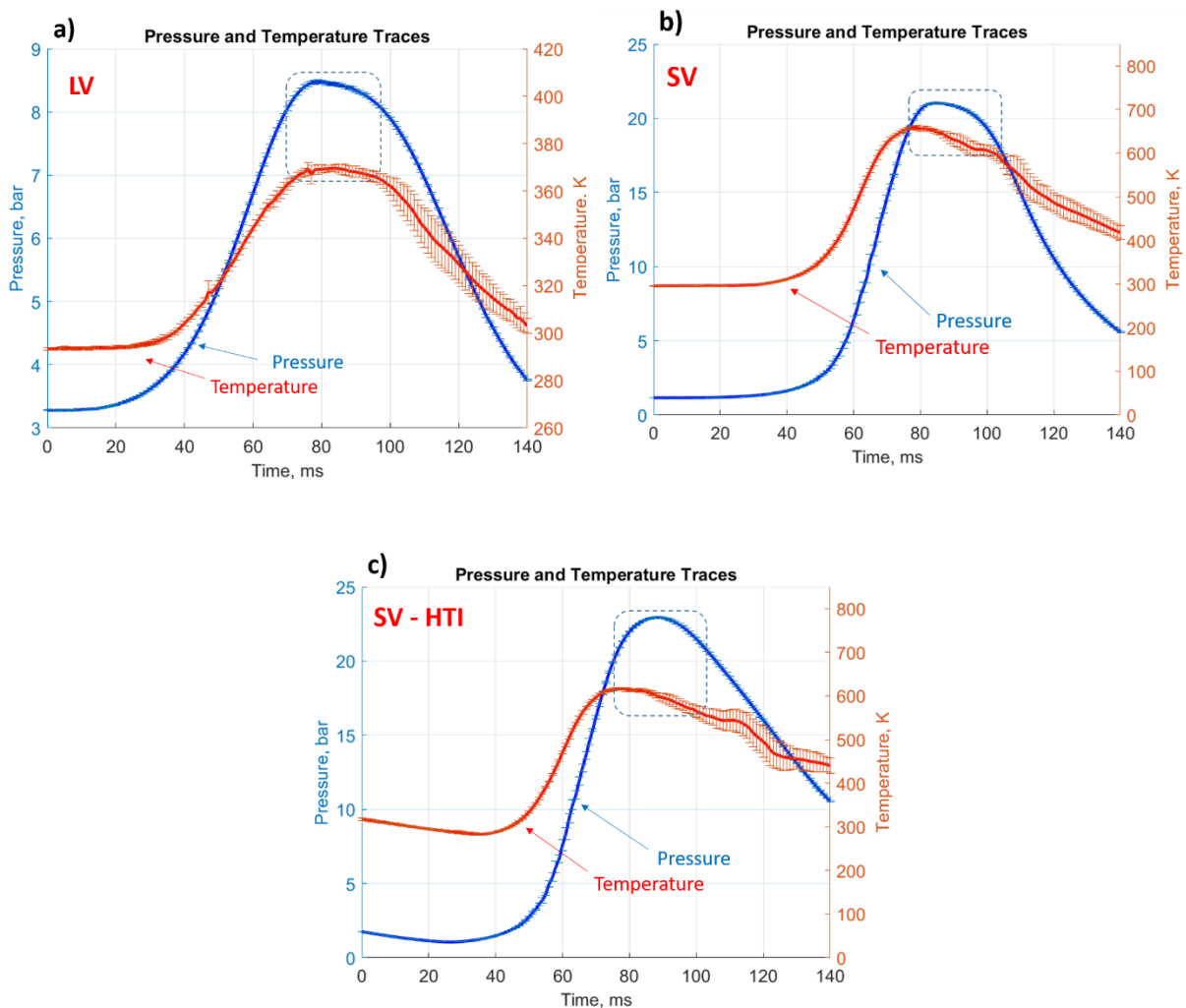


Figure 45. Results of repeatability tests for 10 tests for each configuration. a) Large Volume; b) Small Volume with standard trajectory; c) Small Volume with High Turbulent Intensity.

### 3.4. NOSE LAMINAR CONFIGURATION

Large Volume configuration, without grid, can be used to generate a flow characterized by very low mean velocity, despite the dynamicity of the system. In fact, the large initial and final volumes and the low compression ratio allow increasing the thermodynamic conditions at TDC avoiding turbulence auto-generation. Clearly, at the same time, the low CR strongly limits the gain in final temperature and pressure. Therefore, the strategy to get high final thermodynamic conditions consists in setting high initial pressure and temperature at the BDC.

Initial pressure at BDC is fundamentally limited by the electric motor power. Designed trajectories need a real-time control and it was found out that with an initial pressure greater than 7.2 bar the motor cannot correctly follow any useful trajectory. On the other hand, initial temperature is limited at 396 K by the current heating system of the additional volume. Thus, targeting a final pressure of 21 bar and a final temperature at least equal to the one achievable on the spherical vessel, it was necessary to accordingly tailor the CR. To achieve this goal, the piston body was modified as shown in Figure 46. A piece with an height of 58.09 mm was interposed between the core of the piston and the piston head. This allowed to increase the LV compression ratio from 1.99 to 2.45. In this way it is possible to get, and maintain during the *plateau*, a TDC pressure of 21 and a maximum temperature of 525 K.

An example of the flow obtained with LV configuration, without grid, will be shown in the next section.

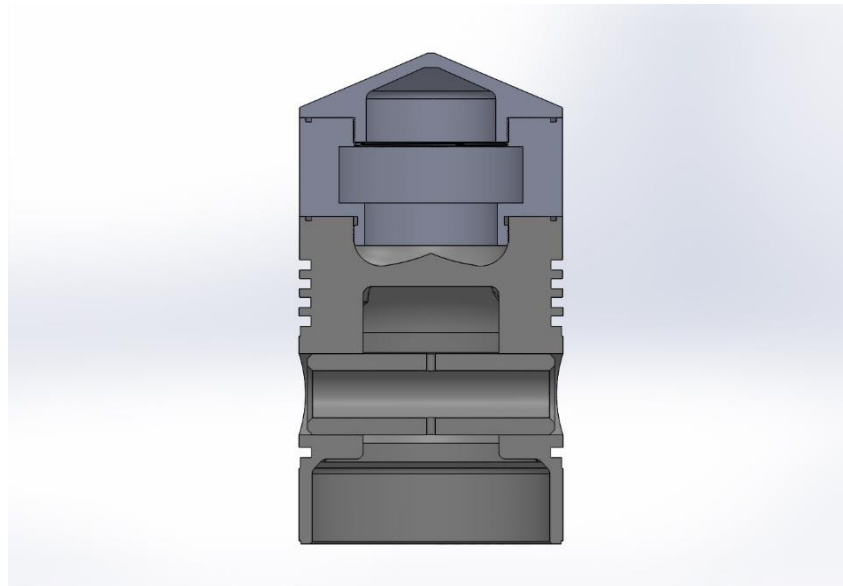


Figure 46. Piston body modification to increase the CR in LV configuration.

## 3.5. AERODYNAMIC CHARACTERIZATION

### 3.5.1. Characteristics of the Turbulence

As previously discussed in Section 2.2, Homogeneous Isotropic Turbulence (HIT) is an idealized condition of a turbulent flow. It allows to study the impact of turbulence on a system using a simplified mathematical approach without neglecting any basic physical process [109]. Homogeneity is defined as the property of the statistical quantities to be invariant with respect to the translation of the reference system. While isotropy assures the independence on rotation and reflection of the coordinate axes, as it is an idealized condition, HIT does not exist in real systems. Moreover, it is normally even difficult to reproduce similar conditions in an experimental set-up. In order to obtain a real flow closed to the HIT condition several set-up concepts have been proposed and used. For example, the most common strategy is to let a steady flow pass through a grid or a mesh [110], [111]. The 2D flow fields parallel to the grid result well approximated with the HIT conditions, but an intrinsic anisotropy exists due to the turbulence spatial decay after the grid. Strategy of the present work consists in using a perforated plate (grid) to modify the initial conditions of the normal recirculation phenomenon inside the chamber, due to the wall effects. In other words, the grid was not designed to directly generate a specific turbulence. On the contrary, the desired turbulent structures appear later, as result of the grid perturbation on the flow before the effect of the walls confinement and recirculation. The aim is to obtain a 3D turbulence closed to HIT condition in the center of the combustion chamber. The grid used for the turbulence generation was designed by partners of IFPEN as part of the MACDIL project, and experimentally validated in the present study. The grid is reported in Figure 47. It presents 5 holes, of which one centered and without inclination. The other 4 holes have the axes inclined of  $27^\circ$  radially and externally directed with respect to the central axis.

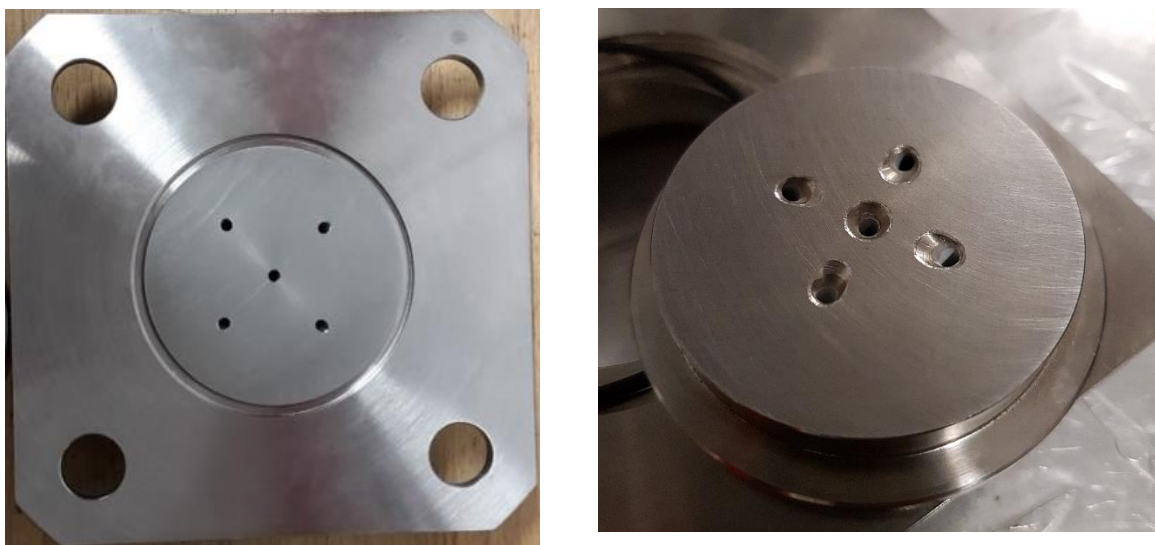


Figure 47. Details of the grid: top view (left); bottom view (right).

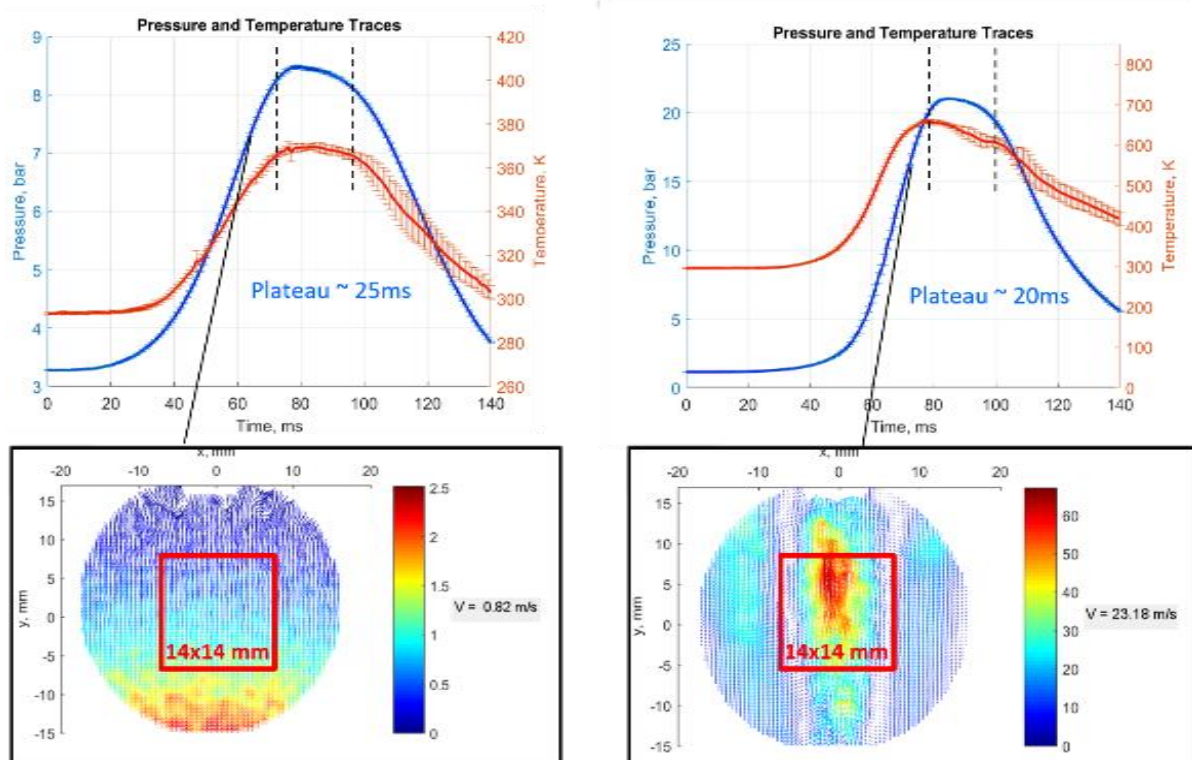


Figure 48. The effect of the grid on the flow: on the left, LV without grid; on the right, SV with grid and standard trajectory. The red squares represent the region of interest of the statistical analysis.

To better understand the effect of the grid on the flow, two extremes cases are reported in Figure 48. The first one, on the left, is inherent to the LV configuration without the grid. The flow field displays the aerodynamic near the end of the compression phase: the velocity field is almost uniform along the  $x$  direction. Velocity vectors are well-oriented in the same direction and only a slight difference in magnitude is observed along the  $y$  direction. Moreover, medium absolute velocity in the center of the chamber is low than 1 m/s. This result is due to the additional inertial effect caused by the additional volume of the LV set-up. In fact, without grid, the very low compression rate and large inertial volume are not sufficient to self-generate turbulence other than at the very end of the *plateau*. The second case, on the right, is obtained for the SV configuration with the presence of the grid and a standard trajectory. At the same instant, one can observe the presence of a central jet with really high maximum velocity in the core. Other jets are outside the laser sheet and, thus, it is possible to detect only their indirect effects on the flow field. This includes the recirculation of the side jets impacting the upper part of the chamber (with a certain inclination) and coming back to the center with lower velocities in the opposite direction with respect to central jet. The combination of these jets, and their interaction during the compression phase, causes the turbulence generation after decaying and the recirculation of the main jets flows.

### 3.5.2. PIV Investigation and Statistical Approach

PIV analysis and subsequent turbulence statistical post-process require high spatial resolution to provide accurate integral length scale. The area used to analyze statistically the turbulence is  $14.29 \times 14.29 \text{ mm}^2$  centered to the center of the chamber. Figure 48 shows this reduced window as a red square. The recording frequency is 10 kHz so, by assuming a plateau of 20 ms, 201 velocity fields per test are available. For each configuration 20 tests were performed. As the turbulence is not continuously forced, it cannot be considered globally stationary. In order to have an idea of the turbulence evolution during the *plateau*, an ensemble average approach is used. One can define the generic velocity component as follows:

$$U_i(t) = \langle U_E \rangle + u_{E,i}(t) \quad (76)$$

Both the instantaneous velocity and the fluctuation of the  $i$ -th run depend on time, while the average is computed with respect to the ensemble of all the tests. The turbulent intensity can be then computed as the root mean square of the fluctuation. In a real engine, the variable  $t$  is more practically substitute by the CAD ( $\theta$ ). Moreover, the actual mean also depends on  $\theta$ , due to the cycle-to-cycle intrinsic variation of the bulk velocity ( $\bar{U}_E = U_E(\theta) + U_{cycle,i}(\theta)$ ). Thus, from Eq. (76) it is not possible to obtain the actual value of the turbulent intensity. A priori, the cycle-to-cycle fluctuation has to be taken into account. As NOSE is basically a non-conventional engine, the mixture inlet, the inside geometry and the turbulence generation drastically differ from those of a real Internal Combustion Engine. But, even if NOSE cycles are independent of each other, the mechanic clearance of the system induces fluctuations, not negligible. Performing a preliminary ensemble average and evaluating the generic fluctuations  $u'_{tot}(t)$  and  $v'_{tot}(t)$ , it is possible to have an idea of the flow aerodynamic evolution inside the chamber. In Figure 49 their temporal evolution is plotted for the three configurations, during the whole *plateau* (considering end of compression phase and beginning of expansion phase). The (0,0) label refers to a single central point of the velocity field. The '20x20' means a spatial average done on the limited centered area with respect to the whole region of interest. Finally, *tot* means an average based on all the points of the field. It is worth to observe that an agreement exists between the restricted spatial average (20x20) and the total one and that the fluctuations globally decrease. At this first step, it is still not possible to identify  $u'_{tot}(t)$  and  $v'_{tot}(t)$  as the fluctuations associated to the turbulence, but to identify a specific time interval in which the phenomenon could be eventually considered close to stationarity conditions. Respectively, for the three configurations LV, SV, SV-HTI), a time interval of 6 ms (which corresponds to 61 instantaneous velocity field) can be identified with a respective beginning of 82 ms, 87 ms and 90 ms.

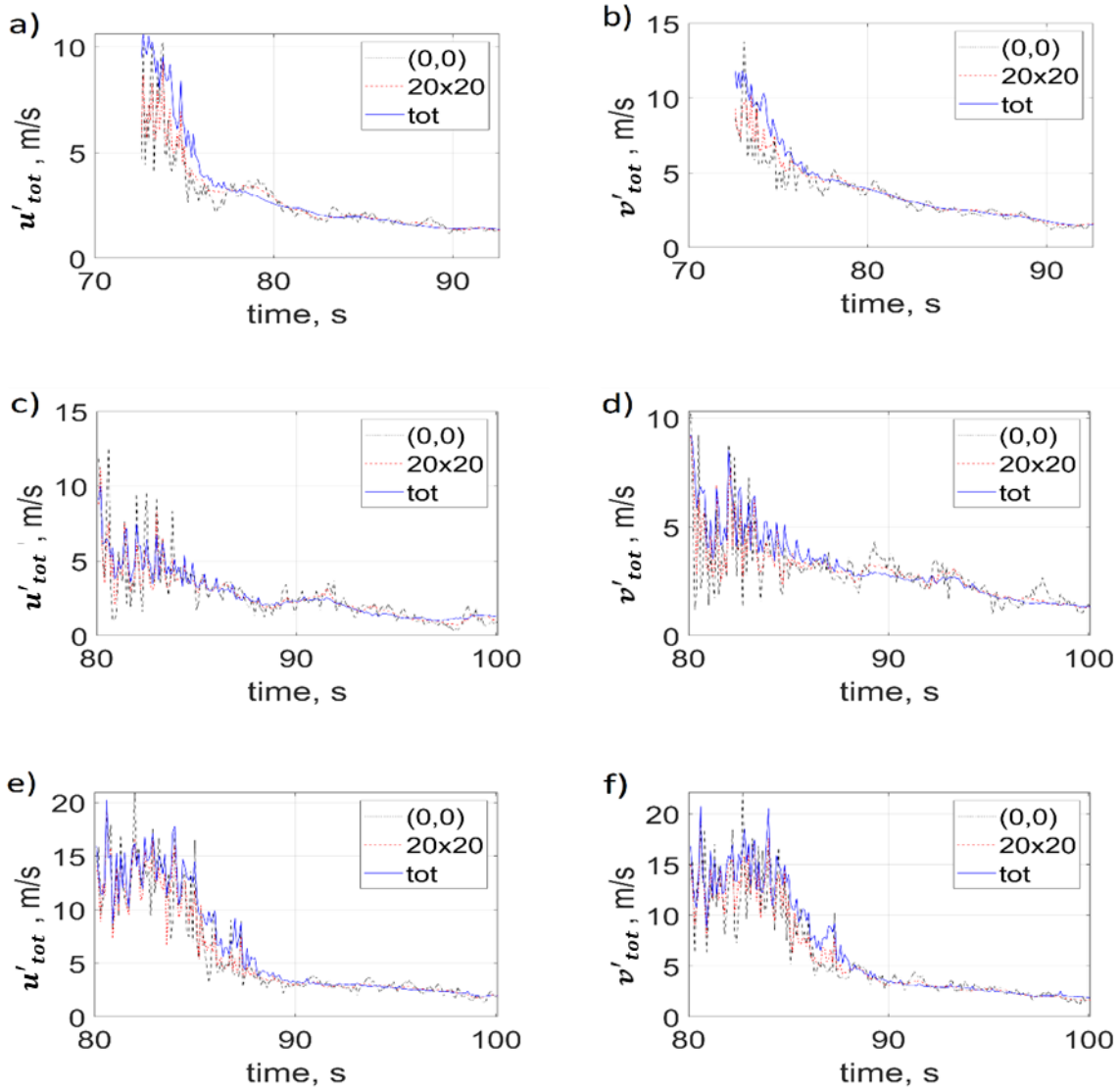


Figure 49.  $u'$  and  $v'$  components evolution in function of time. (a-b) LV; (c-d) SV; (e-f) SV-HTI.

Moreover, exploiting the precision and flexibility of the spark-ignition timing, the combustion can be phased. Possibly, the ignition can be anticipated to let the spark-affected flame develop before this aerodynamically convenient range and let coincide the meaningful radii with the suitable temporal window. Anyway, it is necessary to verify that, within this window, the cyclic fluctuation is negligible and that quasi-stationarity hypothesis is consistent.

One possible approach consists in evaluating the fluctuations convergence using a progressive average. This procedure is applied for the ensemble of all the tests, at fixed time instants. Figure 50, Figure 51 and Figure 52 show the results for the three configurations and four selected time instants. For  $n$  ranging from 2 to  $N$  (number of tests), the ensemble average is performed iteratively for the  $n$  test. This means that at each further step one more test is considered. The procedure is repeated for all the time instants (that is, every velocity field of the 6 ms time interval). The idea is to observe if a convergence of the

fluctuation value exists. LV configuration exhibits a good convergence, even if it can be noticed that the  $v'$  component is generally greater than the  $u'$ , in particular at earlier times. This is less evident on the standard SV configuration. On the contrary,  $u'$  and  $v'$  are in agreement on SV-HTI, even if the convergence is slightly more difficult to obtain at earlier instants, probably due to the still high fluctuations at the beginning of the selected time interval (see Figure 52). Globally, the tests seem consistent to each other. Next step of the analysis consists in performing the progressive average procedure for each single test by increasing time. Figure 53, Figure 54 and Figure 55 show the results for three selected tests for LV, SV and SV-HTI configuration respectively. This second step of the analysis evidences a good convergence for the standard SV configuration, except for one excessively decreasing curve ( $u'$ , test 12). For SV-HTI and LV a slight difference for attained  $u'$  and  $v'$  is observed. Moreover, an increasing evolution of  $v'$  is noticed and it is probably due to the beginning of the expansion that arises at later time instants. Globally, an acceptable convergence is observed.

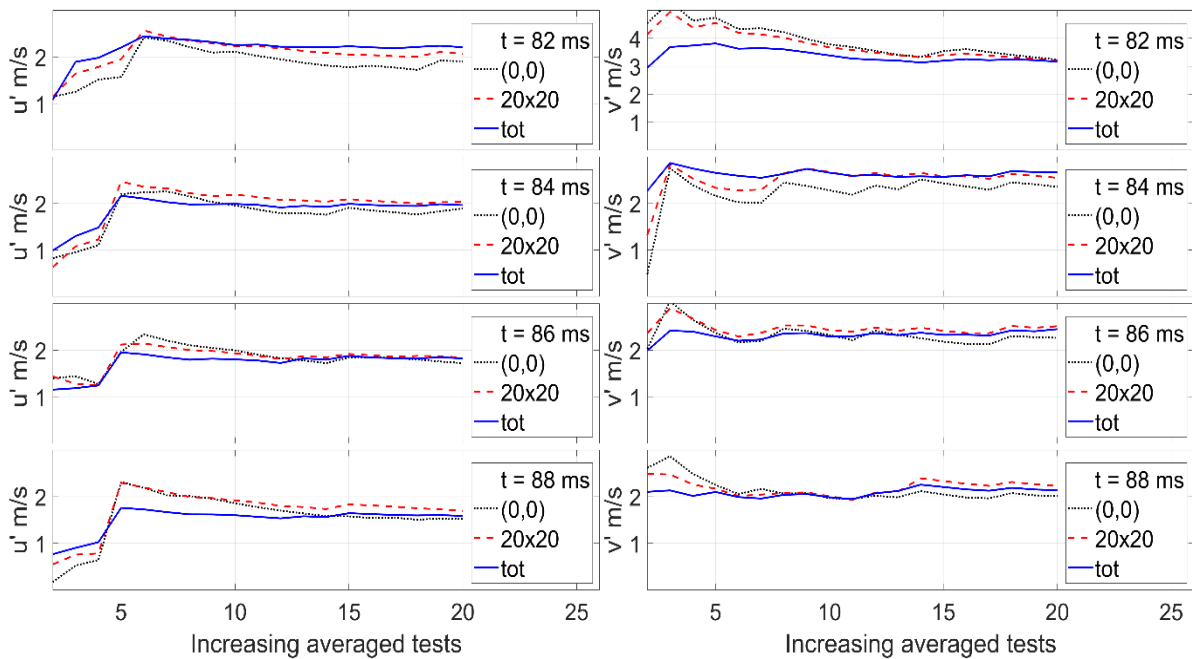


Figure 50. LV: progressive average for increasing number of tests.  $u'$  on the left and  $v'$  on the right.

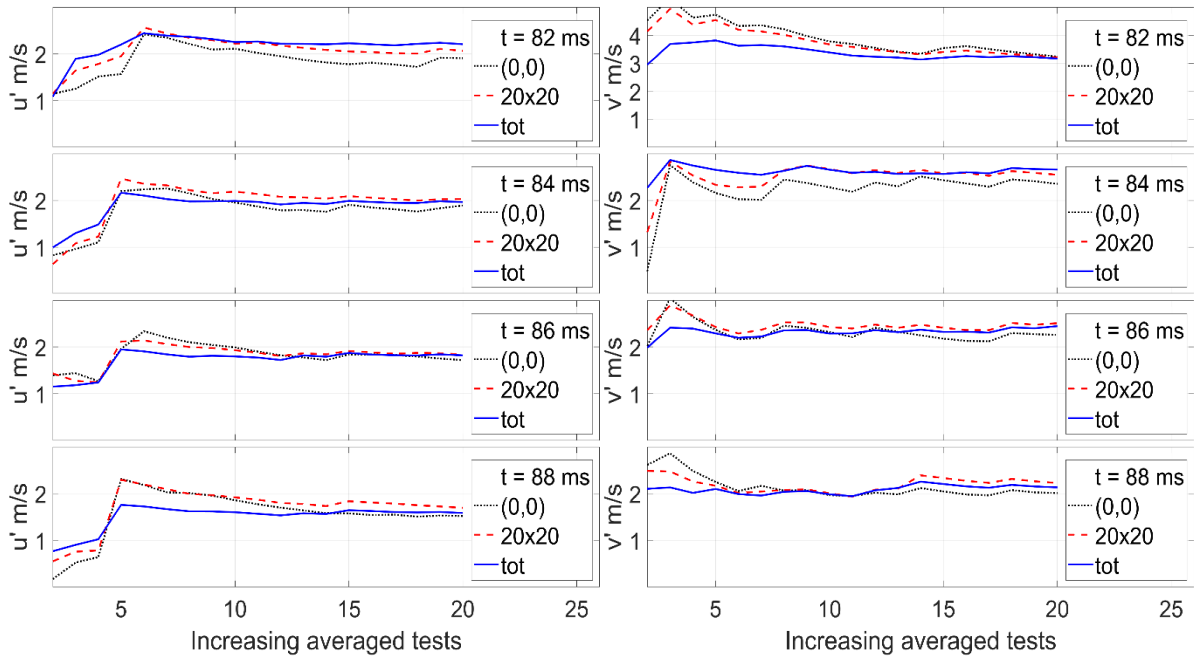


Figure 51. SV: progressive average for increasing number of tests.  $u'$  on the left and  $v'$  on the right.

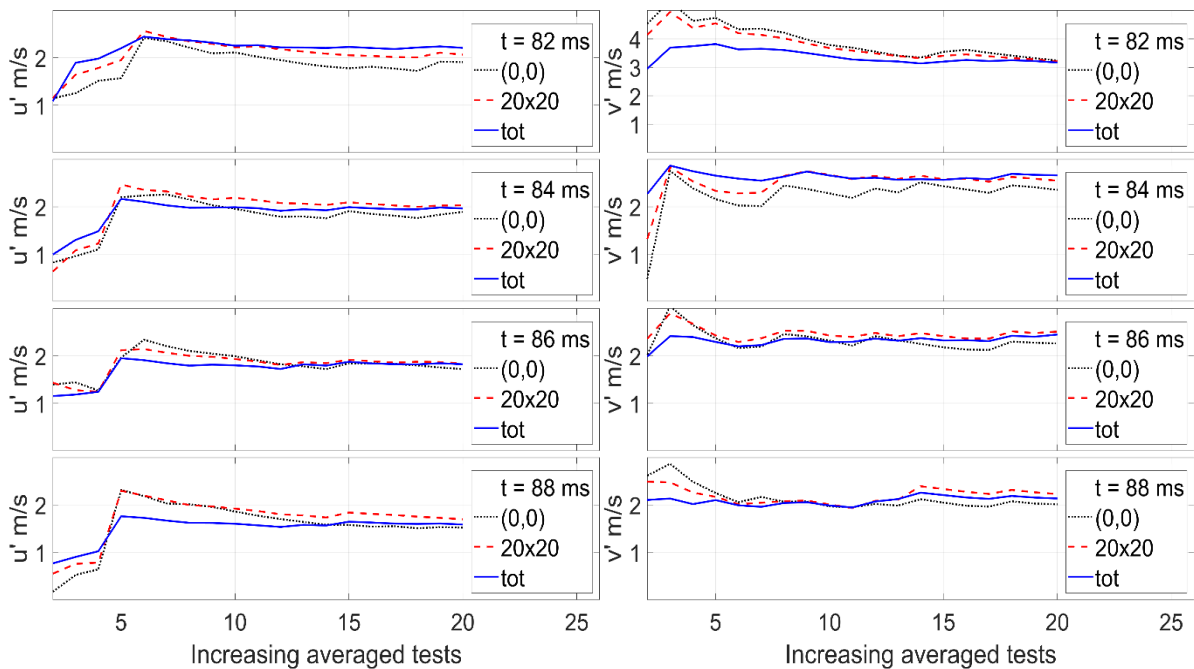


Figure 52. SV-HTI: progressive average for increasing number of tests.  $u'$  on the left and  $v'$  on the right.

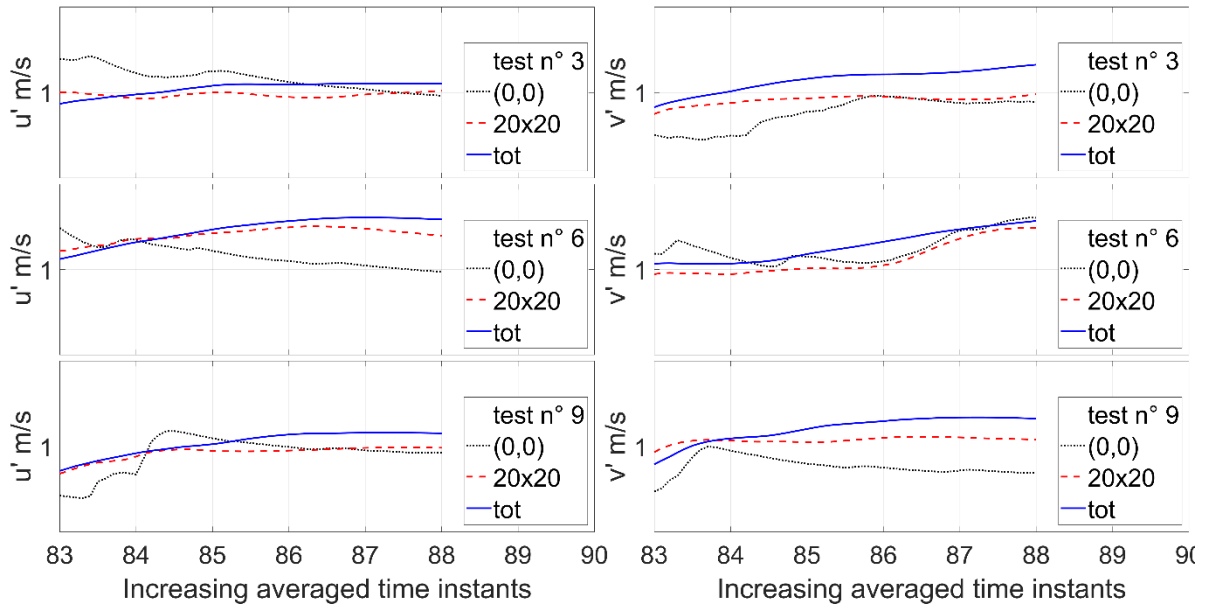


Figure 53. LV: progressive average for increasing time.  $u'$  on the left and  $v'$  on the right.

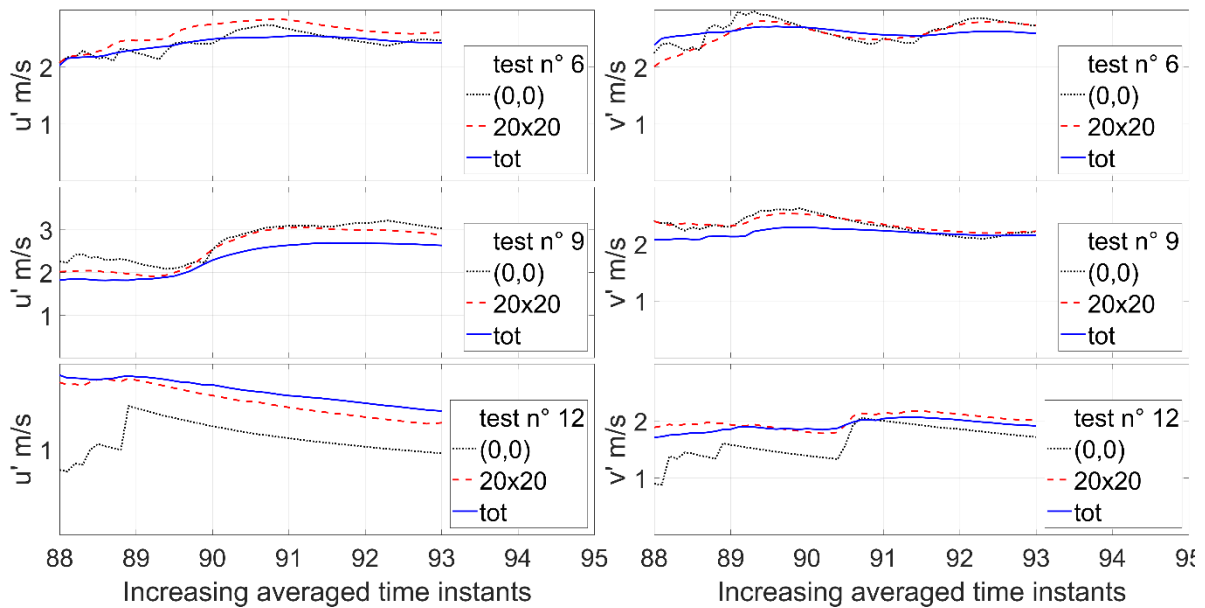


Figure 54. SV: progressive average for increasing time.  $u'$  on the left and  $v'$  on the right.

Thus, one can assume that the several single shots performed by NOSE are actually independent on each other, and no mechanical clearance systematically perturbs the measurements. Moreover, it is possible to approximate the limited selected time interval as quasi-stationary. Considering the 20 tests, then, the statistical analysis quality can be improved by using  $61 \times 20$  points, that is, 1220 velocity fields. It can be assumed that these fields are independent on time and cycle.

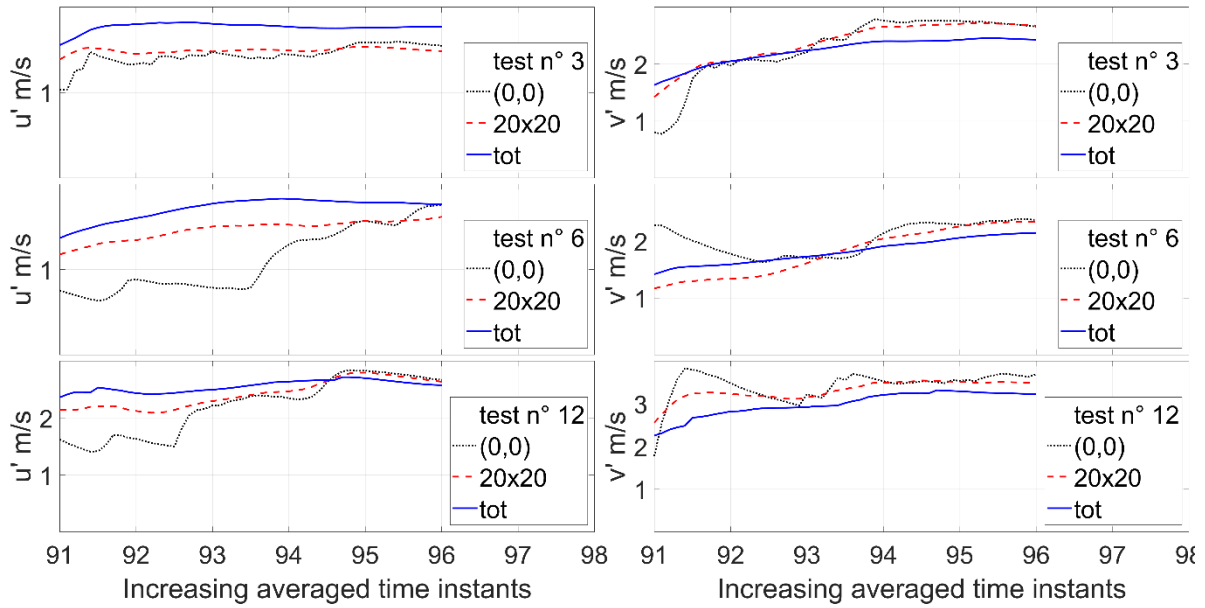


Figure 55. SV-HTI: progressive average for increasing time.  $u'$  on the left and  $v'$  on the right.

### 3.5.3. Turbulence Characterization

To investigate homogeneity and isotropic hypothesis, turbulent intensity components must be evaluated and compared, as well as their longitudinal and transversal integral lengths. Considering the 1220 velocity fields, these quantities are computed using classical definitions presented in Section 2.2. First, the energy spectrum of the turbulent flow, as function of the wavenumber  $\kappa$  is evaluated according to the model of Kolmogorov and Eq. (38). Figure 56, Figure 57 and Figure 58 report the result of this analysis, evidencing the good agreement of the inertial range with respect to the model prevision.

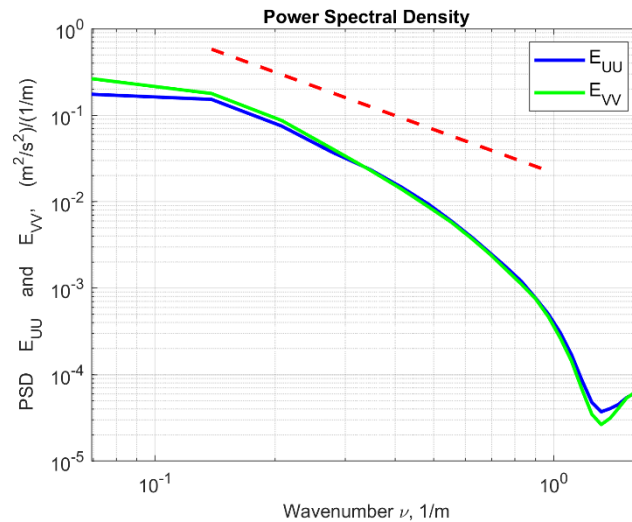


Figure 56. Energy spectrum associated to the turbulent flow in LV configuration.

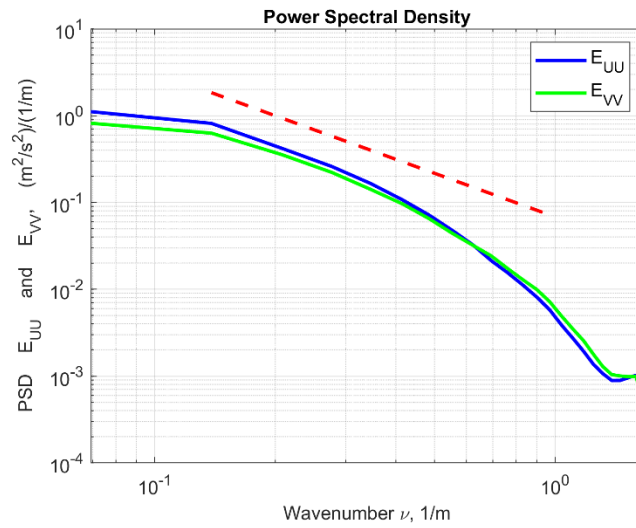


Figure 57. Energy spectrum associated to the turbulent flow in SV configuration.

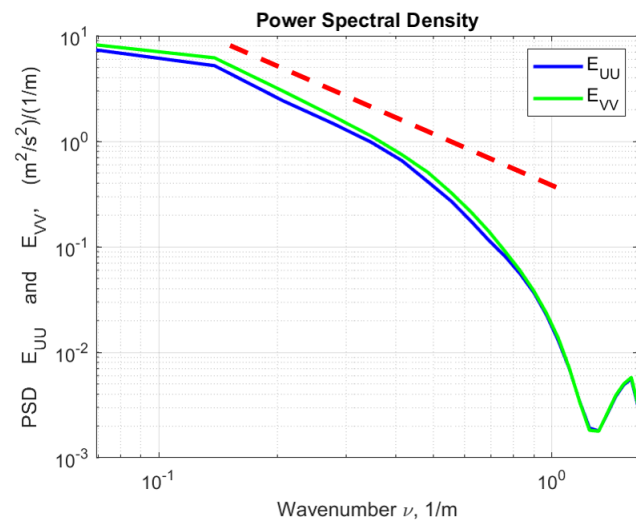


Figure 58. Energy spectrum associated to the turbulent flow in SV-HTI configuration.

To evaluate the properties of HIT, the correlation coefficients are obtained by the auto-correlation analysis of the single velocity field. The integral length scales ( $L_{U_x}, L_{U_y}, L_{V_x}, L_{V_y}$ ) correspond to the area under the curves obtained through the correlation coefficients, as function of space. The autocorrelation coefficients are computed using Eq. (41) and Eq. (42). Instead, the turbulent intensity is calculated using the root mean squared value of the two velocity components seen in Eq. (37), with the turbulent kinetic energy computed through Eq. (36). Figure 59 shows an example of the autocorrelation coefficient curves for the three configuration, exhibiting a shape consistent with the one expected from theory [43]. Figure 60, instead, shows the temporal decaying of turbulent intensity and turbulent kinetic energy, evidencing the differences between the three configurations.

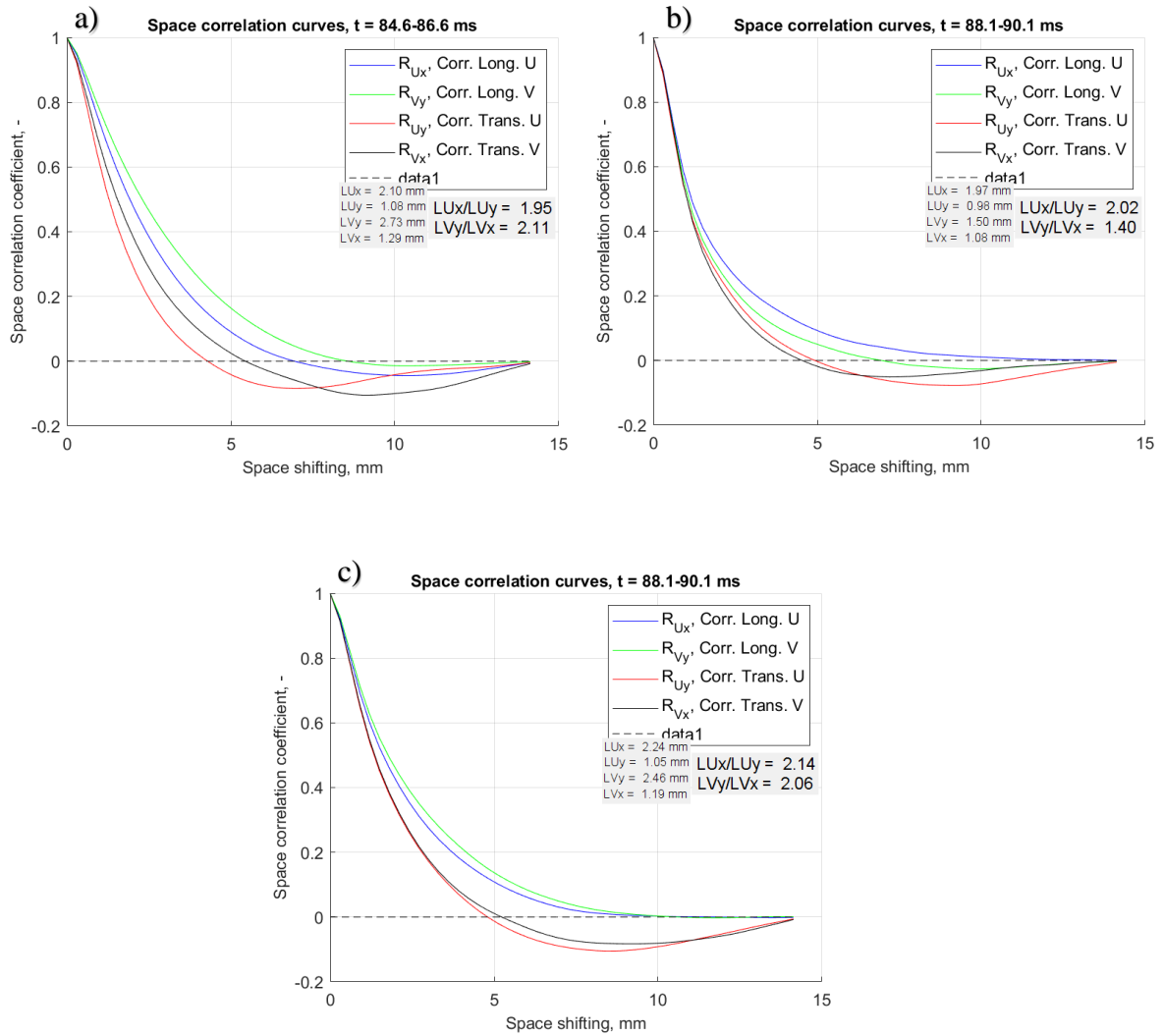


Figure 59. Examples of the extrapolation of the autocorrelation coefficients for the three configurations and a selected temporal sub-range: a) LV; b) SV; c) SV-HTI.

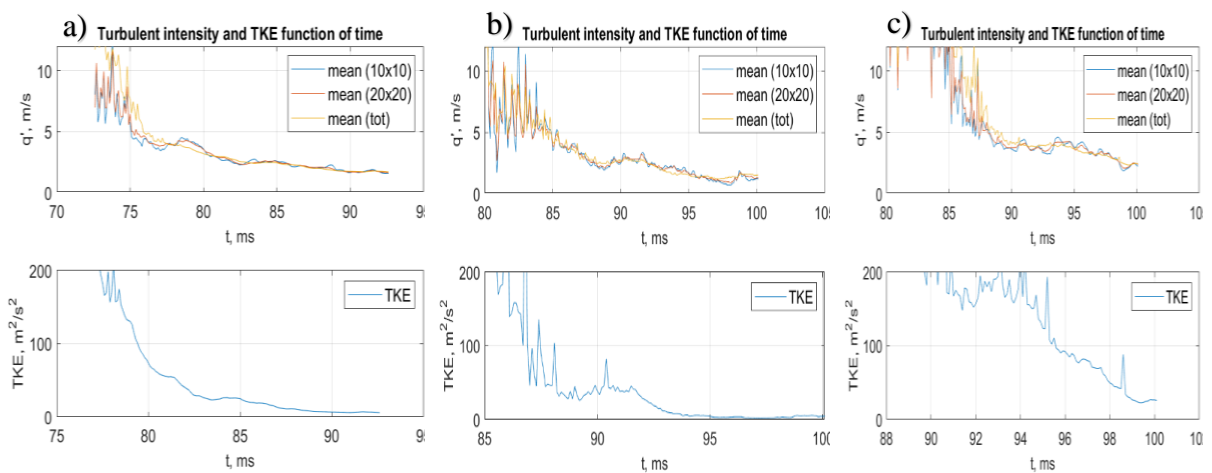


Figure 60. Turbulent intensity and TKE for the three configurations: a) LV; b) SV; c) SV-HTI.

As already shown in Eq. (43) and Eq. (44) [41], [42], HIT condition implies that the ratio between longitudinal and transversal integral lengths must be ideally equal to 2. In addition, one has to verify that  $u'_{rms}{}^2/v'_{rms}{}^2 \approx 1$ . The fundamental turbulent parameters are reported in Table 3, as well as the just discussed fundamental ratios. First consideration concerns the resulting values of  $q'$  and longitudinal integral lengths  $L_{U_x}$  and  $L_{V_y}$ . The values attained with all the three configurations are appreciable and potentially interesting for combustion tests. Anyway, for LV configuration the turbulent intensity vertical component appears to be dominant with respect to the horizontal one. Minor acceptable discrepancy exists also between longitudinal and transversal integral lengths ratio. Standard SV presents an acceptable difference between vertical and horizontal turbulent intensity components, but it exhibits an appreciable  $U_{x/y} \approx 2.1$  which is opposed to  $V_{y/x} \approx 1.4$ . Finally, the SV-HTI offers an almost perfect agreement between vertical and horizontal turbulent intensity components but suffers from a slight discrepancy in the ratios  $U_{x/y}$  and  $V_{y/x}$ .

Table 3. Turbulence properties for the three configurations. Integral lengths expressed in mm.

	$q' (m/s)$	$\frac{u'^2}{v'^2}$	$L_{U_x}$	$L_{U_y}$	$L_{V_x}$	$L_{V_y}$	$\frac{L_{U_x}}{L_{U_y}}$	$\frac{L_{V_y}}{L_{V_x}}$
<b>LV</b>	2.31	0.55	2.09	1.17	1.29	2.61	1.77	2.02
<b>SV</b>	2.70	0.75	2.38	1.14	1.24	1.73	2.07	1.40
<b>SV-HTI</b>	3.29	0.98	2.22	1.43	1.41	1.92	1.55	1.37

### 3.5.4. Summary of NOSE Configurations and Turbulence Properties

Three configurations are considered in this work for the turbulent flames investigation. They differ in terms of pressure and temperature and/or turbulent intensity ranges. The most critical aspects concern the homogeneity and quasi-isotropic hypothesis, while stationarity and independence on cycle variation may be assumed. The dominance of the vertical turbulent intensity component is evident for one configuration (LV), while reduced or inexistent for the other ones. Interesting values of integral lengths and turbulent intensity are offered by the three configurations.

Table 4.  $Ka$  evaluation using both thermo-diffusive and Blint [15] laminar flame thickness.

<b>Config. - <math>L_T(mm)</math></b>	$S_L^0 (cm/s)$	$\delta_L^0 (\mu m)$	$Ka$	$\delta_{L,Blint}^0 (\mu m)$	$Ka_{Blint}$
<b>LV (2.35)</b>	9.7	42.88	18.42	274.45	117.88
<b>SV (2.07)</b>	17.94	18.43	6.38	90.40	31.27
<b>SV-HTI (2.07)</b>	16.83	18.59	9.53	92.94	47.65

Table 4 resumes an evaluation of the Karlovitz number that can be reached using the thermodynamic and turbulent conditions of each configuration. Figure 61 reports these points on Peters-Borghgi diagram. For this evaluation, the stoichiometric mixture is considered, with 25% of EGR dilution. The Karlovitz number range is very promising in order to reproduce combustion-turbulence interaction as in boosted SI engine.

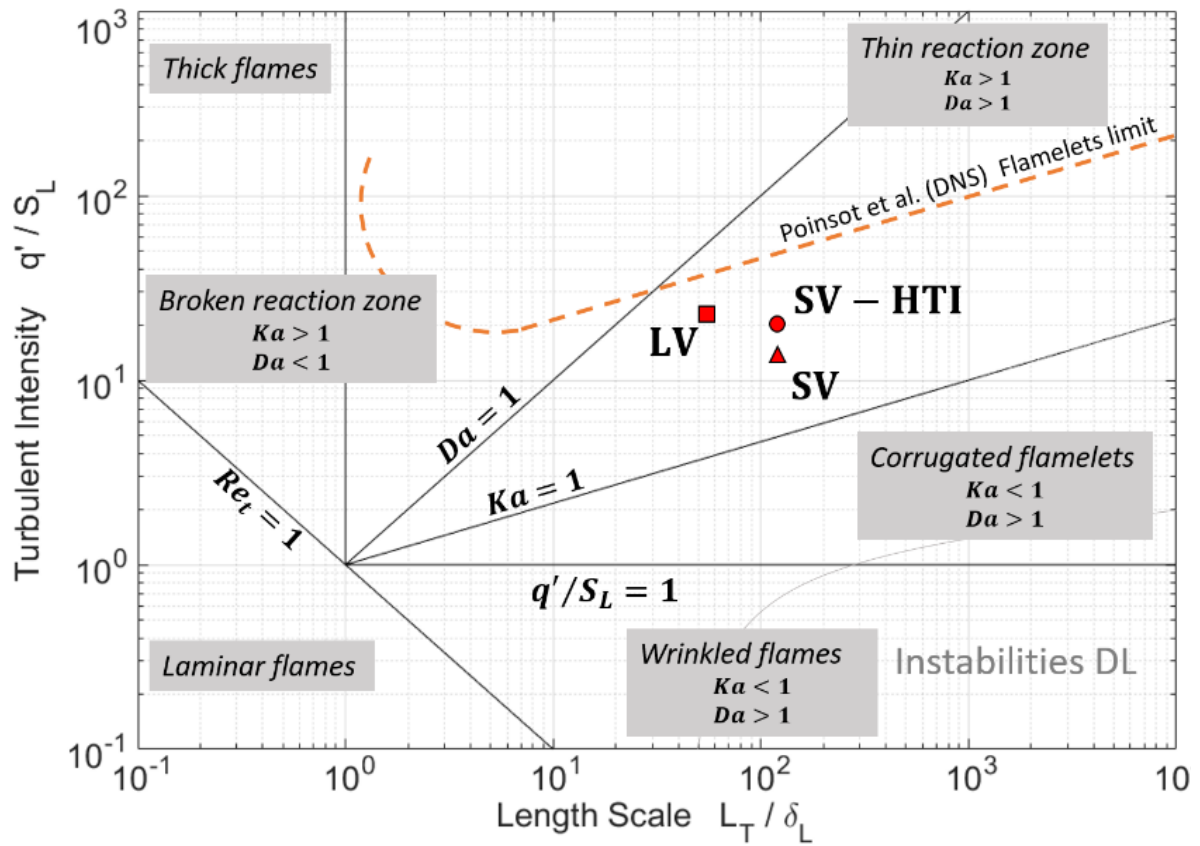


Figure 61. Peters-Borghgi diagram with evaluated Karlovitz number for NOSE set-ups.

### 3.6. CONCLUSIONS

In the present chapter the two experimental set-ups used for the laminar and turbulent flames investigation were presented.

Spherical vessel offers operational simplicity, accuracy in reproduce target ambient conditions and easiness of repeat a large numbers of tests for a large variety of conditions. The apparatus was already characterized in previous work by Galmiche [30], then, in the relative section, the fundamental characteristics of both laminar and turbulent configurations were presented.

On the contrary, NOSE represents a new experimental set-up that required a thorough characterization. This set-up can be used to investigate both laminar and turbulent flames, by changing the configuration. The turbulence, in particular, is generated as indirect consequence of the recirculation caused by a grid. The grid was designed by partner of the MACDIL project and it is placed between the cylinder head and the combustion chamber.

NOSE offers the opportunity to overcome the limits of the spherical vessel in terms of both thermodynamic conditions and turbulence properties. To validate both these aspects, repeatability tests were performed and a PIV set-up was implemented for the aerodynamic characterization. It was found that exists a zone, that was called *plateau*, in which the thermodynamic conditions are repeatable with acceptable accuracy and the turbulence can be considered independent on cycle-to-cycle variations and quasi-stationary. Reducing the turbulence characterization to this range, the fundamental properties of the turbulent flow were evaluated.

For the flame visualization a DVS set-up was used on the spherical vessel and implemented and used, as well, on NOSE. Tomography tests were also performed on NOSE but limits of this strategy were pointed out in Sub-section 3.3.3.





---

## **4. Results: Laminar Flames**

---



## 4.1. INTRODUCTION

In the present chapter, the results of the laminar flames investigation will be presented.

Firstly, the TRF-E will be validated as suitable surrogate for the gasoline fuel considered in the present work. The validation is based on direct comparison of laminar burning velocities of the two fuels for a large number of experimental conditions. Moreover, the Markstein length will be also compared and the dynamic behavior of the two fuels will be evaluated.

Second part provides a focus on the TRF-E. The experimental conditions matrix was widened to increase the available laminar burning velocity database. Using these data, the coefficient of a predictive mathematical correlation are defined and tested for the different combination of pressure, temperature, dilution and equivalence ratio, showing appreciable results. This correlation can be used in CFD simulations or in the evaluation of  $S_L^0$  for the computation of those parameters that will be fundamentals to the turbulent investigation.

In order to further enlarge the laminar burning velocity database and furnish direct measurements under engine-like conditions, the NOSE setup was used. As first step, the measurement procedure and the validity of the tests performed on this new setup must be confirmed. Then, third part of the chapter will discuss the comparison between spherical vessel and NOSE results, considering identical experimental conditions. Good agreement was found, validating the NOSE laminar configuration and defining its experimental limits.

Lastly, points at very high pressure (21 bar) and high temperature (up to 525 K) were investigated and the results will be showed and discussed in the final part of the chapter. The analysis allowed to validate the mathematical correlation derived on the sphere and the chemical mechanism developed by partners in MACDIL project. The new experimental points offered the opportunity to further refine the mathematical correlation and they will be fundamental for the development of future works.

## 4.2. GASOLINE SURROGATE

As discussed in the previous chapter, at present, most of turbulent premixed combustion models are based on the flamelet regime assumption [112]. However, recent work of Mounaim-Rousselle et al. [73] pointed out a possible breach of the flamelet regime in Spark-Ignition (SI) engines for particular operating conditions, such as downsized engine with high rates of Exhaust Gas Recirculation (EGR) [75], [76]. According to the flamelet model, the flame is considered as asymptotically thin and locally laminar even if the turbulence can wrinkle the flame surface [112]. That explains why, in literature, laminar burning speed is a crucial factor in most practical combustion systems and its investigation is still an open research field. Moreover, even though this parameter depends on equivalence ratio, pressure, temperature and diluent gases in the mixture [69], [100], its value is basically a strict characteristic of the fuel itself. To evaluate potential alternative fuels and/or suitable surrogate [113]–[115], the acquisition of complete laminar burning velocities database is required before having access to accurate kinetics mechanism. However, when the target of the investigation is a real commercial gasoline, the validation of a suitable surrogate is the prior step. In fact, commercial gasoline is composed by hundreds of different chemical species that severely increase the complexity, including experimental or numerical approaches [116]. Using surrogate fuel, with well-known composition, allows reducing the complexity to identify the key mechanisms of the reactive mixture [116], [117]. Nonetheless, the surrogate must be representative of the target gasoline. It can be single or multi-components, depending on the purpose of the investigation. As single-component surrogate, iso-octane is widely used for gasoline fuel and may be representative for fundamental phenomena analysis [118]. Nevertheless, Stanglmair et al. [119] pointed out that the differences between gasoline and iso-octane can be significant at high pressure and temperature. Thus, when the surrogates have to explicitly represent the gasoline behavior, the association through the research octane number (RON) is a practical solution. This coupling is obtained by mixing iso-octane and n-heptane, leading to the Primary Reference Fuels (PRFs) that represent suitable surrogates for gasolines and/or under certain conditions [116], [118], [120]. For example, Jerzembeck et al. [121] compared a commercial gasoline with a PRF mixture characterized by RON 87, deducing that the agreement between the two fuels decreases with increasing equivalence ratio. Similarly, Bradley et al. investigated laminar burning speeds of different PRFs up to 10 bar [26], [106]. However, Cruz et al. [117] and Farrell et al. [122] highlighted the fact that PRFs can considerably differ from a pure gasoline due to the different combustion properties of aromatic species with respect to alkanes. Therefore, in order to simulate refinery gasoline, surrogates that include a certain percentage of toluene in the composition represent the actual reference [116]. These are called Toluene Reference Fuels (TRFs) and the best composition in order to fit the gasoline properties is still an open topic as strictly depending on the gasoline target. However, multi-components surrogates of three or more species are the best option when the target is to develop, for example, advanced chemical kinetics

mechanisms. Even if several studies have investigated the flame characteristics of different hydrocarbons used in multi-components surrogates [123]–[125] less studies focused on the determination of the laminar burning speed for gasoline and TRFs, pure [115], [123] or eventually blended with other species (*e.g.* ethanol) [105], [126] are available on the literature. First part of the present work concerns the validation of a specially designed surrogate, the TRF-E (*i.e.* a blend of TRF with ethanol), as a surrogate of the commercial gasoline (*B71 1188 ESSH EURO5 +20, RON 96.6 MON 86.2, Ethanol 5%vol*).

Table 5. Properties and composition of the gasoline (B71 1188 ESSH EURO5 +20) and its surrogate TRF-E.

GASOLINE		TRF-E	
RON	96.6	RON	95
%C, %H, %O (%mass)	85.1/13.1/1.8	%C, %H, %O (%mass)	84.79/13.34/1.87
$\rho$ ( $kg/m^3$ )	753.0	$\rho$ ( $kg/m^3$ )	750.5
Ethanol (%vol)	5.0	Ethanol (%vol)	5.0
<i>n</i> -Heptane (%vol)	3.6	<i>n</i> -Heptane (%vol)	15.0
Olefin (%vol)	6.2	<i>iso</i> -Octane (%vol)	44.0
Aromatic (%vol)	33.7	Toluene (%vol)	36.0
Benzene (%vol)	0.1	-	-
Methyl-cyclohexane (%vol)	1.5	-	-

Effects of pressure, aromatic compounds oxidation and high EGR percentages, in particular, are critical in the development of kinetics mechanisms [127]. It is then fundamental to provide experimental data concerning the combination of all these factors. In fact, current literature includes several studies on mono-component fuels or PRF surrogates diluted by CO<sub>2</sub>, N<sub>2</sub>, H<sub>2</sub>O or a combination of those, like synthetic EGR [69], [100], [101], [105], [126], [128], [129]. In this sense remarkable work was conducted by Marshall et al. [130] using real combustion residuals as diluent with several mono-component fuels. Nonetheless, there is still a lack of data regarding more complex fuels diluted by EGR. Recently, Manna et al. [104] provided a deep investigation on the influence of ethanol and dilution on a gasoline and its surrogate, using real EGR. It was figured out that significant percentages of ethanol (up to 85%) may mitigate the flame speed reduction caused by EGR dilution. Moreover, a stabilization effect due to EGR was observed, comparing delays in the cellularity arising and Markstein lengths of the different blends. As reported in Table 5, the present work focused on a surrogate with relatively low ethanol percentage (5%) and significant toluene percentage (36%). Then, the TRF-E validation and characterization will be crucial in the development of accurate kinetics mechanism, allowing the investigation of aromatics oxidation, high multi-species diluent rate and high pressure effects on the chemistry. On the other hand, the present work aims to furnish the literature with a refined mathematical correlation for laminar burning velocity prediction of TRFE/air/EGR and gasoline/air/EGR blends. Laminar burning velocity of both gasoline and surrogate was measured, using the spherical vessel apparatus, and critically compared. Finally, the laminar burning velocity database of the TRF-E was enlarged to cover all the possible experimental limits of the spherical vessel.

### 4.3. EXPERIMENTAL CONDITIONS

Reference conditions were fixed at 473 K, 0% EGR dilution and 1 bar, where EGR composition is obtained considering the combustion products derived by the stoichiometric mixture ( $\phi = 1$ ). The two fuels were compared for each combination of dilution and pressure at 473 K. Then, the effect of the temperature was evaluated by adding other two experimental points (373 and 423 K) at 1 bar and 0% EGR. The equivalence ratio ( $\Phi$ ) was varied between 0.8 and 1.3. Three tests were performed for each condition. Once that the surrogate validation was accomplished through this first investigation, the TRF-E database was widened with the addition of two other values of temperature, 373 and 423 K for the same combination of pressure, dilution and equivalence ratio. This wide range of experimental points allows to deeply evaluate the mathematical correlation initially proposed by Metghalchi and Keck [131] and widely used in previous works [69], [100]. Details of these two fuels were presented in Table 5, while the experimental conditions are reported in Table 6.

Table 6. Investigated experimental conditions, for each combination of pressure, temperature and EGR dilution, three test were performed at different Equivalence Ratio (0.8, 0.9, 1.0, 1.1, 1.2, and 1.3).

Dilution	Pressure	1 bar	2 bar	3 bar	5 bar
	Temp.				
0% EGR	373 K	TRF-E & Gasoline	TRF-E	TRF-E	TRF-E
	423 K	TRF-E & Gasoline	TRF-E	TRF-E	TRF-E
	473 K	TRF-E & Gasoline	TRF-E & Gasoline	TRF-E & Gasoline	TRF-E & Gasoline
10% EGR	373 K	TRF-E	TRF-E	TRF-E	TRF-E
	423 K	TRF-E	TRF-E	TRF-E	TRF-E
	473 K	TRF-E & Gasoline	TRF-E & Gasoline	TRF-E & Gasoline	TRF-E & Gasoline
20% EGR	373 K	TRF-E	TRF-E	TRF-E	TRF-E
	423 K	TRF-E	TRF-E	TRF-E	TRF-E
	473 K	TRF-E & Gasoline	TRF-E & Gasoline	TRF-E & Gasoline	TRF-E & Gasoline

#### 4.4. MATHEMATICAL CORRELATION

Initially proposed by Metghalchi and Keck [131] and widely used in the literature, the mathematical correlation aims to predict the laminar burning speed of a specific fuel starting from the mixture and thermodynamic parameters. This means that it is possible to write a relationship such that  $S_L^0 = (T_i, P_i, \phi)$ , corresponding to the explicit form

$$S_L^0 = S_{Lref}^0 \left( \frac{T_i}{T_{ref}} \right)^{\alpha_S} \left( \frac{P_i}{P_{ref}} \right)^{\beta_S} \quad (77)$$

Where  $T_{ref}$  and  $P_{ref}$  are respectively the reference temperature and the pressure (expressed in K and in bar) and  $S_{Lref}^0$  the laminar burning speed under these conditions (expressed in cm/s). Anyway, it is possible to use the same mathematical correlation to directly relate the unstretched propagation flame velocity. Then, the terms  $S_{Lref}^0$ ,  $\alpha_S$  and  $\beta_S$  are a function of the equivalence ratio  $\phi$ , hence

$$S_{Lref}^0 = A + B(\phi - \phi_m) + C(\phi - \phi_m)^2 \quad (78)$$

$$\alpha_S = \alpha_0 + \alpha_1(\phi - \phi_m) \quad (79)$$

$$\beta_S = \beta_0 + \beta_1(\phi - \phi_m) \quad (80)$$

with  $\phi_m$  representing the reference equivalence ratio equal to 1.1.

Nevertheless, according to Varea et al. [132], the pressure dependence is not linear and, thus, the pressure term evolves following a quadratic law yielding to a different equation of the exponent  $\beta_S$ , that is

$$\beta_S = \beta_0 + \beta_1(\phi - \phi_m) + \beta_2(\phi - \phi_m)^2 \quad (81)$$

Galmiche et al. [69] proposed to implement the effect of dilution by adding a third term and, thus, a new exponent is introduced

$$\gamma_S = \gamma_0 + \gamma_1(\phi - \phi_m) \quad (82)$$

leading to the following complete relationship

$$S_L^0 = S_{Lref}^0 \left( \frac{T_i}{T_{ref}} \right)^{\alpha_S} \left( \frac{P_i}{P_{ref}} \right)^{\beta_S} \left( \frac{v_{O_2i}}{v_{O_2ref}} \right)^{\gamma_S} \quad (83)$$

In this new correlation the term  $v_{O_2}$  takes into account the percentage of oxygen in the global mixture of synthetic air and diluent, thus

$$v_{O_2} = \frac{n_{O_2(air)}}{n_{O_2(air)} + n_{N_2(air)} + n_{(diluent)}} \times 100 \quad (84)$$

where  $n$  refers to the number of moles of the different mixture components.

The global optimization consists in resolving the minimization problem in which the objective function is the mean squared error between the experimental data and the correlation (Eq. (83)). In order to find all the coefficient the optimization process is developed in two phases:

- First, the coefficients A, B and C are determined under the reference conditions, therefore only the relative experimental data are taken into account;
- In the second step are then included all the other points. In this way it is possible to compute the coefficients that appear in Eq. (79), Eq. (81) and Eq. (82), obtaining the exponents  $\alpha_S$ ,  $\beta_S$  and  $\gamma_S$ .

Moreover, in the present study, the optimization process is performed in two steps for both the procedures just discussed. In other words, starting from a generic initial guess (*e.g.* a vector of zeroes) a raw solution is calculated and, successively, this is used as initial guess for a second iteration. It was found that for the coefficient A, B and C this process is redundant, as the algorithm converges to the final optimized solution also with the first generic initial guess. On the contrary, the determination of the exponents is strongly affected by the 2-step process leading to a significant difference of the results. The difference between the 1-step and the 2-step derived coefficients is illustrated in Figure 62. The figure highlights the enhancement of accuracy of the 2-step coefficients, in particular for rich mixtures. Anyway, it was observed that any further iterative process led to the same problem solution obtained at the second step, independently on the initial generic guess of the first step. The results of this investigation are reported in Table 7 and Table 8. The TRF-E coefficients are further refined by extending the experimental matrix. Other two temperatures were investigated, combining the full range of considered dilution and pressure.

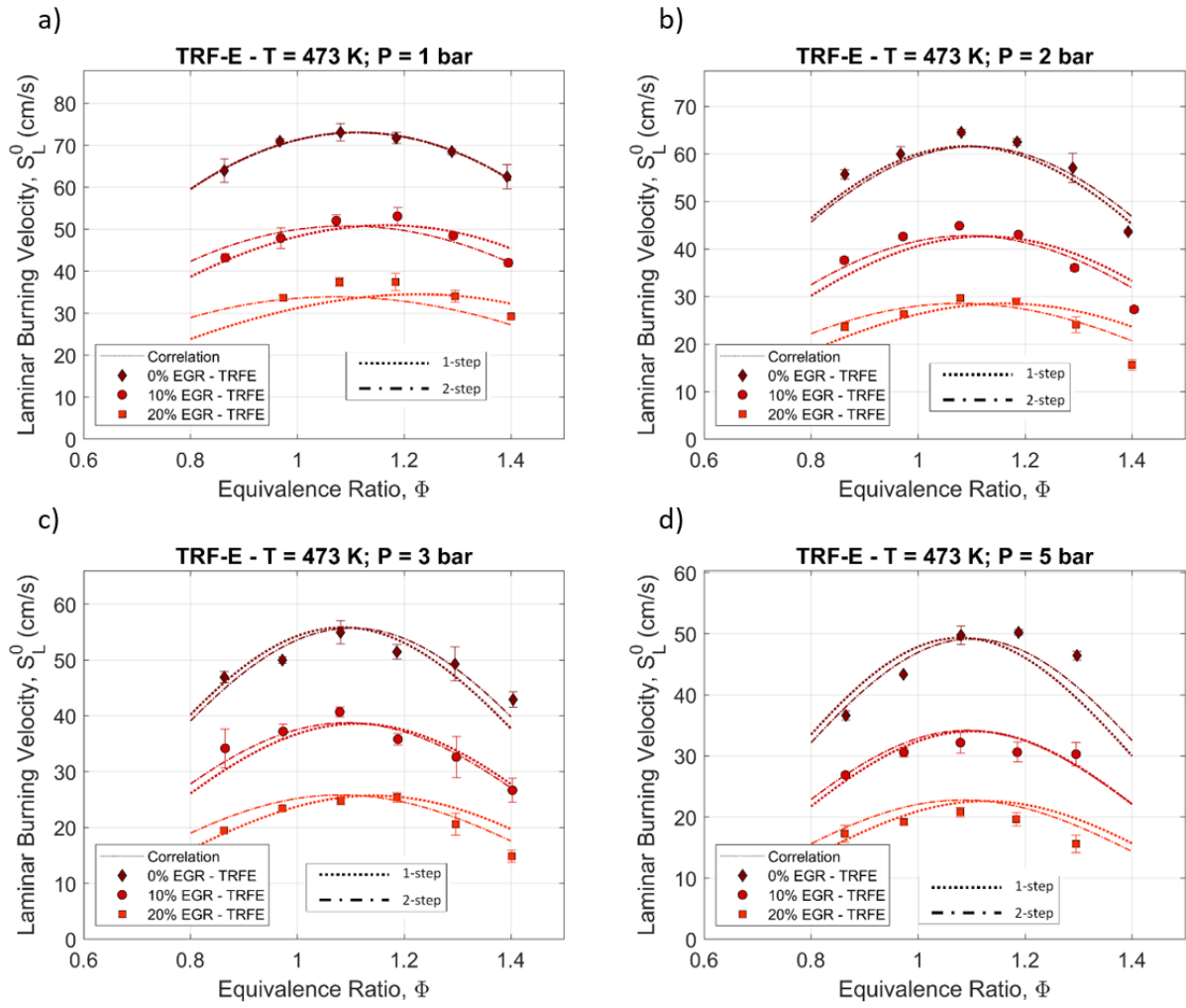


Figure 62. TRF-E laminar burning velocities at different pressure values (Figures a, b, c, d) and fixed temperature ( $T = 473$  K) for three dilution rates: experimental points and correlation curves with comparison between 1-step and 2-step optimization.

Table 7. Mathematical correlation coefficients (relative to the laminar burning velocity) for both TRF-E and gasoline determined at fixed temperature and different values of equivalence ratio, pressure and dilution. Coefficients A, B, C refer to the equivalence ratio fitting equation at reference conditions. First column of each fuel displays the classic one-step method that solves the global optimization problem only once. The second column consists of a further system resolution using the 1-step coefficients as initial guess.

Coefficient	Optimized value – Gasoline		Optimized value – TRF-E	
	1-step	2-step	1-step	2-step
A	71.2043	71.2043	73.0208	73.0208
B	2.7185	2.7185	3.5315	3.5315
C	-142.8526	-142.8526	-138.1265	-138.1265
$\alpha_0$	0.8259	1.6437	1.4977	1.7696
$\alpha_1$	-0.7370	-0.8478	-1.1148	0.3151
$\beta_0$	-0.17857	-0.1926	-0.2325	-0.2463
$\beta_1$	-0.2150	-0.1195	-0.0428	-0.0242
$\beta_2$	-2.0643	-1.5001	-2.2700	-1.5983
$\gamma_0$	3.3959	3.3782	3.4994	3.4494
$\gamma_1$	-0.1844	1.3476	-0.0872	0.7151

Table 8. Mathematical correlation coefficients (relative to the laminar burning velocity) for TRF-E fuel determined at fixed temperature and different values of equivalence ratio, pressure and dilution firstly, and then including temperature variation in the global optimization problem. Coefficients A, B, C refer to the equivalence ratio fitting equation at reference conditions. First column of each fuel displays the classic one-step method that solves the global optimization problem only once. The second column consists of a further system resolution using the 1-step coefficients as initial guess.

Coefficient	Optimized value – TRF-E (any temperature variation)		Optimized value – TRF-E (with temperature variation)	
	1-step	2-step	1-step	2-step
A	73.0208	73.0208	73.0208	73.0208
B	3.5315	3.5315	3.5315	3.5315
C	-138.1265	-138.1265	-138.1265	-138.1265
$\alpha_0$	1.4977	1.7696	1.7702	1.7495
$\alpha_1$	-1.1148	0.3151	-1.2579	-0.1010
$\beta_0$	-0.2325	-0.2463	-0.2453	-0.2481
$\beta_1$	-0.0428	-0.0242	-0.1499	0.0232
$\beta_2$	-2.2700	-1.5983	-1.7451	-1.7739
$\gamma_0$	3.4994	3.4494	3.5018	3.4143
$\gamma_1$	-0.0872	0.7151	-1.9900	0.4252

## 4.5. TRF-E VALIDATION AS GASOLINE SURROGATE

In order to evaluate how the TRF-E surrogate fits the properties of the investigated gasoline, the comparison of the different unstretched laminar burning velocities is performed under several experimental conditions as seen in Table 6. In particular, the accordance between the two fuels must be evaluated under reference conditions and, then, by changing the relevant parameters. This will allow appreciating how the surrogate responds to this variation and how it “follows” the gasoline behavior, quantifying the differences.

As introduced in the previous section, an error is normally introduced in the calculation of the gasoline expansion factor using the TRF-E composition. Anyway, evaluating the dynamic behavior of the two fuels (that is, the propagation speed as function of the stretch rate and, thus, the Markstein length) it is possible the strength of this approximation. Figure 63 reports the stretched propagation speed as function of the stretch rate for both the TRF-E and the gasoline, for one representative condition ( $T = 473\text{ K}$ ,  $P = 3\text{ bar}$ ,  $\phi = 1.0$  and 10% EGR). It seems clear that, in this case, the dynamic behavior of TRF-E and gasoline is similar. Figure 64 summarizes the comparison between Markstein lengths of the two fuels under the investigated conditions. Figure 64 (a) and (b) evidence a very good agreement between TRF-E and gasoline for every equivalence ratio. With increasing pressure, anyway, the Markstein length determination becomes tougher. Figure 64 (c) highlights points scattering in the rich zone, with also large error bar, while Figure 64 (d) presents large uncertainties over all the equivalence ratio range. However, at the end of this consideration, it has sense to assume that the error in the computation of the expansion factor could be negligible since the two fuels exhibit similar dynamic behavior.

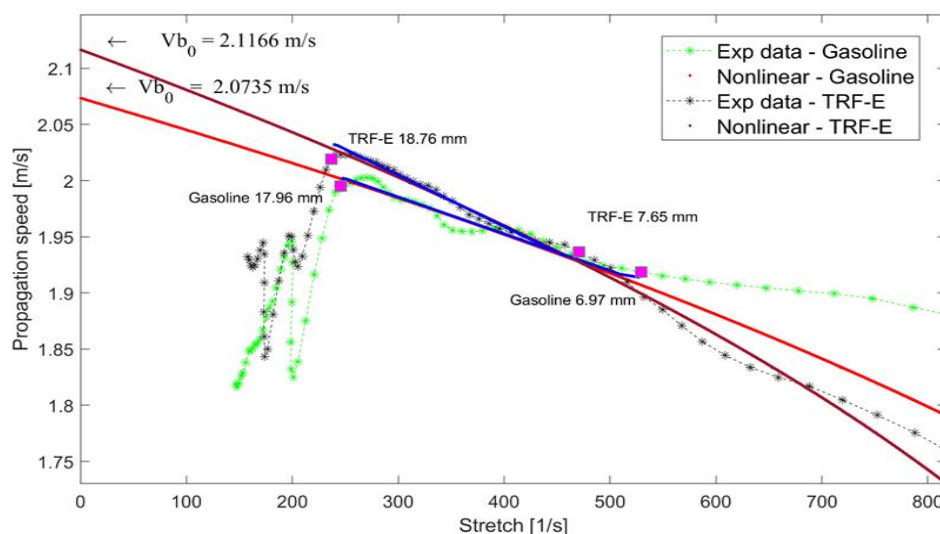


Figure 63. TRF-E and gasoline propagation speed function of stretch rate. The data are extrapolated from test performed at pressure of 3 bar, dilution of 10% EGR and temperature of 473 K. Experimental data are reported as well as nonlinear Kelly and Law correlation. Extrapolated unstretched propagation speed and radii range analyzed are reported.

According to Figure 65, under reference conditions ( $T_{ref}, P_{ref}, EGR_{ref}$ ), the unstretched propagation flame velocity of TRF-E with respect to gasoline is in an relative short interval ( $-6.53\%$ ,  $-3.06\%$ , see Figure 65 (b)) among all investigated ER range. On the other hand, decreasing temperature affects the laminar burning velocity of the two fuels in a different way. In fact, though the TRF-E shows a constant lowering for all ER values, maintaining the same curve shape, the gasoline exhibits a stronger slowdown in lean conditions with respect to the rich zone that, on the contrary, seems to be less influenced. That corresponds to a change in the curve shape and a slight shifting of the maximum gasoline  $S_L^0$  value to higher ER. As seen in Figure 65 (a), at  $T = 423\text{ K}$ , gasoline laminar burning velocity is still lower than the TRF-E one for lean mixtures. The laminar burning velocity of the two fuels is similar after  $\phi = 1.1$ . On the contrary, at  $T = 373\text{ K}$ , after  $\phi = 1.1$ , gasoline rich mixtures are faster than TRF-E ones. Figure 65 (b) quantifies the gap between the two fuels at  $T = 373\text{ K}, 423\text{ K}$  and  $473\text{ K}$ .

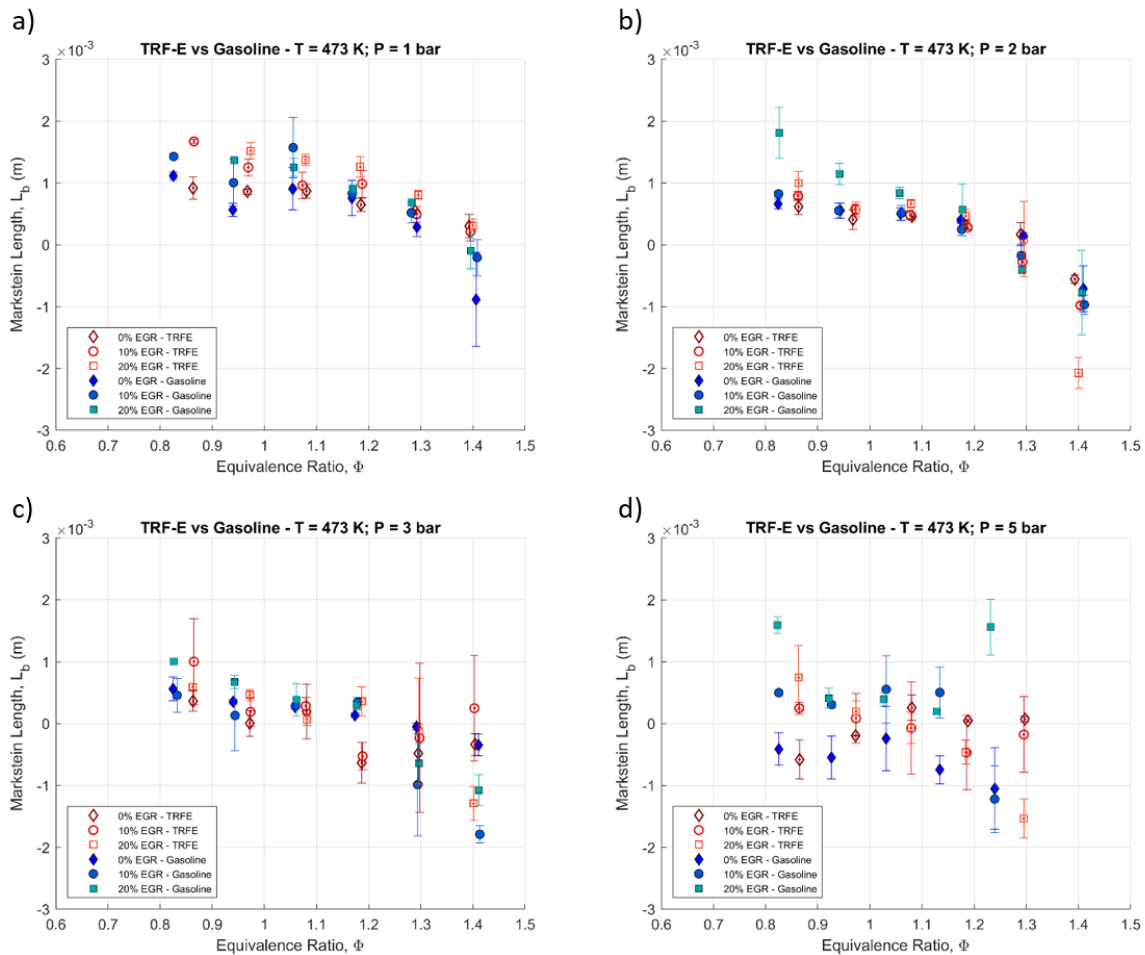


Figure 64. TRF-E and gasoline Markstein lengths comparison at different pressure values (Figures a, b, c, d) and fixed temperature ( $T = 473\text{ K}$ ) for three dilution rates.

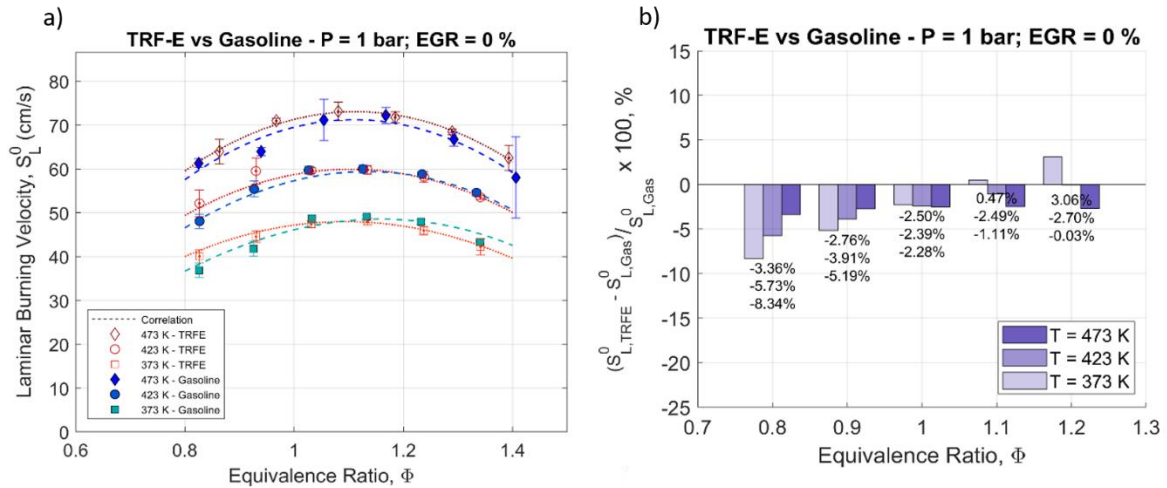


Figure 65. TRF-E and gasoline laminar burning velocities comparison at 1 bar initial pressure without dilution for three initial temperature conditions.

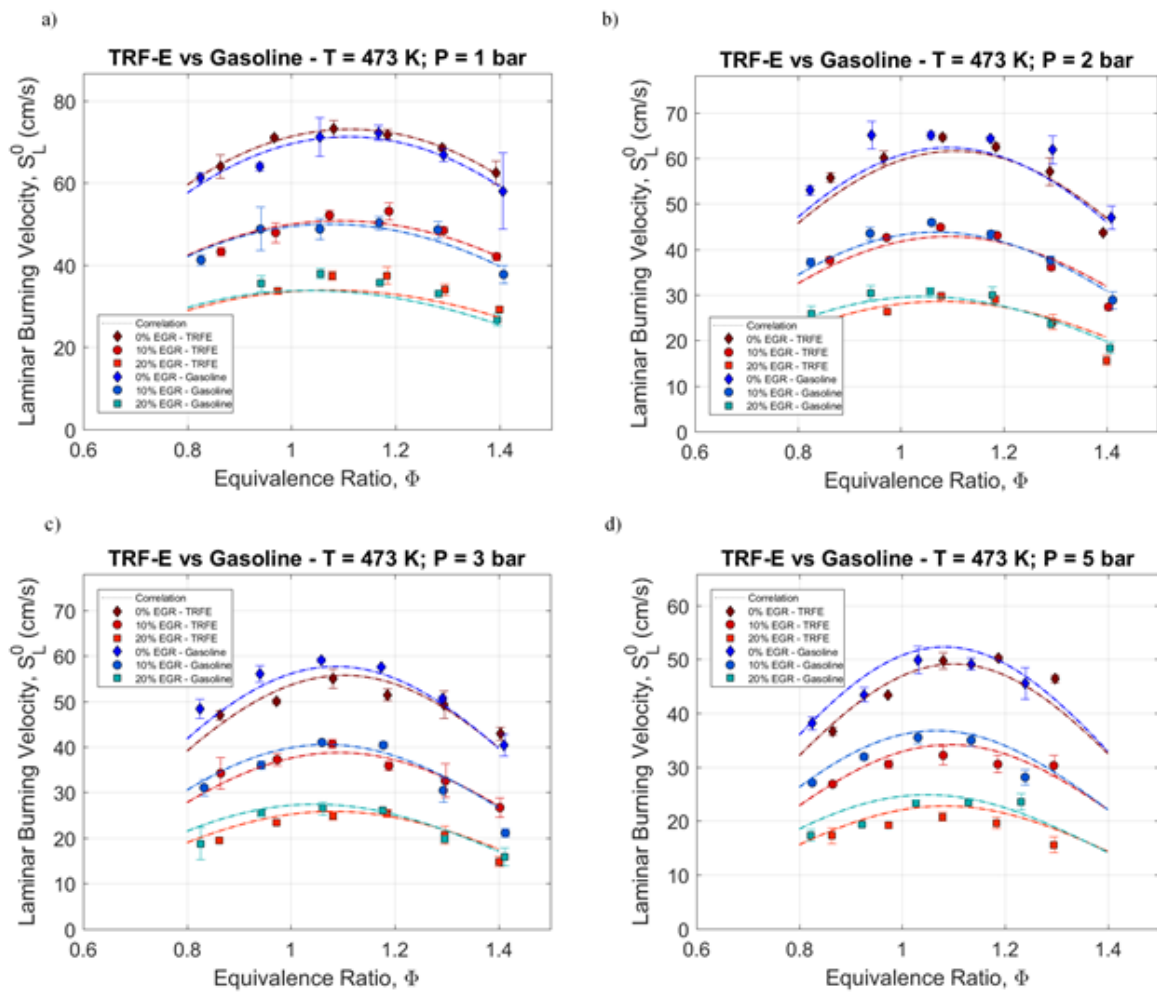


Figure 66. TRF-E and gasoline unstretched laminar burning velocities comparison at different pressure values (Figures a, b, c, d) and fixed temperature ( $T = 473$  K) for three dilution rates.

Figure 66 displays the laminar burning velocities of the two fuels for all different investigated pressures by varying the dilution rate at fixed temperature ( $T = 473\text{ K}$ ). Increasing EGR rate produces an opposite effect with respect to the previously discussed temperature reduction. Therefore, the leaner is the gasoline mixture, the less it is influenced by the increase of dilution. This leads to the trend inversion with respect to temperature case as highlighted in Figure 66 (a-b). This behavior induces an intersection of the two fuels curves, as seen in Figure 66 (b), as the TRF-E is equally affected within all the ER range. For the other graphs, that is, Figure 66 (c-d), this phenomenon is partially hidden by the pressure influence. In fact, increasing pressure decreases significantly the flame propagation velocity more strongly TRF-E than the gasoline, independently of the ER (in Figure 66 (d) TRF-E has become slower than gasoline among the whole ER range). As reported in Figure 67 (a-d) the combination of dilution rate and pressure increase leads to an appreciable difference between the flame propagation velocities of the two fuels for lean mixtures. On the contrary, this discrepancy is less evident for increasing  $\phi$  values. The gap between the two fuels is quantified in Figure 67, where the dependency on the ER is also put in emphasis.

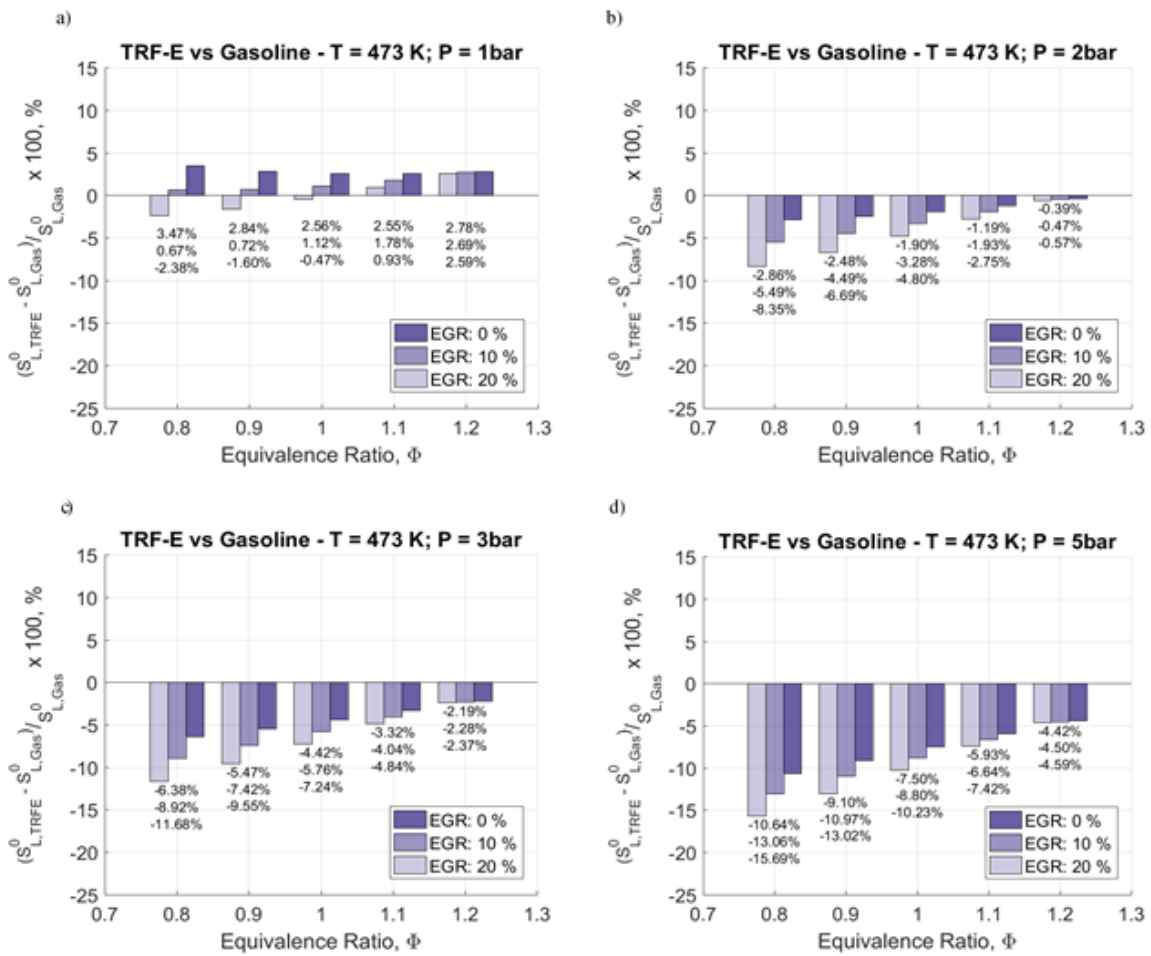


Figure 67. TRF-E and gasoline unstretched laminar burning velocities difference at different equivalence ratio for increasing pressure (Figures a, b, c, d) and dilution (EGR = 0, 10, 20 %) at fixed temperature ( $T = 473\text{ K}$ ).

The mathematical correlation, as observed in the graphs reported in the present section, leads to quite precise results evidencing a good predictability of the fuels behavior. As expected, the hardest conditions underlie the largest discrepancies, that is, high pressure or high dilution rate or the combination of both (Figure 66 (d)). The optimized coefficients are reported in Table 7, for both the 1-step and the 2-step coefficients. The fact that the gasoline and TRF-E coefficient are significantly close supports the appreciable properties of the TRF-E as gasoline surrogate. This is also confirmed by the accordance of the experimental data under the great part of the investigated conditions, evidencing large discrepancy in the unstretched flame propagation velocity values only under the hardest condition (high dilution and pressure and low equivalence ratio). Anyway, this gap is limited to ~15 % in the worst cases (see Figure 67 (d)).

## 4.6. TRF-E EXTENDED CONDITIONS

Once the direct comparison between the gasoline and its surrogate was performed and critically analyzed, the experimental conditions matrix was extended for the TRF-E in order to increase the mathematical correlation precision and enlarge the data availability for future kinetics model improvement or simulations, by adding temperature variation. All data are plotted in Figure 68 and for sake of clearance, the temperature and dilution variation curves are reported for each different considered pressure. This approach points out some limitations on the database, due to some ignition problems (as example, at high dilution rate) or during the post-processing, the limitation of the meaningful radii to avoid thermo-diffusive instabilities or problem of flame cellularity for rich mixture at high pressure, as it can be seen in Figure 68.

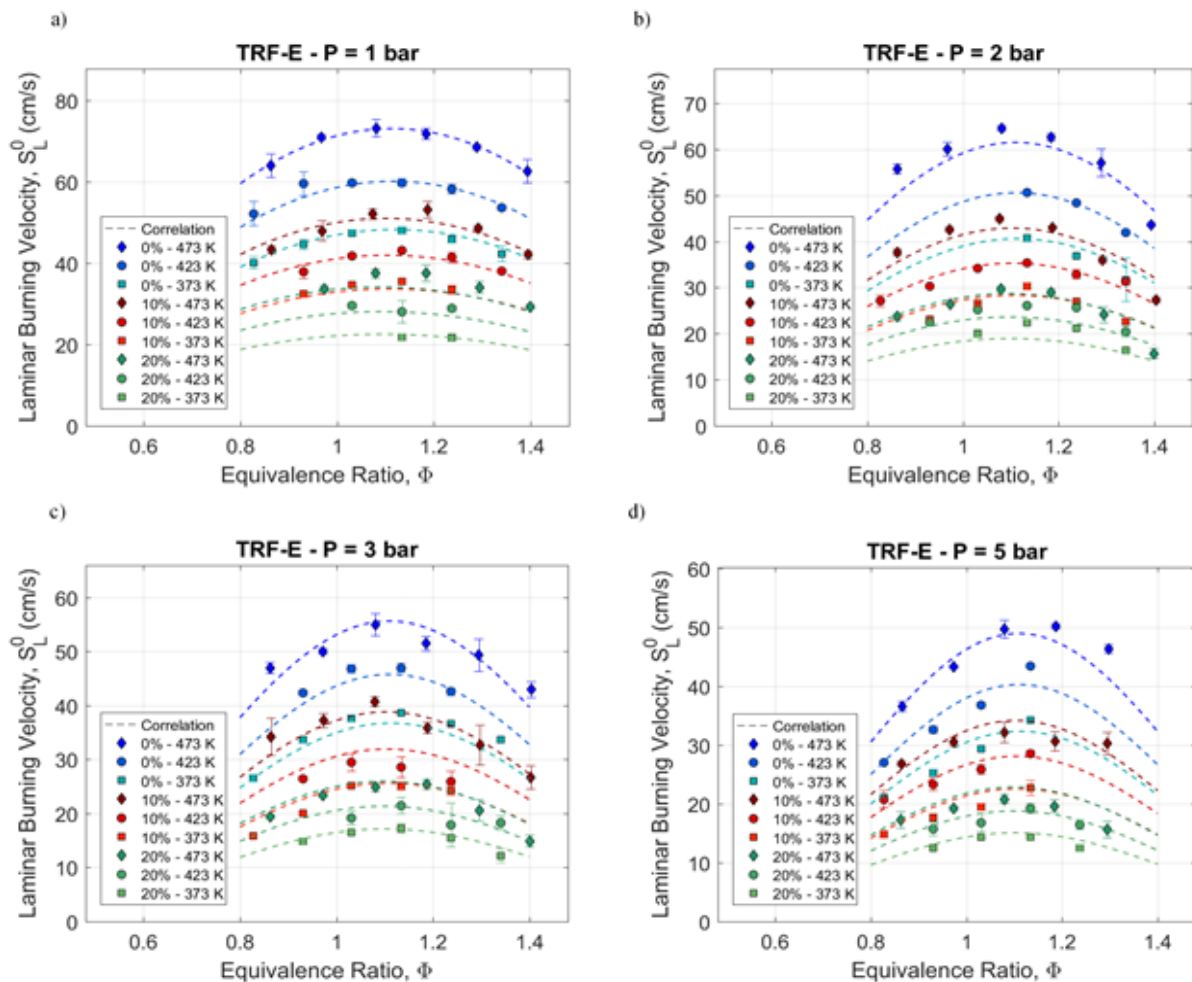


Figure 68. TRF-E laminar burning velocity comparison at different pressure values (Figures a, b, c, d), switching both temperature ( $T = 373 - 423 - 473$  K) and dilution percentages (EGR = 0 - 10 - 20 %).

Even if the consequence is that the most of data are for lean mixtures a, the correlation is in a very good agreement with the experimental data even though a not negligible overestimate is observed for 10 and 20 % dilution rate at 3 and 5 bar when the temperature is 423 or 473 K (Figure 68 (c), 71 (d)). On the contrary, lower pressure (i.e. 1 and 2 bar) leads to a slight underestimate for 20 % of dilution rate (Figure 68 (a), 71 (b)). Table 8 presents the coefficients of the correlation obtained at fixed temperature but with pressure and dilution variations and the ones computed by taking also into account temperature variations.

Figure 69 summarizes the differences in terms of absolute error between the laminar burning velocity estimate thanks to the correlation and the experimental data. The bars height and color proportionally indicate the relative error (in %). Each combination of dilution and pressure is reported for the three equivalence ratios (1.0, 1.1, 1.2). Figure 69 (a) illustrates the fitting quality at  $T = 373\text{ K}$  in which the major differences are obtained for 2 bar, 20% dilution and 5 bar, 10% dilution. Beside these cases, the error is limited to 6-7%. On the contrary, at  $T = 423\text{ K}$ , the error at low (10%) or zero dilution is lower except at 2 bar ( $\phi = 1.2$ ) and 3 bar ( $\phi = 1.1 - 1.2$ ). At 20% and a pressure higher than atmospheric one, the error remains around 10%. For  $T = 473\text{ K}$ , the reference temperature, the error is low (less than 6%) except at 20% dilution and 1 bar and 5 bar (for all equivalence ratio) as indicated in Figure 72 (b).

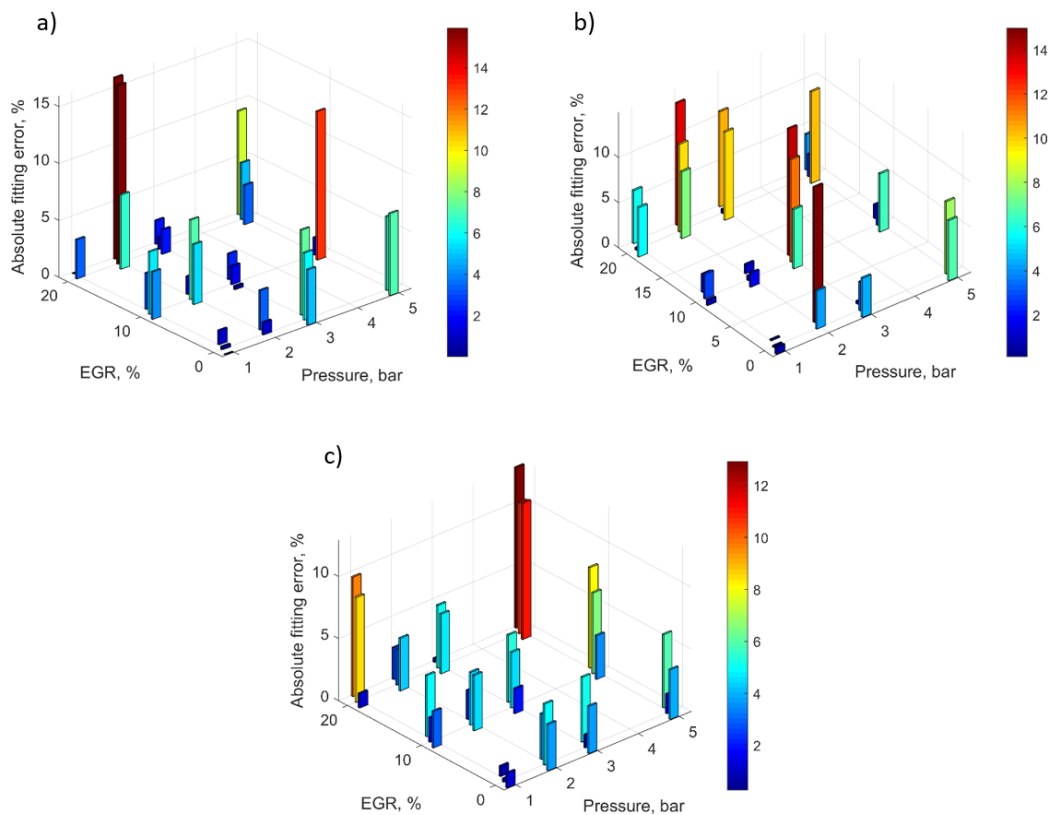


Figure 69. The relative value of the error (in %) between the experimental and the correlation predicted values as a function of pressure and dilution rate. a)  $T = 373\text{ K}$ , b)  $T = 423\text{ K}$ , c)  $T = 473\text{ K}$ . Both color and height of the bar are representative of the %. At each point, three bars are plotted corresponding to 1, 1.1 and 1.2 ER.

## 4.7. VALIDATION OF NOSE LAMINAR CONFIGURATION

To perform experiments in NOSE at laminar configuration, presented in Section 3.4, it is possible to enlarge the initial conditions range, in terms of temperature and pressure, even if the main drawback could be the effect of the mean vertical flow on the flame shape evolution. Typically, the flame initially spherical, is then flattened by the surrounding fresh gases motion. Last, the flame becomes elongated due to the beginning of the piston expansion. Besides this, the radii range to estimate flame propagation speed is also drastically reduced due to smaller optical access (window diameter of 36 mm versus 70 mm in the spherical vessel) and the lower volume of the combustion chamber itself. Therefore, the experiments cannot be done in order to obtain accurate data in the case of lean flames at high pressure for dilution rate higher than 10%.

Figure 70 shows an example of this limit at initial conditions of 21 bar, 525 K and 20% EGR. In order to be consistent with the assumed thermodynamic ambient conditions, the considered radii range must be limited by the users at relatively small radius. On the other hand, to consider the specificity of the non-spherical shape, a dedicated post-process was used. Figure 70 (a) and (b) show an example of this approach: four radius estimates were determined based on the perimeter, the area, the volume (thanks to the two side views of the flame) and the maximum and minimum radius of the ellipse as a better representation of the flame shape. These last two radii can be considered as the maximal and minimal errors from the equivalent spherical radius estimation. Even in critical conditions as the case in Figures 73, in which the flame is strongly flattened by the surrounding flow, the different radii estimates are consistent and within the minimum and maximum fitted ellipse radii values. The main difference is with the equivalent volume radius at first stages of flame propagation. Therefore, the flame radius  $R_S$ , considered for the flame propagation speed estimation is the one based on the volume evaluation, that enables to represent the flame propagation as seen in both views. Moreover, this equivalent ratio, after the threshold of  $R_{min} \sim 4 - 5$  mm is well centered with respect to the minimum and maximum fitted ellipse radii values, justifying the consistency of the shape approximation.

In order to validate the use of NOSE in laminar configuration, first tests were performed at low pressure, i.e. 5 bar and 473 K to compare with the data from the spherical vessel. In Figure 71, the unstretched laminar burning velocity from both experiments is plotted as a function of the equivalence ratio for two cases of dilution, i.e. 10 and 20%. As for this condition, there are no aforementioned experimental limitations, the maximal radius can be fixed at the limit suggested by Burke et al. [133], as already discussed in Section 3.1.1. This value was set to 12.5 mm for NOSE combustion chamber. On the other hand, as the conditions used in NOSE experiments are quite far from the one used by Galmiche [30] for the ignition effects study, the spark release could differently affect the first instants of flame propagation in NOSE set-up. Especially, slow flames may probably absorb the spark release energy during a relative long time still having an equivalent radius lower than 5 mm. By considering, as limits, 5 mm for

$R_{min}$  and 12.5 mm for  $R_{max}$ , it can be noted that a good agreement is obtained between the values obtained in both set-ups, especially at 10% dilution case, validating the use of NOSE for laminar purpose.

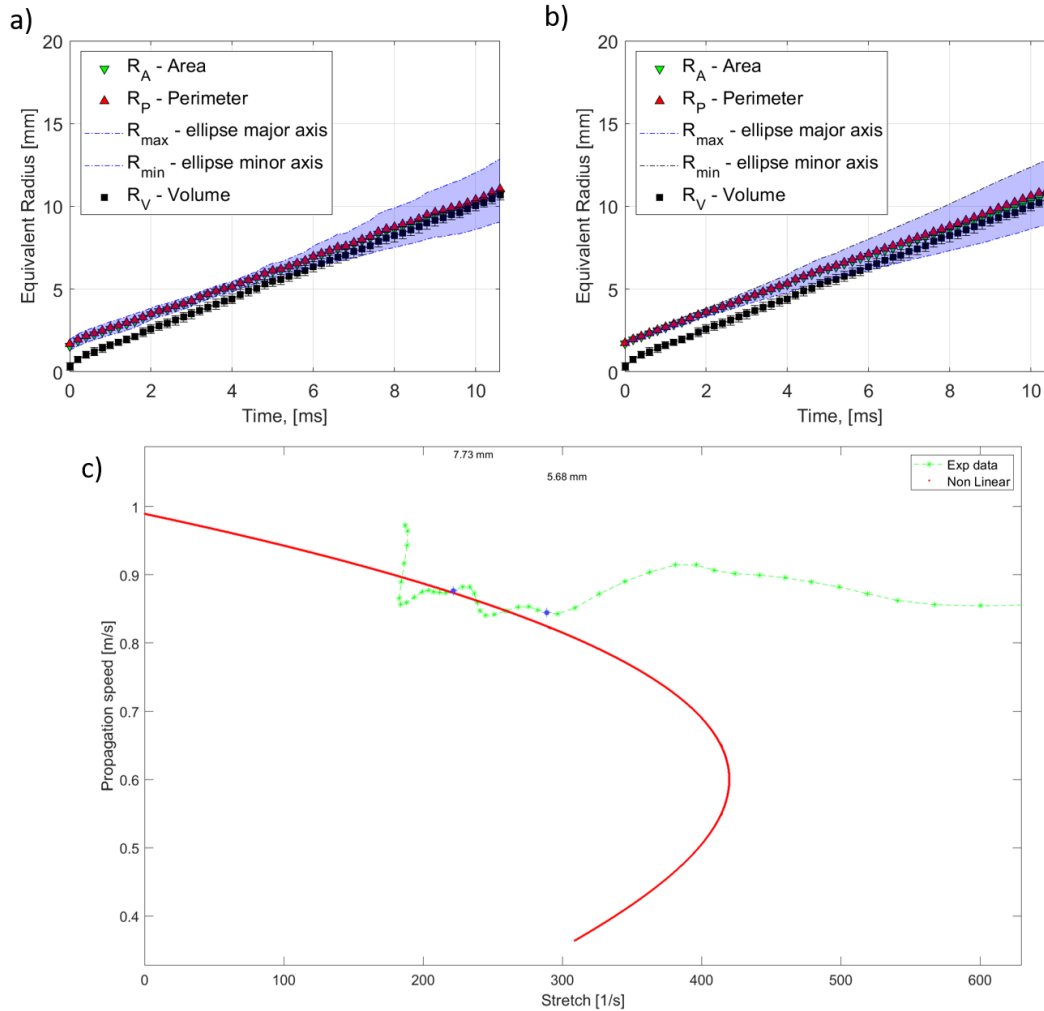


Figure 70. Temporal evolution of the radius from left (a) and right (b) DVS image and evolution of propagation speed as a function of stretch rate (c).  $P = 21$  bar,  $T = 525$  K,  $EGR = 20\%$ ,  $ER = 1.1$ .

Last, a comparison with data obtained with NOSE at 21 bar and the values obtained by kinetics simulation thanks to the kinetics mechanism currently under development in MACDIL project (under publication) confirms the accuracy of the data obtained with NOSE, as shown in Figure 72 (a). Furthermore, Figure 72 (b) evidences the appreciable prediction of the mathematical correlation developed on the spherical vessel in the present work, even at very high pressure (21 bar) in comparison to atmospheric case. The mathematical correlation was improved by taking into account the results obtained with NOSE set-up, the corresponding new coefficients are then presented in Table 9.

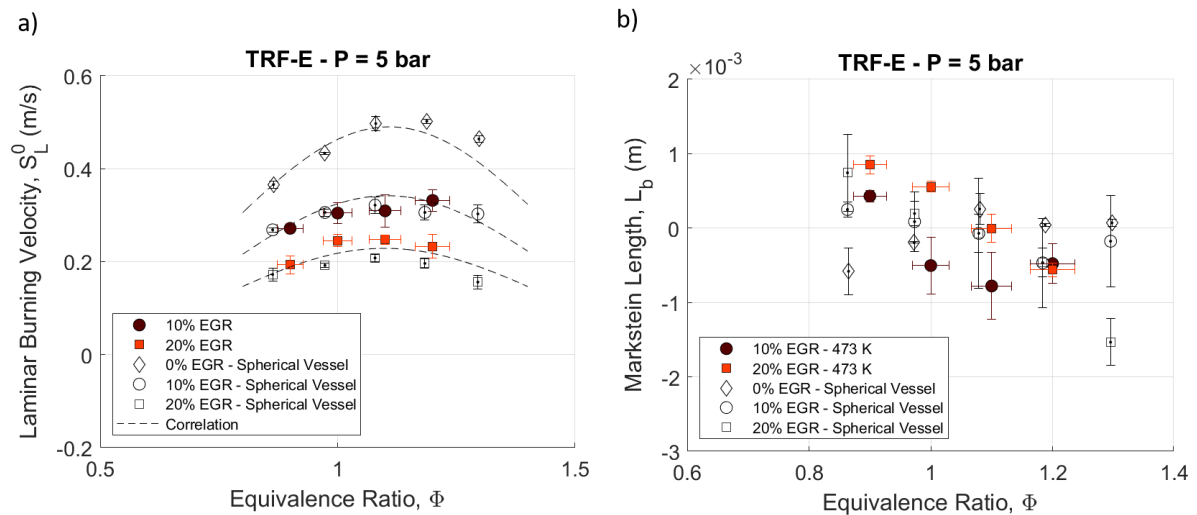


Figure 71. Comparison between unstretched laminar burning velocities estimated in the spherical vessel and in NOSE (color symbols) as a function of the equivalence ratio and different dilution rates.  
 $P = 5 \text{ bar}$ ,  $T = 473 \text{ K}$

In Figure 73, the predicted values from the correlation (improved one and previous one) are compared to the experimental values obtained in NOSE at 21 bar while Figure 74 presents the estimated Markstein lengths. The new correlation better fits the experimental points but with always an underestimate. The best prediction is at low dilution rate and reference temperature (423 K). Figure 75 highlights the limitation of the prediction as a function of the dilution rate: at 30% there is no overestimation of the laminar burning velocity. But the experimental data have to be considered carefully as under high ambient pressure conditions, reproduced in NOSE, the cellularity phenomenon strongly limits the experimental range. As example, for 10% dilution, the flames at  $\phi = 1.2$  are too cellular since first instants to extract flame propagation speed estimate from the radius data. On the contrary, for 20% dilution, the cellularity arises later but still a low flame propagation radius, limiting the exploiting range. This can be seen in the images presented in Figure 76 in which two flames with 20% dilution are presented: the first (top) at  $\phi = 1.2$  exhibits strong cellularity when the flame radius is still relatively low; the second one (bottom) at  $\phi = 1.0$  exhibits the ellipsoid-like shape thanks to the lower  $\phi$  and the higher temperature. Similarly, Figure 77 at 525 K, shows the positive effect of dilution rate on cellularity insurgence: the first image (top) at  $\phi = 1.2$  and 20% dilution exhibits early cellularity arising even if in a less severe way with respect to the case at lower temperature (Figure 76 (top)); the second image (bottom) at  $\phi = 1.2$  and 30% exhibits the ellipsoid-like shape thanks to higher dilution rate. Anyway, flames at lower temperature than 525 K do not offer meaningful radii ranges at 30% dilution since they burn too slowly, exceeding the “constant conditions” *plateau* limits.

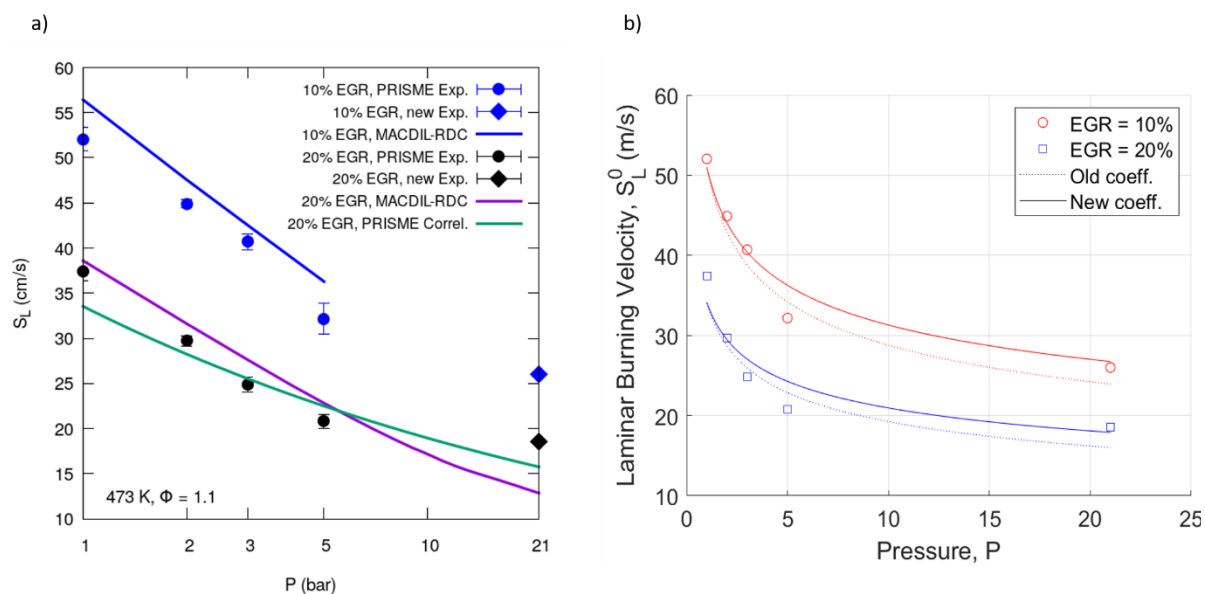


Figure 72. (a) Comparison between the experimental laminar burning velocities (the data at 21 bar is obtained with NOSE set-up and the other ones in spherical vessel) and the simulated ones thanks to kinetics mechanism under development (MACDIL project) (b) Improvement of the mathematical correlation by taking into account the estimate of laminar burning velocity at 21 bar (reference temperature and equivalence ratio).

Table 9. Mathematical correlation coefficients (relative to the laminar burning velocity) for TRF-E fuel obtained using the spherical vessel experimental data (first series) and refined using the high pressure and temperature measurements performed on NOSE (second series). Coefficients A, B, C refer to the equivalence ratio fitting equation at reference conditions.

Coefficient	Optimized value – TRF-E (spherical vessel tests)	Optimized value – TRF-E (with NOSE High Pressure and Temperature tests)
A	73.0208	73.0208
B	3.5315	3.5315
C	-138.1265	-138.1265
$\alpha_0$	1.7495	1.7890
$\alpha_1$	-0.1010	-0.0971
$\beta_0$	-0.2481	-0.2121
$\beta_1$	0.0232	0.0491
$\beta_2$	-1.7739	-1.7834
$\gamma_0$	3.4143	3.4070
$\gamma_1$	0.4252	0.4312

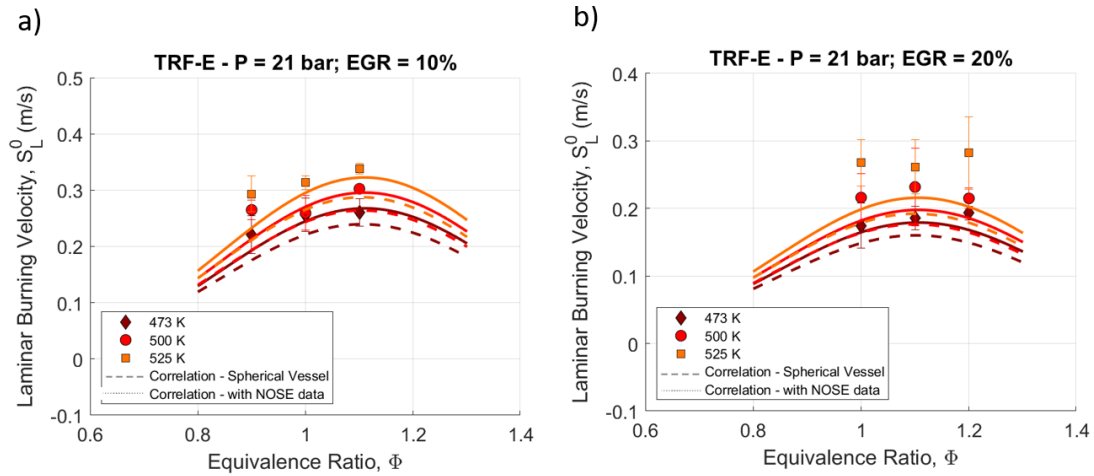


Figure 73. Laminar burning velocity measured in NOSE and predicted values from the correlation at 21 bar for 3 initial temperatures (a) EGR = 10%, (b) EGR = 20%, and for 3 dilution rates

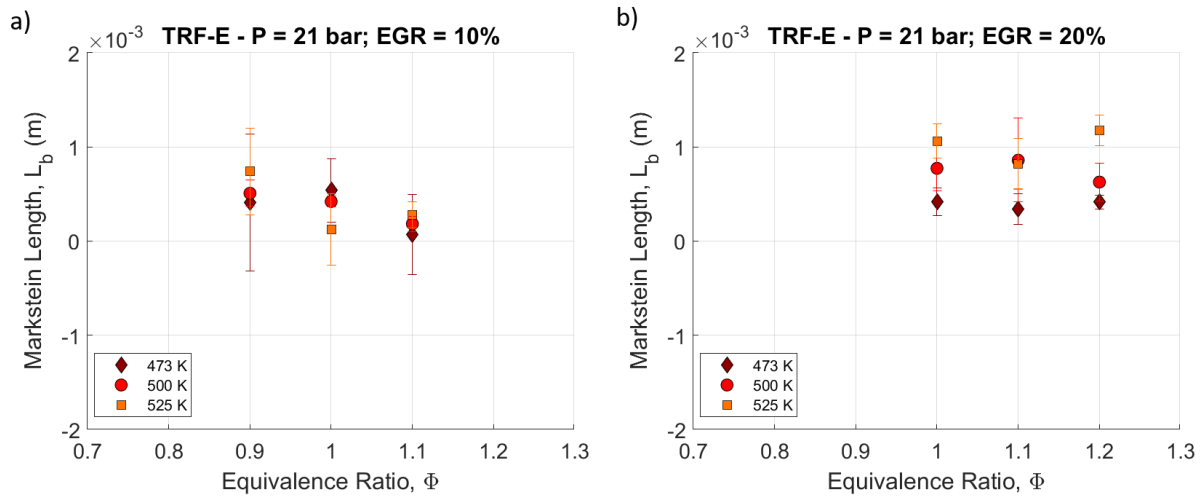


Figure 74. Markstein length derived from NOSE laminar configuration tests: (a) EGR = 10%, P = 21 bar and comparison between three different temperatures; (b) EGR = 10%, P = 21 bar and comparison between three different temperatures. Points at 1.2 equivalence ratio are altered by strong and early arise of cellularity.

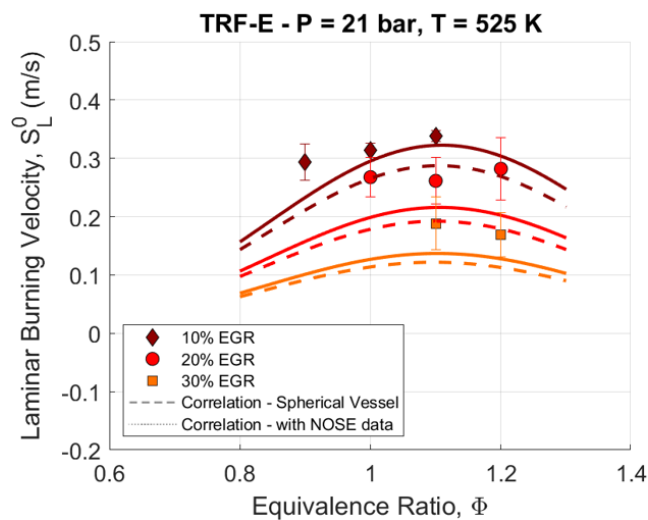


Figure 75. P = 21 bar and T = 525, EGR ranges from 10 to 30%.

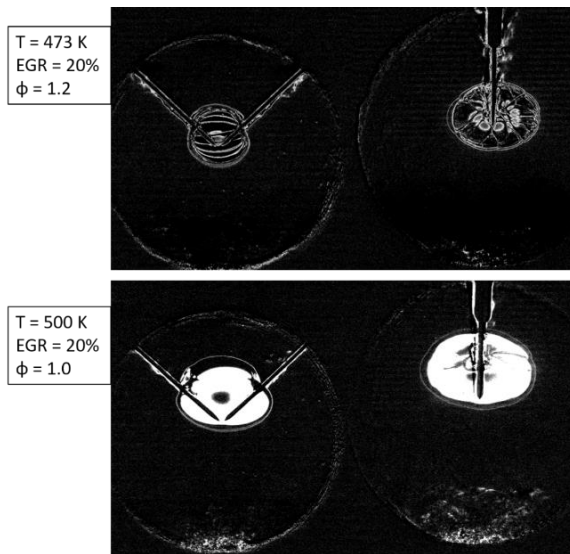


Figure 76. Example of laminar flame visualization in NOSE a) early arise of intense cellularity due to rich mixture b) ellipsoid-like geometry evolution for a leaner mixture.

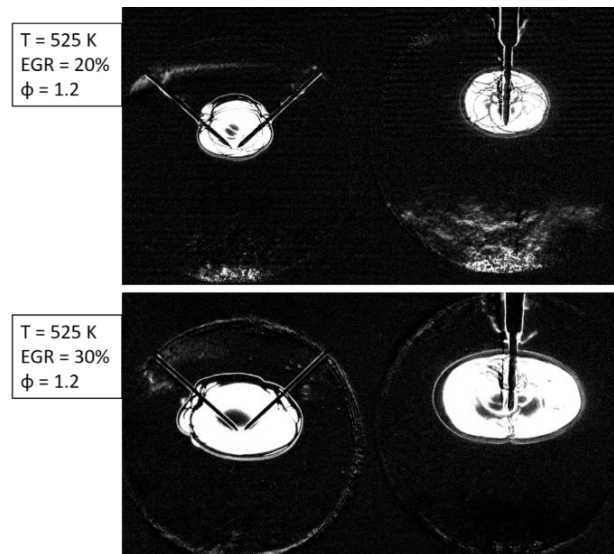


Figure 77. Example of laminar flame visualization in NOSE a) early arise of intense cellularity due to rich mixture b) ellipsoid-like geometry evolution due to the increase of dilution rate.

## 4.8. CONCLUSIONS

In the present chapter a wide database is set up for a pure gasoline (B71 1188 ESSH EURO5 +20, RON 96.6 MON 86.2, Ethanol 5% vol) and its four-components surrogate named TRF-E. Markstein lengths of the two fuels were also analyzed and compared. It was found that the Markstein length trend is similar over an appreciable range of experimental conditions. The comparison lacks in precision just at relatively high values of pressure. In fact, at 3 bar, and for rich mixtures, negative Markstein lengths can be observed for both fuels with large error bars. In addition, at 5 bar the direct comparison of the Markstein length is even more complex due to the uncertainties in the determination of the gasoline Markstein length at 10% or 20% dilution. Despite this, dynamic behavior of the two fuels (i.e., propagation speed dependence on stretch rate) is similar. Moreover, it was observed a good agreement of the laminar burning velocity values. Over a wide range of pressure, dilution and temperature, the difference in laminar burning velocity between gasoline and TRF-E is limited at  $\sim 15\%$  for the worst case (5 bar, 473 K, 20% EGR and 0.8 equivalence ratio). In general, the major divergence between the behavior of the two fuels is caused by the pressure increase. The effect of dilution is low, highlighting the fact that the TRF-E can replicate the gasoline properties at high dilution rate. Temperature variation, as well, has a similar effect on both the fuels even if a dependence on the equivalence ratio was observed. In fact, it was found out that for  $\phi > 1$  the TRF-E properly follows the gasoline response to pressure, temperature and dilution variations. On the contrary, for lean mixtures the differences are accentuated. As a consequence TRF-E is an acceptable surrogate for the examined gasoline. Anyway, it has to be remarked that a further increase in pressure (with respect to the investigated 5 bar) may lead to non-negligible difference in laminar burning velocity, in particular for lean mixtures.

The gathered data permitted to determine the optimized coefficients of the well-known mathematical correlation proposed by Metghalchi and Keck [131] and extended by Galmiche et al. [69] to include the dilution rate with an acceptable precision even under experimental conditions far from the reference ones. A further step in this direction is represented by the extended experimental grid for the TRF-E that allowed to additionally refine the optimized coefficients. Moreover, the thoroughness of the investigated experimental points yields an optimal pool for the future development of highly refined chemical kinetic mechanisms. In fact, the database includes not only range of each fundamental parameter (temperature, pressure, dilution rate and equivalence ratio) with respect to the reference conditions, but also a total combination of all their different values within the investigated ranges. The correlation error with respect to the experimental points was evaluated, leading to the conclusion that a good agreement generally exists among the great part of the investigated conditions.

Next step consisted in validating NOSE laminar configuration by exactly replicating the same experimental conditions realized on the spherical vessel and performing a direct comparison. A pressure of 5 bar and a temperature of 473 K represent the thermodynamic conditions replicable on both the set-

ups. It was observed that the results obtained on NOSE are in good agreement with those obtained on the spherical vessel, even if NOSE flames are evaluated on shorter radii range and exhibit an ellipsoid-like shape. To take into account the latter phenomenon the volume-based equivalent radius was used for flame propagation speed extrapolation on NOSE, using the two images obtained with the DVS.

Once experimental measurements on NOSE were validated, the experimental points at high pressure (21 bar) were taken into account. It was observed that the calculated laminar burning velocities are consistent with the kinetic model developed in the context of the MACDIL project, just by using the spherical vessel results. Moreover, high pressure points are well predicted by the mathematical correlation developed through the measurements obtained on the spherical vessel. Natural follow-up consisted in refining the mathematical correlation with the high pressure points, investigated at three different temperatures (473, 500, 525 K) and different dilution rates (10%, 20% and also 30% for the case at 525 K). The result is an improved mathematical correlation that correctly predicts the change in pressure even far from the  $P_{ref}$ . Limits of this model arise when, together with pressure increase, more than two parameters change significantly with respect to the reference ones, that is, temperature from 473 K, dilution from 0% and equivalence ratio from 1.1.



---

## **5. Results: Turbulent Flames**

---



## 5.1. INTRODUCTION

The investigation of turbulent flames was carried out thanks to both, the spherical vessel and the NOSE setup, as for the laminar flame study. While for laminar cases, the difference between results obtained in both experimental set-ups is mainly due to the different thermodynamic conditions, for the turbulent flame cases, it would be mainly to the turbulent properties themselves. More than one hundred conditions have been investigated, all detailed parameters are given in ANNEX D (Table 2, Table 3 and Table 4) and are indicated in the Figure 78 thanks to the Borghi-Peters diagram. It has to be noted that a wide range of  $Da$  values is obtained thanks to both set-ups but some similar conditions for  $Da$  and  $Re$  can be reached in both set-ups and that the flames in NOSE set-up will interact with very small Komogorov eddies (around  $5 \mu\text{m}$  in comparison to  $15 \mu\text{m}$  in spherical set-up). The classic effect of the equivalence ratio variation is visible in the Karlovitz change: from leaner mixture, the Karlovitz number decreases and then increases for richer conditions as it can be seen in Figure 78, as the size of symbols is proportional to the equivalence ratio. It is necessary to remember that the Reynolds number used on the Peters-Borghi diagram is usually the one that refers to laminar flame, given by  $Re_L = \frac{u' L_T}{s_L^0 \delta_L^0}$ .

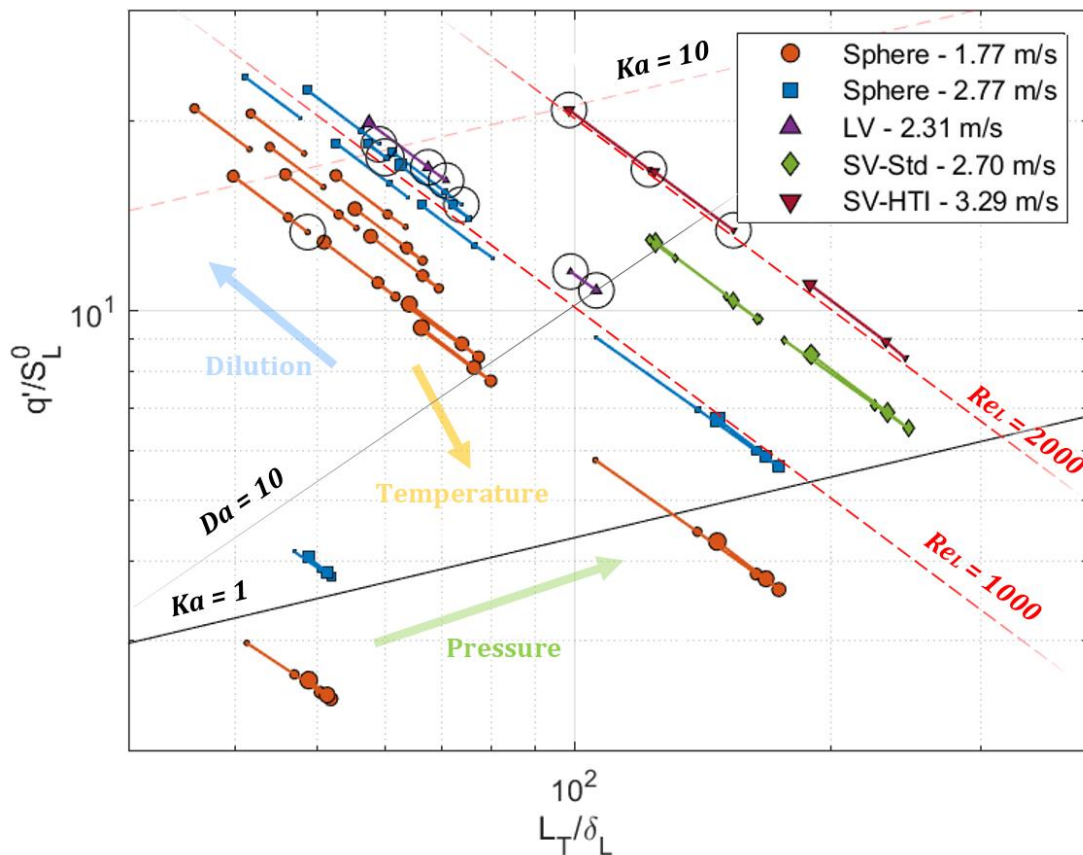


Figure 78. All investigated experimental data in Peters-Borghi diagram. Size of symbol proportional to the equivalence ratio. Circle markers indicate the flames slowed down during their evolution.

As for laminar flame studies, the Double-View Schlieren was set-up to record the flame evolution. Some examples of flames are presented in Figure 79, it can be seen that for some cases, some flame fragments or pockets can be distinguished. The continuous insurgence of these phenomena during the flame propagation leads to a kind of erosion of the flame hindering its propagation. It will be shown in the following sections that it happens in particular for  $q'/S_L^0 > 10$  and  $L_T/\delta_L^0 > 50$ , in the case of high turbulent intensity combined with low temperature or high diluted mixtures. These particular conditions are indicated by circles in Figure 78. Limit cases could verify when the flame surface is strongly fragmented, as shown in Figure 80, but the turbulence is not enough intense to stretch the flame front until local extinction. This yields to false the contour detection as the presence of pockets can increase the observed contour (see Figure 81). One case in which this was verified corresponds to the spherical vessel configuration at  $P = 5$  bar,  $T = 343$  K,  $EGR = 25\%$  and  $q' = 1.77$  m/s. In this case  $\frac{d^2R_S}{dt^2} > 0$ , so even if the dominant phenomena actually hinder the flame propagation, this visualization by Schlieren technique gives an overestimate of  $V_T(R_S)$ .

As pointed out by Bradley et al. [58] and recently discussed by Brequigny et al. [90], as the Schlieren technique overestimates  $R_p$  in comparison to the radius obtained from laser tomography technique, a correction factor has to be used to provide data independent to the measurement techniques. But due to the high ratio of  $q'/S_L^0$  (see Table 2, Table 3 and Table 4) and the non-perfect sphericity of most of flame shape, no correction has been used in the following data of raw radius,  $R_S$ . Moreover, during some 'extreme' conditions, the flames are strongly wrinkled and corrugated by the turbulence with a significant shift of its barycenter from the central position of the combustion chamber, as displayed in Figure 79. To help the knowledge about the flame wrinkling, the ratio between the contour length and the perimeter from the equivalent radius  $R_S$  will be also estimate. Due to the flames shape characteristics, the radii extrapolation from the images requires a different approach with respect to the laminar case. The shape deformation and the barycenter shifting hinder the full observation of the flame propagation and limit the number of available extrapolated radii from one single test. Therefore, to have sufficient statistics, a minimum of 6 tests and a maximum of 10 tests were performed for each condition, as a function of the recorded images quality. Therefore, for each experimental condition, the number of available radii is not the same for the all tests, as illustrated in Figure 82. Therefore, the average of the radius is done by considering all the scattered data within a limited interval of radius (for the spherical vessel, between 5 and 15 mm, for NOSE between 4 and 12 mm) and a fit allows the interpolation of the missing points.

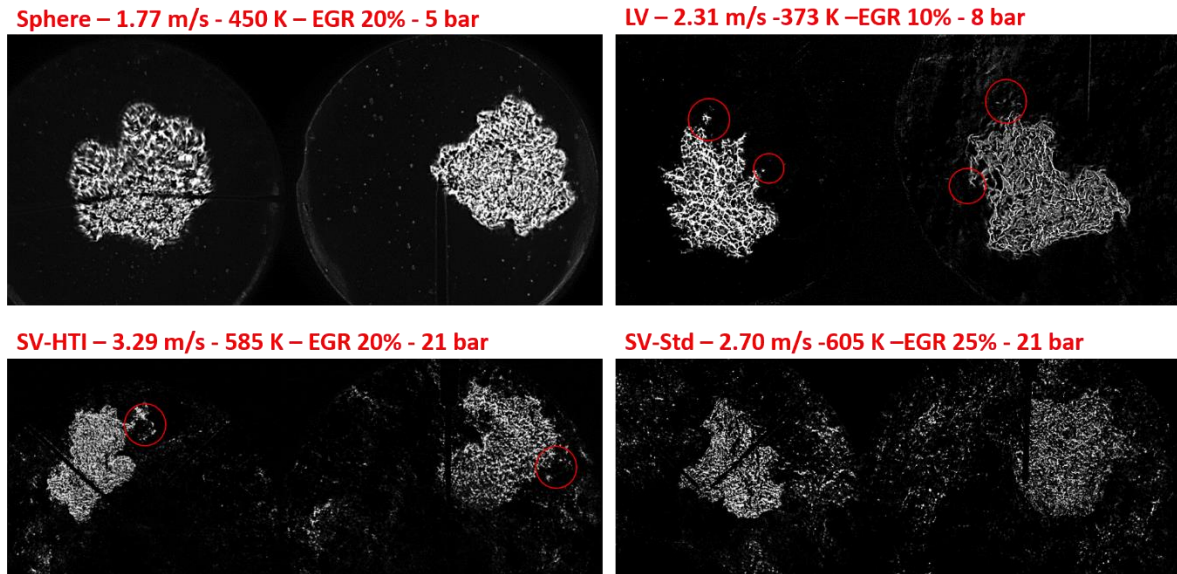


Figure 79. Flames examples for the low turbulent spherical vessel and the three NOSE configurations.

It has to be noted also that for some conditions, the temporal evolution of the radius is slow down, indicated by the negative value of  $\frac{d^2R_S}{dt^2}$  as in Figure 82 (b) and (c). As the temporal growth rate of the radius decreases, the turbulent flame propagation speed,  $V_T$ , will be also reduced as a function of the time. This could be due to the presence of local fragments and detachment of some flame pockets into the fresh gases, certainly to the interaction between small scales of turbulence with the flame front under certain conditions.

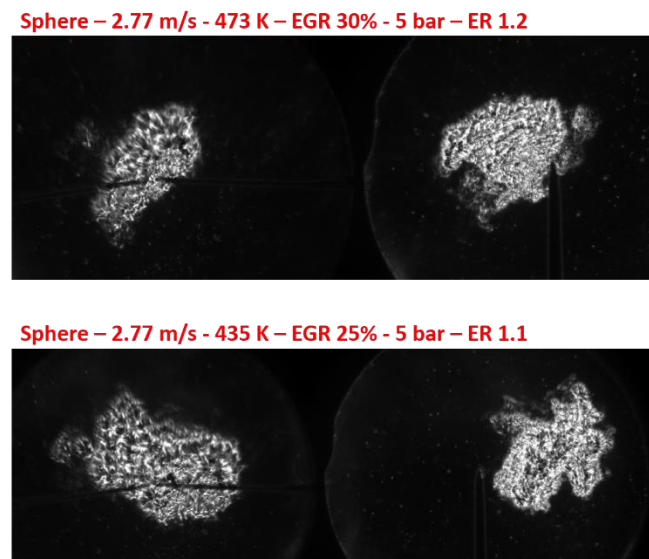


Figure 80. Flames examples - Presence of insurgence of pockets on the flame surface.

Sphere – 1.77 m/s  
 343 K – EGR 25% - 5 bar – ER 1.2

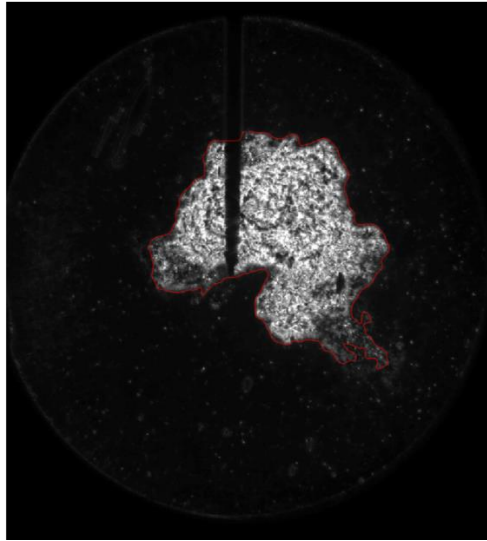


Figure 81. Problem of false contour detection for limit case in low turbulent spherical vessel.

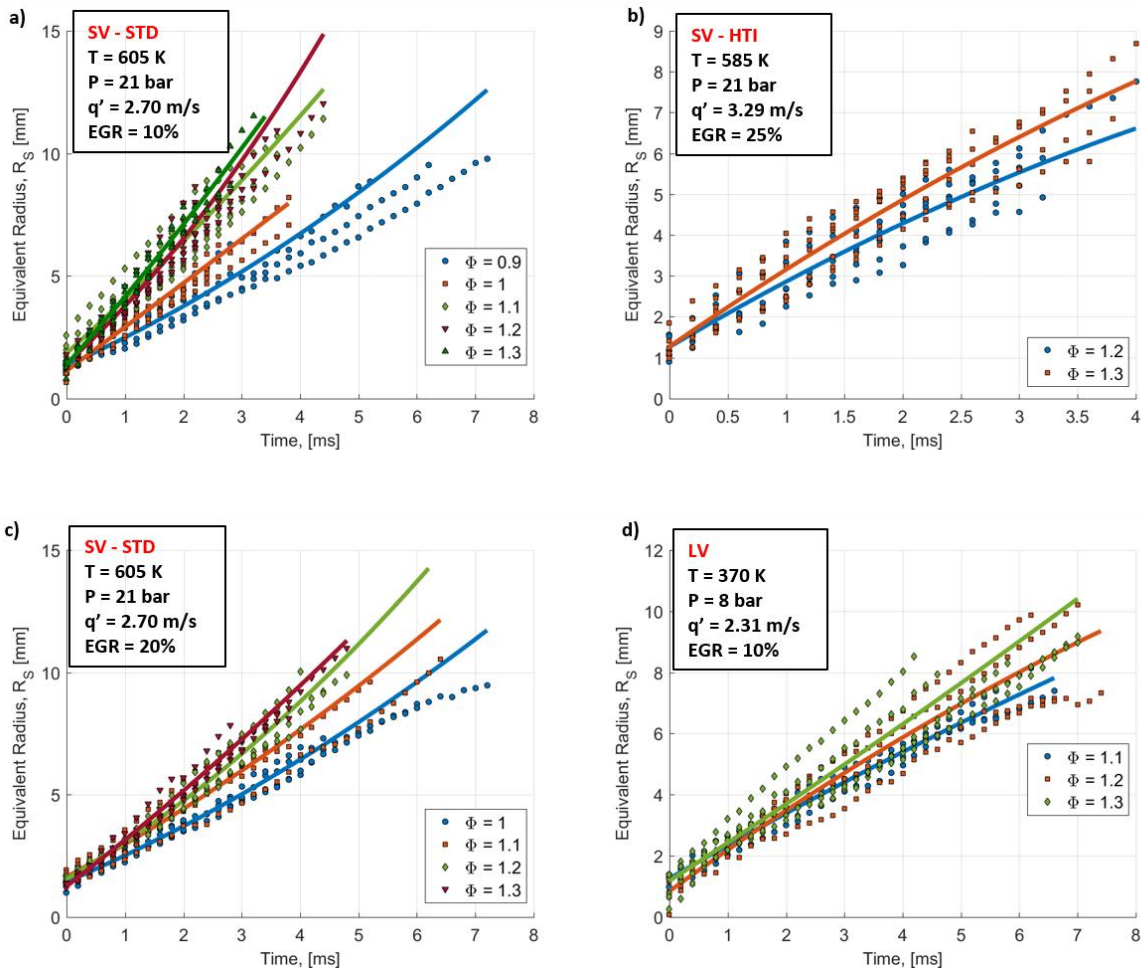


Figure 82. Examples of radii extrapolation, for different cases.

## 5.2. SPHERICAL VESSEL TURBULENT FLAME SPEED

### 5.2.1. Insight on Flame Characteristics

As introduced in the previous section, under certain conditions, the flame front may undergo local fragmentation yielding pockets formation. The appearance and the size of these structures seem to change with the turbulent flow properties. In the spherical vessel, the detected contour may be overestimated if these pockets stagnate on the flame surface. This phenomenon is likely to happen in particular for the low turbulence and high dilution rates (above 25%). In these conditions, moreover, it was observed that flames may undergo to local quenching. Similar quenching phenomena were observed by Wu et al. [83] for high  $q'$  (5.4 m/s) but  $\phi = 0.8$  and no diluent. An example is given in temporal flames evolution reported in Figure 83 and Figure 84. The flame represented in Figure 83 was realized for  $P = 5$  bar,  $T = 423$  K,  $EGR = 20\%$ ,  $\phi = 1.1$  and a turbulent intensity of  $q' = 2.77$  m/s. First, the flame shape is drastically affected by the largest turbulence eddies and during its propagation the flame itself shifts and rotates. In the second image, this phenomenon causes a local thinning of a part of the flame that leads to a subsequent local fragmentation of the flame (as evidenced in the third image). The immediate consequence is a local quenching of the flame.

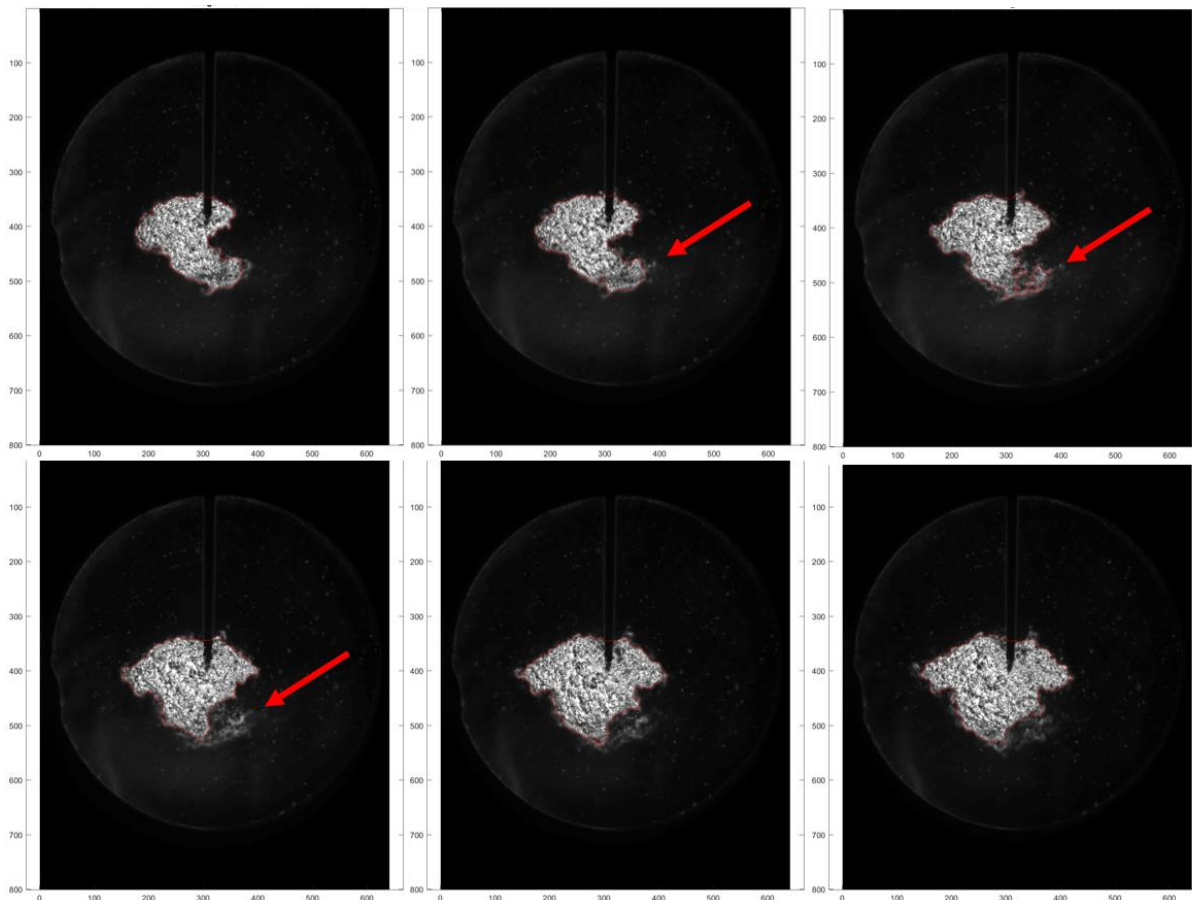


Figure 83. Examples of temporal flame evolution in spherical vessel ( $q' = 2.77$  m/s, integral length 3.4 mm,  $P = 5$  bar,  $T = 423$  K,  $EGR = 20\%$ ,  $ER=1.1$ ,  $Ka=7$ ). Red arrows highlight local detachment and flame quenching.

Similarly, at lower turbulent intensity ( $q' = 1.77 \text{ m/s}$ ), but also lower temperature ( $T = 373 \text{ K}$ ), the flame contour exhibits local fragmentation with detachment of some flame pockets into the fresh gases (see Figure 84). This phenomenon involves both small pockets and consistent portions of the flame, as highlighted in the third image of Figure 84, where it is marked the moment at which a significant part of the flame is detached and blown away. In NOSE, similar phenomena are observed but the resulting pockets are usually significantly smaller, as in Figure 79. Generally, the ensemble of these occurrences invalidates the measurements of flames whose conditions seem to lie in a particular zone of the Peters-Borghgi diagram. As pointed out by Meneveau and Poinso [134] some parametric limits for flames with partial or total quenching may correspond to the correlation  $\frac{q'}{S_L^0} > 4 Re_L^{0.25}$ .

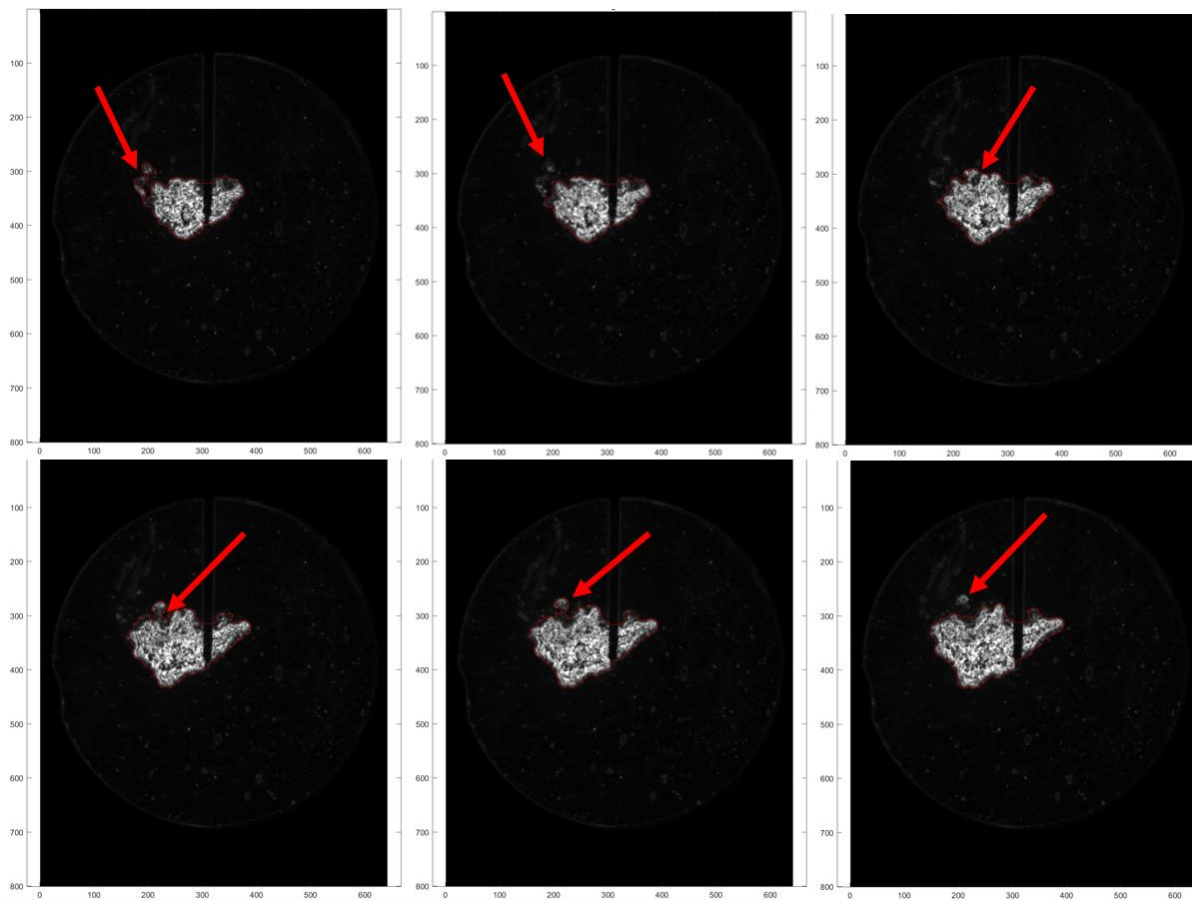


Figure 84. Test realized on spherical vessel ( $q' = 1.77 \text{ m/s}$ , integral length 3.4 mm,  $P = 5 \text{ bar}$ ,  $T = 343 \text{ K}$ ,  $\text{EGR} = 20\%$ , Equivalence Ratio of 1.1 and Karlovitz number about 4). Example of local corrugation of the flame surface. Final instants of a local detachment and quenching of the flame are reported in the first two frames. In the third it appears evident the broken of the flame surface in a significant portion of the volume. This cause a subsequent detachment and local erosion of the flame surface.

### 5.2.2. Reference Cases, Wrinkling Factor and Barycenter Displacement

As reported in Table 2 and Table 3 (ANNEX D), tests performed on the spherical vessel were realized at a pressure of 5 bar, except for 2 reference cases (0% EGR, 1bar) for both turbulent intensities, 1.77 and 2.77 m/s. As well known, the pressure increase affects less the  $Ka$  number than the temperature change. For this reason, to cover a large range of  $Ka$ , a range of temperatures, between 343 and 473 K was investigated for both turbulent intensities, to recover the full range of points achievable in NOSE. The main difference is that, with NOSE, the almost unexplored zone of Peters-Borghgi diagram (as it can be seen in Figure 78) at very high values of  $q'/S_L^0$  and  $L_T/\delta_L^0$  can be investigated. But the comparison for same value of  $Ka$  remains not so evident due to the difference also in integral length values (3.4 mm for spherical vessel, while 2.07 mm for NOSE SV and 2.35 mm for NOSE LV).

Figure 85 shows the results for the reference cases at 1 bar and different  $q'$  (Figure 85 (a) and (b)), compared with an increase of pressure (from 1 to 5 bar, at 0% dilution, Figure 85 (a)) and an increase of dilution (from 0% to 20%, at 5 bar, Figure 85 (d)).

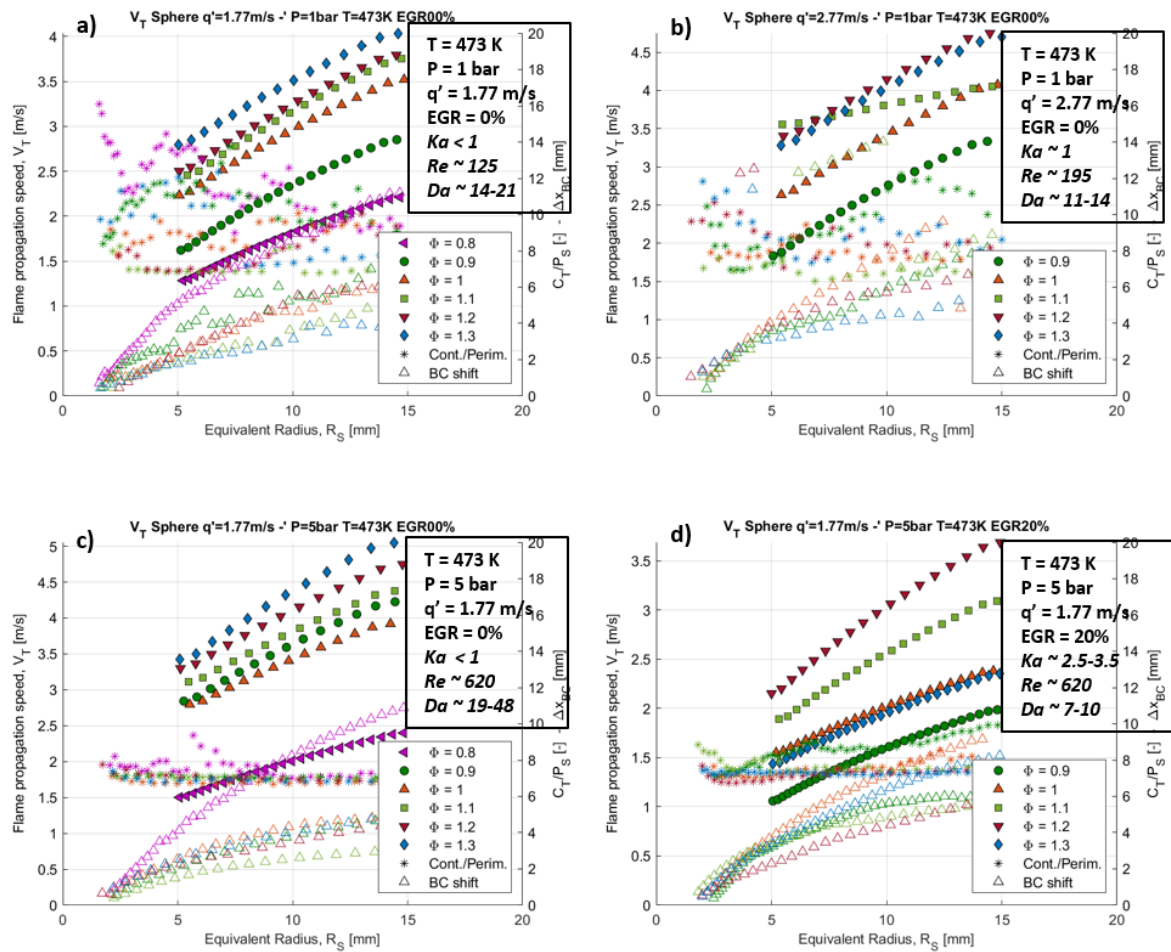


Figure 85. Turbulent flame propagation speed (left y axis), absolute barycenter displacement in the tridimensional domain (x, y, z directions) and ratio of flame contour and perimeter based on the equivalent spherical radius (right y axis) measured on spherical vessel for different experimental conditions.

First observation concerns the dependence of  $V_T$  with the equivalence ratio. But as highlights in Figure 86 for values of  $V_T$  evaluated at a radius of 10 mm, the evolution of  $V_T$  as a function of  $\phi$  is not symmetrical as laminar flame speed but it increases with the equivalence ratio. This increase, however, is less evident once in the rich zone, but it is quite stronger before stoichiometry. As example, at 0.8 equivalence ratio, the resulting mean turbulent speed is almost the half of the maximum one obtained for  $\phi = 1.3$  as can be seen in Figure 86. In the rich side, the dependence of the turbulence flame speed with  $\phi$  is strongly reduced. This trend it was already observed in previous study of Lawes et al. [89] and could involve the effect of the decreasing effective Lewis number, as pointed out by Han and Huh [135].

In Figure 87 and Figure 88, the effect of the dilution rate is evaluated for an initial pressure of 5 bars with turbulent intensity of 2.77 m/s. Without dilution, the increase of initial pressure seems to be benefit for the turbulent flame front (Figure 85). In fact, it promotes the “stabilization” of the wrinkling ratio, ' $C_T/P_S'$ ', approximated here as the ratio between the contour detected and the perimeter given by the equivalent radius. This phenomenon can be observed comparing Figure 85 (a) and (c) and, for higher  $q'$ , comparing Figure 85 (b) and Figure 87 (a). On the contrary, the increase of the dilution rate induces the decrease of the flame wrinkles (Figure 87), so as the  $Ka$  number increases, even if this ratio has to be considered carefully due to the superimposition of 3D flame surface due to the Schlieren technique itself. This is also highlighted in Figure 88, with the plot of the turbulent propagation speed (at  $R_S = 10\text{mm}$ ). Generally, at fixed conditions, the value of the wrinkling factor tends to converge with increasing equivalence ratio. Moreover, the higher the  $\phi$  the less are the oscillations, even if the mean value does not vary significantly.

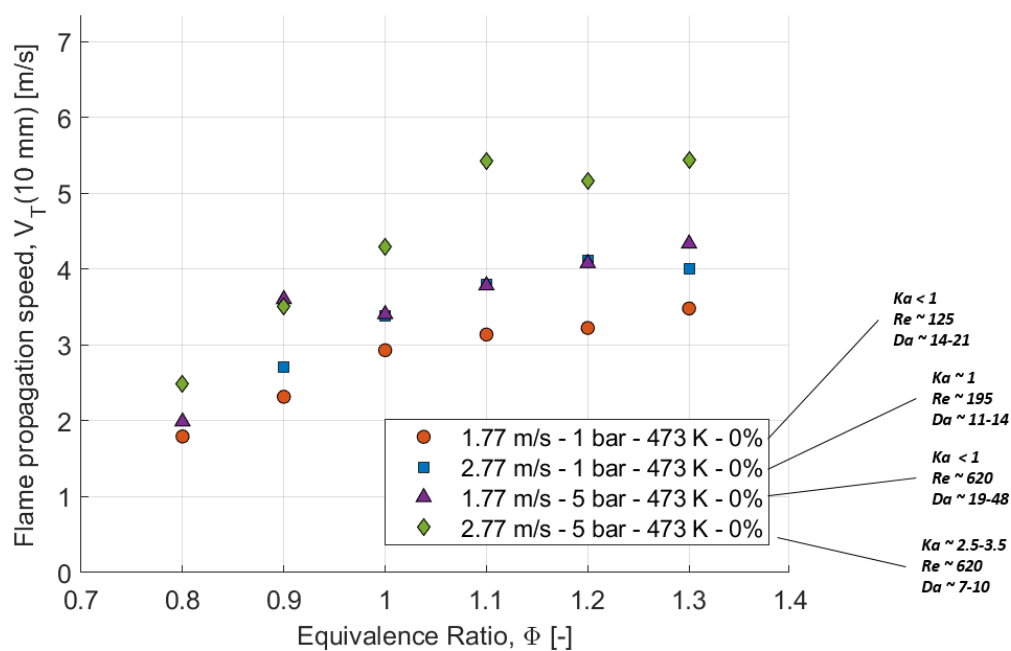


Figure 86 Effect of turbulent intensity and pressure on flame propagation speed at  $R_S=10$  mm.

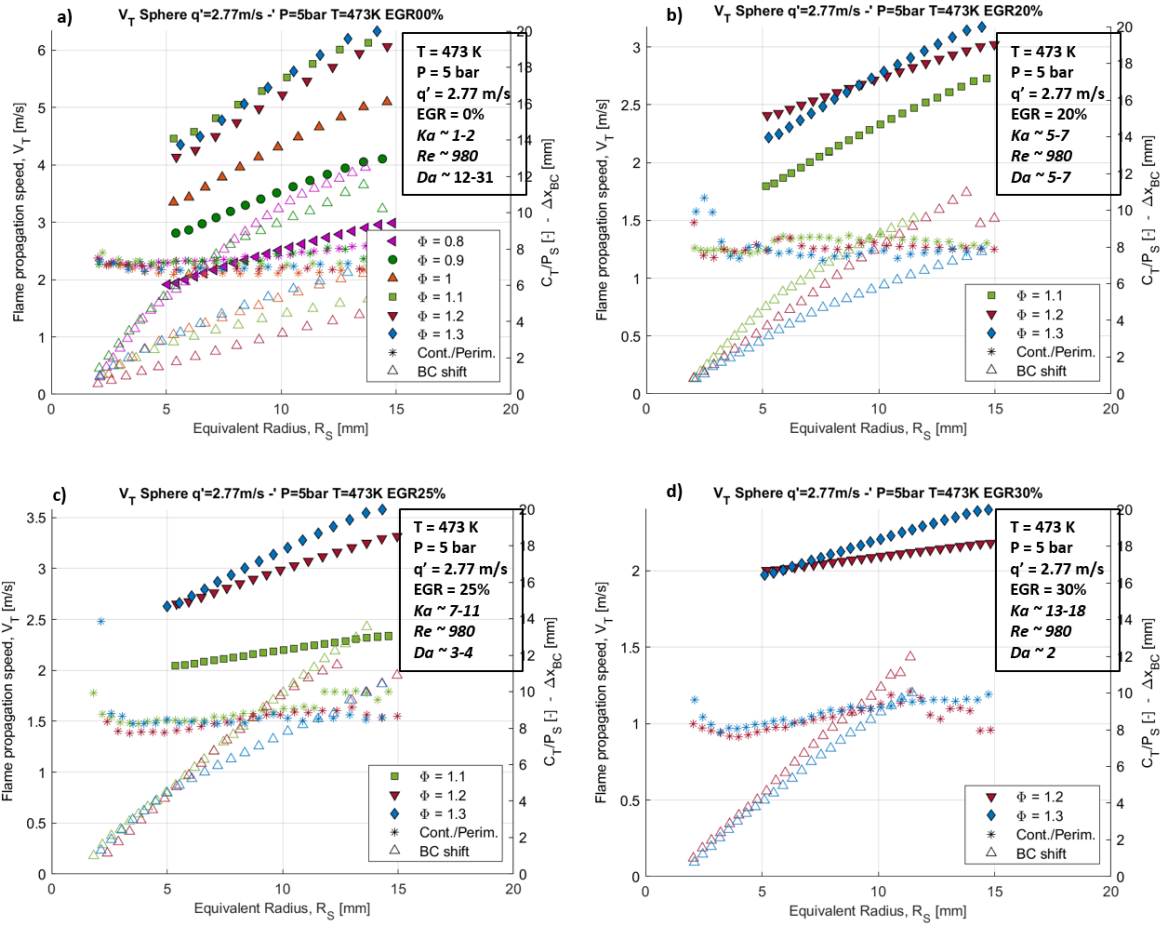


Figure 87. Effect of dilution - Turbulent flame propagation speed (left y axis), absolute barycenter displacement in the tridimensional domain (x, y, z directions) and ratio of flame contour and perimeter based on the equivalent spherical radius (right y axis) measured on spherical vessel for different experimental conditions.

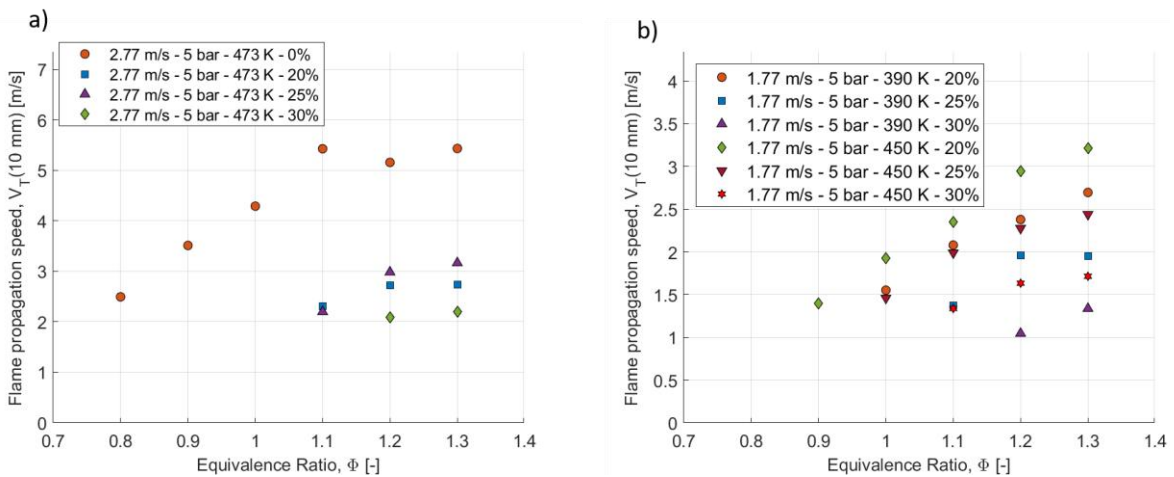


Figure 88. Effect of dilution on flame propagation speed at  $R_S=10\text{ mm}$ , for both turbulent intensities.

For sake of readability, the ensemble of diagrams of  $V_T(R_S)$ ,  $C_T/P_S$  and barycenter displacement,  $\Delta x_{BC}$ , for the other conditions, will be reported in the ANNEX D, grouped by common range of Karlovitz number.

Evolution of the wrinkling factor similar to the ones discussed are observed for cases in Figures 7, 8, 9 and 10 in ANNEX D. For what concerns the flames shifting, in all the reported figures it is also traced the absolute value of the flame barycenter shift with respect to the center of the chamber. It must be specified that this value is computed considering the displacement in the space, so using the three coordinates obtained by the DVS technique. By looking at Figure 85, it seems that this displacement is not related to the ambient pressure. On the contrary, it could be significantly increased by an increase of the turbulent intensity. At the same way, dilution increase from 0% to 20% and, successively, from 20% to 25% and 30%, causes an increase of the mean barycenter displacement, as shown in Figure 85. Moreover, the increase of mixture richness, generally associated to an increase of the propagation speed, tends to reduce the flame shifting. Thus, one can observe that, for a given range of  $\phi$ , the faster is the propagation the minor is the flame barycenter displacement and the oscillations of ratio  $C_T/P_S(R_S)$ , with only few exceptions observed.

### 5.2.3. Karlovitz-based Comparison

As pointed out by Wang et al. [136], by considering the flame surface wrinkling as a key factor in the flame propagation speed, the Reynolds and the Karlovitz numbers have a direct influence. Indeed, the increase in  $Re$  increases the spectrum of scales that will increase the flame surface area through its wrinkling. On the contrary,  $Ka$  increase reduces the flame wrinkling and then causes the reduction of the flame turbulent propagation speed, even if this effect is weaker than the impact of  $Re$ . It has to be noticed that, for all considered experimental conditions, the Reynolds number, at one given temperature for fixed  $q'$  and  $L_T$ , is almost constant for all dilution rates and equivalence ratio. On the contrary, it obviously depends on the turbulent intensity and on the pressure due to its impact on both  $S_L^0$  and  $\delta_L^0$ . As expected, the increase of  $Re$  contributes to the increase of the turbulent flame propagation speed. For this reason, all the plots in the following will be assembled by group of similar range of  $Ka$ .

Figure 89 shows some turbulent propagation flame speed (at  $R_S = 10\text{mm}$ ) for different cases (different temperature, turbulent intensity, but same levels of dilution by grouping together a similar range of Karlovitz numbers, due to the variation of  $\phi$ ). It is clearly identified here the boosting effect, over the whole range of the equivalence ratio due to the higher  $Re$  value, reached in higher turbulence conditions. Moreover, the curves of  $C_T/P_S(R_S)$  and barycenter shift are also similar for these experimental conditions (as plotted in Figures 7, 8, 9 and 10 in ANNEX D).

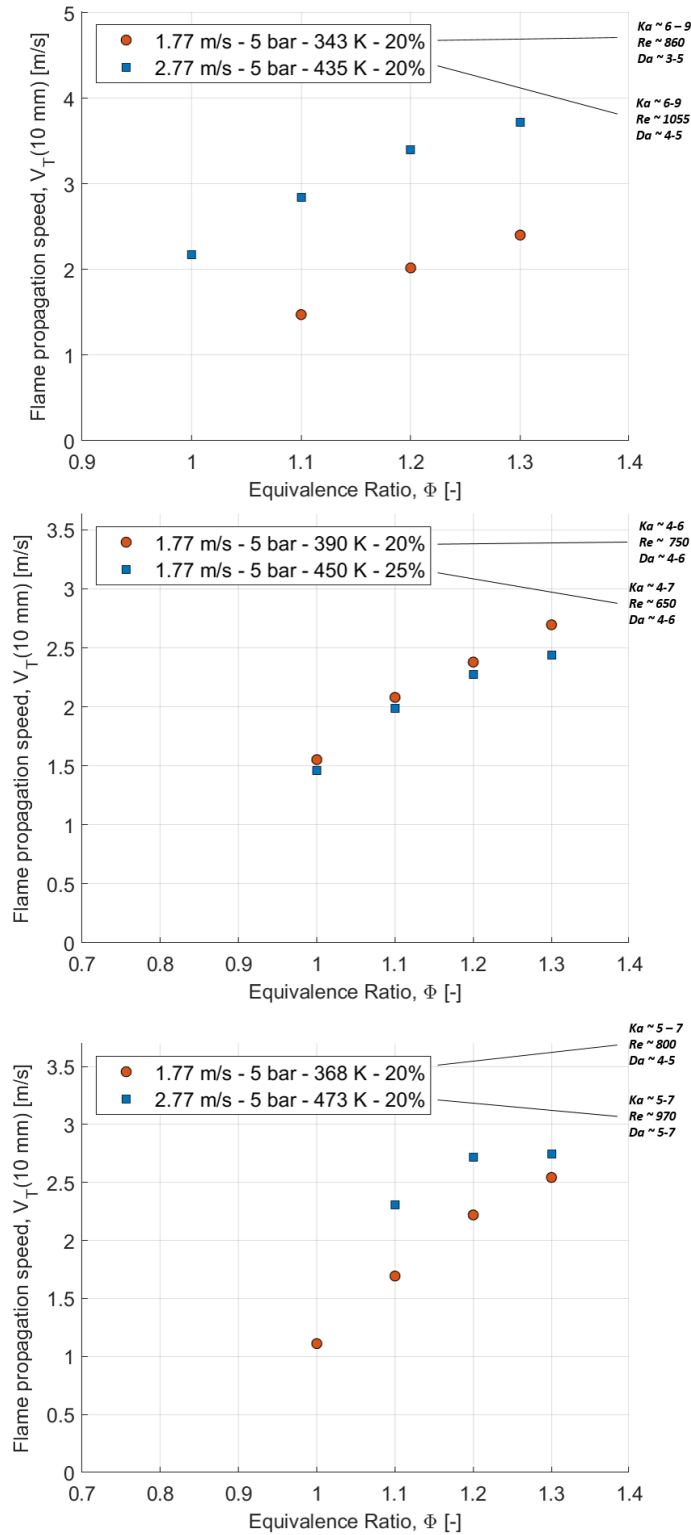


Figure 89. Effect of Re on flame propagation speed (at  $R_5=10$  mm) as a function of the equivalence ratio for different conditions regrouped for same Ka range.

It can be noticed that the effect of temperature variation seems to be already taken into account once flames with similar Karlovitz number are compared. This is confirmed, on the Peters-Borghgi diagram, where the variation in temperature is in the same direction as  $Ka$  variations.

Figure 90 (a) reports the evolution  $V_T(10)$  as a function of  $\phi$ , for the lowest turbulent configuration ( $q' = 1.77$  m/s), and the highest turbulent one ( $q' = 2.77$  m/s) for some other  $Ka$  ranges and  $Re$  values. There again, the impact of  $Re$  is clear underlined:  $Re \sim 750$  case induces  $V_T(10)$  trends slightly higher than the  $Re \sim 650$  case, almost coincident with the  $Re \sim 800$ , at higher  $Ka$ . It has to be noted that for  $q' = 1.77$  m/s, a kind of stabilization of  $V_T(10)$  value is reached. In fact, as observed in previous work by Lawes et al. [89], the monotonic increase of  $V_T(10)$  starts to be dominant at moderate turbulent intensity ( $q' \sim 2$  m/s).

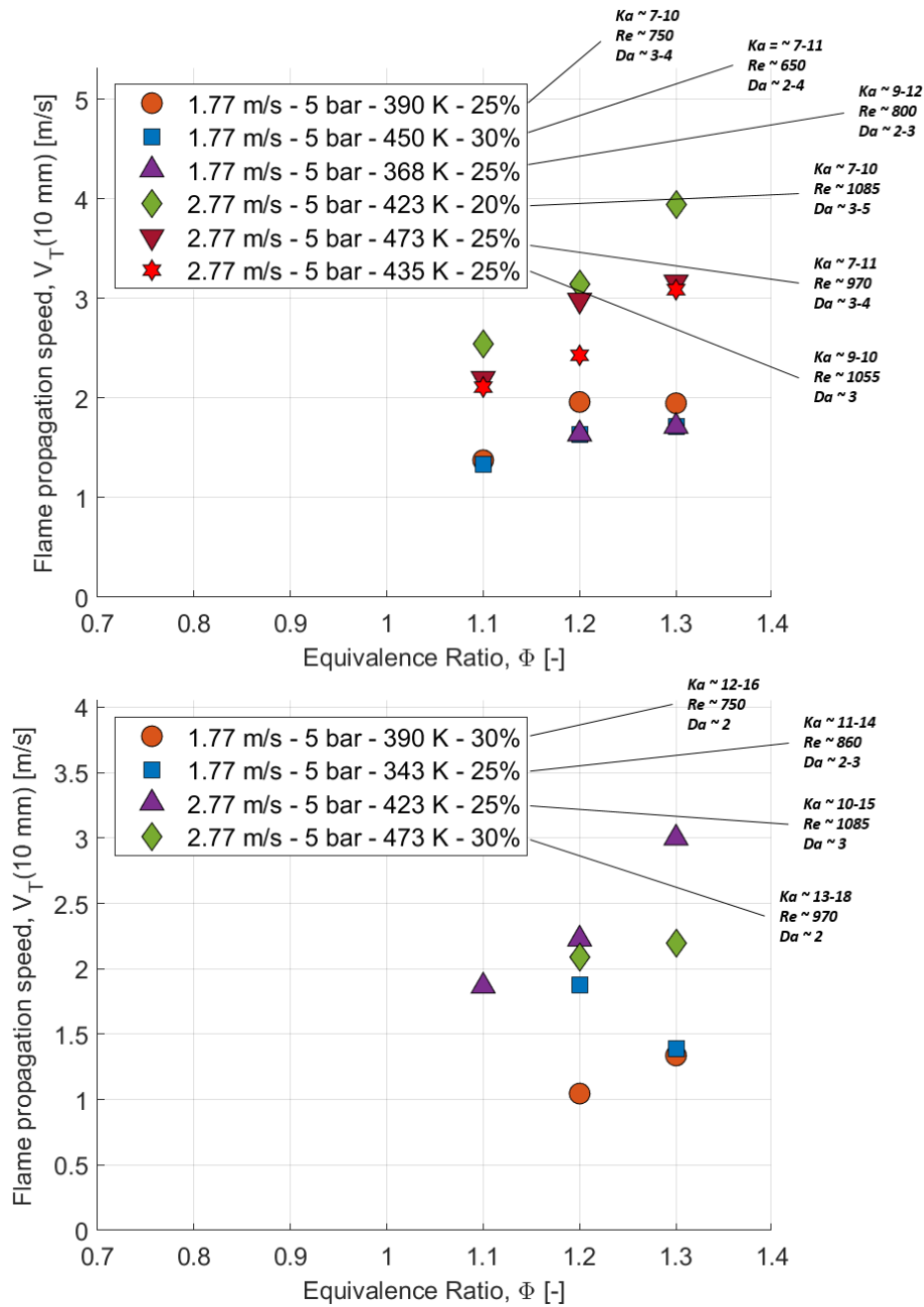


Figure 90. Peters-Borghi diagram. All the investigated experimental points are reported. The smaller is the symbol the lower the equivalence ratio. The classic effect of

Finally, Figure 90 (b) reports data for the highest  $Ka$  range ( $>10$ ), usually reached for low temperature and/or high dilution level ( $>25\%$ ). Under these drastic conditions it is easy to observe the limits of the estimate of  $V_T$ , as previously discussed in Section 5.1 and highlighted in Figure 10 - ANNEX D. Figure 10 (c), as already mentioned, displays an overestimation for an equivalence ratio of 1.2 for  $Re \sim 751$ .

Figure 91 qualitatively summarizes all the aforementioned observations in the case of tests performed in the spherical vessel. The size of the symbols is proportional to the turbulent flame propagation speed, evaluated at  $R_S = 10$  mm. Despite the variations due to the different equivalence ratio for the same experimental conditions, it is possible to observe the average increase of  $V_T$  for increasing Reynolds number and, additionally, its drop for increasing Karlovitz number.

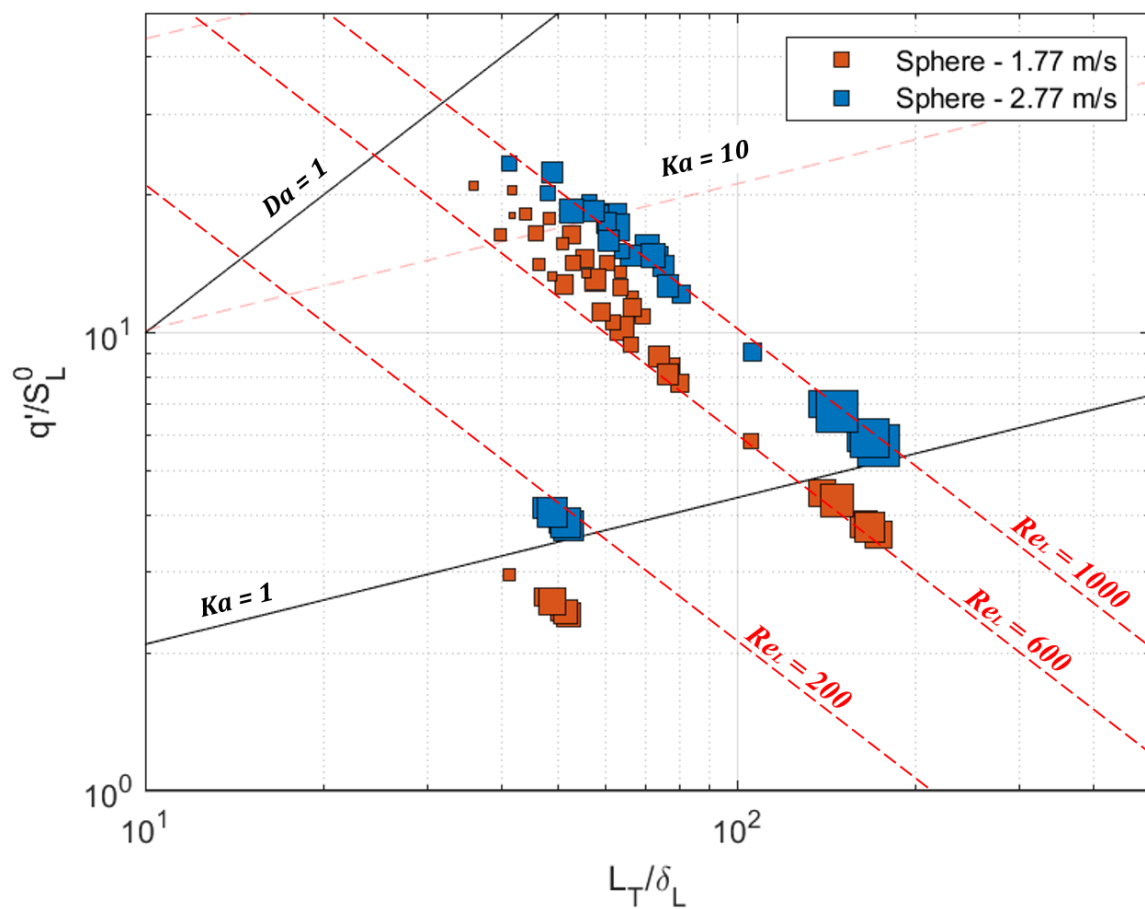


Figure 91. Indication of turbulent flame propagation speed value in Borghi-Peters diagram.

### 5.3. NOSE TURBULENT FLAME SPEED

Tests conducted on NOSE exhibit Karlovitz numbers in the same order of magnitude than those obtained on the spherical vessel, but with Reynolds numbers significantly higher for NOSE-SV conditions as shown in Figure 92. Nevertheless, to compare the accuracy of the data obtained in Nose in comparison to those obtained in the spherical vessel, the LV configuration allows similar pressure and temperature conditions and slight lower turbulent intensity (2.31 m/s versus 2.77 m/s). Only limited dilution rates and equivalence ratios conditions were performed and therefore, the difficulty in contour detection and flame propagation estimate, as described in Section 5.1 becomes more important.

In order to better compare the different configurations and the effect of individual parameters, as done in Figure 91, Figure 93 highlights the values of turbulent propagation flame speed reached at  $R_S = 10$  mm ( $V_T(10)$ ), for NOSE conditions in comparison to those in spherical vessel.

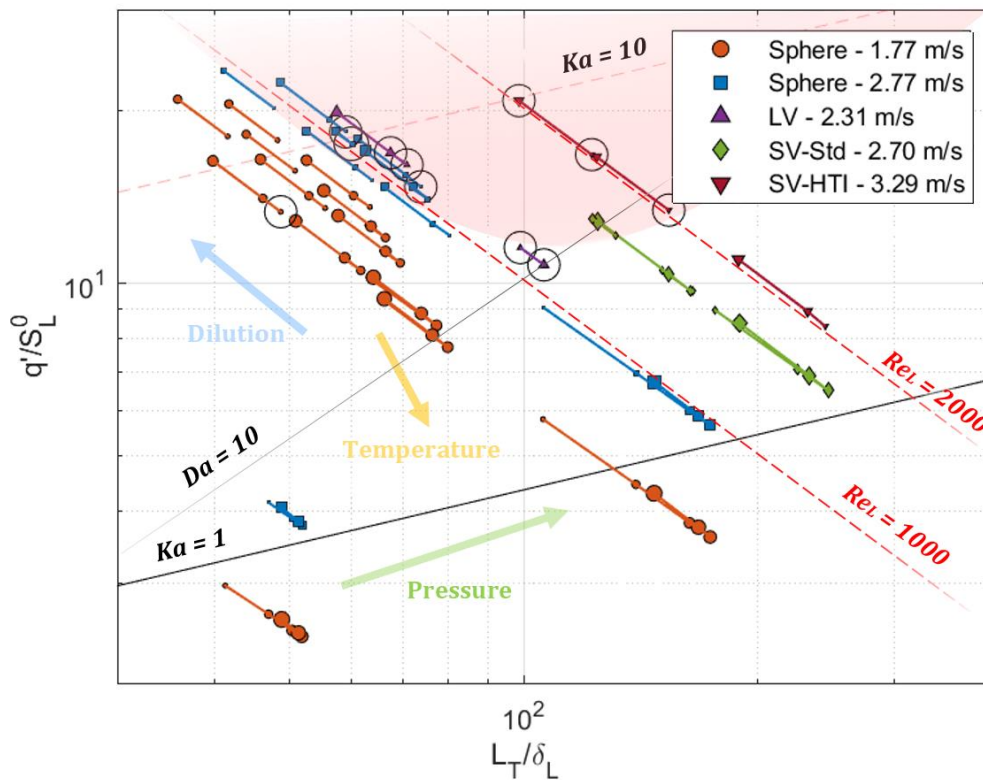


Figure 92. Peters-Borghi diagram including all 5 bar spherical vessel tests and NOSE tests. The zone in which experimental difficulties were encountered is highlighted.

It can be observed that the turbulent flame speed is lower as a function of the decrease of  $L_T/\delta_L$ , so when the mixture is lean or diluted. Moreover, it can be noticed the effect of increase in  $Ka$ , that hinders flame propagation, and the opposite effect of increase in  $Re$ , that promotes the surface wrinkling and, thus, the

turbulent propagation speed. By considering the NOSE SV points at the lowest Karlovitz number (Figure 92), obtained for 10% EGR in both SV-Std ( $q' = 2.7$  m/s) and SV-HTI ( $q' = 3.29$  m/s) conditions, one can notice that the expected shift due to the pressure increase is not verified. Even if the pressure affects both  $S_L^0$  and  $\delta_L^0$ , the quadratic evolution of  $S_L^0$  as a function of the pressure (see Figure 72), yields to a slight reduction of  $S_L^0$  when the pressure becomes larger than 10 bar, especially in comparison to the sharp decrease between 1 and 5 bar. Therefore, a similar trend is observed on the Peters-Borghgi diagram when the pressure increases, explaining the position of NOSE-SV points. This configuration induces Karlovitz number ranges similar to the configuration at highest turbulent intensity in the spherical vessel (0% dilution). The effect of the lower integral length (left-shifting) and the temperature increase that decreases  $Ka$  must be taken into account. Despite this, the points are located in a part lower than expected, suggesting a change in pressure effect.

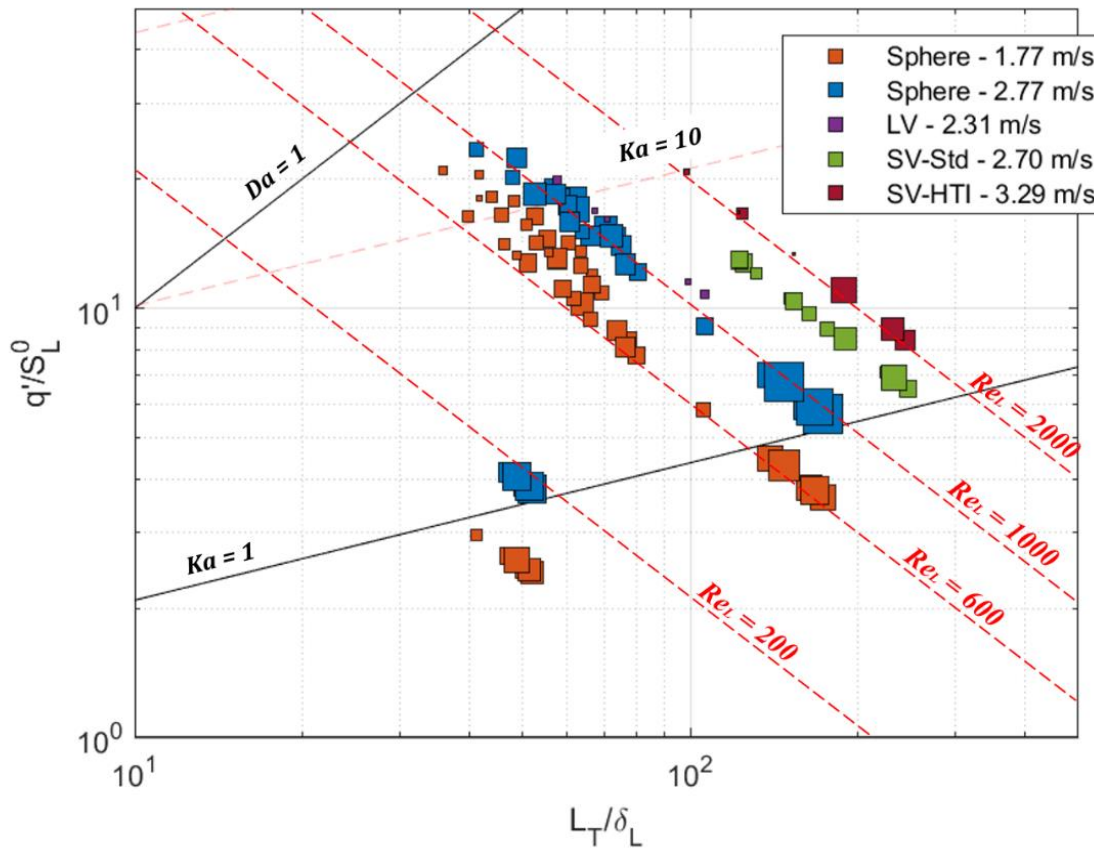


Figure 93. Importance of turbulent propagation flame speed at  $R_S=10$  mm in Borghi-Peters diagram for all experimental conditions.

Figure 94 reports the evolution of  $V_T(10)$  as function of  $\phi$ . Figure 94 (a) shows the comparison between the results in the spherical vessel and in NOSE for similar Karlovitz number range.

Despite the higher  $Re$  in NOSE than in spherical vessel, any significant boost of the flame propagation velocity is noticed. On the contrary,  $V_T(10)$  for NOSE SV-Std (EGR 20%), with  $Re \sim 1600$ , is similar

to the other tests only for  $\phi = 1$ . While, with the  $\phi$  increase, the flame propagation speed increase is less pronounced, leading to a difference of about 30% at  $\phi = 1.3$ . The points relative to NOSE SV-HTI, characterized by  $Re \sim 2060$ , follows same trends than data in spherical vessel. By considering the lower Reynolds numbers in spherical vessel ( $\sim 620$ - $650$ ), it seems that when the pressure drastically increases the dependence on Reynolds number for  $V_T(10)$ , previously observed on the spherical vessel cases cannot be observed. By looking at Figure 94 (b), the evolutions at same pressure (21 bar) with 10% EGR for SV-Std and SV-HTI conditions, seem similar, highlighting the balancing effect between  $Re$ , from 1600 to 2060, and  $Ka$ , from 2-3 to 3-4.

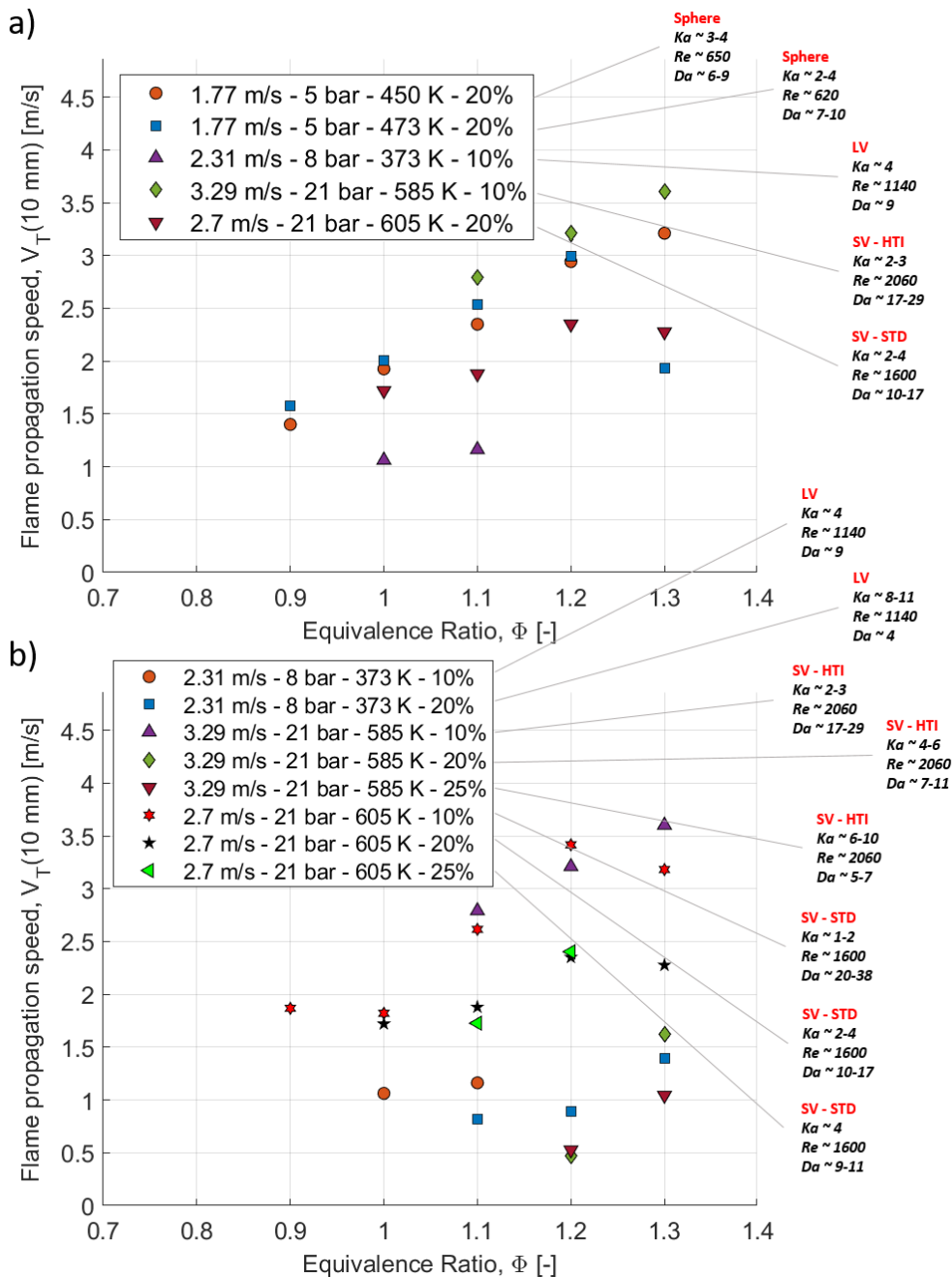


Figure 94. Evolution of turbulent flame propagation speed as a function of the equivalence ratio for different Ka range.

The main difference between experiments in NOSE and in the spherical vessel is the high level of pressure reached and the effect of pressure increase on the turbulent flame propagation is the reduction of the chemical reactions characteristic time, represented by the Damkohler number, as it is the ratio between the integral turbulence temporal scale with this chemical time. The evolution of  $V_T(10)$  for SV-Std is linked to the effect of integral length on the propagation velocity and its different value (2.07 mm on SV Std in comparison to 3.4 mm on spherical vessel). It was pointed out by Wang et al. [136] that small Kolmogorov scales can actually decrease the flame surface increase, partially counteracting the wrinkling enhancement due to the turbulent intensity, in the case of  $q'/S_L^0$  up to 10. In their work, when the Kolmogorov scale was less than 20% of the flame thickness, the turbulent burning velocity reaches a plateau.

### 5.3.1. Evaluation of Classical Correlation for Turbulent Flames

In the present section, more recent correlations from the literature, to express the turbulent velocity as a function of initial parameters, are considered. Due to the impossibility to extrapolate a rigorous value of  $V_T^0$  in this present study, the turbulent propagation velocity  $V_T(10)$  is considered by multiplying by the expansion factor, in order to be consistent with the correlations. Therefore, in the correlations, the  $S_T$  will be substituted by  $V_T(10) \frac{\rho_b}{\rho_u}$ . One of the most usual correlation of the ratio  $\frac{S_T}{S_L}$  is as following [97]:

$$\frac{S_T}{S_L} = 1 + C \left( \frac{q'}{S_L} \right)^n \quad (85)$$

Figure 95 shows the evolution of all experimental  $\frac{V_T(10) \rho_b}{S_L^0 \rho_u}$  as a function of  $\frac{q'}{S_L^0}$  for three equivalence ratios (1.1, 1.2, 1.3). Each symbol represents a temperature condition but SV conditions are for 585 K and 605 K together, and different colors refer to the specific configuration of set-up. The size is related to the dilution rate: smallest size for highest dilution level. A global good agreement is observed but some of data in NOSE are overestimated and more dispersion is observed for change in dilution rate with the increase of the equivalence ratio.

Following the work of Nguyen et al. [99], other three correlations are tested and, eventually improved. The first one is from Kobayashi et al. [84], [85], obtained for methane/air ( $Le \sim 1$ ) jet flames as:

$$\frac{S_T}{S_L} \propto \left[ \left( \frac{q'}{S_L} \right) \left( \frac{p}{p_0} \right) \right]^{0.38} \quad (86)$$

The second one was proposed by Chaudhuri et al. [82], for statistically spherical turbulent flames with  $Le \sim 1$ :

$$\frac{S_T}{S_L} \propto \left[ \left( \frac{q'}{S_L} \right) \left( \frac{\langle \bar{R} \rangle}{\delta_L^0} \right) \right]^{0.5} \quad (87)$$

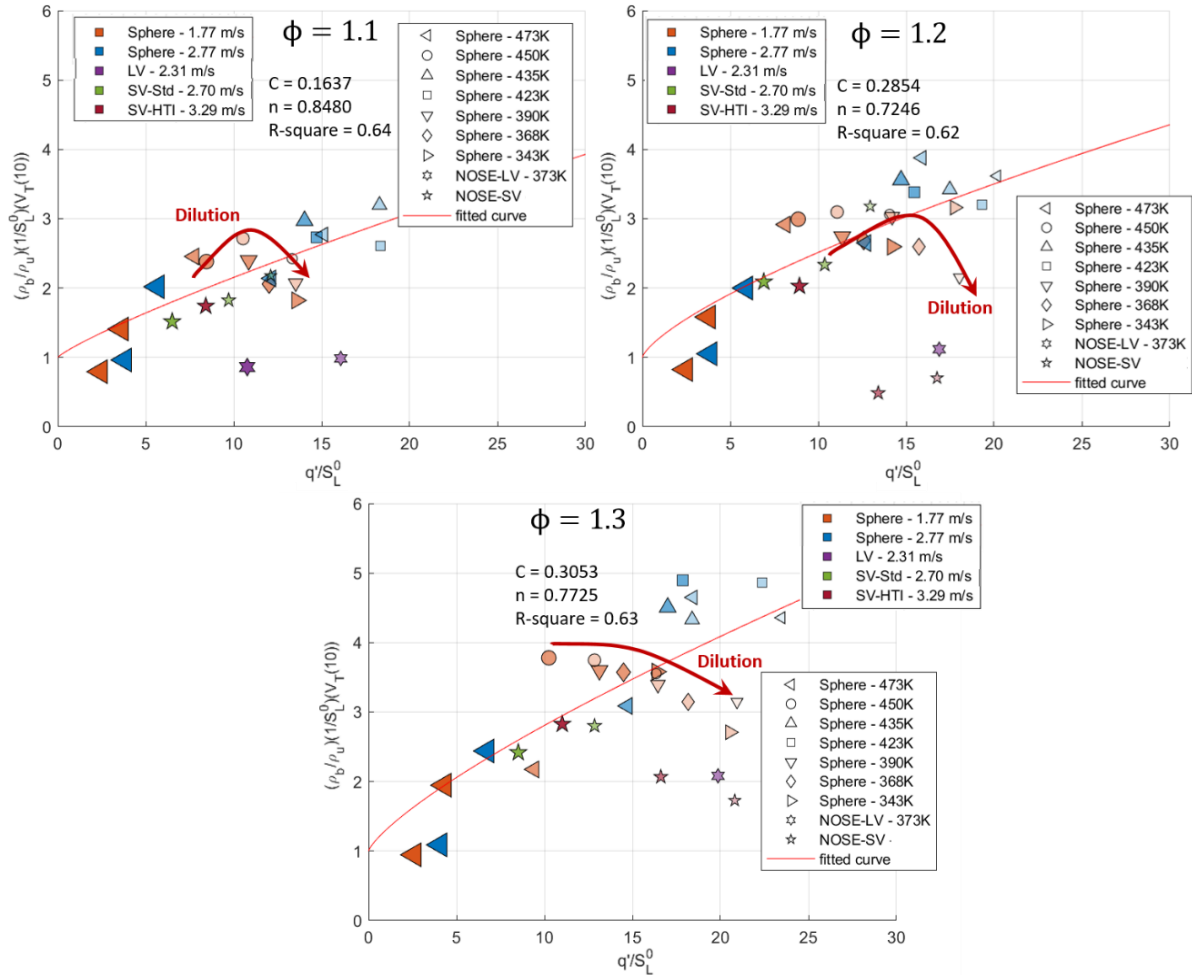


Figure 95. Validity of  $\frac{S_T}{S_L} = 1 + C \left( \frac{q'}{S_L} \right)^n$  correlation in experimental data by considering  $S_T$  as  $V_T(10)$ .

Last, Liu et al. [81] introduced a correlation to take into account the Damkohler number:

$$\frac{S_T}{q'} \propto Da^{0.5} \quad (88)$$

Nguyen et al. [99] pointed out the importance of including the Lewis number if tests are performed under high-pressure values (1-5 atm in their study). Results obtained for fuels whose Lewis number varied from 0.58 to 1.43 confirmed that.

In this work, the Lewis number of the surrogate fuel based on three components was not computed. For sake of completeness, preliminary considerations are done by using Lewis number of iso-octane as the

major component of the surrogate. But differently by the work done by Nguyen et al. [99], this approach did not produce significant results and any experimental points collapse was observed. Therefore, Figure 96 reports these three correlations in their classic form for the three equivalence ratios (from 1.1 to 1.3) without considering  $Le$ .

In Figure 96, each symbol represents a temperature (NOSE-SV temperatures of 585 K and 605 K were considering with the same symbol). Different colors refer to the specific configuration of set-up used. The bigger is the symbol the higher is the equivalence ratio and, finally, the more transparent is the symbol the higher is the dilution rate.

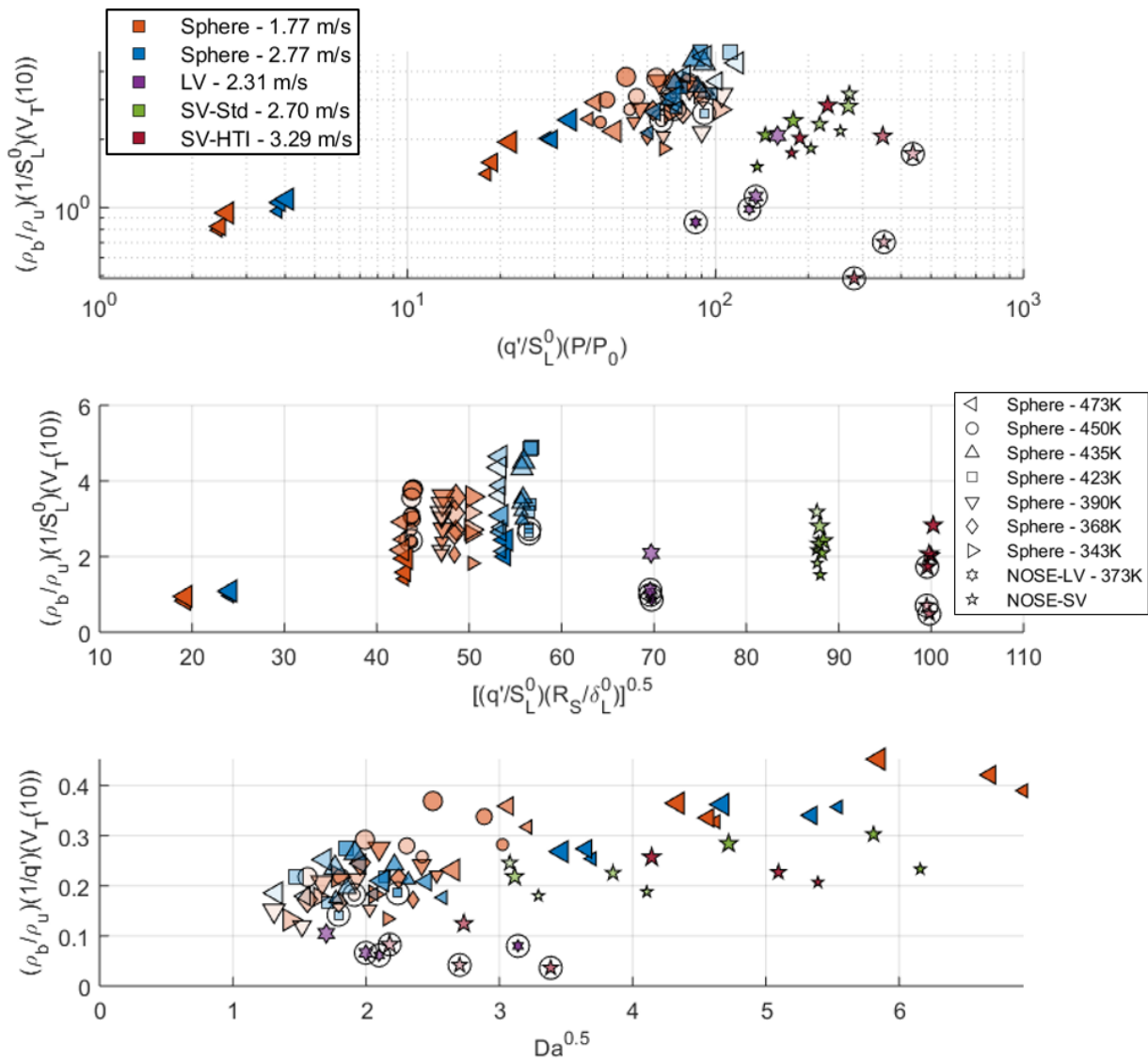


Figure 96. Evaluation of three correlations to predict turbulence effect on flame propagation speed. Circled points correspond to the experimental limit cases.

In Figure 96 (a), the data obtained in spherical vessel are in a good agreement with the correlation in Eq. (86), except for minor scattering due to temperature and dilution variations. But, on the other hand,

the correlation fails in the prediction of NOSE points, even for lower pressure (NOSE-LV) at 10% dilution rate. The fact that all NOSE experimental data are in the same zone may suggest an effect of the integral length scale on the resulting turbulent burning velocity, not considered in the present correlation.

In Figure 96 (b), the vertical placement of some experimental data is mainly due to the dilution rate and equivalence ratio increase. The effect of turbulent intensity and pressure increase is more evident for the data obtained in the spherical vessel. Points obtained in NOSE are not in the same predictive location. To deep investigate this behavior, enlarged version of correlation in Eq. (87) [83] is evaluated in Figure 97. The ensemble of the extrapolated radii is plotted against the relative  $V_T(R_S)$ , instead of using averaged  $R_S$  and extrapolated value of  $V_T$ . In Figure 97 (a), the effect of pressure change from 1 to 5 bar, turbulent intensity and equivalence ratio increase is highlighted only for spherical vessel data. Different symbols correspond to different equivalence ratio.

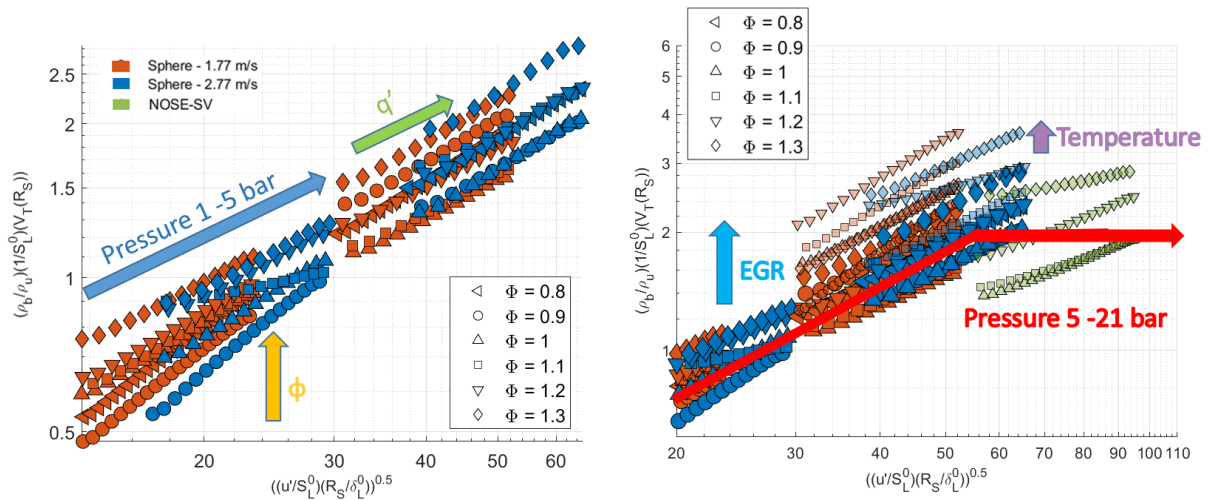


Figure 97. Evaluation of correlation proposed by Chaudhuri et al. (check ref.) considering all the extrapolated radii and relative  $V_T(R_S)$ .

By adding the experimental conditions obtained in Nose in Figure 97 (b), one can observe minor effects of temperature and dilution, but as a function of the pressure, the NOSE points are located in the right zone but not in top zone of the diagram. They are on the same level than spherical vessel data performed at  $q' = 2.77$  m/s and 0% EGR. This drop may be related to the integral length reduction but also to pressure dependence quadratic law, similar to what was observed on the Peters-Borghgi diagram and discussed previously. In a recent numerical study, Wang et al. [136] observed a plateau in the  $S_T$  trend for  $\frac{q'}{S_L} > 8$  m/s and fixed integral length. But, when  $\frac{q'}{S_L}$  was fixed and the integral length doubled, the  $S_T$  increased by more than 50%. The explanation of these results is that when  $q'$  increases two opposite phenomena are verified, leading to an overall balance in the resulting  $S_T$ . The first is the broadening of the spectrum of turbulent eddies that increases flame surface area. The second is the reduction of

Kolmogorov scale that leads to smaller small-scales eddies that can affect the flame surface resulting in the loss of surface area through strain and curvature effects. On the contrary, when the integral length is doubled, the two phenomena act in the same sense, with both the broadening of eddies spectrum and the decrease of small-scale weakening effect.

Last correlation, in Figure 97 (c), seems to better unify the experimental conditions of the different configurations and set-ups, evidencing the possible effect of the Damkohler number in turbulent burning velocity.

By exploiting the observed dependence of the turbulent burning velocity on Karlovitz number, one may suppose:

$$\frac{S_T}{S_L} \frac{1}{Da} \propto Ka \quad (89)$$

that yields the plots in Figure 98, with a fit equation as following:

$$\log\left(\frac{V_{T10} \rho_b}{S_L^0 \rho_u} \frac{1}{Da}\right) = a + b \log(Ka) \quad (90)$$

For the gathered experimental database,  $a$  is  $-2.727$  and  $b$  is  $1.231$ , with an  $R$ -square of  $0.90$ .

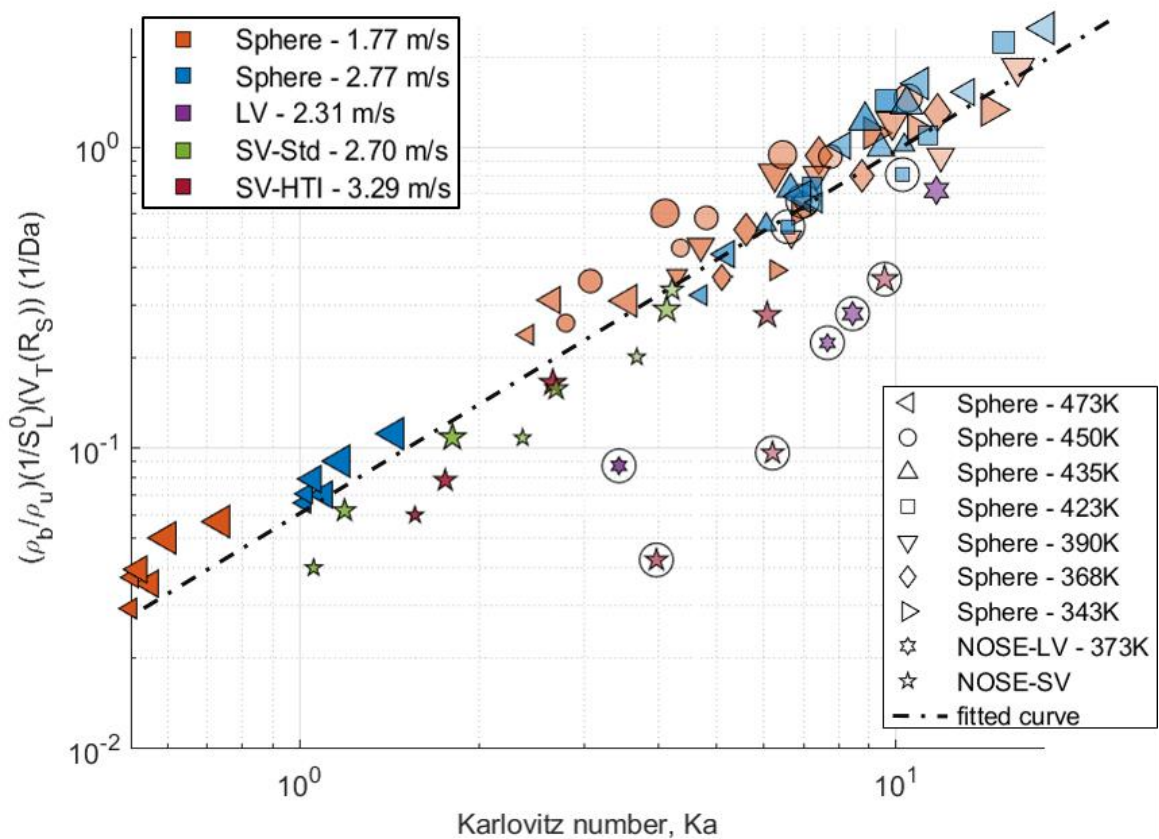


Figure 98. Correlation proposed in Eq. (90) for all the experimental conditions. Circled points correspond to the experimental limit cases.

## 5.4. CONCLUSIONS

In this chapter, the results of the turbulent flames investigation were presented for both spherical vessel and NOSE. The great part of tests performed on the spherical vessel were performed at 5 bar and covered a wide range of Karlovitz numbers, by varying temperatures, turbulent intensity and dilution. Reference tests at 1 bar, 473 K and 0% dilution were used as direct comparison to observe effect of increasing dilution and pressure variation between 1 and 5 bar. Large increase of dilution rates, from 20% to 30%, yields a reduction of turbulent flame propagation speed,  $V_T$ . While, pressure increase from 1 to 5 bar leads to an increase of  $V_T$ . On the other hand, both pressure and dilution contribute in decreasing the oscillations of the evaluated wrinkling factor, even though it must be taken into account that contour derives from Schlieren images.

Usually, it was observed a dependence of the flame propagation speed on the Reynolds and Karlovitz number. It was noticed that under the experimental conditions investigated on the spherical vessel, the increase of  $Ka$  leads to a slight reduction of  $V_T$ . On the contrary, increasing the Reynolds number enhance the resulting propagation speed. Other study correlated similar evidences to the increase of  $Ka$  and  $Re$  that reduces or increases, respectively, the flame surface wrinkling. In addition, the observed flame propagation speed enhancement due to the equivalence ratio increase is confirmed by other studies.

NOSE LV configuration represents the experimental continuity between the two set-ups used in the present study. Anyway, it was showed that the sensibly lower integral length, for this configuration and, above all, for the two SV configurations, yields very low values of the Kolmogorov length scale. The direct consequence is an evident change in the flame structure that was confirmed by the flames images of the three configurations compared with those of the spherical vessel.

Firstly, it was found out that the points displacement on the Peters-Borghgi diagram due to a pressure increase (up to 21 bar), follows the quadratic law of the laminar burning velocity decrease. This trend becomes evident only when pressure drastically increases with respect to the low pressure range previously investigated (1-5 bar).

The comparison between tests performed on the two NOSE SV configurations shows that the effect of  $Re$  and  $Ka$  variations is similar to what is observed on the spherical vessel at lower pressure and higher integral length.

Last, recent correlations between turbulent flame propagation speed, laminar flame velocity and turbulent intensity proposed in literature were tested. It seems, that all data can follow the correlation:

$$\frac{S_T}{S_L} \frac{1}{Da} \propto Ka.$$





---

## **6. Conclusions and Perspectives**

---



This present work had as objective to fill an existent gap in the current literature for what concerns the investigation of turbulent premixed flames under drastic conditions, more and more reached in application devices, as gas turbines and Internal Combustion engines. Since recent technologies are evolving to become cleaner and more efficient, the necessity to develop accurate models for these conditions, in order to help the design, is one priority. To succeed this challenge, it still needs some complementary numerical and experimental approaches. This present work is one of the experimental tasks done during the ambitious ANR project 'MACDIL' (Moteur Allumage Commandé à fort taux de DILution, ANR-15-CE22-0014), having as final purpose to provide a predictive model for the design of the next future downsized SI engines, useful for car manufacturers. The operating conditions of this type of ICE are still not totally explored for what concerns both laminar and turbulent expanding premixed flames fundamental investigation. Indeed, downsized SI engines operate with highly diluted mixtures, under high-pressure/high-temperature conditions, in a strong turbulent environment. In order to improve simulation tools, it was firstly necessary to validate a surrogate, called TRF-E, as four-components, for a target commercial gasoline (B71 1188 ESSH EURO5 +20, RON 96.6 MON 86.2, Ethanol 5% vol).

This first part of the study was performed on a spherical vessel, previously developed and fully characterized. Thanks to the investigation with Double View Schlieren technique, the analysis is mainly focused on the determination and the comparison of the laminar burning velocity and the Markstein length for both fuels. Over a wide range of pressure, dilution and temperature, the difference in laminar burning velocity between gasoline and TRF-E is limited at  $\sim 15\%$  for the worst case (5 bar, 473 K, 20% EGR and 0.8 equivalence ratio). In general, the major divergence between the behavior of both fuels is caused by the pressure increase. The effect of dilution is low, highlighting the fact that the TRF-E can reproduce the gasoline properties at high dilution rate. Temperature variation, as well, has a similar effect on both the fuels even if a dependence on the equivalence ratio was observed. In fact, it was found out that for  $\phi > 1$  the TRF-E properly follows the gasoline response to pressure, temperature and dilution variations. On the contrary, for lean mixtures the differences are accentuated. In conclusion, it was proved that TRF-E can be considered as an acceptable surrogate for this considered gasoline. Thanks to the gathered database, optimized coefficients of the well-known mathematical correlation, proposed by Metghalchi and Keck [131] and extended by Galmiche et al. [69] to include the dilution rate, were determined with an acceptable precision even under experimental conditions far from the reference ones. A further step in this direction was represented by the extension of the experimental grid for the TRF-E that allowed to additionally refine the optimized coefficients. The correlation error with respect to the experimental points was evaluated, leading to the conclusion that a good agreement generally exists among the great part of the investigated conditions. Moreover, the database will be also used to develop highly accurate chemical kinetic mechanism by one of Partner of the project.

The second part was done in order to optimize and validate another experimental set-up, the so-called New One Shot Engine to investigated unexplored experimental conditions. Then a large part of the

present work was dedicated to the development of optimized procedures on this set-up, the characterization of the reproducible thermodynamic conditions, the improvement of repeatability and reliability capacities. In addition, the aerodynamic characterization of the set-up was performed by using a PIV technique. Four configurations were selected and used in the present work: three were used for the turbulent flames investigation and one to study laminar expanding flames under very high values of pressure and temperature, 21 bar and 473, 500 and 525 K, respectively. Therefore, some comparisons in laminar configurations were done with the results obtained with the spherical vessel, at 5 bar and 473 K. Due to the fact that NOSE is a rapid compression machine, to reach the aforementioned high thermodynamic conditions, it must operate dynamically. Main working principle, anyway, consists in accurate and real-time control of the purposely designed piston trajectory. This allows maintaining target conditions for a sufficient temporal range, in which the flame must be triggered with an adequate spark-time phasing, but it causes a deformation of the flame shape, as flattened at first instance and, then, elongated near the end of the observable propagation range. And, for the flames with slow propagation speed, it is not possible to completely propagate before the beginning of the expansion phase. Despite this, through the comparison with the spherical vessel ones, the hypothesis of spherical flame can be used. Last, the results obtained at 21 bar, at same temperature and dilution rate tested at 5 bar on the spherical vessel, are in agreement with the predicted value from the mathematical correlation. But it has to be kept in mind that limitation consists in laminar burning velocity prediction when more than two parameters drastically deviate from reference conditions. It will be interesting, as future work to increase the number of experimental points to refine correlation laws (for example for dilution and pressure evolution), by using the large experimental possibilities offered by NOSE.

Once a solid analysis and a large database were established for laminar cases, the two experimental set-ups were used in turbulent configurations. The major objective is to investigate a zone of the well-known Peters-Borghini diagram characterized by high Karlovitz and Reynolds numbers in which the effect of dilution and high pressure is still not demystified in current literature. Flames sharing similar dimensionless numbers are supposed to be still in the combustion regime of the corrugated flamelets, even if  $Ka > 1$ . Despite this, the fact of reaching these dimensionless numbers by changing parameters whose exact effect is still an open topic, may actually cause a transition to another combustion regime. To be more precise, the effect of high dilution rates and engine-like integral length and pressure was never approached with a fundamental investigation. Thus, the study of turbulent flames propagating under these conditions is a priority to correctly modify and refine existing flamelet models or even predict combustion regime transition. The strategy of the present work consisted in exploiting the sphere flexibility to set up a large number of experimental conditions. The results gathered from this pool of data were then used to understand and explain more complex phenomena in engine-like conditions, through NOSE.

The great part of tests performed on the spherical vessel were performed at 5 bar and covered a wide range of Karlovitz numbers (between around 0.5 and 18, according to the classic definition), by varying temperatures, turbulent intensity and dilution. Reference tests at 1 bar, 473 K and 0% dilution were used also as direct comparison to observe effect of increasing dilution and pressure variation between 1 and 5 bar. Large increase of dilution rates, from 20% to 30%, yields a reduction of turbulent flame propagation speed,  $V_T$ , while the pressure increase from 1 to 5 bar leads to an increase of  $V_T$ . On the other hand, both pressure and dilution contribute in decreasing the oscillations of the evaluated wrinkling factor. Measurements of the barycenter displacement confirm the significant flame shift of the flame during the propagation when conditions are particularly severe, distinguishable thanks to the Double View Schlieren. Increasing the equivalence ratio usually helps in reducing the flame displacement with respect to the combustion chamber center zone. For  $\frac{q'}{S_L} > 10$  and  $\frac{L_T}{\delta_L^0} > 50$ , occurrences of flame local quenching and pockets formation on the flame surface were observed. For unfavorable thermodynamic conditions (EGR > 25% and T < 400 K) and moderate turbulence (for example  $q' = 1.77$  m/s in the spherical vessel), the pockets originated on the flame surface lie on the flame front. This behavior may cause an overestimation of the flame propagation speed. When Reynolds number increases over  $\sim 1000$  the pockets are detached from the flame front and almost immediately quenched. Therefore, during the propagation, the flame is actually eroded by this kind of phenomena, leading to an evolution of  $V_T$  as a function of  $R_s$ , constant or decreasing. All the just discussed phenomena are most likely to appear in lean, stoichiometric or even slightly rich mixtures.

Generally, it was observed a dependence of the flame propagation speed on the Reynolds and Karlovitz numbers. It was noticed that under the experimental conditions investigated on the spherical vessel, the increase of  $Ka$  leads to a slight reduction of  $V_T$ . On the contrary, increasing the Reynolds number enhance the resulting propagation speed. Other studies correlated similar evidences to the increase of  $Ka$  and  $Re$  that reduces or increases, respectively, the flame surface wrinkling. In addition, the observed flame propagation speed enhancement due to the equivalence ratio increase is also confirmed by other studies.

Three configurations were used in NOSE: LV configuration to represent similar conditions than in spherical vessel and two others, SV-HTI and SV-Std configurations which provide lower value of the Kolmogorov scale, with as direct consequence a change in the flame structure. Thanks to these three configurations, higher turbulent intensity and dilution rates could be reached.

Firstly, it was found out that the points displacement on the Peters-Borghgi diagram due to a pressure increase (up to 21 bar), follows the quadratic law of the laminar burning velocity decrease. This trend becomes evident only when pressure drastically increases with respect to the low pressure range previously investigated (1-5 bar). Moreover, the turbulent flame propagation speed results lower than expected for the three configurations. Comparing same Karlovitz number ranges, the flames obtained in

NOSE are at higher Reynolds numbers. According to what observed in other works and in the present study, within the flamelet regime, increase of  $Re$  leads to an increase of flame surface wrinkling and, thus, to an enhanced turbulent speed. One possible explanation to the relatively low propagation speed observed on NOSE concerns the integral length decrease. In literature, it was supposed that the lower is the integral length the more exists a weakening effect on the flame front wrinkling. When  $\frac{q'}{S_L}$  was fixed and the integral length doubled, the turbulent flame speed increased by more than 50%, certainly due to two phenomena counter balanced. When  $q'$  increases, there is the broadening of turbulent spectrum, increasing the flame surface, but, in other hand, the smaller small-scales eddies affect the flame surface resulting in the loss of surface area through strain and curvature effects. On the contrary, when the integral length is doubled, the two phenomena act in the same sense, with both the broadening of eddies spectrum and the decrease of small-scale weakening effect. Nevertheless, the comparison between tests performed on the two NOSE SV configurations shows that the effect of  $Re$  and  $Ka$  variations is similar to what is observed on the spherical vessel at lower pressure and higher integral length. Other possibility concerns an effect of pressure that becomes dominant over certain threshold. In literature it was found that changing pressure at constant  $Re$  yields a reduction of turbulent flame speed, while if  $Re$  increases accordingly to the pressure increase, the flame propagation is enhanced. This effect, anyway, was observed between 1 and 5 bar.

Last, recent correlations proposed in literature were tested. As expected, the classical form  $\frac{S_T}{S_L} = 1 + C \left(\frac{q'}{S_L}\right)^n$ , fades in following dilution variation, drastic pressure increase and integral length reduction. Finally all the data obtained follow a trend through the correlation:  $\frac{S_T}{S_L} \frac{1}{Da} \propto Ka$ . A natural improvement of this form could be the investigation of a dependence on the Lewis number or a deep investigation of the integral length effect exploiting the NOSE LV configuration.

## 6.1. PERSPECTIVES

The new encouraging results obtained lead to the conclusion that it would still be interesting to consider further development and optimization of the NOSE for both, laminar and turbulent, configurations.

First, the possibility to increase the final temperature and pressure will allow to improve better the kinetics mechanisms but also, the investigation of intermediate pressures, as between 5 and 21 bar. In this way, it will allow to refine semi-physical and empirical correlations and to investigate a possible improvement in the predictive laws of pressure and dilution increases. For that, some suggested improvement of NOSE set-up could be the refinement of the used trajectories, by optimizing the control of the electric motor. By increasing the range of the ‘plateau’ will allow the study of slower flames but also the decrease of the flame shape deformation.

For what concerns the turbulent flames investigation, a first step in future work should be focused on the continuity of the experimental conditions provided between the spherical vessel and NOSE, that in this study was just partially achieved. In fact, the two experimental set-ups were compared by investigating conditions at similar  $Ka$  and  $Re$ . But, it was observed that the effect of turbulence integral length, at same thermodynamic conditions and identical  $q'$  has to be also studied. In this respect, the LV configuration should be used. By exploiting the experimental conditions covered by the spherical vessel and the NOSE LV, it will be possible to deeper investigate the phenomenon of pockets formation observed in the present work only for some limited cases, not well defined until now.

Finally, to investigate the effect of pressure on turbulent flames, the three configurations could be used to investigate a large range of pressure (between 5 and 16 bar on NOSE LV and between 15 and 60 bar on NOSE SV). On the other hand, to evaluate the possible impact of the Lewis number in drastic change of pressure, dilution and integral length, other fuels may be considered to complete the test matrix.

Thanks to this new set-up, even if for the moment some drawbacks still limit the results, it is clear that for both cases, laminar and turbulent, the results obtained will extend the available data in literature to understand better turbulence-flame interaction in drastic conditions to help a better predictability of the models.



---

## 7. References

---

- [1] “[https://www.eia.gov/outlooks/ieo/.](https://www.eia.gov/outlooks/ieo/)” .
- [2] International Energy Agency (IEA), “CO2 Emissions From Fuel Combustion,” 2016.
- [3] T. F. Stocker, D. Qin, G.-K. Plattner, M. M. B. Tignor, and S. K. Allen, “Climate Change 2013: The Physical Science Basis. Contribution of Working Group I to the Fifth Assessment Report of the Intergovernmental Panel on Climate Change,” *Intergov. Panel Clim. Chang. Work. Gr. I Contrib. to IPCC Fifth Assess. Rep. (AR5)*(Cambridge Univ Press. New York), p. 1535, 2013.
- [4] “<https://www.epa.gov/ghgemissions/global-greenhouse.>” .
- [5] A. Bandivadekar and Z. Yang, “Light-duty vehicle greenhouse gas and fuel economy standards,” 2017.
- [6] “[https://www.eea.europa.eu/data-and-maps/.](https://www.eea.europa.eu/data-and-maps/)” .
- [7] J. D. Miller and C. Façanha, “The state of clean transport policy - A 2014 synthesis of vehicle and fuel policy developments,” *ICCT Rep.*, p. 73, 2014.
- [8] U.S. Energy Information Administration, “Transportation Sector Energy Consumption,” vol. 2016, pp. 127–137, 2016.
- [9] B. Galmiche, N. Mazellier, F. Halter, and F. Foucher, “Turbulence characterization of a high-pressure high-temperature fan-stirred combustion vessel using LDV, PIV and TR-PIV measurements,” *Exp. Fluids*, vol. 55, no. 1, 2014.
- [10] C. Endouard, “Etude expérimentale de la dynamique des flammes de prémélange iso-octane/air en expansion laminaire et turbulente fortement diluées,” 2016.
- [11] T. Poinsoot and D. Veynante, *Theoretical and Numerical Combustion*. Edwards, 2005.
- [12] J. Abraham, F. A. Williams, and F. V. Bracco, “Discussion of turbulent flame structure in premixed charges,” *SAE Pap.*, vol. 850345, 1985.
- [13] J. Jarosinski, “The thickness of laminar flames,” *Combust. Flame*, vol. 56, no. 3, pp. 337–342, 1984.
- [14] S. M. Candel and T. J. Poinsoot, “Flame Stretch and the Balance Equation for the Flame Area,” *Combust. Sci. Technol.*, vol. 70, no. 1–3, pp. 1–15, 1990.
- [15] R. J. Blint, “The Relationship of the Laminar Flame Width to Flame Speed AU - BLINT, RICHARD J.,” *Combust. Sci. Technol.*, vol. 49, no. 1–2, pp. 79–92, Sep. 1986.
- [16] P. Clavin, “Dynamic behavior of premixed flame fronts in laminar and turbulent flows,” *Prog. Energy Combust. Sci.*, vol. 11, no. 1, pp. 1–59, 1985.
- [17] B. Karlovitz, D. W. Denniston, D. H. Knapschaefer, and F. E. Wells, “Studies on Turbulent flames,” *Symp. Combust.*, vol. 4, no. 1, pp. 613–620, 1953.
- [18] G. H. Markstein, “Non-steady flame propagation,” 1964.

- 
- [19] F. A. Williams, "A review of some theoretical considerations of turbulent flame structure," *Agard Conf Proc.*, vol. 164, 1974.
- [20] S. H. Chung and C. K. Law, "An invariant derivation of flame stretch," *Combust. Flame*, vol. 55, no. 1, pp. 123–125, 1984.
- [21] F. Creta and M. Matalon, "Strain rate effects on the nonlinear development of hydrodynamically unstable flames," *Proc. Combust. Inst.*, vol. 33, no. 1, pp. 1087–1094, 2011.
- [22] C. J. Mueller, J. F. Driscoll, D. J. Sutkus, W. L. Roberts, M. C. Drake, and M. D. Smooke, "Effect of unsteady stretch rate on OH chemistry during a flame-vortex interaction: To assess flamelet models," *Combust. Flame*, vol. 100, no. 1–2, pp. 323–331, 1995.
- [23] D. Bradley, P. H. Gaskell, and X. J. Gu, "Burning velocities, Markstein lengths, and flame quenching for spherical methane-air flames: A computational study," *Combust. Flame*, vol. 104, no. 1–2, pp. 176–198, 1996.
- [24] G. Darrieus, "Propagation d'un front de flamme. Essai de théorie des vitesses anormales de déflagration par un développement spontané de turbulence.," *Congrès Mécanique Appliquée (unpublished Work.)*, 1945.
- [25] L. D. Landau, "On the theory of slow combustion," *Acta Physicochim. URSS*, vol. 19, pp. 77–85, 1944.
- [26] D. Bradley, R. A. Hicks, M. Lawes, C. G. W. Sheppard, and R. Woolley, "The measurement of laminar burning velocities and Markstein numbers for iso-octane-air and iso-octane-n-heptane-air mixtures at elevated temperatures and pressures in an explosion bomb," *Combust. Flame*, vol. 115, no. 1–2, pp. 126–144, 1998.
- [27] F. A. Williams, *Combustion Theory: The Fundamental Theory of Chemically Reacting Flow System*, 2nd Editio. Massachusetts: Perseus Books Group, 1985.
- [28] J. K. Bechtold and M. Matalon, "The dependence of the Markstein length on stoichiometry," *Combust. Flame*, vol. 127, no. 1–2, pp. 1906–1913, 2001.
- [29] R. J. K. A.E. Lutz, F.M. Rupley, "Equil: A Chemkin Implementation of Stanjan for Computing Chemical Equilibria, Sandia National Laboratories Livermore, CA 94551." 1992.
- [30] B. Galmiche, "Caractérisation expérimentale des flammes laminaires et turbulentes en expansion.," 2014.
- [31] A. Bonhomme, L. Selle, and T. J. Poinso, "Curvature and confinement effects for flame speed measurements in laminar spherical and cylindrical flames.," *Combust. Flame*, vol. 160, no. 7, pp. 1208–1214, 2013.
- [32] G. H. Markstein, "Experimental and theoretical studies of flame-front stability," *J. Aeronaut. Sci.*, vol. 18, no. 3, pp. 109–209, 1951.
- [33] P. Clavin and F. A. Williams, "Effects of molecular-diffusion and thermal-expansion on the structure and dynamics of premixed flames in turbulent flows of large-scale and low intensity," *J. Fluid Mech.*, vol. 116, pp. 251–282, 1982.
- [34] M. Matalon and B. J. Matkowsky, "Flames as gasdynamic discontinuities," *J. Fluid Mech.*, vol. 124, pp. 239–259, 1982.
- [35] F. Halter, T. Tahtouh, and C. Mounaïm-Rousselle, *Nonlinear effects of stretch on the flame*
-

- front propagation*, vol. 157. 2010.
- [36] A. P. Kelley and C. K. Law, "Nonlinear effects in the extraction of laminar flame speeds from expanding spherical flames," *Combust. Flame*, vol. 156, no. 9, pp. 1844–1851, 2009.
- [37] Z. Chen and Y. Ju, "Theoretical analysis of the evolution from ignition kernel to flame ball and planar flame.," *Combust. Flame*, vol. 11, no. 3, pp. 427–453, 2007.
- [38] Y. Ju, G. Masuya, and P. D. Ronney, "Effects of radiative emission and absorption on the propagation and extinction of premixed gas flames.," *Symp. Combust.*, vol. 27, no. 2, pp. 2619–2626, 1998.
- [39] J. Park *et al.*, "Flame characteristics in H<sub>2</sub>/CO synthetic gas diffusion flames diluted with CO<sub>2</sub>: Effects of radiative heat loss and mixture composition.," *Int. J. Hydrogen Energy*, vol. 33, no. 23, pp. 7256–7264, 2008.
- [40] J. Jayachandran, R. Zhao, and F. N. Egolfopoulos, "Determination of laminar flame speeds using stagnation and spherically expanding flames: Molecular transport and radiation effects," *Combust. Flame*, vol. 161, no. 9, pp. 2305–2316, 2014.
- [41] G. I. Taylor, "Statistical Theory of Turbulence," *Proc. R. Soc. A Math. Phys. Eng. Sci.*, vol. 151, no. 873, pp. 421–444, 1935.
- [42] T. de Karman and L. Howarth, "On the Statistical Theory of Isotropic Turbulence," *Proc. R. Soc. A Math. Phys. Eng. Sci.*, vol. 164, no. 917, pp. 192–215, 1938.
- [43] G. I. Taylor, "The spectrum of turbulence," *Proc. R. Soc. A Math. Phys. Eng. Sci.*, vol. 164, no. 919, pp. 476–490, 1938.
- [44] R. G. Abdel-Gayed, K. J. Al-Khishali, and D. Bradley, "Turbulent Burning Velocities and Flame Straining in Explosions," *Proc. R. Soc. A Math. Phys. Eng. Sci.*, vol. 391, no. 1801, pp. 393–414, 1984.
- [45] J. O. Hinze, *Turbulence*, 2nd Ed. McGraw-Hill, 1975.
- [46] P. Burattini, P. Lavoie, and R. A. Antonia, "On the normalized turbulent energy dissipation rate," *Phys. Fluids*, vol. 17, 2005.
- [47] R. W. Borghi, *On the structure and morphology of turbulent premixed flames. In Recent Advances in the Aerospace Science (ed. C. Casci)*. 1985.
- [48] N. Peters, "Laminar flamelet concepts in turbulent combustion," *Symp. Combust.*, vol. 21, no. 1, pp. 1231–1250, 1988.
- [49] R. A. Kenneth K. Kuo, "Fundamentals of Turbulent and Multiphase of Turbulent Combustion," 2012.
- [50] P. Boudier, S. Henriot, T. Poinsot, and T. Baritaud, "A model for turbulent flame ignition and propagation in spark ignition engines," *Proc. Combust. Inst.*, vol. 24, no. 1, pp. 503–510, 1992.
- [51] O. Colin and A. Benkenida, "3D Modelling of Mixing, Ignition and Combustion Phenomena in Highly Stratified Gasoline Engines," *Ecfm*, vol. 58, no. 1, pp. 47–62, 2003.
- [52] G. Damköhler, "Der Einfluss der Turbulenz auf die Flammgeschwindigkeit in Gasgemischen," *Zeitschrift für Elektrochemie und Angew. Phys. Chemie*, vol. 46, no. 11, 1940.

- [53] J. F. Driscoll, "Turbulent premixed combustion: Flamelet structure and its effect on turbulent burning velocities," *Proc. Energy Combust. Sci.*, vol. 34, no. 1, pp. 91–134, 2008.
- [54] K. N. C. Bray, "Studies of the Turbulent Burning Velocity," *Proc. R. Soc. A Math. Phys. Eng. Sci.*, vol. 431, no. 1882, pp. 315–335, 1990.
- [55] T. Poinso, D. Veynante, and S. Candel, "Diagrams of premixed turbulent combustion based on direct simulation," *Symp. Combust.*, vol. 23, no. 1, pp. 613–619, 1991.
- [56] N. Peters, "The turbulent burning velocity for large-scale and small-scale turbulence," *J. Fluid Mech.*, vol. 384, pp. 107–132, 1999.
- [57] F. Dinkelacker, "Experimental validation of flame regimes for highly turbulent premixed flames," *Proc. Eur. Combust. Meet.*, pp. 158–163, 2003.
- [58] D. Bradley *et al.*, "Turbulent burning velocity, burned gas distribution, and associated flame surface definition," *Combust. Flame*, vol. 133, no. 4, pp. 415–430, 2003.
- [59] M. Z. Haq, "Fundamental Studies of Premixed Combustion."
- [60] B. Renou, A. Boukhalfa, D. Puechberty, and M. Trinité, "Effects of stretch on the local structure of freely propagating premixed low-turbulent flames with various lewis numbers," *Symp. Combust.*, vol. 27, no. 1, pp. 841–847, 1998.
- [61] S. Chaudhuri, A. Saha, and C. K. Law, "On flame-turbulence interaction in constant-pressure expanding flames," *Proc. Combust. Inst.*, vol. 35, no. 2, pp. 1331–1339, 2015.
- [62] M. Matalon, "On Flame Stretch," *Combust. Sci. Technol.*, vol. 31, no. 3–4, pp. 169–181, 2007.
- [63] P. Brequigny, F. Halter, C. Mounaïm-Rousselle, and T. Dubois, "Fuel performances in Spark-Ignition (SI) engines: Impact of flame stretch," *Combust. Flame*, vol. 166, pp. 98–112, 2016.
- [64] R. G. Abdel-Gayed, D. Bradley, M. N. Hamid, and M. Lawes, "Lewis number effects on turbulent burning velocity," *Symp. Combust.*, vol. 20, no. 1, pp. 505–512, 1985.
- [65] D. Bradley, A. K. C. Lau, and M. Lawes, "Flame Stretch Rate as a Determinant of Turbulent Burning Velocity," *Ph. Transcr. R. Soc. A Math. Phys. Eng. Sci.*, vol. 338, no. 1650, pp. 359–387, 1992.
- [66] S. A. Filatyev, J. F. Driscoll, C. D. Carter, and J. M. Donbar, "Measured properties of turbulent premixed flames for model assessment, including burning velocities, stretch rates, and surface densities," *Combust. Flame*, vol. 141, no. 1–2, pp. 1–21, 2005.
- [67] M. Z. Haq, C. G. W. Sheppard, R. Woolley, D. A. Greenhalgh, and R. D. Lockett, "Wrinkling and curvature of laminar and turbulent premixed flames," *Combust. Flame*, vol. 131, no. 1–2, pp. 1–15, 2002.
- [68] S. Daniele, P. Jansohn, K. Mantzaras, and K. Boulouchos, "Turbulent flame speed for syngas at gas turbine relevant conditions," *Proc. Combust. Inst.*, vol. 33, no. 2, pp. 2937–2944, 2011.
- [69] B. Galmiche, F. Halter, and F. Foucher, "Effects of high pressure, high temperature and dilution on laminar burning velocities and Markstein lengths of iso-octane/air mixtures," *Combust. Flame*, vol. 159, no. 11, pp. 3286–3299, 2012.
- [70] R. G. Abdel-Gayed, D. Bradley, M. N. Hamid, and M. Lawes, "Lewis number effects on turbulent burning velocity," *Symp. Combust.*, vol. 20, no. 1, pp. 505–512, 1985.

- [71] S. Richard, "Simulation aux grandes échelles de la combustion dans les moteurs à allumage commandé," *Techniques*, vol. 33, 2005.
- [72] D. Linse, C. Hasse, and B. Durst, "An experimental and numerical investigation of turbulent flame propagation and flame structure in a turbo-charged direct injection gasoline engine," *Combust. Theory Model*, vol. 13, no. 1, pp. 167–188, 2009.
- [73] C. Mounaïm-Rousselle, L. Landry, F. Halter, and F. Foucher, "Experimental characteristics of turbulent premixed flame in a boosted Spark-Ignition engine," *Proc. Combust. Inst.*, vol. 34, no. 2, pp. 2941–2949, 2013.
- [74] E. Maistret *et al.*, "Recent developments in the coherent flamelet description of turbulent combustion," *Proc. Third Int. Conf. Numer. Combust.*, pp. 98–117, 1989.
- [75] S. Richard, O. Colin, O. Vermorel, A. Benkenida, C. Angelberger, and D. Veynante, "Towards large eddy simulation of combustion in spark ignition engines," *Proc. Combust. Inst.*, vol. 31 II, pp. 3059–3066, 2007.
- [76] O. Vermorel, S. Richard, O. Colin, C. Angelberger, A. Benkenida, and D. Veynante, "Towards the understanding of cyclic variability in a spark ignited engine using multi-cycle LES," *Combust. Flame*, vol. 156, no. 8, pp. 1525–1541, 2009.
- [77] W. Li, Z. Liu, Z. Wang, and Y. Xu, "Experimental investigation of the thermal and diluent effects of EGR components on combustion and NO<sub>x</sub> emissions of a turbocharged natural gas SI engine," *Energy Convers. Manag.*, vol. 88, pp. 1041–1050, 2014.
- [78] S. Lee, S. Park, C. Kim, Y. M. Kim, Y. Kim, and C. Park, "Comparative study on EGR and lean burn strategies employed in an SI engine fueled by low calorific gas," *Appl. Energy*, vol. 129, pp. 10–16, 2014.
- [79] L. Francqueville and J. B. Michel, "On the Effects of EGR on Spark-Ignited Gasoline Combustion at High Load," *SAE Int. J. Engines*, vol. 7, no. 4, pp. 1808–1823, 2014.
- [80] L. Landry, "Etude expérimentale des modes de combustion essence sous forte pression et forte dilution," 2009.
- [81] C. C. Liu, S. S. Shy, M. W. Peng, C. W. Chiu, and Y. C. Dong, "High-pressure burning velocities measurements for centrally-ignited premixed methane/air flames interacting with intense near-isotropic turbulence at constant Reynolds numbers," *Combust. Flame*, 2012.
- [82] S. Chaudhuri, F. Wu, D. Zhu, and C. K. Law, "Flame Speed and Self-Similar Propagation of Expanding Turbulent Premixed Flames," *Phys. Rev. Lett.*, vol. Article 04, p. 108, 2012.
- [83] F. Wu, A. Saha, S. Chaudhuri, and C. K. Law, "Propagation speeds of expanding turbulent flames of C<sub>4</sub> to C<sub>8</sub> n-alkanes at elevated pressures: Experimental determination, fuel similarity, and stretch-affected local extinction," *Proc. Combust. Inst.*, vol. 35, no. 2, pp. 1501–1508, 2015.
- [84] H. Kobayashi, K. Seyama, H. Hagiwara, and Y. Ogami, "Burning velocity correlation of methane/air turbulent premixed flames at high pressure and high temperature," *Proc. Combust. Inst.*, vol. 30, no. 1, pp. 827–834, Jan. 2005.
- [85] H. Kobayashi, H. Hagiwara, H. Kaneko, and Y. Ogami, "Effects of CO<sub>2</sub> dilution on turbulent premixed flames at high pressure and high temperature," *Proc. Combust. Inst.*, vol. 31, no. 1, pp. 1451–1458, Jan. 2007.

- [86] L. J. Jiang, S. S. Shy, W. Y. Li, H. M. Huang, and M. T. Nguyen, "High-temperature, high-pressure burning velocities of expanding turbulent premixed flames and their comparison with Bunsen-type flames," *Combust. Flame*, vol. 172, pp. 173–182, Oct. 2016.
- [87] A. N. Lipatnikov and J. Chomiak, "Effects of premixed flames on turbulence and turbulent scalar transport," *Prog. Energy Combust. Sci.*, vol. 36, no. 1, pp. 1–102, 2010.
- [88] P. Brequigny, F. Halter, and C. Mounaïm-Rousselle, "Lewis number and Markstein length effects on turbulent expanding flames in a spherical vessel," *Exp. Therm. Fluid Sci.*, vol. 73, pp. 33–41, 2016.
- [89] M. Lawes, M. P. Ormsby, C. G. W. Sheppard, and R. Woolley, "The turbulent burning velocity of iso-octane/air mixtures," *Combust. Flame*, vol. 159, no. 5, pp. 1949–1959, 2012.
- [90] P. Brequigny, C. Endouard, F. Foucher, and C. Mounaïm-Rousselle, "Improvement of turbulent burning velocity measurements by Schlieren technique, for high pressure iso-octane-air premixed flames," *Combust. Sci. Technol.*, 2019.
- [91] J. Sosa, J. Chambers, K. A. Ahmed, A. Poludnenko, and V. N. Gamezo, "Compressible turbulent flame speeds of highly turbulent standing flames," *Proc. Combust. Inst.*, vol. 37, no. 3, pp. 3495–3502, 2019.
- [92] Q. Tang, H. Liu, M. Li, M. Yao, and Z. Li, "Study on ignition and flame development in gasoline partially premixed combustion using multiple optical diagnostics," *Combust. Flame*, vol. 177, pp. 98–108, 2017.
- [93] A. W. Skiba, T. M. Wabel, C. D. Carter, S. D. Hammack, J. E. Temme, and J. F. Driscoll, "Premixed flames subjected to extreme levels of turbulence part I: Flame structure and a new measured regime diagram," *Combust. Flame*, vol. 189, pp. 407–432, Mar. 2018.
- [94] Z. S. Li, B. Li, Z. W. Sun, X. S. Bai, and M. Aldén, "Turbulence and combustion interaction: High resolution local flame front structure visualization using simultaneous single-shot PLIF imaging of CH, OH, and CH<sub>2</sub>O in a piloted premixed jet flame," *Combust. Flame*, 2010.
- [95] Z. Wang *et al.*, "Structure and burning velocity of turbulent premixed methane/air jet flames in thin-reaction zone and distributed reaction zone regimes," *Proc. Combust. Inst.*, vol. 37, no. 2, pp. 2537–2544, 2019.
- [96] J. F. Driscoll, J. H. Chen, A. W. Skiba, C. D. Carter, E. R. Hawkes, and H. Wang, "Premixed flames subjected to extreme turbulence: Some questions and recent answers," *Prog. Energy Combust. Sci.*, vol. 76, p. 100802, Jan. 2020.
- [97] N. Peters, "The turbulent burning velocity for large-scale and small-scale turbulence," *J. Fluid Mech.*, vol. 384, pp. 107–132, 1999.
- [98] S. E. Trautwein, A. Grudno, and G. Adomeit, "The influence of turbulence intensity and laminar flame speed on turbulent flame propagation under engine like conditions," *Symp. Combust.*, vol. 23, no. 1, pp. 723–728, 1991.
- [99] M. T. Nguyen, D. W. Yu, and S. S. Shy, "General correlations of high pressure turbulent burning velocities with the consideration of Lewis number effect," *Proc. Combust. Inst.*, vol. 37, no. 2, pp. 2391–2398, 2019.
- [100] C. Endouard, F. Halter, C. Chauveau, and F. Foucher, "Effects of CO<sub>2</sub>, H<sub>2</sub>O, and Exhaust Gas Recirculation Dilution on Laminar Burning Velocities and Markstein Lengths of Iso-Octane/Air Mixtures," *Combust. Sci. Technol.*, vol. 188, no. 4–5, pp. 516–528, 2016.

- [101] B. Galmiche, F. Halter, F. Foucher, and P. Dagaut, "Effects of Dilution on Laminar Burning Velocity of Premixed Methane / Air Flames," pp. 948–954, 2011.
- [102] D. Bradley, C. G. W. Sheppard, I. M. Suardjaja, and R. Woolley, "Fundamentals of high-energy spark ignition with lasers," *Combust. Flame*, vol. 138, no. 1–2, pp. 55–77, 2004.
- [103] S. M. CANDEL and T. J. POINSOT, "Flame Stretch and the Balance Equation for the Flame Area," *Combust. Sci. Technol.*, vol. 70, no. 1–3, pp. 1–15, Mar. 1990.
- [104] O. A. Manna, M. S. Mansour, W. L. Roberts, and S. H. Chung, "Influence of Ethanol and Exhaust Gas Recirculation on Laminar Burning Behaviors of Fuels for Advanced Combustion Engines (FACE-C) Gasoline and Its Surrogate," *Energy and Fuels*, vol. 31, no. 12, pp. 14104–14115, 2017.
- [105] J. X. Zhou, M. Cordier, C. Mounaïm-Rousselle, and F. Foucher, "Experimental estimate of the laminar burning velocity of iso-octane in oxygen-enriched and CO<sub>2</sub>-diluted air," *Combust. Flame*, vol. 158, no. 12, pp. 2375–2383, 2011.
- [106] J. P. J. Van Lipzig, E. J. K. Nilsson, L. P. H. De Goey, and A. A. Konnov, "Laminar burning velocities of n -heptane , iso-octane , ethanol and their binary and tertiary mixtures," *Fuel*, vol. 90, no. 8, pp. 2773–2781, 2011.
- [107] R. J. Moffat, "Describing the uncertainties in experimental results," *Exp. Therm. Fluid Sci.*, vol. 1, no. 1, pp. 3–17, 1988.
- [108] O. Nilaphai, "Vaporization and Combustion Processes of Alcohols and Acetone-Butanol-Ethanol (ABE) blended in n-Dodecane for High Pressure-High Temperature Conditions: Application to Compression Ignition Engine," 2018.
- [109] A. Tsinober, "An Informal Introduction to Turbulence," in *Fluid Mechanics and its Applications*, vol. 63, 2004, p. 332.
- [110] P.-Å. Krogstad and P. A. Davidson, *Near-field investigation of turbulence produced by multi-scale grids*, vol. 24. 2012.
- [111] T. Kurian and J. H. M. Fransson, "Grid-generated turbulence revisited," *Fluid Dyn. Res.*, vol. 41, no. 2, 2009.
- [112] N. Peters, "Laminar flamelet concepts in turbulent combustion," *Symp. Combust.*, vol. 21, no. 1, pp. 1231–1250, 1988.
- [113] X. Wu *et al.*, *Laminar Burning Velocities and Flame Instabilities of 2,5-Dimethylfuran-Air Mixtures at Elevated Pressures*, vol. 158. 2011.
- [114] P. Brequigny, G. Dayma, F. Halter, C. Mounaïm-Rousselle, T. Dubois, and P. Dagaut, "Laminar burning velocities of premixed nitromethane/air flames: An experimental and kinetic modeling study," *Proc. Combust. Inst.*, vol. 35, no. 1, pp. 703–710, 2015.
- [115] O. Manna, M. S. Mansour, W. L. Roberts, and S. H. Chung, "Laminar burning velocities at elevated pressures for gasoline and gasoline surrogates associated with RON," *Combust. Flame*, vol. 162, no. 6, pp. 2311–2321, 2015.
- [116] W. J. Pitz, N. P. Cernansky, F. L. Dryer, F. N. Egolfopoulos, J. T. Farrell, and D. G. Friend, "Development of an Experimental Database and Chemical Kinetic Models for Surrogate Gasoline Fuels," 2007.

- [117] A. P. Cruz *et al.*, “A complex chemical kinetic mechanism for the oxidation of gasoline surrogate fuels : n heptane , iso octane and toluene - Mechanism development and validation To cite this version : HAL Id : hal-00370855,” 2009.
- [118] T. Edwards *et al.*, “Development of an Experimental Database and Kinetic Models for Surrogate Jet Fuels,” in *45th AIAA Aerospace Sciences Meeting and Exhibit*, American Institute of Aeronautics and Astronautics, 2007.
- [119] R. H. Stanglmaier *et al.*, *Measurement of Laminar Burning Velocity of Multi-Component Fuel Blends for Use in High-Performance SI Engines*. 2003.
- [120] R. Bounaceur *et al.*, *Modeling The Laminar Flame Speed of Natural Gas and Gasoline Surrogates*, vol. SAE. 2010.
- [121] S. Jerzembeck, N. Peters, P. Pepiot-Desjardins, and H. Pitsch, “Laminar burning velocities at high pressure for primary reference fuels and gasoline: Experimental and numerical investigation,” *Combust. Flame*, vol. 156, no. 2, pp. 292–301, 2009.
- [122] J. T. Farrell, R. J. Johnston, and I. P. Androulakis, “Molecular Structure Effects On Laminar Burning Velocities At Elevated Temperature And Pressure,” 2004.
- [123] L. Sileghem *et al.*, “Laminar burning velocity of gasoline and the gasoline surrogate components iso-octane, n-heptane and toluene,” *Fuel*, vol. 112, pp. 355–365, 2013.
- [124] D. Bradley, M. Lawes, K. Liu, S. Verhelst, and R. Woolley, “Laminar burning velocities of lean hydrogen – air mixtures at pressures up to 1 . 0 MPa,” vol. 149, pp. 162–172, 2007.
- [125] S. G. DAVIS and C. K. LAW, “Determination of and Fuel Structure Effects on Laminar Flame Speeds of C1 to C8 Hydrocarbons,” *Combust. Sci. Technol.*, vol. 140, no. 1–6, pp. 427–449, Dec. 1998.
- [126] T. Tahtouh, F. Halter, E. Samson, and C. Mounaïm-Rousselle, “Effects of hydrogen addition and nitrogen dilution on the laminar flame characteristics of premixed methane-air flames,” *Int. J. Hydrogen Energy*, vol. 34, no. 19, pp. 8329–8338, 2009.
- [127] H. J. Curran, “Developing detailed chemical kinetic mechanisms for fuel combustion,” *Proc. Combust. Inst.*, vol. 37, no. 1, pp. 57–81, 2018.
- [128] J. Santner, F. L. Dryer, and Y. Ju, “The effects of water dilution on hydrogen, syngas, and ethylene flames at elevated pressure,” *Proc. Combust. Inst.*, vol. 34, no. 1, pp. 719–726, 2013.
- [129] F. Halter, F. Foucher, L. Landry, and C. Mounaïm-Rousselle, “Effect of Dilution by Nitrogen and/or Carbon Dioxide on Methane and Iso-Octane Air Flames,” *Combust. Sci. Technol.*, vol. 181, no. July 2014, pp. 813–827, 2009.
- [130] S. P. Marshall, S. Taylor, C. R. Stone, T. J. Davies, and R. F. Cracknell, “Laminar burning velocity measurements of liquid fuels at elevated pressures and temperatures with combustion residuals,” *Combust. Flame*, vol. 158, no. 10, pp. 1920–1932, 2011.
- [131] M. Metghalchi and J. C. Keck, “Burning velocities of mixtures of air with methanol, isooctane, and indolene at high pressure and temperature,” *Combust. Flame*, vol. 48, no. C, pp. 191–210, 1982.
- [132] E. Varea, V. Modica, B. Renou, and A. Boukhalfa, *Pressure effects on laminar burning velocities and Markstein lengths for Isooctane–Ethanol–Air mixtures*, vol. 34. 2013.

- [133] M. P. Burke, Z. Chen, Y. Ju, and F. L. Dryer, “Effect of cylindrical confinement on the determination of laminar flame speeds using outwardly propagating flames,” *Combust. Flame*, vol. 156, no. 4, pp. 771–779, 2009.
- [134] C. Meneveau and T. Poinso, “Stretching and quenching of flamelets in premixed turbulent combustion,” *Combust. Flame*, vol. 86, no. 4, pp. 311–332, 1991.
- [135] I. Han and K. Y. Huh, “Roles of displacement speed on evolution of flame surface density for different turbulent intensities and Lewis numbers in turbulent premixed combustion,” *Combust. Flame*, vol. 152, no. 1–2, pp. 194–205, 2008.
- [136] Z. Wang, V. Magi, and J. Abraham, “Turbulent Flame Speed Dependencies in Lean Methane-Air Mixtures under Engine Relevant Conditions,” *Combust. Flame*, vol. 180, pp. 53–62, 2017.



# 1. ANNEX A: Flame Stretch

The idea of the flame stretch rate was figured out by the works of Clavin [16], Karlovitz [17] and Markstein [18]. With the term stretch rate one refers to two different phenomena acting on the flame evolution: the flame front curvature and the velocity gradients acting in front of the flame front. Stretch may cause variations of the flame propagation speed [17], [18] and, thus, of the laminar burning velocity. Local flame extinctions may arise if the stretch rate is too intense. However, these phenomena also depend on the thermodynamic conditions and on the mixture composition.

The stretch rate represents the rate at which the surface of an element on the flame surface increases during the flame front propagation. Therefore, according to Williams [19] the stretch rate can be computed as:

$$K = \frac{1}{A} \frac{dA}{dt} \quad (91)$$

where  $A$  is the surface of an element of the flame front surface. In the literature several mathematical definitions of the stretch rate  $K$  exist [20]–[22]. In the following, the one developed from earlier work of Candel and Poinot [14] will be presented, using the support of the scheme in Figure 99. Being  $\vec{G}$  a vector, the variation rate of the flux of this vector through the surface  $A(t)$  is

$$\frac{d}{dt} \int_{A(t)} \vec{G} \cdot \vec{n} dA \quad (92)$$

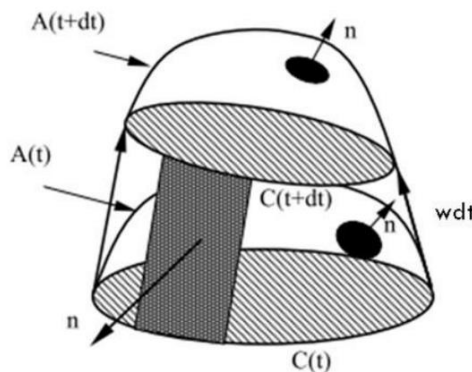


Figure 99. Laminar flame displacement at  $t$  and  $t + dt$  at speed  $w$ , with element surface  $A(t)$  and flame contour  $C(t)$  [14].

where  $\vec{n}$  is the versor normal to the surface  $A$ . The surface element itself translates with the velocity  $\vec{w}$ .

It is necessary, then, to apply the transport law to the flux variation rate evaluation:

$$\frac{d}{dt} \int_{A(t)} \vec{G} \cdot \vec{n} dA = \frac{d}{dt} \int_{A(t)} \left[ \frac{\partial \vec{G}}{\partial t} + \vec{w} \cdot \vec{\nabla} \vec{G} - \vec{G} \cdot \vec{\nabla} \vec{w} + \vec{G} \vec{\nabla} \cdot \vec{w} \right] \cdot \vec{n} dA \quad (93)$$

considering the generic vector  $\vec{G}$  to be equal to  $\vec{n}$ , one obtains:

$$\frac{d}{dt} \int_{A(t)} dA = \frac{d}{dt} \int_{A(t)} \left[ \frac{\partial \vec{n}}{\partial t} + \vec{w} \cdot \vec{\nabla} \vec{n} - \vec{n} \cdot \vec{\nabla} \vec{w} + \vec{n} \vec{\nabla} \cdot \vec{w} \right] \cdot \vec{n} dA \quad (94)$$

but, being  $\vec{n}$  a versor (then, unitary), normal to the surface, one can simplify:

$$\frac{\partial \vec{n}}{\partial t} \cdot \vec{n} = \frac{1}{2} \frac{\partial \vec{n}^2}{\partial t} = 0 \quad (95)$$

$$(\vec{w} \cdot \vec{\nabla} \vec{n}) \cdot \vec{n} = \vec{w} \cdot \vec{\nabla} \left( \frac{1}{2} \vec{n}^2 \right) = 0 \quad (96)$$

such that the equation Eq. (94) results:

$$\frac{d}{dt} \int_{A(t)} dA = \frac{d}{dt} \int_{A(t)} (-\vec{n} \vec{n} : \vec{\nabla} \vec{w} + \vec{\nabla} \cdot \vec{w}) dA \quad (97)$$

remembering that  $\vec{n} \vec{n} : \vec{\nabla} \vec{w} = n_i n_j \partial w_i / \partial x_j$ .

finally, the stretch rate is

$$K = \frac{1}{A} \frac{dA}{dt} = -\vec{n} \vec{n} : \vec{\nabla} \vec{w} + \vec{\nabla} \cdot \vec{w} \quad (98)$$

where the velocity  $\vec{w}$  is the sum of the fresh gases velocity  $\vec{u}_g$  and the flame front velocity in the normal direction  $\vec{n}$ , that is,  $S_L^0 \vec{n}$ , yielding:

$$K = -\vec{n} \vec{n} : \vec{\nabla} \vec{u}_g + \vec{\nabla} \cdot \vec{u}_g + S_L^0 \vec{\nabla} \cdot \vec{n} \quad (99)$$

It is then possible to separate the effects of the flame curvature, term  $S_L^0 \vec{\nabla} \cdot \vec{n}$ , and the effects of the shear stresses along the normal and tangential direction, so that:

$$K_S = -\vec{n} \vec{n} : \vec{\nabla} \vec{u}_g + \vec{\nabla} \cdot \vec{u}_g \quad (100)$$

$$K_C = S_L {}^0\vec{\nabla} \cdot \vec{n} \quad (101)$$

And, thus, obtain the total stretch rate as sum of two different contributes:

$$K = K_S + K_C \quad (102)$$

Bradley and co-workers [23] found that these two components of the stretch rate proposed by Candel and Poinso [14] can be re-written in the simple form:

$$K_S = \frac{2}{R_f} u_g \quad (103)$$

and

$$K_C = \frac{2}{R_f} S_L \quad (104)$$

if a laminar spherical flame is considered.

The mutual relations between  $S_L$ ,  $u_g$  and  $V_L$ , lead to the following equation for the stretch rate:

$$K = \frac{2}{R_f} V_L \quad (105)$$

---

## 2. ANNEX B: Minimum and Maximum Radius

### Minimum radius $R_{min}$ : ignition effects

The influence of the ignition system of the spherical vessel was analyzed by Galmiche [30] using different discharging energy between the electrodes. This energy is driven by the coil charging time. Several laminar premixed flames tests were performed under the same reference conditions: isooctane/air mixture at  $P_{ref} = 1$  bar,  $T_{ref} = 423$  K and equivalence ratio  $\phi = 1$ . Figure 100 (a) and (b) resumes the obtained results.

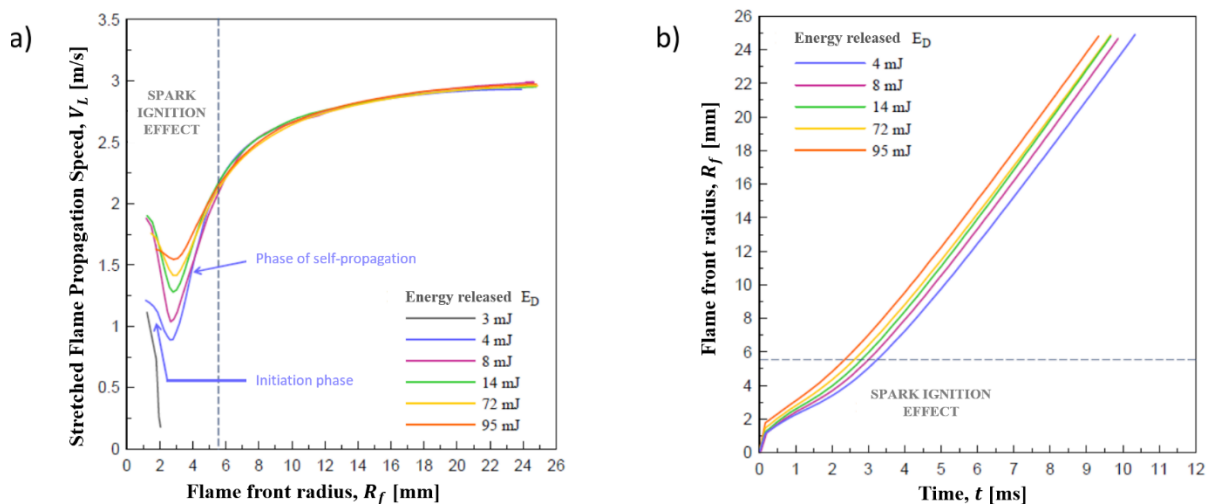


Figure 100. Evaluation of the  $R_{min}$  due to the spark ignition effect, adapted from [30].

Figure 100 (a) represents the flame propagation speed  $V_L$  as function of the radius  $R_f$ . It is evident that reducing the discharging energy directly causes a decrease of the speed  $V_L$  after the spark. Then an increase is observed, except for the discharging energies too low to allow the propagation of the flame. In the same way, Figure 100 (b) displays the radius  $R_f$  evolution as function of the time for the different discharging energies. In the first instants, the curves show different behavior but successively they evolve in the same way. These results demonstrate that the correct  $R_{min}$  should be between 5 and 6 mm in order to avoid the effects of the ignition system on the velocity evaluation. In the following a minimal discharging energy will be used to reduce the ignition effects on the flame propagation [36]. It is worth to note that the so-evaluated  $R_{min}$  depends on time and, also, on the mixture propagation speed under

certain thermodynamic conditions. It seems plausible that, for slower flames, the threshold showed in Figure 100 (b) might be located at lower radii. Anyway, this heuristic assumption needs further experimental investigation.

### Maximum radius $R_{max}$ : confining and flame/wall interaction effects

The confinement and the flame/wall interaction may affect the isobaric flame propagation hypothesis. The closed geometry of the vessel avoid the exhaust of the burned gases during the combustion. This clearly produces a pressure increase as in a common ICE. Galmiche [30] has gathered the pressure trace evolution during the flame propagation for all the performed tests in order to verify the isobaric propagation hypothesis. The pressure trace shows a quasi-constant value in the first propagation phase and, then, the pressure start to rapidly increase reaching the maximum when the flame approaches the wall. As for the  $R_{min}$  investigation, the same reference conditions were maintained for all the tests. A constant volume resolution approach was used to determine the radius evolution in function of time. Figure 101 shows the results of this investigation, evidencing the consistency of the isobaric hypothesis.

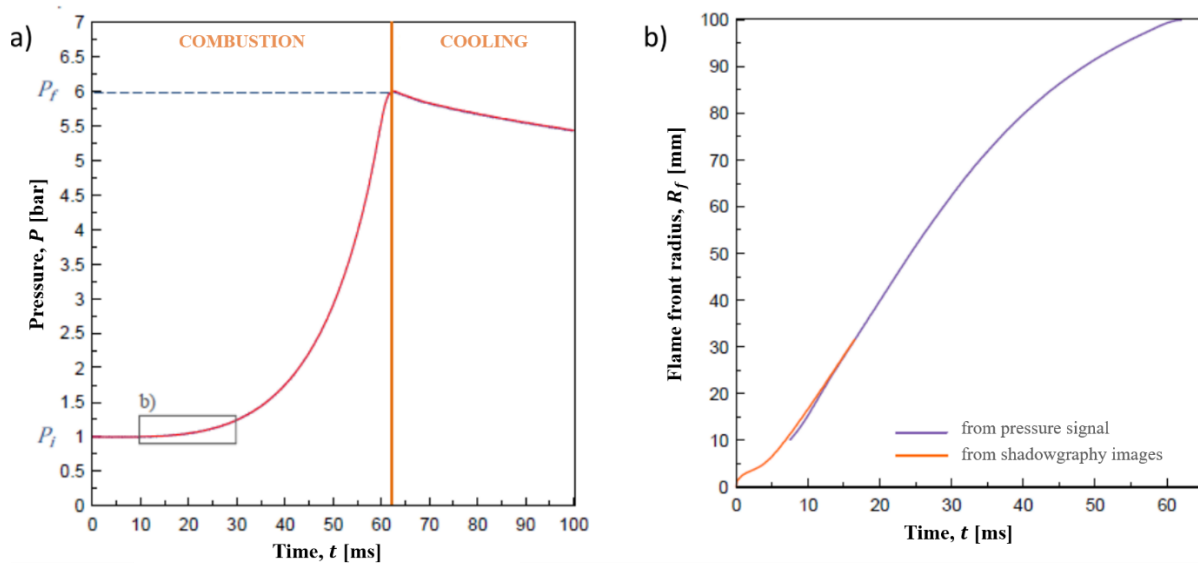


Figure 101. Evaluation of the  $R_{max}$  due to the confinement effect, using the pressure trace, adapted from [30].

The 2% pressure increase during the observable flame propagation can be considered negligible in the laminar burning velocity evaluation. This means that the isobaric flame propagation is consistent up to at least 15 ms, that is, an  $R_{max}$  of 27.9 mm. Anyway, different initial mixture and thermodynamic conditions may change this radius value, that is why a safety  $R_{max}$  of 25 mm will be used to consider valid the hypothesis. This radius corresponds just to the 1.6 % of the whole volume of the vessel, justifying the slight pressure increase and, thus, the isobaric flame propagation hypothesis.

The confinement can affect the fresh gases velocity outside the spherical flame front. The propagation push the fresh gases compressing them between the flame front and the wall. Burke et al. [133] evaluated that this confinement effect can be considered negligible if the radius is less than the 30 % of the spherical vessel radius. The spherical vessel used in the present work has a radius  $R_0 = 100$  mm and, thus, the  $R_{max}$  previously fixed is already lower than the 30% of this radius. In this respect, the confinement effects are negligible in the present analysis.

As sum of this discussion, the present study will take into account only flame radii,  $R_f$ , comprised in the range  $R_{min} = 5$  mm and  $R_{max} = 25$  mm to determine the unstretched laminar burning velocity  $S_L^0$ .

---

### 3. ANNEX C: Details of NOSE Set-up

NOSE offers a certain flexibility degree in the initial Compression Ratio (CR) that can vary from 12.3:1 eventually to 15:1, considering the original design volumes at the Bottom Dead Center (BDC) and at the Top Dead Center (TDC). This compression ratio range is actually different due to the modified cylinder head that alters the initial and final volumes. The initial and final volumes can be varied by adding a plate of specific thickness between the head and the body of the piston (see Table 10 and Figure 102 (a) and (b)). Figure 102 (c), instead, shows the scheme of the removable thermocouple and the blowing out effect.

Table 10. The compression ratio variation according to the thickness of the metallic plate.

<i>Plate thickness</i>	<i>Volume at BDC [cm<sup>3</sup>] (original design)</i>	<i>Volume at TDC [cm<sup>3</sup>] (original design)</i>	<i>Resulting CR</i>
4.00	3601.6	240.4	15
2.55	3629.8	268.7	13.5
1.55	2648.7	287.5	12.7
1.23	3658.2	297.0	12.3

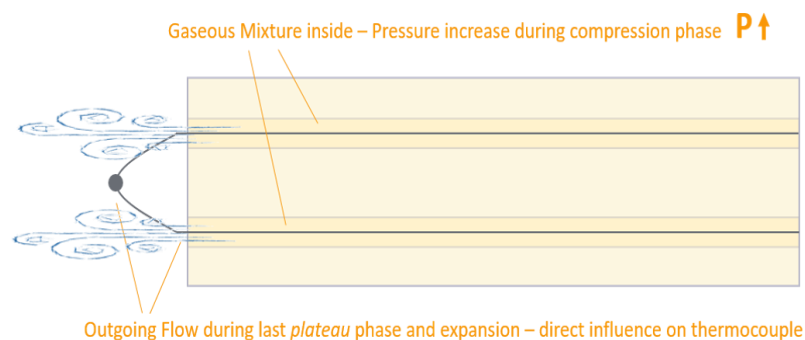
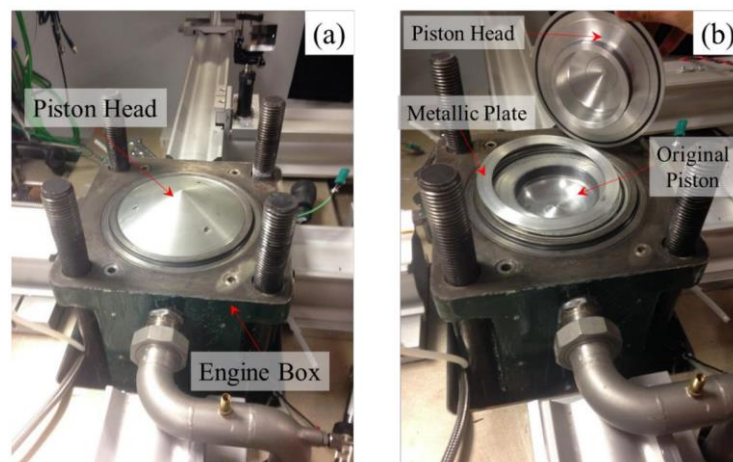


Figure 102. (a) and (b) details of NOSE piston and removable plates to change the compression ratio, adapted from [108]; (c) scheme of the removable thermocouple and blowing out effect during the expansion.

### Error in the evaluation of the internal temperature

Even though the fine wire thermocouple grants a fast temporal response, a priori, it would be necessary to evaluate the influence of heat transfer between the thermocouple wire (bead), the hot gases and the walls. In previous work, with higher temperature and faster piston trajectories, Nilaphai [108] showed that the difference between the measured temperature and the corrected one is limited to the compression and expansion phases. During the *plateau*, instead, the error is generally in the range of the instrument precision (Figure 103 (b)). The ambient temperature  $T_{amb}$  was evaluated using the Dupont's correlation:

$$T_{corr} = T_{amb} + \left( \frac{\rho_w c_w d_b^2 [1 + 0.5(d_w^2/d_b^2)]}{6 Nu_b k} \right) \frac{dT_{amb}}{dt} + \frac{\epsilon \sigma}{h} (T_{amb}^4 - T_w^4) \quad (106)$$

where the subscripts  $w$  and  $b$  refer, respectively, to wall or bead quantities,  $\epsilon$  is the emissivity of the thermocouple bead,  $\sigma$  is the Stefan-Boltzmann constant ( $5.6703 \cdot 10^{-8} [Wm^{-2}K^{-4}]$ ),  $h$  is the heat transfer coefficient [ $Wm^{-2}K^{-1}$ ],  $d$  is a diameter,  $k$  the thermal conductivity of the gas [ $Wm^{-1}K^{-1}$ ], while  $Nu$  is the Nusselt number of the thermocouple (assuming a spherical shape). The conduction heat transfer of the wire can be neglected due to small diameter (13  $\mu m$ ). The radiation heat transfer is taken into account in the last term, while the second one is the time response of the thermocouple with respect to the temperature variations. Figure 103 reports the results of this analysis. Since in the present work we will focus the flame investigation within the *plateau* limits, the evidenced error on compression and expansion phase will be not considered.

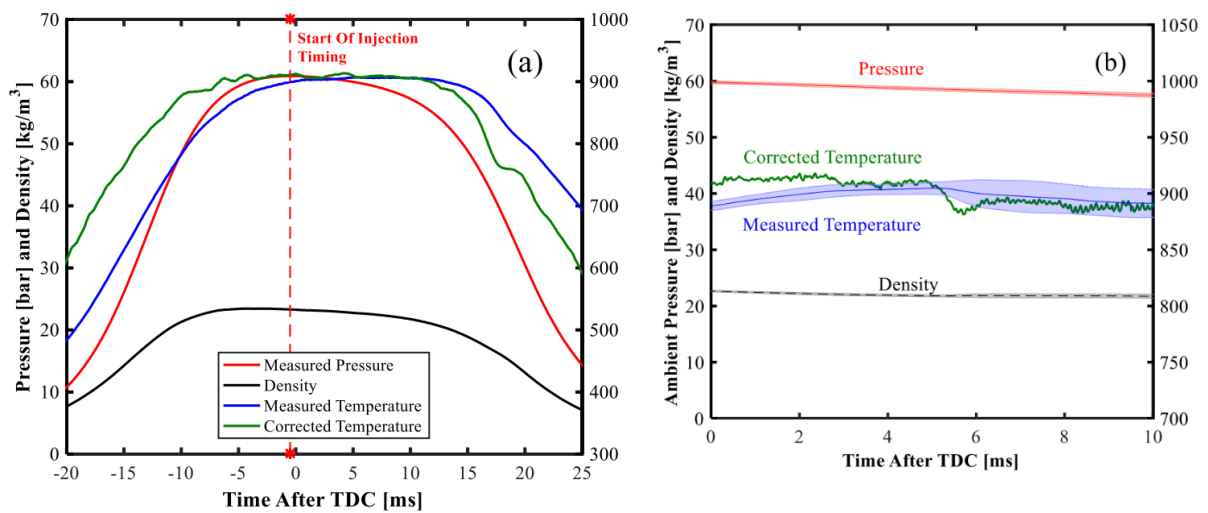


Figure 103. Temperature error evaluation, adapted from [108].

# 4. ANNEX D: Complementary Data for Turbulent Flames Investigation

In this Annex, complementary data collected from the investigation of turbulent flames are presented.

Table 11, Table 12 and Table 13 report the evaluation of the fundamental parameters for comparison of turbulent premixed flames.

Table 11. Investigated experimental conditions on spherical vessel with  $q' = 2.77$  m/s and evaluation of the fundamental parameters for the turbulent flames analysis.

Sphere $q' = 2.77$ m/s – $L_T$ 3.4 mm			$q'/S_L^0$	$L_T/\delta_L^0$	$L_T/\delta_L^B$	$Ka$	$Ka_B$	$Da$	$Re_T$	$\eta_K$ [ $\mu\text{m}$ ]	
<b>P</b> <b>1 bar</b>	<b>T</b> <b>473K</b>	0.9	4.15	46.97	7.78	1.23	17.45	11.33	194.80	51.67	
		1	3.89	50.36	8.17	1.08	15.57	12.96	195.68		
		1.1	3.79	51.82	8.36	1.03	14.84	13.66	196.56		
		1.2	3.85	51.32	8.37	1.05	15.04	13.34	197.44		
		1.3	4.06	48.83	8.12	1.17	16.37	12.02	198.32		
<b>P</b> <b>5 bar</b>	<b>T</b> <b>423K</b>	<b>20%</b>	1.1	14.73	73.72	12.30	6.58	42.97	5.00	1085.98	13.40
			1.2	15.44	70.53	11.44	7.23	48.45	4.57	1089.37	
			1.3	17.84	61.24	10.04	9.63	63.75	3.43	1092.67	
		<b>25%</b>	1.1	18.36	59.03	10.14	10.24	64.94	3.21	1083.86	
			1.2	19.31	56.21	9.52	11.31	72.77	2.91	1085.15	
			1.3	22.36	48.65	8.13	15.16	98.66	2.18	1088.11	
	<b>T</b> <b>435K</b>	<b>20%</b>	1	14.71	71.45	12.89	6.68	40.94	4.86	1051.13	13.86
			1.1	14.03	75.29	12.77	6.05	39.42	5.37	1056.08	
			1.2	14.71	72.01	11.88	6.65	44.44	4.89	1059.32	
		<b>25%</b>	1.1	18.29	57.46	10.45	10.32	62.76	3.14	1050.91	
			1.2	17.48	60.18	10.74	9.42	58.39	3.44	1052.30	
			1.3	18.39	57.39	9.88	10.41	66.78	3.12	1055.21	
	<b>T</b> <b>473K</b>	<b>0%</b>	0.8	9.07	106.06	19.88	2.65	16.29	11.69	961.97	15.94
			0.9	6.98	139.44	22.85	1.56	10.91	19.97	973.64	
1			5.98	163.48	26.11	1.14	8.18	27.32	978.06		
1.1			5.66	173.73	27.70	1.02	7.29	30.72	982.48		
1.2			5.88	167.83	27.21	1.10	7.71	28.54	986.86		
1.3			6.74	147.14	24.39	1.44	9.86	21.84	991.25		
<b>20%</b>		1.1	12.12	80.34	14.09	4.70	30.69	6.63	973.34		
		1.2	12.72	76.29	13.24	5.19	34.29	6.00	970.15		
		1.3	14.71	66.16	11.59	6.94	45.31	4.50	973.12		
<b>25%</b>		1.1	15.10	63.92	11.72	7.34	45.98	4.23	965.26		
		1.2	15.90	60.80	10.99	8.13	51.61	3.82	966.39		
		1.3	18.44	52.56	9.38	10.92	70.13	2.85	969.04		
<b>30%</b>	1.2	20.18	47.80	8.91	13.11	80.80	2.37	964.41			
	1.3	23.47	41.12	7.60	17.73	110.27	1.75	965.15			

ANNEX D: COMPLEMENTARY DATA FOR TURBULENT FLAMES INVESTIGATION

Table 12. Investigated experimental conditions on spherical vessel with  $q' = 1.77$  m/s and evaluation of the fundamental parameters for the turbulent flames analysis.

Sphere $q' = 1.77$ m/s – $L_T$ 3.4 mm			$q' / S_L^0$	$L_T / \delta_L^0$	$L_T / \delta_L^B$	$Ka$	$Ka_B$	$Da$	$Re_T$	$\eta_K$ [ $\mu\text{m}$ ]	
<b>P 1 bar</b>	<b>T 473K</b>	<b>0%</b>	0.8	2.97	41.30	7.93	0.80	9.81	13.89	122.78	72.29
			0.9	2.65	46.97	7.78	0.63	8.91	17.72	124.47	
			1	2.48	50.36	8.17	0.55	7.95	20.28	125.04	
			1.1	2.42	51.82	8.36	0.52	7.58	21.38	125.60	
			1.2	2.46	51.32	8.37	0.54	7.68	20.87	126.16	
			1.3	2.60	48.83	8.12	0.60	8.36	18.82	126.73	
<b>P 5 bar</b>	<b>T 343K</b>	<b>20%</b>	1.1	13.58	63.41	9.17	6.29	42.46	4.67	861.27	14.23
			1.2	14.21	60.40	8.60	6.89	47.37	4.25	858.42	
			1.3	16.38	52.55	7.59	9.15	61.90	3.21	861.05	
		<b>25%</b>	1.2	17.76	48.22	7.07	10.78	72.01	2.71	856.57	
			1.3	20.54	41.75	6.15	14.40	95.76	2.03	857.43	
			1.1	12.62	62.92	10.30	5.65	35.15	4.99	793.95	
	<b>T 368K</b>	<b>20%</b>	1.1	12.01	66.42	10.18	5.11	33.82	5.53	797.67	15.62
			1.2	12.57	63.63	9.47	5.59	38.08	5.06	800.14	
			1.3	14.51	55.32	8.34	7.43	49.87	3.81	802.58	
		<b>25%</b>	1.2	15.72	50.80	7.78	8.74	57.92	3.23	798.41	
			1.3	18.18	43.95	6.76	11.69	77.17	2.42	799.20	
			1	11.39	65.76	11.13	4.74	29.34	5.77	749.16	
	<b>T 390K</b>	<b>20%</b>	1.1	10.85	69.37	11.02	4.29	28.24	6.39	752.69	16.81
			1.2	11.37	66.42	10.25	4.70	31.81	5.84	754.98	
			1.3	13.12	57.72	9.01	6.26	41.74	4.40	757.29	
		<b>25%</b>	1.1	13.52	55.54	9.10	6.67	42.64	4.11	751.20	
			1.2	14.21	52.93	8.54	7.36	47.72	3.73	752.06	
			1.3	16.45	45.85	7.30	9.85	64.60	2.79	754.11	
<b>30%</b>		1.2	18.03	41.62	6.93	11.87	74.58	2.31	750.50		
		1.3	20.94	35.87	5.92	15.99	101.46	1.71	751.09		
		<b>T 450K</b>	<b>20%</b>	0.9	10.24	63.10	12.43	4.13	23.63	6.16	
1	8.86			73.43	13.21	3.08	19.22	8.29	650.30		
1.1	8.45			77.23	13.36	2.79	18.13	9.14	652.33		
1.2	8.86		73.83	12.43	3.07	20.44	8.33	654.32			
1.3	10.24		64.06	10.90	4.10	26.96	6.25	656.32			
<b>25%</b>	1		11.01	58.96	10.94	4.76	28.87	5.36	649.14		
	1.1	10.53	61.73	11.24	4.35	26.87	5.86	649.99			
	1.2	11.08	58.84	10.33	4.81	30.74	5.31	651.78			
<b>30%</b>	1.3	12.84	50.90	8.82	6.45	41.73	3.96	653.56			
	1.1	13.33	48.69	9.15	6.97	41.76	3.65	648.78			
	1.2	14.06	46.18	8.57	7.76	47.07	3.28	649.37			
1.3	16.35	39.82	7.15	10.47	65.60	2.44	650.95				
<b>T 473K</b>	<b>0%</b>	0.8	5.80	105.89	20.32	1.36	8.14	18.27	613.69	22.31	
		0.9	4.46	139.44	22.85	0.80	5.57	31.25	622.15		
		1	3.82	163.48	26.11	0.58	4.18	42.76	624.97		
		1.1	3.61	173.73	27.70	0.52	3.72	48.08	627.79		
		1.2	3.76	167.83	27.21	0.56	3.94	44.67	630.59		
		1.3	4.30	147.14	24.39	0.74	5.04	34.18	633.40		
	<b>20%</b>	0.9	9.38	65.83	11.86	3.54	22.57	7.02	617.44		
		1	8.11	75.94	14.07	2.65	16.46	9.36	616.11		
		1.1	7.74	79.83	14.22	2.41	15.53	10.31	618.03		
		1.2	8.13	76.29	13.24	2.65	17.52	9.39	619.92		
		1.3	9.40	66.16	11.59	3.54	23.14	7.04	621.81		

Table 13. Investigated experimental conditions on NOSE, for the three turbulent configurations, m/s and evaluation of the fundamental parameters for the turbulent flames analysis

				$\frac{q'}{S_L^0}$	$L_T/\delta_L^0$	$L_T/\delta_L^B$	$Ka$	$Ka_B$	$Da$	$Re_T$	$\eta_K [\mu m]$	
<b>LV</b> $L_T = 2.35$ <b>mm</b> $q' = 2.31$ m/s	<b>T</b> <b>373 K</b> <b>P</b> <b>8 bar</b>	<b>10%</b>	1	11.54	99.00	14.12	3.94	28.70	8.58	1142.37	8.358	
			1.1	10.77	106.15	15.11	3.43	25.03	9.86	1143.08		
			1.1	16.09	70.76	10.60	7.67	53.29	4.40	1138.21		
		<b>20%</b>	1.2	16.88	67.41	10.10	8.45	58.71	3.99	1137.95		
			1.3	19.86	57.47	8.74	11.67	79.87	2.89	1141.39		
<b>SV-HTI</b> $L_T = 2.07$ <b>mm</b> $q' = 3.29$ m/s	<b>T</b> <b>585 K</b> <b>P</b> <b>21 bar</b>	<b>10%</b>	1.1	8.41	244.39	46.74	1.56	9.49	29.05	2056.16	5.404	
			1.2	8.93	231.85	43.64	1.75	10.80	25.95	2071.52		
			1.3	11.01	188.89	36.22	2.66	16.03	17.16	2079.21		
		<b>20%</b>	1.2	13.41	153.70	30.44	3.96	23.24	11.46	2061.78		
			1.3	16.61	124.06	24.50	6.08	35.75	7.47	2060.76		
		<b>25%</b>	1.2	16.76	122.32	24.56	6.20	35.99	7.30	2050.08		
			1.3	20.81	98.61	19.83	9.56	55.35	4.74	2052.12		
<b>SV-Std</b> $L_T = 2.07$ <b>mm</b> $q' = 2.70$ m/s	<b>T</b> <b>605 K</b> <b>P</b> <b>21 bar</b>		0.9	8.98	176.41	37.86	2.02	11.02	19.66	1583.34	6.532	
			1	7.09	225.28	43.96	1.26	7.49	31.78	1596.81		
			<b>10%</b>	1.1	6.50	246.53	47.00	1.06	6.43	37.92		1602.82
				1.2	6.91	232.94	44.70	1.19	7.18	33.73		1608.85
				1.3	8.51	189.71	37.07	1.80	10.67	22.29		1614.82
			<b>20%</b>	1	10.53	150.99	30.94	2.78	15.83	14.33		1590.55
				1.1	9.71	163.79	33.52	2.36	13.47	16.87		1590.73
				1.2	10.37	153.88	30.70	2.69	15.70	14.84		1595.63
				1.3	12.84	124.61	25.08	4.12	23.81	9.70		1600.50
				<b>25%</b>	1.1	12.10	131.20	27.59	3.67	20.38		10.84
			1.2		12.96	122.68	25.46	4.21	23.66	9.47		1589.44

Figure 104, Figure 105, Figure 106, Figure 107 and Figure 108 report the evaluation of the  $V_T$ , the contour to perimeter factor and the barycenter displacement, for test performed on the spherical vessel. Images are grouped by common range of Karlovitz number. On the contrary, Figure 109 and Figure 110 represent the same analysis but grouped by used configuration.

Discussion on these images and obtained results is proposed in Chapter 5.

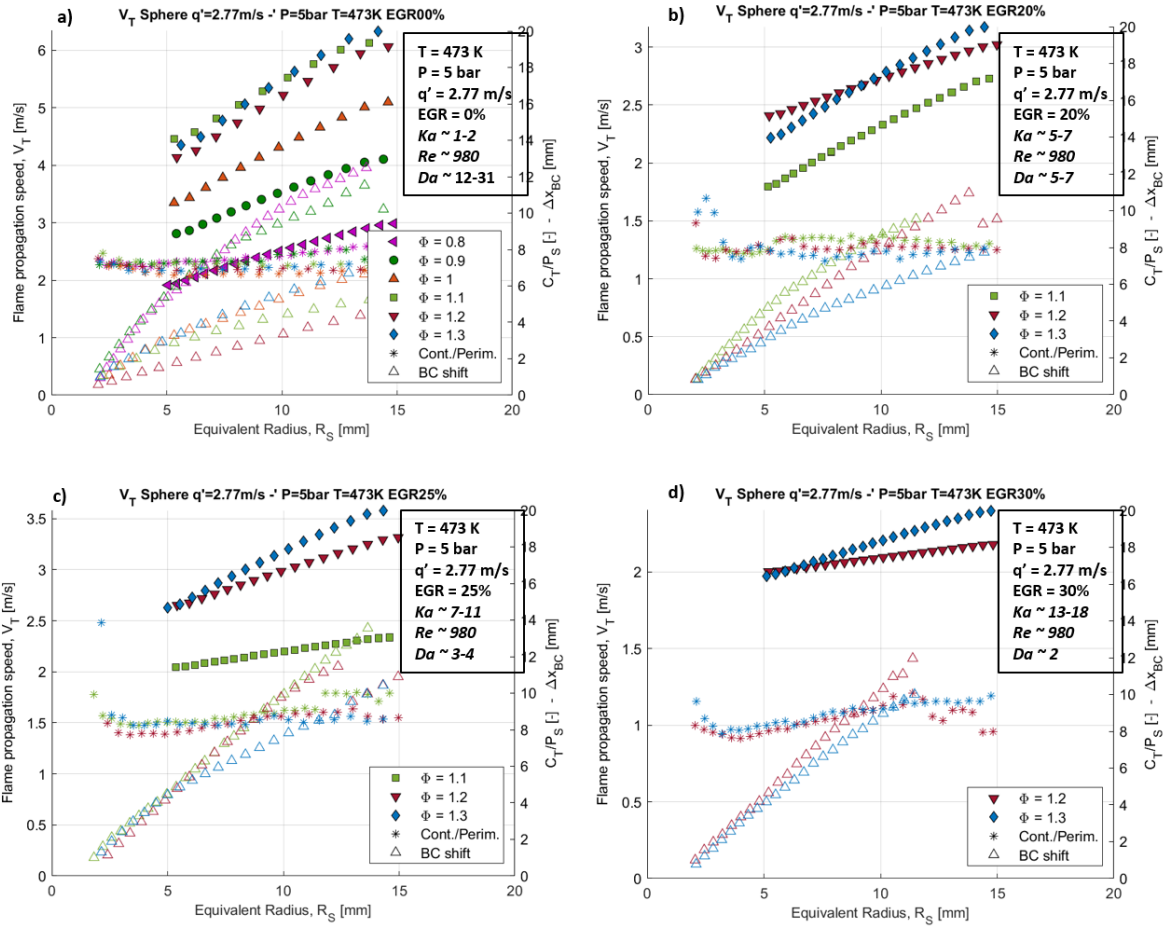


Figure 104. Turbulent flame propagation speed (left y axis), absolute barycenter displacement in the tridimensional domain (x, y, z directions) and wrinkling ratio (right y axis) measured on spherical vessel for different initial parameters.

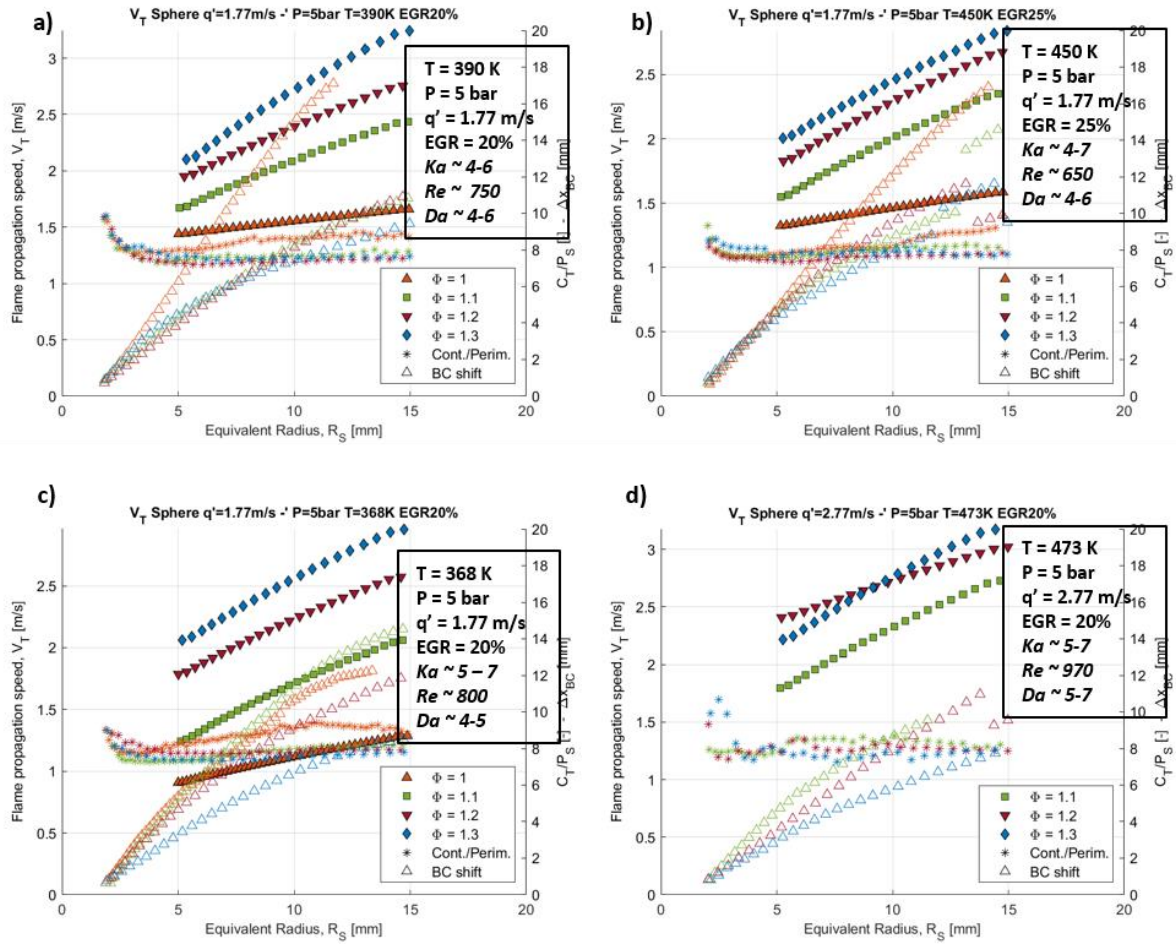


Figure 105. Turbulent flame propagation speed (left y axis), absolute barycenter displacement in the tridimensional domain (x, y, z directions) and wrinkling ratio (right y axis) measured on spherical vessel for different initial parameters covering a Karlovitz number range from about 4 to 7.

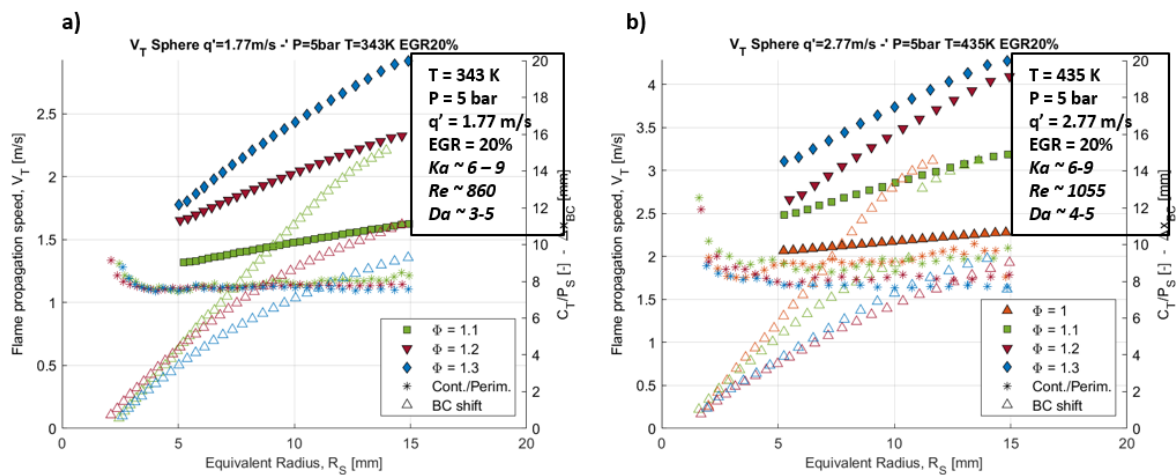


Figure 106. Turbulent flame propagation speed (left y axis), absolute barycenter displacement in the tridimensional domain (x, y, z directions) and wrinkling ratio (right y axis) measured on spherical vessel for different initial parameters covering a Karlovitz number range from about 6 to 9.

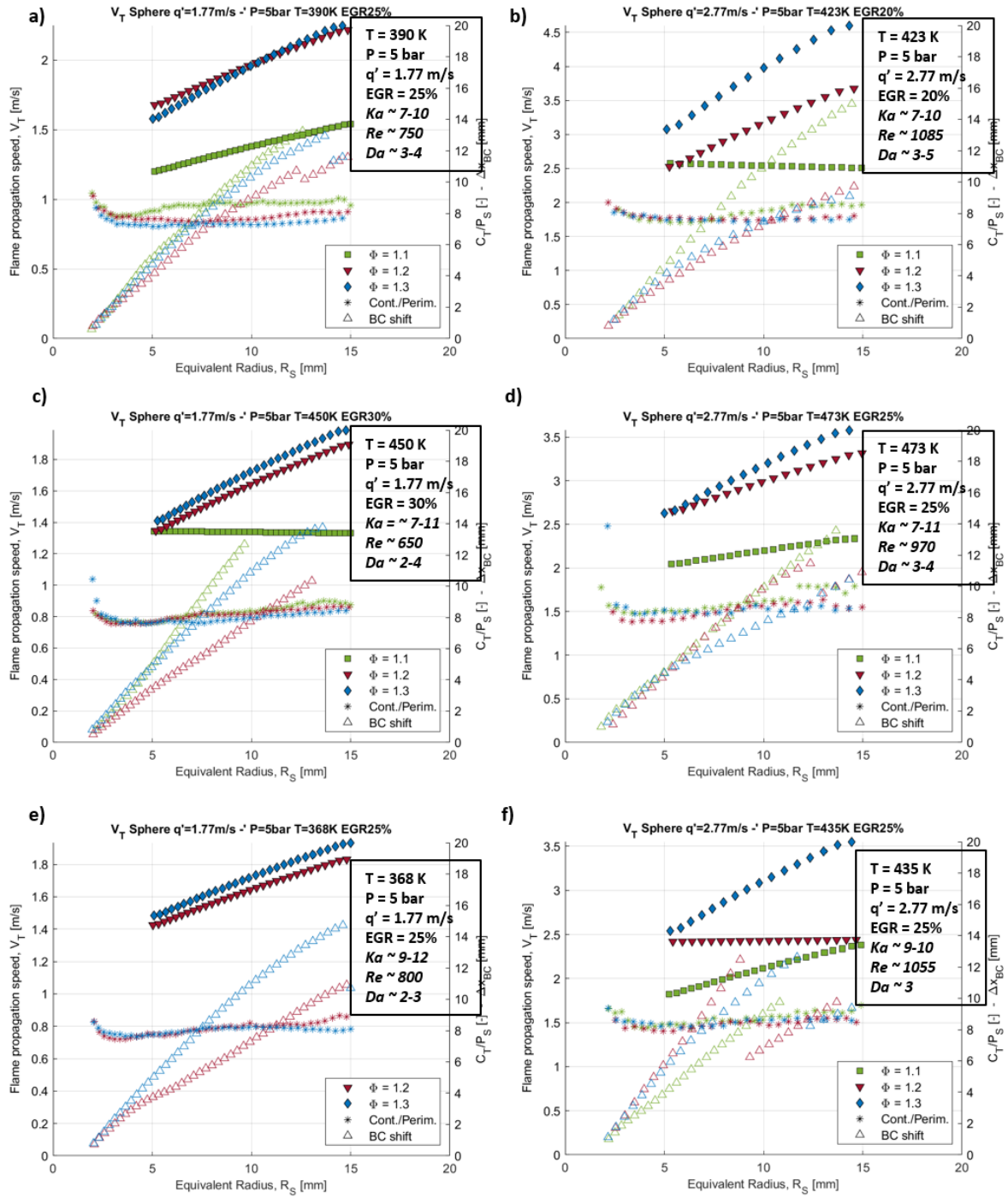


Figure 107. Turbulent flame propagation speed (left y axis), absolute barycenter displacement in the tridimensional domain (x, y, z directions) and wrinkling ratio (right y axis) measured on spherical vessel for different initial parameters covering a Karlovitz number range from about 7 to 12.

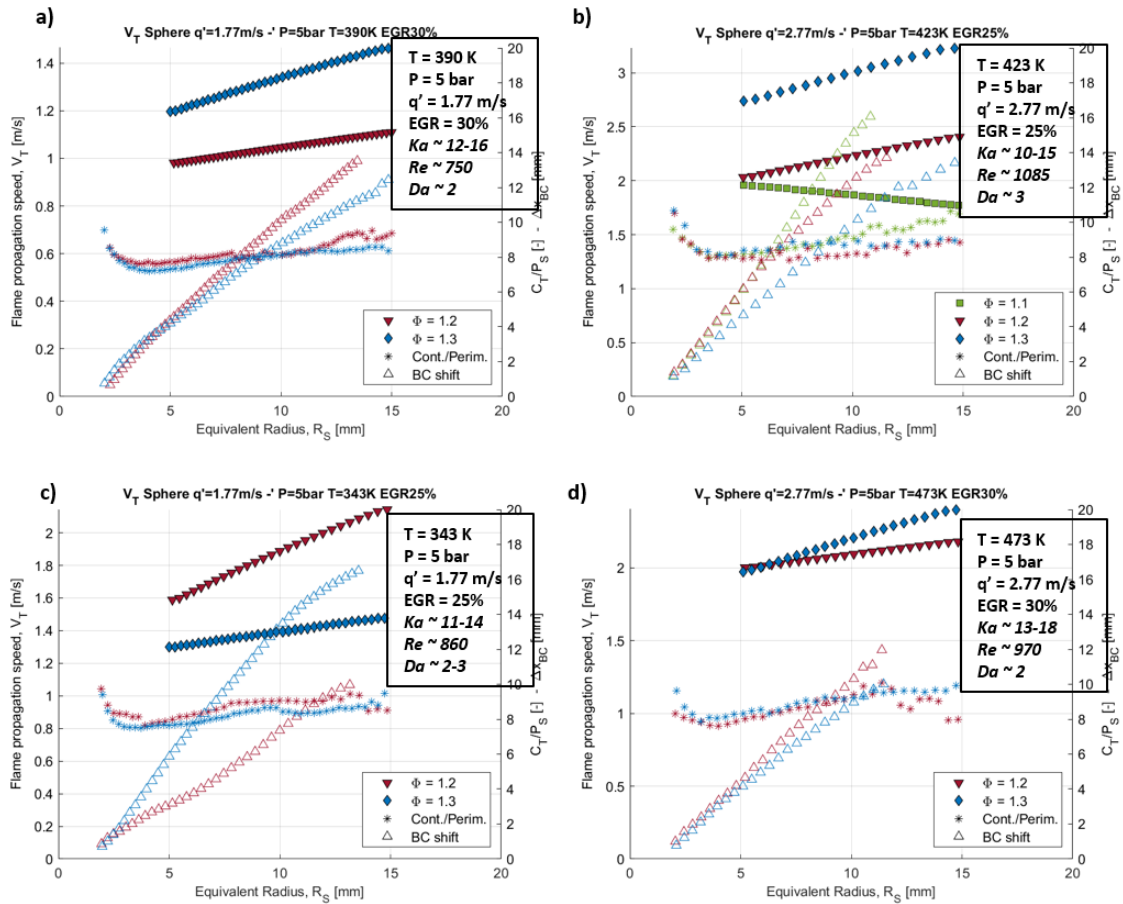


Figure 108. Turbulent flame propagation speed (left y axis), absolute barycenter displacement in the tridimensional domain (x, y, z directions) and wrinkling ratio (right y axis) measured on spherical vessel for different initial parameters covering a Karlovitz numbers higher than 10.

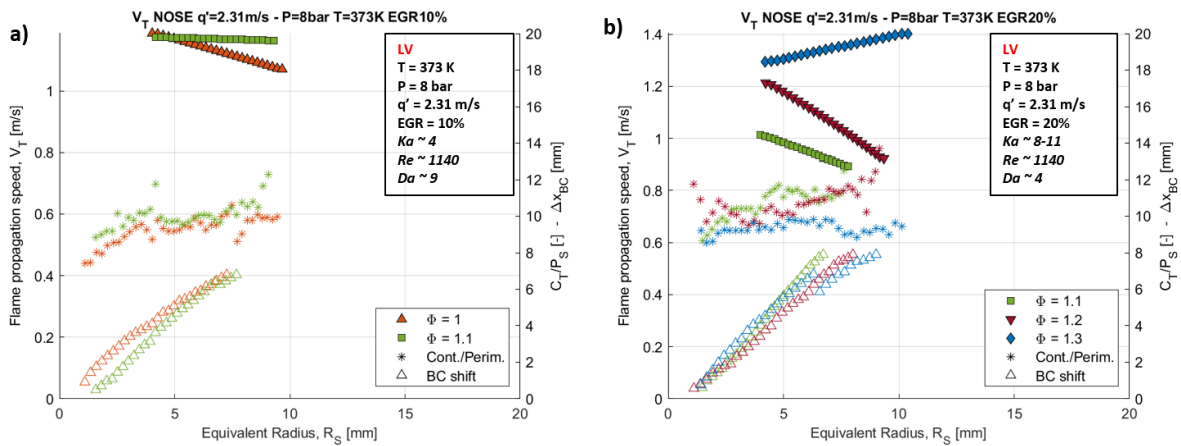


Figure 109. Turbulent flame propagation speed (left y axis), absolute barycenter displacement in the tridimensional domain (x, y, z directions) and wrinkling ratio (right y axis) measured on NOSE LV configuration.

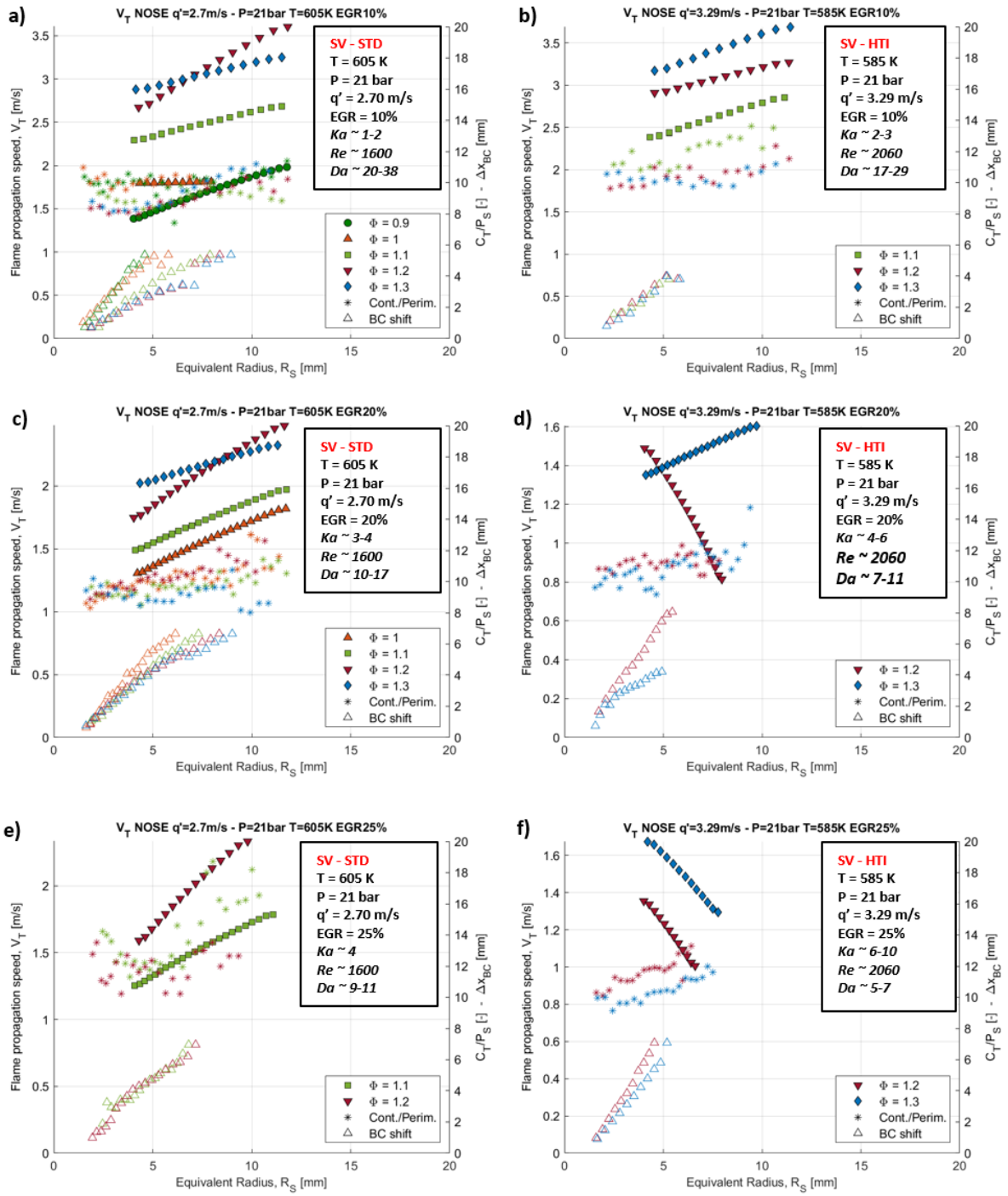


Figure 110. Turbulent flame propagation speed (left y axis), absolute barycenter displacement in the tridimensional domain (x, y, z directions) and wrinkling ratio (right y axis) measured on NOSE SV-Std configuration (on the left) and NOSE SV-HTI configuration (on the right).

---

Marco DI LORENZO

## Étude expérimentale des flammes turbulentes à prémélange dans des conditions d'un moteur à allumage commandé actuel

Parmi les solutions technologiques proposées pour réduire les polluants atmosphériques et les émissions de gaz à effet de serre, le mode de fonctionnement dit "downsizing" des moteurs à combustion interne est considéré comme l'un des plus prometteurs. En augmentant la pression de l'air d'admission, ce mode de fonctionnement permet d'atteindre un meilleur rendement et donc de réduire les émissions polluantes. Mais prédire le processus de combustion dans ces conditions draconiennes (haute pression, température élevée et taux de dilution élevé) reste difficile car les modèles classiques de combustion turbulente de prémélange ne sont pas adaptés. Par conséquent, il est encore nécessaire de fournir des données expérimentales afin de développer et d'améliorer des modèles prédictifs adéquats pour ce procédé de combustion de prémélange turbulente non habituelle.

Pour cela, la première étape a été le choix d'un carburant-modèle simple pour représenter une essence commerciale. Le TRF-E a été choisi et validé en caractérisant ses propriétés intrinsèques fondamentales, en les comparant à celles de l'essence commerciale et en créant une base de données solide de vitesses de flamme laminaires de prémélange air/TRF-E pour une large gamme de conditions thermodynamiques. Ensuite, l'étude des flammes turbulentes de prémélange air/TRF-E a été réalisée grâce à deux montages expérimentaux complémentaires notamment dans une zone du digramme Peters-Borghì, caractérisée par des nombres de Karlovitz et Reynolds élevés où l'effet de dilution ou de haute pression est encore mal identifié. Les conditions de flammes avec ces nombres adimensionnels similaires sont supposées être encore dans le régime de combustion des flammes plissées. Au cours de ce travail expérimental, il a été souligné que générer des conditions de  $Ka$  ou de  $Re$  élevé avec des flammes en expansion à des taux de dilution élevés et une longueur et une pression intégrale de type moteur entraîne une transition vers un autre régime de combustion. En conclusion, des études expérimentales complémentaires sont encore nécessaires pour explorer les limites de ces régimes de combustion et l'adaptation des modèles actuels de flammes dans ces conditions limites constitue une priorité.

*Mots-clés : Flammes turbulentes ; Flammes laminaires ; Combustion fortement diluée ; Moteurs à allumage commandé ; Nombre de Karlovitz*

## Experimental investigation of turbulent premixed flames under modern Spark-Ignition engine-like conditions

Among the technological solutions proposed to reduce air pollutants and greenhouse gases emissions, the so-called "downsizing" operating mode for Internal Combustion Engines is considered one of the most promising. By boosting the intake air pressure, this operating mode allows reaching higher efficiency and, thus, reducing the pollutant emissions. But to predict the combustion process in these drastic conditions (High pressure, high temperature and high dilution rate) remains challenging as the classical turbulent premixed models can be put in default. Therefore, to provide experimental data in order to develop and improve adequate predictive models for this unusual turbulent premixed combustion process is still needed.

For that, as preliminary step, the choice of a surrogate for commercial gasoline has to be validated. ATRF-E was chosen and validated by characterizing its fundamental intrinsic properties, comparing them to those of the commercial gasoline and doing a solid database of laminar premixed air/TRF-E flame speed under a wide range of thermodynamic conditions. Then, the investigation of turbulent premixed air/TRF-E flames was done thanks to two complementary experimental setups especially in a zone of the well-known Peters-Borghì diagram, characterized by high Karlovitz and Reynolds numbers in which the effect of dilution or high pressure is not well identified. Flames sharing similar dimensionless numbers are assumed to be still in the corrugated flamelet combustion regime. During this experimental work, it was highlighted that reaching high  $Ka$ , or high  $Re$  with expanding flames at high dilution rates and engine-like integral length and pressure causes a transition to another combustion regime. As conclusion, complementary experimental studies are still needed to explore the limitation of these combustion regimes and the adaptation of current flamelets models in these limit conditions represents a priority.

*Keywords: Turbulent Flames; Laminar Flames; Highly diluted combustion; Spark-Ignition engines; Karlovitz number*



PRISME, 8 rue Léonard de Vinci, 45072 Orléans Cedex 2